Max-Planck-Institut für Kolloid- und Grenzflächenforschung

INTEGRATED BIOREFINERY IN CONTINUOUS FLOW SYSTEMS USING SUSTAINABLE HETEROGENEOUS CATALYSTS

Dissertation

zur Erlangung des akademischen Grades

„Doctor rerum naturalium“

(Dr. rer. nat.)

in der Wissenschaftsdisziplin „Kolloid- und Polymerchemie“

Eingereicht an der

Mathematisch- Naturwissenschaftlichen Fakultät

der Universität Potsdam

Von

Francesco Brandi

Ort und Tag der Disputation: Potsdam, 25.01.2022

Hauptbetreuer: Prof. Dr. Dr. h.c. Markus Antonietti
Betreuerinnen: Prof. Dr. Helmut Schlaad

Gutachterinnen: Prof. Dr. Dr. h.c. Markus Antonietti
Prof. Dr. Helmut Schlaad
Prof. Dr. Bert Sels

Published online on the
Publication Server of the University of Potsdam:
https://doi.org/10.25932/publishup-53766
https://nbn-resolving.org/urn:nbn:de:kobv:517-opus4-537660

Graphical abstract

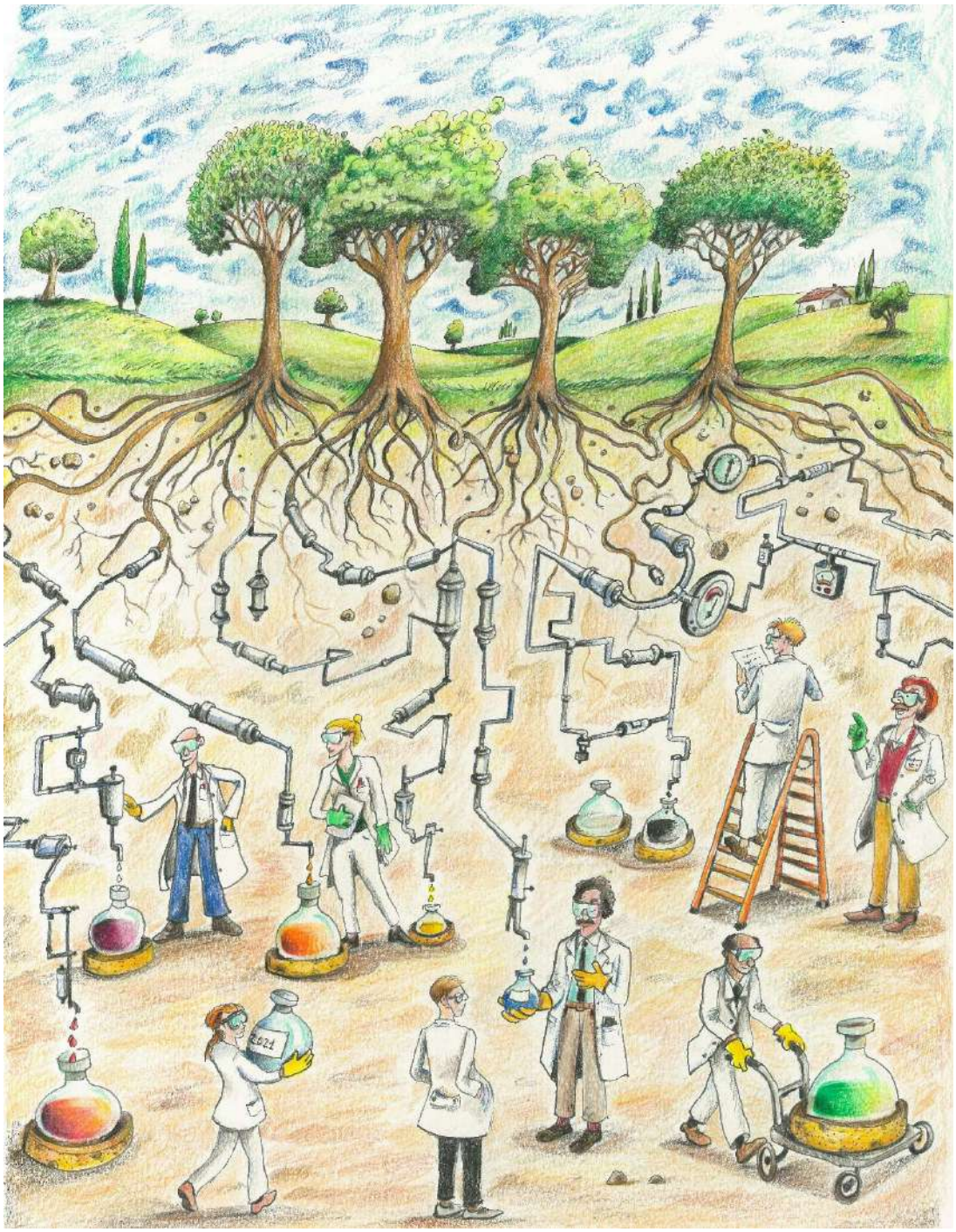

Abstract

The negative impact of crude oil on the environment has led to a necessary transition toward alternative, renewable, and sustainable resources. In this regard, lignocellulosic biomass (LCB) is a promising renewable and sustainable alternative to crude oil for the production of fine chemicals and fuels in a so-called biorefinery process. LCB is composed of polysaccharides (cellulose and hemicellulose), as well as aromatics (lignin). The development of a sustainable and economically advantageous biorefinery depends on the complete and efficient valorization of all components. Therefore, in the new generation of biorefinery, the so-called biorefinery of type III, the LCB feedstocks are selectively deconstructed and catalytically transformed into platform chemicals. For this purpose, the development of highly stable and efficient catalysts is crucial for progress toward viability in biorefinery. Furthermore, a modern and integrated biorefinery relies on process and reactor design, toward more efficient and cost-effective methodologies that minimize waste. In this context, the usage of continuous flow systems has the potential to provide safe, sustainable, and innovative transformations with simple process integration and scalability for biorefinery schemes.

This thesis addresses three main challenges for future biorefinery: catalyst synthesis, waste feedstock valorization, and usage of continuous flow technology. Firstly, a cheap, scalable, and sustainable approach is presented for the synthesis of an efficient and stable 35 wt.-% Ni catalyst on highly porous nitrogen-doped carbon support (35Ni/NDC) in pellet shape. Initially, the performance of this catalyst was evaluated for the aqueous phase hydrogenation of LCB-derived compounds such as glucose, xylose, and vanillin in continuous flow systems. The 35Ni/NDC catalyst exhibited high catalytic performances in three tested hydrogenation reactions, i.e., sorbitol, xylitol, and 2-methoxy-4-methylphenol with yields of 82 mol%, 62 mol%, and 100 mol% respectively. In addition, the 35Ni/NDC catalyst exhibited remarkable stability over a long time on stream in continuous flow (40 h). Furthermore, the 35Ni/NDC catalyst was combined with commercially available Beta zeolite in a dual–column integrated process for isosorbide production from glucose (yield 83 mol%).

Finally, 35Ni/NDC was applied for the valorization of industrial waste products, namely sodium lignosulfonate (LS) and beech wood sawdust (BWS) in continuous flow systems. The LS depolymerization was conducted combining solvothermal fragmentation of water/alcohol mixtures (i.e.,methanol/water and ethanol/water) with

catalytic hydrogenolysis/hydrogenation (SHF). The depolymerization was found to occur thermally in absence of catalyst with a tunable molecular weight according to temperature. Furthermore, the SHF generated an optimized cumulative yield of lignin-derived phenolic monomers of 42 mg g_{LS}^{-1}. Similarly, a solvothermal and reductive catalytic fragmentation (SF-RCF) of BWS was conducted using MeOH and MeTHF as a solvent. In this case, the optimized total lignin-derived phenolic monomers yield was fo und of 247 mg g_{KL}^{-1}.

Table of Contents

Dedicated to Flaminea

who taught me

the bitterness of wild herbs

the saltiness of pizza

the sweetness of cakes

Acknowledgements

For me, this thesis is the end of a very valuable journey that has enriched me personally and professionally. During this journey there are so many people that I have met and I would like to thank.

Firstly, I would like to express my gratitude to Prof. Dr. Dr. h.c. Markus Antonietti for giving me the great opportunity to pursue my doctoral work in the colloid department at MPIKG, for his supervision, for the support I received, and for the innumerable inspiring conversations. The time I spent working in your department will remain unique in my memory.

I would like acknowledge Prof. Dr. Helmut Schlaad for being my second supervisor and for giving me the opportunity of teach in his lab course of polymer chemistry.

I would like to express my deepest gratitude to Dr. Majd Al-Naji, *el comandante*. Thanks for the working philosophy and ethic you taught me, for putting at first the personal and scientific development of your coworkers, for the innumerable scientific exchange, discussions, and fights we had (and still are having), for the patience in explanation and corrections. I owe you a big share of my growth as a researcher. Thanks also for the unique time spent beyondwork. Thus, thanks for being a Friend rather than only a supervisor.

My warmest thanks the present and past members of the Biorefinery and Sustainable Chemistry Group. Firstly, thanks to Irina who guided me through the lab and showed me the importance of working with calm (who knows if I will really learn it). Thanks also to Marius for all everything you have taught me, it was indeed a lot. Thanks to Valerio, for giving me some very wise advice. Thanks to Josè Alirio for being the best lab-mate I could imagine. Thanks also to our master students Bruno and Josè, for bringing freshness and passion to our group. A special thanks to Bruno for his hard work during his master thesis. It has been a huge honor and pleasure work together in the last years.

I would like to acknowledge the all the MPIKG technicians for their crucial support. Without it, this work would not have been possible, special thanks to

Marco Bott from the mechanical workshop for the heating unit of the reactor, Jessica Brandt for ICP analysis, Marlis Gräwert for GPC analysis, Antje Völkel for TGA and EA analysis, Heike Runge, Bolortuya Badamorj, and Rona Pitschke for SEM, TEM, and HRTEM images.

Thanks also to our collaborators, Dr. Iver Lauermann of Helmholtz Zentrum Berlin and Dr. Ibrahim Kahlil of KU Leuven.

Additionally, in the last year the people of colloids department has become a second family for me. The times I spent at the institute will always stay in my memory thanks to all the nice persons I have met here. Then I would like firstly to acknowledge Ivan, Milena, Ralf, Nikki, Ipek, Baris and Daniel for the nice welcome I received at MPI when I was a newcomer, and for all the nice time spent together afterwards. I am also grateful to Alexander and Konstantin, we have started together the amazing journey of PhD. Thanks to the best (and most beautiful) PhD representatives we could imagine, Diana and Bradley. Special thanks to Enrico for reminding me always what is important and was is not. Thanks also to my chez-briel master mate Janina. I am grateful to Cansu for the swimming lessons. Thanks to Zhenia for the never ending ping pong sessions. I would like also to extent the acknowledgment to Sylvain, Nieves, Pedro, Sasha, Volker, Huize, Baile, Nadja, Svitlana, Ester, Simon, Tobias, Ushi, Katharina, Ivo, Alex, Yajun, Jianrui, Qian, Julya, Martin, Elionor, Christene, Ryan, Runyu, Shaowen, Agata, Saveh and Guigang. Thanks also to all the nice and crazy people I met in Chez Briel, mostly to Chandradish, Melis, Giulio, Pietro, Mara, and Joao.

I would like also to acknowledge my classmate in the german class at GOIN for the funny lessons we had together, thanks to Mike, Alice, Anastasia, Sho, Peter, and to our teacher Arnim.

I am also grateful to the *Scopaccioni* guys for the nice cultural exchanges of last months, thanks to Filippo, Enrico, Camillo, and Vittorio.

I could not be here without my amazing office mates in the Italian office: Paolo, and Alessandro. Although we have been reunited in the “Italian office” for short time it was a great pleasure and an honor having you as office mates, talentless swimmers, gossip masters, and as friends.

I would like to express my immense gratitude here to my step-family members, Stefano and Elena, for taking care of me and Sofia, for the amazing bike trips, for the reciprocal help, and for the unforgettable Rewe missions.

I also would like to thanks to old friends, time passes but, even at a distance true friendship do not change; thanks to Federico (Fonde), Daniele, Irene, Leonardo, Claudia, Eleonora, Delfina, Federico, Alessandro, Lorenzo (Baldo), Matteo (Cioni), Matteo (Bocca), Gaia, Lorenzo (Tino), Andrea (Sorre), Andrea (Peppe), Leo, Sebastiano, Jacopo, and Gabriel.

A huge thanks to my family, to my parents, Alessandro and Donatella, for the education that you gave me, for the support I always received, for the environment you have choose to grow me up; to my brother Giovanni, our bond cannot change. Thanks also to my cousin Matteo, for the design of the graphical abstract and for the innumerable time spent together. Thanks also to my uncles, Anna, Gloria and Massimo.

Finally, I would like to express my gratitude to Sofia for making me feel special. So you are.

List of used abbreviation

LCB	Lignocellulosic biomass
IUPAC	International Union of Pure and Applied Chemistry
NDC	Nitrogen-doped carbon
35Ni/NDC	35 wt.-% Nickel supported on nitrogen doped carbon
S	Siringyl unit (in lignin structure)
G	Guaiacyl unit (in lignin structure)
H	*p*-Hydroxylphenol unit (in lignin structure)
DoE	U.S. Department of Energy
HMF	5-Hydroxymethylfurfural
DMF	2,5-Dimethylfuran
Glu	Glucose
Sor	Sorbitol
Xyl	Xylose
Xyt	Xylitol
MeTHF	2-methyltetrahydrofuran
V	Vanillin
MMP	2-Methoxy-4-methylphenol, or G6
VA	Vanillyl alcohol
RCF	Reductive catalytic fractionation
SEM	Scanning electron microscopy
TEM	Transmission electron microscopy
HR-TEM	High resolution scanning TEM
EDX	Energy dispersive X-ray spectroscopy
TGA	Thermogravimetric analysis
XRD	X-Ray diffraction spectroscopy

XPS	X-Ray photo-emission spectroscopy
NH_3-TPD	Temperature-programmed desorption of NH_3
CO-TPD	Temperature programmed desorption of CO
EA	Combustion elemental analysis
ICP-OES	Elemental analysis using Inductively coupled plasma optical emission spectroscopy detector
NRM	Nuclear magnetic resonance spectroscopy
2DHSQC NMR	Two dimensional heteronuclear single quantum coherence NMR
SEC	Size-exclusion gel permeation chromatography
BET	Brunauer-Emmett-Teller model
BJH	Barrett-Joyner-Halenda model
QSDFT	Quenched-solid density functional theory
FTIR	Fourier transformed infra-red spectroscopy
Pyr-IR	Pyridine probed FTIR
ELSD	Evaporative vapor scattering detector
HPLC(MS)	**H**igh-performance liquid chromatography (coupled with mass spectrometer detector)
GC-MS(-FID)	Gas chromatography coupled with a mass spectrometer detector (flame ionization detector)
ECN	Effective carbon number
RT	Retention time
NIST	U.S. national institute for standards and technology
UV-vis	Ultraviolet-visible spectrometry
TOF	Turnover frequency
TOS	Time on Stream
35Ni/NDC_U_x	Spent 35Ni/NDC catalyst for the *x* reaction
35Ni/NDC_R_x	Regenerated 35Ni/NDC catalyst after the *x* reaction
BAS	Brønsted acid site

LAS	Lewis acid site
LS	Sodium lignosulfonate
BWS	Beech wood sawdust
SF	Solvothermal fragmentation
SHF	Solvothermal fragmentation combined with catalytic hydrogenation/hydrogenolysis
SF-RCF	Solvothermal combined with reductive catalytic fractionation
MeOH	Methanol
EtOH	Ethanol
G1	4-Propyl guaiacol
G2	4-Ethyl guaiacol
G3	Homovanillic alcohol
G4	Dihydroconiferyl alcohol
G5	Guaicol
G6	2-Methoxy-4-methylphenol, or MMP
G7	Isoeugenol
H1	4-Propylphenol
K_L	Klason lignin (acid insoluble lignin)
ASL	Acid-soluble lignin
BHT	Butylated hydroxytoluen
S1	Syringol
S2	4-Methyl syringol
S3	4-Ethyl syringol
S4	4-Propyl syringol
S5	Syringol ethyl alcohol
S6	Dihydrosinapyl alcohol
S7	Allyl syringol
S8	Isoallyl syringol

List of used Symbols

$\mathbf{A_{BET}}$	Specific surface area calculated with the BET model
$\mathbf{A_{meso}}$	Specific surface area of mesopores
$\mathbf{A_{Ni}}$	Specific surface area of Ni
$\mathbf{V_p}$	Specific pore volume
$\mathbf{V_{meso}}$	Specific mesopores volume
$\mathbf{V_{ads}}$	Adsorbed N_2 volume
Ti	Temperature of the *i*-reaction/reactor
$\mathbf{p_i}$	Pressure of the *i*-reaction/reactor
$\mathbf{m_i}$	Mass of the *i*-compounds
$\mathbf{Q_i}$	Flow rate of the *i*-species
$\mathbf{c_i}$	Concentration of the *i*-compound
X*i*	Conversion of the *i*-compound
$\mathbf{Y_i}$	Yield of the *i*-compound
$\boldsymbol{\tau_i}$	Space time of the *I* reaction/reactor
$\mathbf{STC_i}$	Space time conversion of the *i*-compound
$\mathbf{STY_i}$	Space time yield of the *i*-compound
$\mathbf{D_p}$	Average-pore diameter
$\mathbf{t_i}$	Reaction/residence time of the *I* reaction/reactor
M_w	Mass-averaged molecular weight distribution
M_n	Number-averaged molecular weight distribution
Đ	Dispersity

Motivation

Climate change is one of the major challenges we face as a civilization. Progressive temperature increase, as well as more frequent climate-induced natural disasters, have shown that our modern lifestyle has become unsustainable. In this context, during the 2015 Paris United Nations Climate Change Conference, it was agreed on limiting yearly global warming below 2 K, compared to pre-industrial levels.[1]

The main cause of global warming is greenhouse gases emitted primarily by crude oil combustion for energy purposes. Beyond environmental aspects, crude oil presents other major issues, such as limited availability and uneven distribution, leading to economic crises and political conflicts. Additionally, crude oil is also the core feedstock for consumable plastics and platform chemicals. Therefore, the energy supply and availability of crude oil-derived products are indispensable for our society's prosperity. Moreover, modern lifestyle and a growing world population are demanding increasing amounts of energy and consumables.

As a result of this reality, the search for sustainable alternatives to crude oil for both energy and platform chemicals become urgent science and technological questions. Although renewable sources of energy such as solar, wind, and hydroelectric power are already established; renewable energy production is not growing fast enough to meet global demand and replace crude oil entirely.[2] In addition, the need of materials, plastics, and general consumables is growing alongside the world population**.** Furthermore, due to the urgent need, an alternative to crude oil has to be rapidly found and implemented in existing industrial processes.[3]

One of the most promising resources to meet all of these requirements is lignocellulosic biomass (LCB), i.e., plants. Indeed, LCB plays a crucial role in the carbon cycle, scavenging atmospheric CO_2 and potentially closing the carbon cycle.[4] In contrast to crude oil, LCB is globally available, renewable, and sustainable. However, LCB is not a new resource as it has been historically used for chemical and energy purposes before the industrial revolution, until being replaced by crude oil. In other words, humankind, science, and technology have

neglected LCB in favor of crude oil, and it is, therefore, time to renew interest in LCB.

Aiming to valorize LCB toward a sustainable platform for chemicals, materials, and fuels, the engineering concept of biorefinery has been proposed as a solution. Indeed, the concept of biorefinery describes a facility where raw biomass feedstock is processed toward refined and valuable chemicals. Beyond a scientific result, to play a role in the actual economic market, LCB derivatives must be competitive with crude oil derivatives.

The transition toward sustainable biorefineries should also include the technological process required. Indeed, the 12 principles of green chemistry from Anastas and Werner in 1998 have already shown the way to develop sustainable and benign chemical products and engineering processes. Therein, concepts such as waste prevention, usage of renewable feedstocks, atom economy, energy efficiency, and catalysis, among the others, have been highlighted as “commandments” for a sustainable future.[5] Indeed, the development of more active, stable, selective, and sustainable catalysts has a pivotal role in future biorefineries. Furthermore, the International Union of Pure and Applied Chemistry (IUPAC) has highlighted the usage of flow processes among the emerging technologies that will make our planet more sustainable.[6] Therefore, in an ideal biorefinery, the valorization of sustainable feedstock, such as LCB, is embraced with sustainable catalyst design and performed in continuous flow systems.

1. Biorefinery using heterogeneous catalysts

1.1 Lignocellulosic biomass

Lignocellulosic biomass (LCB) is the total weight of organic matter produced by plants in the metabolic cycle. LCB is produced by capturing atmospheric CO_2 and in combination with water and sunlight generates nutrients via photosynthesis. Thus, the carbon that constitutes LCB has been directly captured from the air, which allows LCB to be carbo-negative and intrinsically sustainable.[7-9] With an estimated amount of 550 Gton, LCB is the most abundant biomass on the planet and the second biggest organic reservoir of carbon after soil humic matter.[9, 10] For these reasons, LCB is considered the most promising candidate to replace crude oil for the production of chemicals and fuels.[4, 7, 9, 11-15]

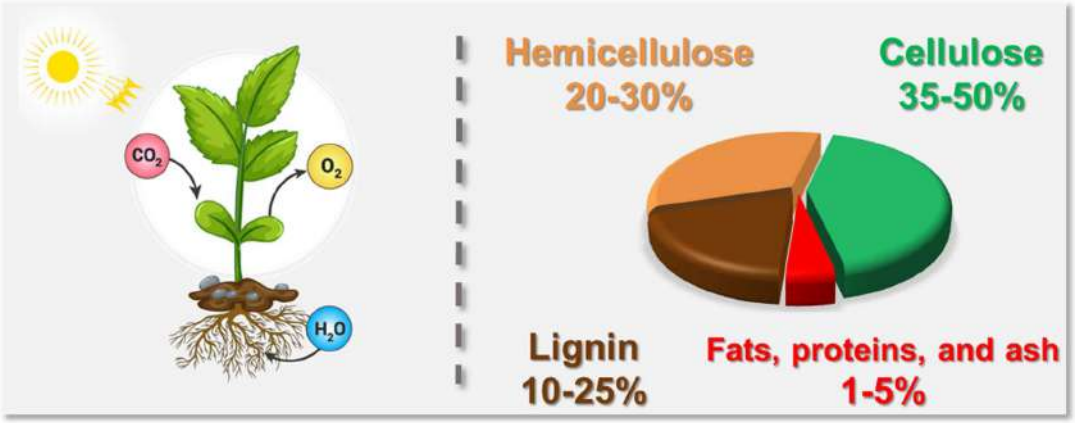

Figure 1.1. (Left): Plants produce lignocellulosic biomass through photosynthesis; (**Right):** The predominant composition of lignocellulosic biomass, i.e., cellulose, hemicellulose and lignin.

LCB composition is extremely variable depending on source plant species, tissue, and age.[8] Generally, the main LCB components are polysaccharides, mostly C_6 and C_5 sugars that form cellulose (35-50%) and hemicellulose (~20-30%), (**Figure 1.1**).[8, 14] In addition, lignin (10-25%) which is mainly composed of aromatic units. Besides those three components, the residual (1-5%) are other compounds such as fats, proteins, and minerals, which are listed in Figure 1 as

"other".[8, 14] The three major components, i.e., cellulose, hemicellulose, and lignin, are polymers arranged in an entangled and highly heterogeneous supramolecular structure.[8] The biological function of this structure is to provide plants resistance against degradation, as well as skeletal support to growth.[16, 17]

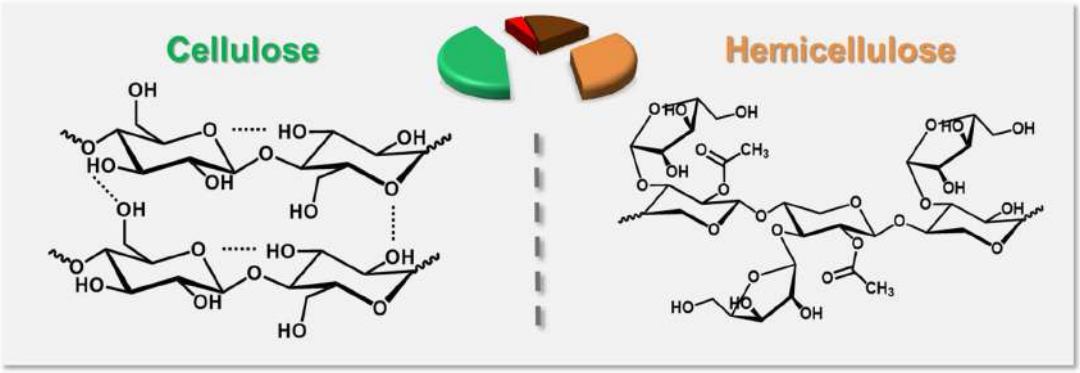

Figure 1.2. (**Left)**: structure of cellulose; (**Right):** structure of hemicellulose.

The largest LCB component, cellulose, is a linear homo-polysaccharide composed of glucose units bonded by a β(1-4) glycosidic bond (**Figure 1.2**). Typically, the number of glucose units can range from 300 to 10,000 according to the plant species.[18] Cellulose presents a strong network of inter- and intra-molecular hydrogen bonding organized in fibrillary structures, which results in a crystalline structure with high tensile strength.[8, 16] Evolution has selected these properties to provide plants with mechanical and chemical resistance as a defense against exogenous agents. However, these properties make cellulose recalcitrant against chemical treatments for the purpose of valorization.[16]

Hemicellulose, the second main component of LCB, is a class of hetero-polysaccharides formed by condensed C_5 and C_6 monosaccharide units such as xylose, arabinose, glucose, and mannose (**Figure 1.2**).[16, 17] Unlike cellulose, hemicellulose presents short and highly branched chain of C_5 and C_6 sugars.[19] Therefore, hemicellulose has a random, amorphous structure with lower chemical and mechanical strength when compared to cellulose.[17] The biological function of hemicellulose is to support the plants skeleton via interaction with other components, i.e., cellulose and lignin.[19] Accordingly, hemicellulose is typically adsorbed on the surface of cellulose microfibrils, and can have chemical bonding with lignin.[17, 19]

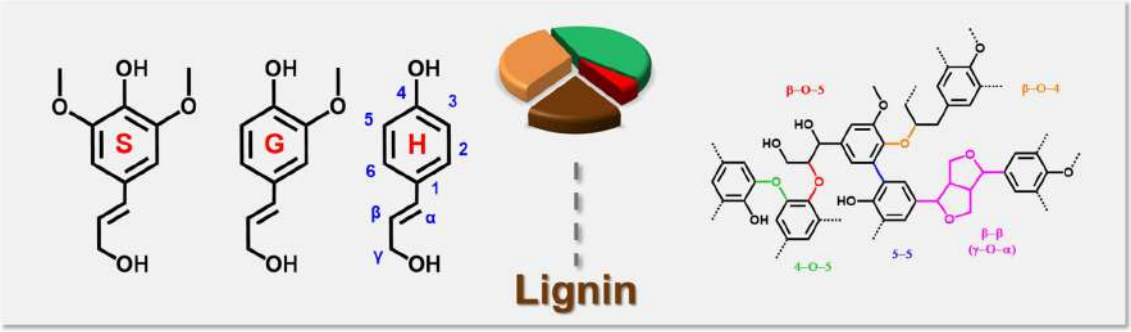

Figure 1.3. (Left): Structure of monolignols: sinapyl alcohol (**S**), coniferyl alcohol (**G**) and *p*-coumaryl alcohol (**H**); (**Right):** simplified lignin structure with highlighted ether (β-O-4, 4-O-5, β-O-5, γ-O-α) and carbon-carbon (5-5 and β-β) linkages.

The third main component of LCB is lignin, which represents the most abundant renewable source of aromatic compounds on the planet.[20-23] However, lignin is a complex polymer due to the highly cross-linked, randomly oriented, and heterogeneous structure.[20, 24-26] The structure of lignin is still debated and not yet completely identified, and has thus been defined as “supramolecular chaos”.[22, 27] Generally, lignin is formed by three phenylpropanoid building blocks called monolignols: sinapyl (S), coniferyl (G) and *p*-coumaryl (H) alcohol, corresponding to syringyl, guaiacyl and *p*-hydroxylphenol, respectively (**Figure 1.3**).[23, 28] During lignin biosynthesis in the plant, monolignols condense via oxidative radical coupling, yielding various inter-unit linkages, such as ether bonds, *e.g.* β-O-4, 4-O-5, β-O-5, γ-O-α, and strong carbon-carbon bonds, *e.g.,* 5-5 and β-β. Generally, the β-O-4 ether bonds are most abundant, as well as being easiest to cleave among lignin linkages.[23, 28] Hence, the β-O-4 bonds are commonly targeted in catalytic lignin valorization.[29] Additionally, it should be considered that all lignin properties can vary considerably depending on plant species, maturity and growing environment.[29] Nevertheless, the biological function of lignin is to protect plants against fungi and antimicrobial organisms as well as to act as a glue for cellulose.[21, 30] Owing to these functions, lignin is particularly robust against chemical treatment.

Finally, due to the diversity of the LCB composition, as well a higher O/C ratio than crude oil, LCBs could potentially be utilized not only use for the replacement of

crude oil, but also for synthesizing a larger variety of innovative and unconventional compounds.[14, 15]

1.2 State of the art of biorefinery

1.2.1 Principles of biorefinery

The paradigm of biorefinery was proposed in the 1990s to indicate the facility for chemical and fuel production from biomass, with the intention of sustainability.[31, 32] Therefore, analogous to a traditional petro-refinery, in a biorefinery the raw feedstock, i.e., LCB, is separated into useful and treatable intermediate compounds. These so-called platform chemicals, are further valorized toward value-added products.**[14, 31-35]** In addition, a biorefinery should also maximize the efficiency of its processes to maximize profitability and decrease the carbon footprint of its products.[31]

However, the usage of renewable resources, such as LCB, is not enough to guarantee a completely sustainable process. For this reason, a biorefinery must implement standard guidelines for green chemistry, which has its roots in the 1990s. Anastas and Werner presented these guidelines, the so-called *12 principles of green chemistry*, to design chemical processes sustainably and safely (**Figure 1.4**).[5] One of the essential tenets of green chemistry is the complete utilization of feedstock, minimizing by-products and waste, and promoting a circular bio-economy.[34, 36-39] Indeed, in a circular bio-economy all low-value waste materials are re-processed or re-cycled toward new valuable products.[38, 39] Therefore, replacing non-sustainable feedstocks with sustainable resources, *e.g.* LCB, should be combined with process optimization and design to avoid and reduce waste.[39]

In addition, green chemistry promotes the usage of non-hazardous and renewable chemicals in all process steps, and thus feedstocks and solvents. Therefore, several reaction media have been proposed as innovative green solvents, such as ionic liquids, supercritical CO_2, and biphasic solvents.[40] Nevertheless, water is the most ideal green solvent, due to being inexpensive,

abundant, nontoxic, and non-flammable. [40] However, as it is not always possible to use water as a solvent, there are a wide number of bio-based solvents which can be produced from LCB within a biorefinery, such as ethanol, propanol, tetrahydrofuran, 2-methyl tetrahydrofuran, and acetone.[41]

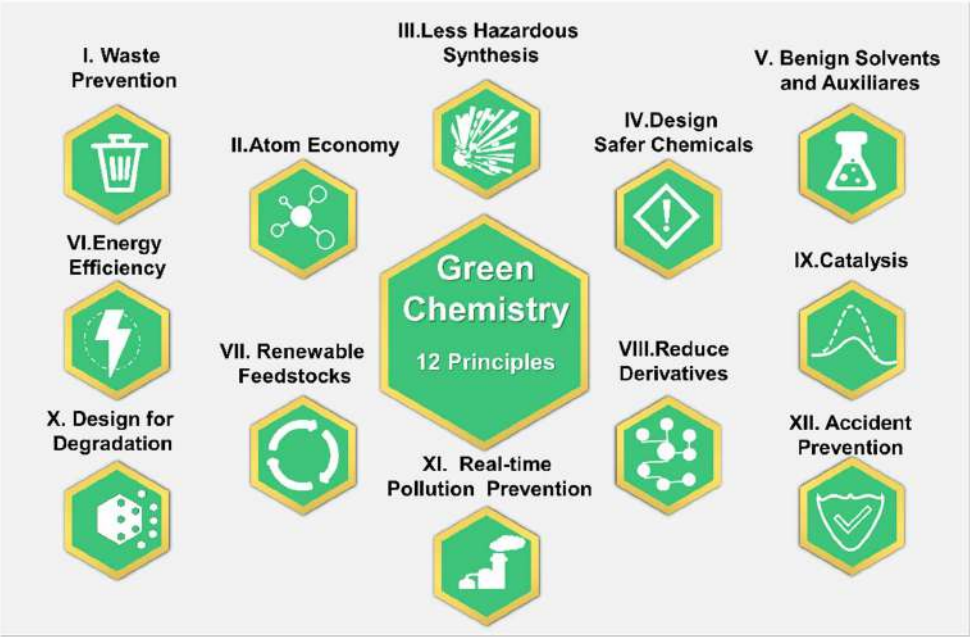

Figure 1.4. The 12 principles of Green Chemistry.[42, 43]

However, technologies that are not economically profitable will not be sustainable long term.[36] For this reason, biorefinery must compete economically with the petro-refinery. To date, biorefinery is still commercially inconvenient with respect to petro-refinery, due to several critical differences.[31, 44] The major disadvantage lies within the physical state of the feedstock, as LCB is a solid, whereas crude oil is a viscous fluid. As a result, in a petro-refinery, the crude oil components can be separated simply *via* distillation. In contrast, biorefinery requires more sophisticated and cost-ineffective fractionation processes.[4] The first fractionation steps are commonly called pre-treatments and encompass a large variety of different processes, which aim to lower the LCB complexity via separation into major components, i.e., cellulose, hemicellulose, and lignin.[16] Pretreatment can be classified into four main categories: physical (sawing, chopping, and milling), thermal (pyrolysis, liquefaction, and gasification), chemical

(acid/base hydrolysis), and biological (fermentation and enzymatic) methods, which are often combined together in multistep processes.[11, 31, 32, 45, 46] These processes generally require product separation, purification, as well as solvent recuperation, which are cost-ineffective steps.[45, 47] For these reasons, pretreatment still represents the main economic bottleneck for biorefinery as a whole, due to higher cost when compared to petro-refinery.[4, 45, 47]

For these reasons, it is clear that the biorefinery paradigm is still in its infancy. Therefore, the development of an economically viable, efficient, and sustainable biorefinery will require scientific and technological advancements in-step.[31, 35]

1.2.2 Modern integrated biorefinery

An integrated biorefinery converts LCB into any combination of fuels, heat, and chemicals; making full use of the feedstock by applying multiple concatenate steps including pretreatment, chemical transformation, energy production, heat exchange, and product separation methods.[48, 49] Therefore, an integrated biorefinery can take advantage of the multiple LCB components to maximize the products value and minimize cost.[31, 50, 51] In addition, the integration of multiple steps in a single facility, or an industrial cluster, would reduce transportation costs and the overall product footprint.[50]

Generally, the design of an integrated biorefinery implies the selection of LCB feedstock, the technological paths to connect raw feedstock to platform chemicals and products, and all the process conditions and engineering to maximize the yield and quality of the target products.[50, 52] Thus, the future of an integrated biorefinery lies in the development, implementation, and combination of different technologies.[50, 52, 53]

Biorefinery processes have been categorized by various criteria such as the applied feedstock, process type, and applied technology.[31, 32, 54] Among them, biorefinery can be classified into three types, based on the applied feedstock and valorization strategy, summarized in **Table 1.1**.[17, 35, 55]

Table 1.1. Different biorefinery types according to the feedstock used and the valorization strategy.[31, 32]

Biorefinery	Feedstock	Valorization Strategies	Advantages	Disadvantages
Type I	Crops (edible LCB)	Hydrolysis and fermentation	Minimal pretreatment, simple separation of products.	Single feedstock, food vs fuel controversy, land degradation, no product diversification.
Type II	Non-edible LCB	Gasification or pyrolysis	Multiple feedstocks, diversified process.	Harsh reaction condition, difficulty to control product selectivity
Type III	Non-edible wet LCB	Combined multistep process	Multiple feedstocks, mild conditions, controlled products, diverse products	Separation steps, high costs, reactor design.

Type I biorefineries are a non-diversified process, where a single edible crop is used as a feedstock. For type I, feedstock valorization targets one compound in particular. The most prominent example of type I is the synthesis of bioethanol from crops such as sugar beet or sugarcane.[7, 12, 15, 56] The major advantage of type I biorefinery lies in the minimal pretreatment required and the simple separation of products.[49] However, the usage of edible crops has been strongly criticized due to competition with food, in the Fuel vs Food controversy.[4, 14] In addition, the used crops are cultivated via intensive farming, which is considered responsible for soil erosion.[49] For these reasons, type I biorefinery is not considered a valid sustainable alternative to crude oil.[57]

Type II biorefinery applies a relatively diversified process where non-edible LCB feedstock, such as forest, agricultural, and food waste is valorized toward various products. The most prominent example is the thermal valorization processes (*e.g.* pyrolysis and gasification) for the production of bio-oil and syngas.[12, 58, 59] This process has the advantage of using non-edible waste feedstock with a diversified process.[32] However, type II biorefinery has some inherent disadvantages, such as

harsh conditions in the process, difficult control, and a low value resulting product.[60]

Finally, a biorefinery of type III is a highly integrated and diversified process where multiple wet LCB feedstocks (mostly non-edible) are valorized toward a wide pool of platform and fine chemicals.[31, 32] Typically, these processes selectively deconstruct the LCB toward its major components, i.e., cellulose, hemicellulose, and lignin, and then catalytically transform them into platform chemicals by applying relatively mild conditions. Then, the produced platform chemicals can be further processed into value-added and fine chemicals.[32] The main advantage of type III biorefinery is the selective deconstruction of LCB to a diversified number of valuable products. In addition, the possibility to use the products as intermediates for further synthesis can allow further process integration, and higher utilization for valuable products.

For the aforementioned reasons, type III biorefinery is the most integrated and modern process, and has the highest potential to drive a transition from an oil-derived chemical industry toward a sustainable bio-based industry.[50, 51] However, type III biorefinery requires cost-ineffective products separation steps, as well as high solvent volume, and the design of innovative reactors. Thus, type III biorefinery is still in its infancy, and to be commercially competitive with oil-refinery would require the development of more integrated and efficient process methodologies, as well as innovative synthetic pathways. This thesis will focus only on biorefinery type III as the model integrated biorefinery.

Nowadays, a major focus in the modern integrated biorefinery corresponds to C_5 and C_6 sugar valorization, i.e., cellulose and hemicellulose, as they are the majority of LCB (~75%).[4, 11, 61] These polysaccharides can be deconstructed in C_5 and C_6 monosaccharides, *e.g.* glucose and xylose primarily *via* hydrolysis, and then catalytically converted toward platform and fine chemicals.[9, 11, 12, 62, 63] In this context, the U.S. Department of Energy (DoE) has identified 12 building blocks as the “top value-added chemicals from biomass”, i.e., ethanol, glycerol, lactic acid, 3-hydroxypropanoic acid, succinic acid, furfural, levulinic acid, xylitol, isoprene, 2,5 furan dicarboxylic acid, 5-hydroxymethyl furfural and sorbitol (**Figure 1.5**).[64, 65] These compounds are platform chemicals, which can be derived from the sugar

fraction of LCB. Moreover, the “top 12” have been selected as being precursors for a wide series of compounds with potential applications in polymer, pharmaceuticals, food, cosmetics industries.[8, 9, 44, 62] Therefore, they represent a valuable portfolio of molecules, which can contribute to replace the existing oil- with LCB-derived compounds. However, these chemicals were selected in 2010, based on the technology and industrial demands of that time.[64] Hence, technological innovations, and changes in industrial demands could expand or modify that list.[64]

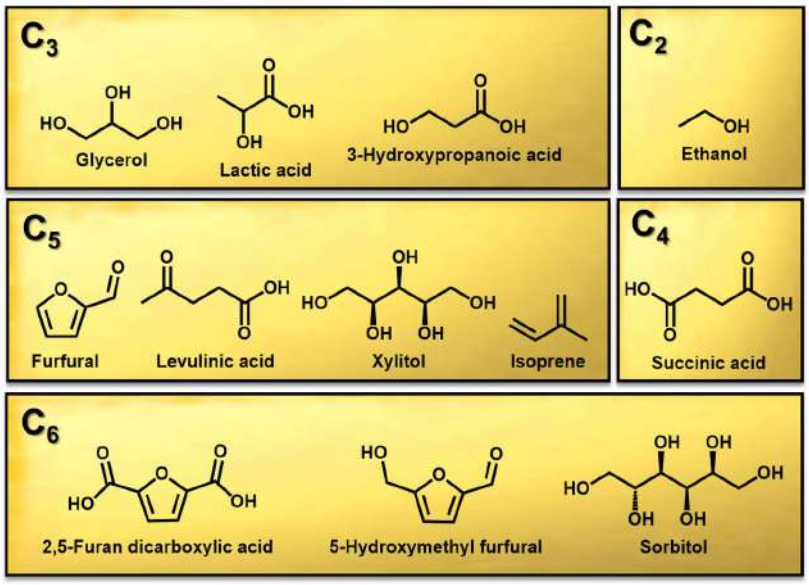

Figure 1.5. The 2010 revised “Top 12” value-added chemicals from biomass according to the U.S. Department of Energy (DoE) grouped according to their carbon content.[64, 65]

Nowadays there are some examples of integrated industrial processes for sugar valorization, such as Avantium YXY® technology for furandicarboxylic acid production[66], the BASF Succinity® process for the synthesis of succinic acid [67], and the Biofine process for levulinic acid production[49, 68]. Among these processes, the Biofine process is one of the first integrated biorefinery processes demonstrated on a large schale. Therein, levulinic acid is produced with a comparably high yield (46 wt.- %) with formic acid, furfural ad char as byproducts, (**Figure 1.7**).[32] The by-products are further valorized as platform chemicals, in the case of furfural and formic acid, or thermally treated to recover heat, in the case of char.[32]

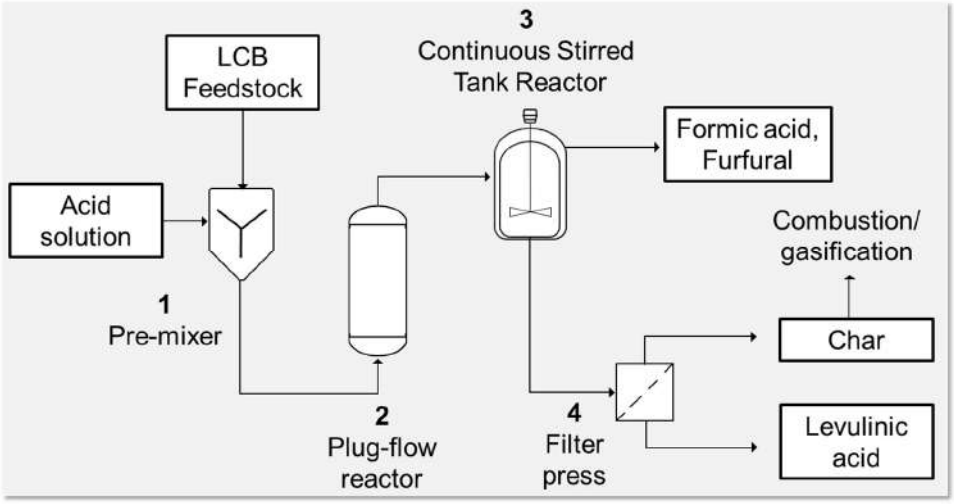

Figure 1.7. Schematic representation of Biofine process for the production of levulinic acid, formic acid, and furfural.[32]

The Biofine process uses homogeneously acid-catalyzed hydrolysis (primarily aqueous H_2SO_4) LCB valorization, combining a plug flow reactor with a continuously stirred tank reactor, or batch system (**Figure 1.7**). In the reactor, the cellulosic C_6 and C_5 sugars from LCB feedstock are hydrolyzed and converted to 5-hydroxymethylfurfural (HMF) and furfural at a temperature of 483-503 K. Then, in the second reactor, HMF is converted to levulinic acid with furfural, formic acid, and char as by-products at a temperature of 468-488 K (**Figure 1.7-3**). Afterward, formic acid and furfural are isolated and purified via distillation, while levulinic acid and residual solid char are separated via filtration.[32] This example clearly shows the complexity of an integrated biorefinery, where are combined different technological methodologies, such as mixing, continuous flow, batch reactors, and separation steps.

Generally, sugar valorization is still economically inefficient when compared to petro-refinery. Established processes have limited production, which cannot meet societal demand for chemicals. Additionally, the applied technologies rely mostly on batch systems or homogeneously catalyzed flow (*e.g.* the Biofine process), which lead to high operational costs. In this context, a higher degree of interconnection between process steps will lead to lower costs and more efficient production.[69] The discovery of innovative synthetic pathways for the production of platform chemicals as well as for its valorization toward fine products is greatly needed to exploit the full potential of sugar biorefinery.[4, 70]

Sugar valorization has been a primary goal within the general context of biorefinery.[33, 61, 71-73] Cellulose and hemicellulose are also largely used within the paper and pulp industries, which exceeded 400 Mton of global paper production in 2018.[74, 75] In these cases, where cellulose and hemicellulose are valorized, the third major LCB component, lignin (~20%), is generated as a byproduct, and thermally treated as waste.[76, 77] However, profitable and sustainable biorefinery requires valorization of all LCB components, reducing low value by-products.[5, 69] Several studies have indicated lignin valorization is the essential step in the development of a completely integrated biorefinery process.[23, 28, 33, 71, 73, 78-81] The main obstacle of which is the complexity of lignin, and its recalcitrance against treatment. [21, 69] Historically the most direct lignin applications rely on its usage as a macromolecule, *e.g.* additives for composite material, cement, dyes, and polymers.[28, 73, 82, 83] This is noteworthy, as the only relevant process for lignin valorization into chemicals at an industrial scale is vanillin production via oxidative fractionation, mostly by the company Borregaard.[84] However, recently several promising methods for lignin valorization towards molecules have been disclosed.[28, 71, 80, 85, 86] The most advanced method for lignin valorization toward chemicals are reductive[33, 80] and oxidative[87] catalytic fractionation, as well as chemical functionalization mediated fractionation[85]. Indeed, lignin biorefinery is still in its infancy, however, facing the chemical and technological challenges of this field will increase the overall viability of the biorefinery.

There are several challenges that have to be considered in order to establish a holistic, efficient, and profitable biorefinery processes: the complete utilization of the feedstock, design of catalytic process more selective, efficient and working at mild conditions, as well implementation of the processes into existing working technology.[69] To overcome these challenges a multifaceted approach is necessary for the design of new catalytic systems with complete feedstock utilization and implementation of these processes into existing technologies. Owing to those challenges, a holistic fully integrated biorefinery has the potential to increase the sustainability of our society.

1.2.3 Continuous flow systems for integrated biorefinery

The commercial implementation of a biorefinery requires the development of its technology, starting from reactor selection and engineering to process design. Currently, batch systems represent standard operating systems for biorefinery purposes at both laboratory and industrial scale.[88-91] However, in the last decade continuous flow systems have been recognized as a more sustainable and more efficient alternative to batch systems.[88, 89, 92-95] In 2019, the International Union of Pure and Applied Chemistry (IUPAC) has concluded that flow chemistry among the ten chemical innovations that will make the world more sustainable.[6]

Nowadays, several industries already implemented continuous flow technology in their production schemes, mostly in petro-refinery and pharmaceutical industries.[88, 96] However, very few processes applied continuous flow technology for biorefinery. Among these processes, flow reactors are used for gas-phase reactions (such as pyrolysis and gasification) or in liquid phase by applying homogenous catalysts in plug flow reactors.[32, 60] As an example, the Biofine process applies continuous flow but with homogeneous acid catalyst (cf **Chapter 1.2.2**).[32] Surprisingly, there are not established process utilizing heterogeneous-packed bed reactors at an industrial scale for biorefinery purposes.

A typical continuous flow reactor consists of a reaction column, i.e., a tube, embedded in heat exchanger, fed constantly with reactants solution and generally packed with catalyst bed.[88, 93] Despite the usage of small volume capillary reactors in academia, for industrial purposes the most used continuous flow systems rely on heterogeneous catalysts packed-bed reactors.[88, 97]

Continuous flow systems present a series of advantages and limitations when compared to batch, which has to be considered for reactor selection (**Figure 1.8**).[98] Firstly, packed-bed continuous flow reactor are limited to shaped porous catalysts rather than powders to prevent reactor clogging and to minimize the pressure drop. [89, 97] Accordingly, one of the main advantages of a flow system is the straightforward separation of product from the catalyst. Therefore, in contrast to batch, the reaction downstream is simple and does not require expensive catalyst filtration/product separation procedures.[89, 93, 99]

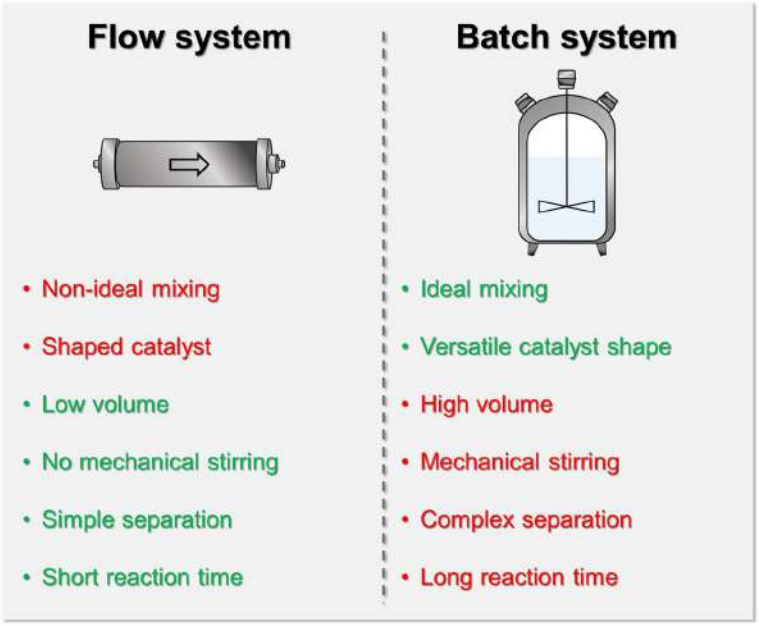

Figure 1.8. Comparison between flow systems (**Left**) and batch systems (**Right**), with respective advantages (green) and disadvantages (red).

In a flow system, mass transfer is regulated only by the solvent flow, whereas batch reactors require mechanical stirring.[80, 89] The absence of stirring can be advantageous, due to reduce operational costs for eventual scale-up. However, stirring guarantees ideal mixing which can be necessary for some reactions. [80] In addition, the residence time of reactants and products inside a flow reactor can be easily regulated with the flow rate. Therefore, the reaction time can be minimized, reducing follow-up reactions or the degradation of products.[90, 92, 99] This is particularly important for biorefinery, due to the natural tendency of LCB-derived compounds to decompose at high temperatures.[100]

In terms of process intensification and integration, flow systems guarantee the straightforward connection of multiple reactors. As a result, different reactors can be coupled with different catalysts to allow simultaneous reactions. This enables the establishment of integrated systems, or the increase of volumetric reaction productivity with multiple reactors in series, i.e., intensify the process.[101] Therefore, connecting multiple reactors reduces the solvent requirement and enables the design of the most direct atom-efficient route, preventing waste.[90, 95] Moreover, continuous flow systems require a lower space, i.e., smaller reactor size

than batch to reach a comparable conversion rate. Due to this lower volume, flow systems present more efficient heat transfer and lower space requirement than batch.[102, 103] Economically, the redesign of a batch process into flow system has been reported to reduce the resource consumption, and thus cost, by up to 30%.[104, 105]

As a result of operating reactions in continuous flow systems, the safety of the process is improved.[106] This applies particularly when toxic chemicals are used (or produced), but also for gas-liquid reactions where high pressure is required.[95, 102] In the case of gas-phase reactions, such as hydrogenation, the inherent safety of flow is due to the lower volume of the reactor as well as the taming of unexpected exothermic reaction via high mass and heat transfer.[95] This increased safety further establishes flow chemistry as a more green option than batch, per the 12 principles of green chemistry.[42]

However, flow systems are not only a sustainable and safer alternative to batch. Recent developments in continuous flow technology revealed that chemistry conducted in flow systems opens new synthetic pathways not yet achieved in a batch process.[88, 98, 107] Therefore, flow chemistry is not only a sustainable and less expensive alternative to batch but also a powerful tool for chemists to discover new synthetic strategies.

Therefore, the implementation of continuous flow systems into the framework of biorefinery has the potential to enhance the development of safe, sustainable, efficient, and commercially viable processes.

1.3 Heterogeneous catalysis for biorefinery

1.3.1 Catalytic valorization of lignocellulosic biomass

In every chemical transformation, a certain amount of energy is required to initiate a chemical reaction, namely, activation energy. A catalyst can be used to decrease the activation energy of a system without altering it thermodynamically.[108] Generally, catalysts can be categorized into homogeneous, heterogeneous, and bio-catalysts.[109] Among them, the most used for industrial purposes are heterogeneous catalysts, which are typically solid and present specific active sites on their surface.[109, 110] Heterogeneous catalysts have the major advantage of simple separation from the reactants/products. Thus, it is estimated that almost 80% of industrial processes use heterogeneous catalysts.[15, 91] New innovative and efficient catalysts can decrease the amount of energy required for a process as well as enable innovative chemical transformation. Therefore, the development of catalysts has vital importance when considering a sustainable, profitable, and integrated biorefinery.

LCB is composed mostly of carbon, oxygen, and hydrogen, where elemental abundance is described as O/C and H/C atomic ratio. The typical LCB ratio can be visualized in the Van Krevelen diagram in comparison to other fossil feedstocks such as peat, lignite, coal anthracite, and crude oil, (**Figure 1.8**).[111, 112] Generally, LCB presents a high O/C ratio, which corresponds at a molecular level to a range of different functionalities comprising, alcohols (polyols), phenols, carboxylic acids and aldehydes. These functionalities represent the chemical richness of LCB and are generally the target for catalytic valorization such as hydrogenations, hydrodeoxygenation, hydrogenolysis, decarboxylation, dehydration, and oxidation.[33, 62, 113] To occur, all the above-mentioned reactions require catalysts with specific active sites such as redox-active catalysts or acid-base catalysts. A growing number of possible catalytic reactions for the LCB valorization toward chemicals and fuels is reported every year.[114, 115] In this thesis, the investigations involved two of the most important catalytic pathways for LCB valorization, such as hydrogenation and dehydration of LCB-derived compounds and reductive catalytic

depolymerization of lignin. Therefore, this chapter presents a survey of possible reactions of hydrogenation and dehydration involving LCB and LCB-derived compounds.

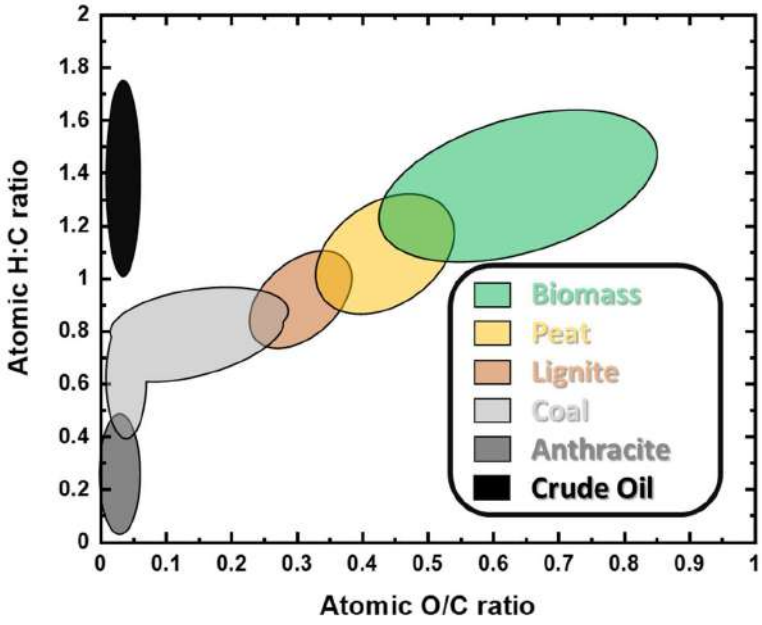

Figure 1.8. Typical van Krevelen diagram with O/C atomic ratio as a function of H:C atomic ratio of several feedstocks.[111]

The major component of LCB, i.e., cellulose, can be converted through hydrolysis in glucose (Glu), giving an entry point for the production of a series of platform chemicals, *e.g.* 5-hydroxymethyl furfural (HMF), 2,5 furandicarboxylic acid, 2,5-dimethylfuran (DMF), levulinic acid ɣ-valerolactone, sorbitol, and isosorbide (**Figure 1.9** and **1.5**).[114-116] Among these products, HMF is widely recognized as the "sleeping giant" of sugar refinery due to its unexpressed potential.[61, 117, 118] The HMF potential is derived from its versatile chemical functionality since it has simultaneously alcoholic, aldehydic, and furanic moieties. Therefore, HMF can be easily upgraded either with an oxidative pathway, *e.g.* to 2,5-furandicarboxylic acid [14, 119], with reductive steps, *e.g.* to DMF[63, 112], or via hydrolysis to levulinic acid.[118] HMF is generally formed from glucose via isomerization into fructose followed by three consecutive dehydration steps using solid acid catalyst, *e.g. Amberlyst 15*, Nafion *NR50,* or graphene oxide.[61, 118, 120]

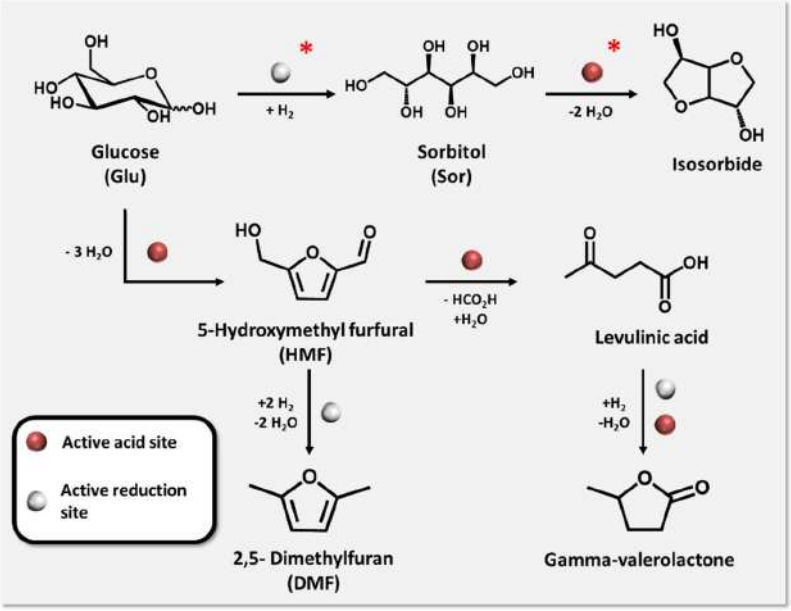

Figure 1.9. Glucose valorization routes via catalytic reduction and dehydration. The red sphere indicates reaction catalyzed by acidic sites while the gray sphere indicates reaction catalyzed by reduction sites. The red star indicates the reaction investigated in this thesis.

Among HMF derivatives, DMF has raised interest due to its potential for several applications. As such, DMF is a high value biofuel, with an energy density comparable to gasoline and diesel of 35 MJ L^{-1}.[118, 121, 122] More interestingly, DMF can also be further upgraded *via* Diels-Alder cycloaddition to produce p-xylene, which is the main industrial precursor for PET and polyester fibers. [123, 124] In 2007, Dumesic's group pioneered work for the HMF hydrodeoxygenation to DMF in a batch system, using a bimetallic Ru-Cu/C, yielding 71 mol% of DMF at 493 K.[112] Furthermore, a series of supported metal catalysts have been efficiently used for the same purpose, such as Pd, Ru, Pt, Rh, Au, Co, Ni, and Cu.[62, 122, 125-128] Beyond DMF, HMF can also be converted via hydrolysis toward levulinic acid, which has a wide range of different applications, *e.g.* solvents, pharmaceuticals, food, and cosmetics industries.[64, 129, 130] In addition, levulinic acid can be further upgraded to other C_5 chemicals, to ɣ-valerolactone among others *via* catalytic hydrogenation combined with dehydration.[129, 131, 132]

Alternatively, Glu can be hydrogenated towards sorbitol (Sor), the global production of which is already higher than 500 kton per year, mostly for cosmetics, food and pharmaceuticals industries (**Figure 1.9**).[133-135] On an industrial scale,

Sor is produced from Glu hydrogenation in batch systems using skeletal Ni catalysts, i.e., Raney Nickel.[133, 136] Additionally, metal-based catalytic reactions have been proposed for the Glu hydrogenation toward Sor, such as Ru (Ru/Al_2O_3, Ru/C, Ru/zeolite and Ru/SiO_2)[135, 137-142], Pt (Pt/Al_2O_3, Pt/SiO_2, and Pt/C)[142-145], Cu (Cu/SiO_2),[146] and Ni (Ni/SiO_2, Ni/TiO_2, Ni/Al_2O_3).[135, 137, 146] However, the usage of non-noble metals, e.g., Ni, has been reported to suffer from rapid catalyst deactivation due to significant Ni leaching within hours under hydrothermal conditions.[135, 137, 146]

Moreover, Sor can also be further upgraded via acid-catalyzed dehydration into isosorbide, a high value bio-based building block (**Figure 1.9**).[70, 147-150] Accordingly, isosorbide is gaining relevance, as it can be used as a building block for a novel class of bio-polymers.[70, 151-154] In this context, there are already commercially available isosorbide-based polycarbonates (*e.g.* POLYSORB®,[155] DURABIO®,[156] and PLANEXT®[157]). In addition, isosorbide derivatives (mostly mono and di-nitrate) are widely utilized as a vasodilator in medicine.[158, 159] Therefore, the market for isosorbide is rapidly growing and is expected to exceed 350 million US$ in coming years.[70, 154] Currently, isosorbide is produced in the industry via homogenous dehydration of sorbitol at 400 K using H_2SO_4 with a yield of 77 mol%.[160-162] However, this process is neither sustainable or economically profitable.[70] Aiming at more sustainable heterogeneous alternatives, several solid acid catalysts, i.e., zeolites, metal phosphate, mixed oxides, and resins have been proposed for isosorbide production from sorbitol.[148, 154, 163-180] However, these attempts are generally based on batch systems,[154] non-scalable molten-phase reactions,[148, 163-176] or water-steam gas phase reactions.[172, 180-182]

Similar to cellulose, hemicellulose can be deconstructed into its pentoses via hydrolysis, mainly xylose (Xyl).[17] Analogous to glucose, Xyl can undergo three consecutive dehydrations to form the respective furanic compound, i.e., furfural (**Figure 1.10**).[122, 183, 184] Furfural is an important raw material for the synthesis of chemicals such as furfuryl alcohol, 2-methyl furan, furan, and 2-methyltetrahydrofuran (MeTHF).[122, 185] Nowadays, furfural is produced at industrial scale directly from raw LCB, mostly agricultural waste, using H_2SO_4 as a homogeneous catalyst.[185] However, several heterogeneous solid acid catalysts have been proposed for aqueous phase

Xyl dehydration to furfural, such as metal oxides (CuO, ZnO and MgO), zeolites and acid resins. [184-187]

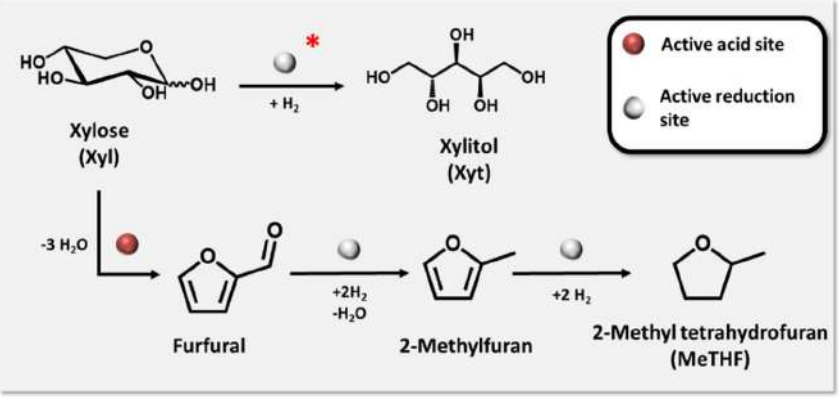

Figure 1.10. Xylose (Xyl) valorization routes via catalytic reduction and dehydration. The red sphere indicates reaction catalyzed by acidic sites while the gray sphere indicates reaction catalyzed by reduction sites. The red star indicates the reaction investigated in this thesis.

On the other hand, Xyl can be hydrogenated towards xylitol (Xyt) by using both noble metals, such as Pt and Pd, or non-noble metals such as Ni, Cu, and Ru.[153, 188-193] Xyt, a natural 5-carbon polyalcohol, is widely used, because of its properties as low caloric content sweetener and anti-cariogenic properties.[153] Typically, investigations for Xyl hydrogenation to Xyt are conducted in batch systems at a temperature range of 393-463 K and H_2 pressure of 2.0-8.0 MPa.[188-193]

At an industrial scale the production of fine chemicals from lignin has not been well established, with the exception of vanillin (V), mostly from Borregaard company.[84] Vanillin is used not only in food, beverages, pharmaceuticals, and fragrances, but also as fuel additives or polymer precursors.[23, 194, 195] However, V can be also used as a platform chemical to produce value added chemicals, via hydrogenation, oxidation, or functionalization.[196] Among these reactions, V hydrogenation can give Vanillyl alcohol (VA) and 2-methoxy-3-methylphenol (MMP), which can be used as promising precursors for sustainable epoxy resins and polymers, or as a fuel additive.[196-198] V hydrogenation is a two-step process consisting of hydrogenation- followed by hydrodeoxygenation to produce VA and then MMP, (**Figure 1.11**). The hydrogenation of V towards VA and MMP can be

conducted using supported metal (Pd, Pt, Ru, Ni, Au, Cu and Rh) catalysts, with a temperature range of 373-423 K.

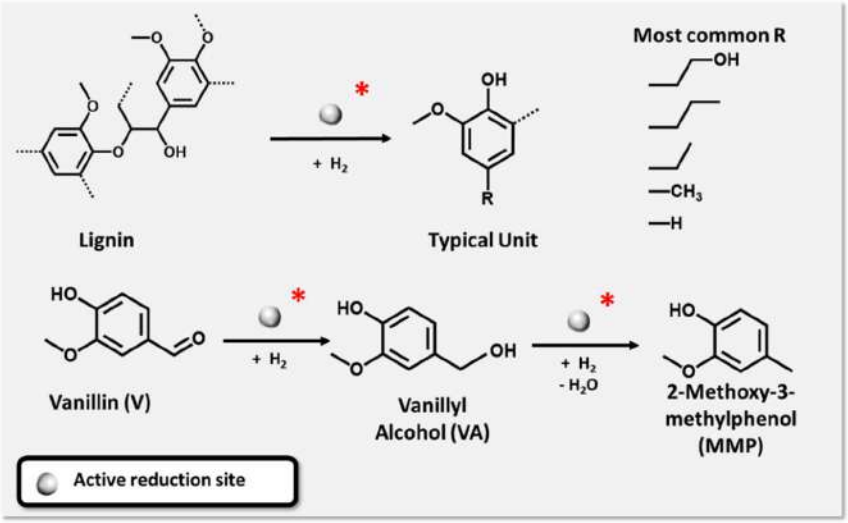

Figure 1.11. Reductive valorization pathways of vanillin and of lignin. The gray sphere indicates reaction catalyzed by reduction sites. The red star indicates the reaction investigated in this thesis.

Additionally, reductive catalysts have been used in the context of LCB valorization to efficiently separate and depolymerize lignin from waste wood in the so-called lignin-first approach.[71, 80] Lignin-first indicates a process in which lignin is liberated from the LCB and its condensation is prevented via active stabilization procedures.[21, 71, 73, 204] In such an approach, lignin, cellulose, and hemicellulose fractions can be effectively valorized in an atom efficient process. To date, several active stabilization strategies have been proposed, such as reductive catalytic fractionation (RCF) and formaldehyde-assisted stabilization.[13, 85, 205-207] RCF was pioneered by the Sels group, and combines lignin extraction from LCB with immediate depolymerization (hydrogenolysis) and protection (hydrogenation) to produce monomers in high yield. [28, 33, 80, 208] Therefore, in a general RCF, the extracted and partially fragmented lignin is depolymerized via catalytic hydrogenolysis of weak bonds (mostly the ethers bond, *e.g.* β-O-4 and α-O-4) to give a wide series of monomers (**Figure 1.3** and **Figure 1.11**).[28] The amount and type of monomers are strongly dependent on several factors, 1) type and size of feedstock (softwood, hardwood or herbaceous sources), 2) solvent (alcohols, ethers or aqueous solvents), 3) type of redox catalyst (noble or non-noble metals)

and 4) reaction conditions (pressure and temperature).[33, 78, 207, 209-211] Several redox catalysts have been applied for RCF, such as Ru, Pt, Rh, Pd, Cu and Ni supported on C or Al_2O_3, operating in a temperature range 403 – 623 K in both organic and aqueous media (or a mixture) with 1-10 MPa of pressurized H_2.[16, 28, 80, 81, 207, 212]

Nevertheless, to be applicable in a mature biorefinery, catalytic valorization of LCB must face several challenges, such as the development of a more efficient process operating at mild conditions. Accordingly, the design of more active, stable and sustainable catalyst is one of the core problems when considering industrialization of biorefinery.[213, 214]

1.3.2 Metal supported shaped catalyst for sustainable biorefinery

In the context of biorefinery, the ultimate goal for any catalytic investigation is to be applicable at an industrial scale.[215] However, typical catalysts used in research contexts are powders produced on mg or g scale. The core of catalyst design in research labs is the search for textural properties (*e.g.* porosity and active site density) combined with the screening of catalytic performance. Whenever a catalyst shows extraordinary performance in laboratory scale, it becomes a candidate for industrial purposes, i.e., to be a technical catalyst. Firstly, technical catalyst performance should be reproducible at industrial scale. Then, the technical catalyst should also respect the industrial requirements for shaping into a macroscopic form (mostly pellet) and scalability (from mg to kg), high activity and selectivity for long operating time, recyclability, and low production costs. Therefore, only a minimal part of the promising research for catalysts reach “the real world”, i.e., commercialization, and require long and expensive technical evaluation prior to commercial success.[110] To better facilitate the transition from a laboratory catalyst toward a technical catalyst, the catalyst design should consider industrial requirements from the earliest laboratory stages.

In addition, flow processes can be conducted solely with shaped catalysts to prevent reactor clogging and to reduce pressure drop.[110] On the other hand, the usage of shaped catalyst rather than powder in batch systems is preferred due to

easier catalyst recovery and product separation.[213] Therefore, in a general scale-up, powder catalysts are shaped via an extrusion step with the addition of several additives such as plasticizers, lubricants, and binders.[216, 217] The addition of external agents can drastically alter catalyst textural properties, such as porosity, active-site density, and crystallinity.[216, 218] Accordingly, the synthesis of shaped catalysts at the laboratory scale would simplify the successive scale-up procedures.

Beyond the catalyst body, the catalytic process is a surface phenomenon that occurs at active sites.[109] Catalysts can be differentiated as bulky if the active site is the whole catalyst, or supported if the active site is a distinct material standing on an inert support.[109] Among supported catalysts, metals are widely used as active sites in a wide range of catalytic reactions involving biomass such as hydrogenation, hydrodeoxygenation, dihydroxylation hydrolysis, and oxidation.[62, 116] Typically, heterogeneous metal catalysts are composed of nanoparticles on a porous support, such as metal oxides, zeolites, or carbon.[219, 220] Among the metals, noble metals such as Pd, Pt, Au, Ru, and Ir are generally preferred to non-noble metals due to their superior catalytic performance in terms of activity and stability.[116] However, the amount of available noble metals is scarce, and consequently, their price is high, i.e., non-sustainable. Therefore, cheaper and more sustainable alternatives are required, mostly relying on cheap and abundant metals such as Ni, Cu, and Fe. However, to be sustainable a catalyst should be able to endure use on stream at temperatures above 373 K in several green solvents, *e.g.* water and ethanol. However, in these conditions, non-noble metal-supported catalysts, such as Ni, have been reported to suffer rapid catalyst deactivation due to leaching and loss in textural properties.[221] Additionally, typical reaction environments, such as slightly acidic conditions (pH < 6), accelerate the leaching process due to increased solubility of metal ions (*e.g.* Ni^{2+}).[135, 137, 146, 222, 223] The effect of leaching in the case of noble metals is lower than non-noble metals due to their high oxidation potential. The resistance of a catalyst to water has been appointed as one of the main challenges for sustainable catalyst design.[15] In addition, metals have high surface free energies and therefore a pronounced tendency to reduce their surface by particle growth, i.e., sintering, and

consequently to decrease the activity. Among non-noble metals, Ni is a well-known catalyst for hydrogenation reaction and is already widely used in industry.

Alongside the metal active sites, the support must be stable for long periods of time under harsh conditions. Traditionally, heterogeneous catalysis is conducted mostly using supports such as Al_2O_3, SiO_2, and zeolite, which barely survive in hot water for long periods of time.[15, 109, 224] Accordingly these materials, when exposed to a temperature above 423 K in water, undergo phase change, causing the porous structure to collapse.[224-226] In contrast to Al_2O_3, SiO_2, and zeolites, porous carbonaceous materials are well-known supports that can resist harsh conditions in water (600-800 K).[227] Further, carbon materials can be synthesized from inexpensive organic waste, and therefore represent a truly sustainable class of supports.[228]

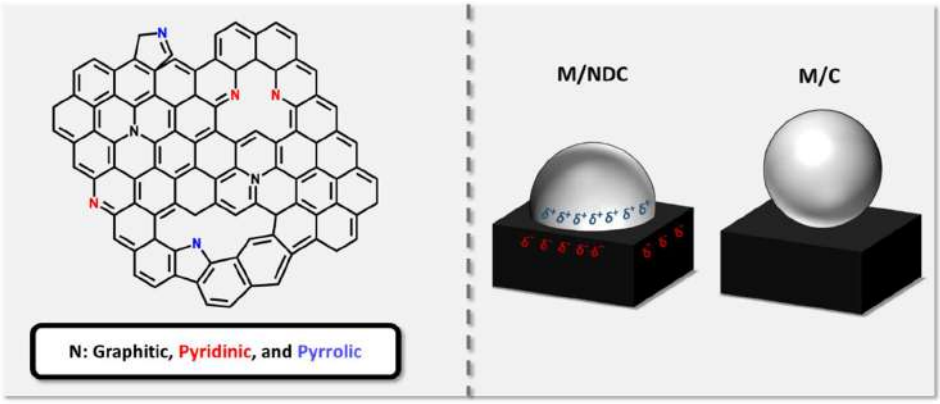

Figure 1.12. (Left): Various N species in a nitrogen-doped carbon; (**Right)**: Idealized charge-transfer stabilization effect between metal nanoparticles and nitrogen-doped carbon (M/NDC) in comparison to M on pristine carbon support (M/C),

While the catalyst support does not take an active part in the reaction, the interaction between support and metals can substantially be influenced by the catalytic performance.[229, 230] Generally, metal-support interaction can involve charge transfer, support architecture, nanoparticle morphology, and strong metal-support interaction.[229] in this regard, carbon electrochemical properties can be easily regulated with heteroatoms selecting the proper precursor.[231-236] Nitrogen is the most applied dopant element due to the similar atomic radius of N compared to C, which allows high inclusion of N without hampering the carbon structure. The carbonaceous material obtained with N inclusion in carbonaceous frameworks is

commonly called nitrogen-doped carbon (NDC).[237, 238] Based on the binding in the carbon structure, N can be divided into three main configurations, namely, pyridinic, pyrrolic, and graphitic (**Figure 1.12**). The type of bonding configuration can vary based on the applied precursor type and ratio as well as on the carbonization temperature.[238]

The incorporation of N into the carbon framework can change the work function of electrons to be more positive when compared to pristine carbon.[232, 237, 238] Consequently, NDCs are more likely to be electron acceptors than donors. This phenomenon allows NDCs to act as ligands for metals, increasing the dispersity of metals over the NDC surface during growth of the nanoparticles, and consequently decreasing the probability of sintering.[231, 239] In addition, when metal nanoparticles are deposited on NDC supports, a charge transfer occurs from the electron-rich metals towards the NDC, resulting in a partial negative charge (δ^-) on the surface of the NDC and a partial positive charge (δ^+) on the metal (**Figure 1.12**).[231, 232, 240] A metal with a δ^+ has more positive oxidation potential, and is therefore more "noble".[237] In solid-state physics, the charge transfer between a metal and a semiconductor, i.e., NDC, takes the name of Mott-Schottky heterojunction. Similarly, a metal on NDC catalyst takes the name of Mott-Schottky catalyst,[237, 241, 242] which have shown higher activity when compared to metals on the pristine carbon support.[232, 237] For example, Xue *et al.* reported high turnover frequency (TOF) for Ni on NDC for methanol hydrodeoxygenation.[242] Similarly, the groups of Xia and Cabrele demonstrated that metal nanoparticles on NDC nanotubes can lower the reaction temperature of about 30 K when compared to non-doped carbon, for Cu,[243] and Ni.[202] Due to the improved performance of non-noble metals on NDC than on non-doped carbon, the implementation of the Mott-Schottky catalyst in biorefinery has the potential to increase the efficiency and the sustainability of the process.

2. Objectives and outline

The objective of this thesis is to provide a tangible step toward a more sustainable and integrated biorefinery concept. Therefore, four major aspects in the development of biorefinery will be addressed, i.e., catalyst design, developments of innovative lignocellulosic biomass (LCB), conversion strategies of waste LCB stream toward chemicals, materials, and fuels using continuous flow systems to valorize LCB downstream.

The primary objective of this work was to synthesize a sustainable and versatile catalyst that can be used in continuous flow systems for the valorization of all different LCB fractions with the potential for rapid scale-up. Based on this, **Chapter 3** will present the synthesis of a 35 wt.-% Ni catalyst supported on nitrogen-doped carbon shaped pellets (35Ni/NDC). This synthesis consists of a simple and scalable methodology using commercially available, inexpensive, and safe chemicals.

Secondly, this thesis investigates the efficiency of the produced 35Ni/NDC catalyst into the hydrogenation reactions in a framework of LCB-derived compounds for a single reaction, as well as to design an integrated process coupling 35Ni/NDC with commercially available catalysts, such as Beta zeolite, for multiple cascade reactions. In **Chapter 4** the 35Ni/NDC will be applied in the aqueous phase hydrogenation of glucose to sorbitol, of xylose to xylitol, and of vanillin to 2-methoxy-4-methylphenol. Moreover, the integrated process from glucose to isosorbide coupling 35Ni/NDC with Beta zeolite will be explored and discussed.

Finally**,** the sustainability of a biorefinery process relies also on the feedstock selection. Therefore, in **Chapter 5,** the usage of waste LCB (sodium lignosulfonate and beech wood sawdust) as biorefinery feedstock will be addressed. In this chapter, the solvothermal fragmentation combined with reductive catalytic valorization of aforementioned waste LCB products will be addressed over 35Ni/NDC in continuous flow systems and using 35Ni/NDC as a catalyst.

3. Synthesis and characterization of a sustainable nickel on nitrogen-doped carbon pellet shaped catalyst [1]

3.1 Introduction

Synthesis of innovative catalytic systems is a core challenge for the development of modern biorefinery (**Chapter 1.3.1**). In this context, catalyst support in pellet shape is required for both conducting a reaction in continuous flow systems as well as to facilitate the catalyst scale-up. At the same time, to be feasible for industrial application the catalyst should exhibit high activity and stability over a long time of stream. Moreover, the usage of non-noble metal-based catalysts is preferred to noble metals due to lower costs and higher sustainability, *cf.* **Chapter 1.3.2.** However, non-noble metals are generally less active and suffer of rapid deactivation when compared with noble metals. Nevertheless, utilizing nitrogen-doped carbon as support can stabilize metals via the Mott-Schottky effect**.**

However, the synthesis of carbon pellets, also called carbon monoliths, presents some challenges, such as the control over mechanical stability, porosity, and macroscopic morphology of the carbonaceous support.[244, 245] Typically, this control is obtained using specific synthetic procedures such as hard, soft, and salt melt templating.[244-247] However, these techniques generally generate powder catalysts, which are hardly scalable.[215] One possible solution can be the direct extrusion of carbon precursor mixed with porogen in order to obtain a pre-shaped catalyst, which can be simply carbonized.

[1] Part of this chapter is adapted from the original work:

1) F. Brandi, M. Bäumel, V. Molinari, I. Shekova, I. Lauermann, T. Heil, M. Antonietti, M. Al-Naji, Nickel on nitrogen-doped carbon pellets for continuous-flow hydrogenation of biomass-derived compounds in water, *Green Chem.* **2020**, 22,9, 2755-2766 (This article is an open access article under the terms of the Creative Commons Attribution License, which permits use, distribution and reproduction in any medium, provided the original work is properly cited.)

Therefore, this chapter is proposing an innovative “kitchen-lab” synthetic methodology of the first generation of pelletized Mott-Schottky catalyst, consisting of Ni on NDC for hydrogenation reaction. This approach is a cheap and non-hazardous methodology, which combines a hard templating approach with traditional food technology.

3.2 Preparation of Ni supported on nitrogen-doped carbon (NDC)

The porous nitrogen-doped carbon (NDC) pellets were synthesized based on a physical mixture of semolina as a sustainable carbon source, urea:glucose: water mixture and ZnO nanoparticle (20 nm) as a porogen. Firstly, the glucose, urea and water mixture as a nitrogen source and binder with a molar ratio of 1:3:11 was prepared at 363 K for 2 h with continuous stirring. Then a 2 kg mixture composed of semolina (48 wt.-% of the mixture) and the previously prepared glucose, urea and water mixture (8 wt.-% of the mixture) and ZnO nanoparticles (20 nm) - (24 wt.-% of the mixture) were mixed together using a commercial kitchen kneader (Bosch, professional home series, model MUMVH48BCN). To provide a consistency that allows for extrusion, 160 mL water (20 wt.-% of the mixture) was slowly added to the mixture as a plasticizer. Finally, the low-moisture mixture was extruded and cut it in pellet form with a dimension of 1 mm (diameter) and 1.5 mm (length) using a commercial noodle extruding machine (La Monferrina P3) equipped with a 1 mm PTFE die and automatic cutting knife, (**Figure C.1** in **Appendix**). The extruded pellets were dried at room temperature for 12 h. The dried pellets were carbonized at 1223 K under N_2 atmosphere using a three-step program: i) purging the oven atmosphere with N_2 at room temperature for 30 min; ii) increasing the temperature to 293 K with a heating rate of 3 K min^{-1} and maintaining for 2 h, this step is to promote crosslinking[248] iii) elevating the temperature to 1223 K with a heating rate of 3 K min^{-1} and keeping for 2 h, then cooled down to a room temperature. Finally, the carbonized pellets have been washed using 0.1 M HCl solution

(15 mL g^{-1} of NDC) under continuous stirring for 10 h to remove the eventual residual Zn from the pellet (**Figure 3.1**).

The Ni with 35 wt.-% as an aimed loading has been incorporated on NDC *via* incipient wetness impregnation. For simplicity, the catalyst will be given the following code over all the thesis: 35Ni/NDC. 35 is referred to the Ni loading (35 wt.-%), NDC is referred to the support (nitrogen-doped carbon). Later, the 35Ni/NDC was calcined in the presence of N_2 atmosphere. Finally and prior the catalytic test, the catalyst was reduced under the flow of forming gas (more details of incipient wetness impregnation can be found in **Section B1** of **Appendix**).

The prepared parent NDC and 35Ni/NDC have been characterized using N_2 sorption, elemental analysis, scanning electron microscopy (SEM), high-resolution scanning transmission electron microscopy (HR-TEM), thermogravimetric analysis (TGA), X-Ray diffraction (XRD), X-ray photoemission spectroscopy (XPS) temperature-programmed desorption of ammonia (NH_3-TPD) and CO-temperature programmed desorption (CO-TPD). The details of characterization procedures are reported in **Section B2** of the **Appendix**.

3.3 Results and discussion

In the novel “kitchen-lab” synthesis of 35Ni/NDC, pellets are produced to be suitable for continuous flow systems. The synthesis protocol follows traditional pasta manufacturing (kg scale) and use commercial semolina and a mixture of urea/glucose as “publicly available” carbon and nitrogen precursors. Beyond its abundance, semolina has been selected as a proof of concept to represent organic waste from food. Accordingly, wheat and cereals represent the major waste product from the food industry, with an estimated 10-15% (~ 2 Mton) of the total global production get wasted every year.[249] Moreover, semolina is relatively rich in protein (12 wt.-%), which provides nitrogen to the carbon framework. Additionally, the semolina high

carbohydrates amount (71wt.-%) combined with the proteins at a temperature above 393 K can give Maillard reaction.[248, 250, 251]

Figure 3.1. Schematic representation of the catalyst synthesis protocol starting from the extrusion, carbonization, calcination, and reduction steps.

The Maillard reaction is a class of reaction between proteins and amino acidic amines well known in food chemistry and daily applied in bakeries.[252] Nevertheless, for the synthesis of stable supports Maillard reaction can create a cross-linked structure that preserves the precursor shape during carbonization. In addition, glucose: urea: water mixture has been added as plasticizer and as a supplementary source of N. To this end glucose: urea mixtures have been reported as a low price, a processable liquid precursor for carbon.[253] ZnO nanoparticles (broadly available as a UV pigment or baby powder), have been added to the mixture as hard-templating porogen. ZnO has been previously utilized as a versatile templating agent since it can be simply removed via thermal treatment at high temperatures (>1173 K) through ZnO carbothermal reduction to Zn which evaporates at that temperature (**Figure 3.1**).[254, 255]

After carbonization, Ni has been selected as a sustainable metal catalyst to be deposited onto the support, *cf.* **Section 1.3.2.** Ni is a sustainable metal for hydrogenation reactions, which supported on NDC possesses a high catalytic performance.[233, 236, 256] NDC, as a support, has been already reported to change the chemical behaviour of metal nanoparticles if compared to pristine carbon supports.[232, 233, 237, 256, 257] The Ni catalyst (35wt.-%) supported on porous nitrogen-doped carbon (NDC) pellets were prepared via incipient wetness impregnation. The parent support (NDC) and

35Ni/NDC were characterized and compared via N_2 sorption, elemental analysis, scanning electron microscopy (SEM), high-resolution scanning transmission electron microscopy (HR-TEM), thermogravimetric analysis (TGA), X-Ray diffraction (XRD), X-ray photoemission spectroscopy (XPS) temperature-programmed desorption of ammonia (NH_3-TPD) and CO-temperature programmed desorption (CO-TPD).

Accordingly, TGA in air showed that NDC is thermally very stable, the and degradation starts at a high temperature of 800 K, which is a typical phenomenon for nitrogen-doped "noble" carbons, (**Figure C3**).[231, 232] In addition, the presence of N makes the work function of the support more positive and promotes a partial charge transfer from the metal to the support, establishing a Mott-Schottky Heterojunction, *cf.* **Chapter 1.3.2**.[237] This effect proposes to result in strong Ni nanoparticles-support interaction, (**Figure 1.12** in **Section 1.3.2)**. Moreover, the charge transfer between Ni nanoparticles (δ^+) leads to strongly "bonded" nanoparticles to the support, which is due to Coulomb interaction, but also to better wetting of the metal to the support. This as such gives to the Ni, a higher reductive character and resistance against oxidation, i.e., against leaching.[231, 237, 241, 256]

Table 3.1 Chemical composition obtained by elemental analysis and textural properties derived from N_2 sorption for the dried NDC precursor, the parent support (NDC), and 35Ni/NDC catalyst. The Ni specific surface area of 35Ni/NDC is determined via CO-TPD.

Catalyst	C / wt.-%	N / wt.-%	C/N ratio	Ni* / wt.-%	Zn* / wt.-	A_{BET} / $m^2\,g^{-1}$	A_{meso} **/ $m^2\,g^{-1}$	V_{meso} **/ $cm^3\,g^{-1}$	V_p / $cm^3\,g^{-1}$	A_{Ni} † / $m^2\,g^{-1}$
Dried NDC Precursor	38	5.2	13	n.a.	34	n.a.	n.a.	n.a	n.a	n.a.
NDC	80	3.5	23	n.a.	<0.2	827	99	0.30	0.57	n.a.
35Ni/NDC	53	2.9	18	35	< 0.2	700	92	0.24	0.42	21

n.a.: Not applicable, *: Measured via ICP-OES, **: Calculated via QSDFT, †: Measured via CO-TPD and ¥: normalized to C

After the carbonization step, porous NDC pellets were obtained with a mass yield of 30 wt.-%. The elemental composition of the porous NDC is listed in **Table 3.1**. After the Ni impregnation, a content of 35 wt.-% of Ni was obtained (characterized via ICP-OES). Upon carbonization and catalyst activation, the

C/N ratio was found to be constant (~20), (**Table 3.1**). The N_2 sorption isotherm of the parent carbonized NDC and 35Ni/NDC presented in **Figure 3.2,** representing type IV, which is characteristic for mesoporous materials. As expected upon the Ni impregnation, the specific surface area (A_{BET}) and specific pore volume (Vp) decreased from 827 m^2 g^{-1} to 700 m^2 g^{-1} and 0.57 cm^3 g^{-1} to 0.42 cm^3 g^{-1}, respectively. The reduction in the textural properties attributed to the change of mass density of the sample, as well as to the coverage of the support surface and pores with Ni.[258] Nevertheless, the specific surface area of the mesoporous was found to be constant (~100 m^2 g^{-1}), (**Table 3.1)**.

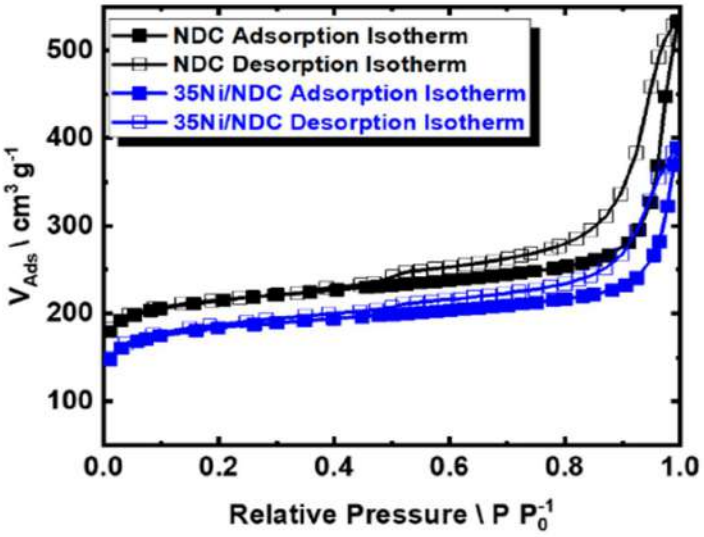

Figure 3.2. N_2 sorption isotherm at 77 K of the parent NDC and 35Ni/NDC.

XRD patterns of parental NDC and freshly reduced 35Ni/NDC showed a main broad reflection at 2θ of 25°, which corresponds to the typical reflection of turbostratic carbon (002), (**Figure 3.3**).[259] The absence of any typical Zn reflections indicates the efficient removal of the template. The freshly reduced 35Ni/NDC presents only typical reflections of Ni^0 at 2θ of 44° and 51°, which indicate the absence of any undesired NiO crystallite after calcination and reduction processes.[258]

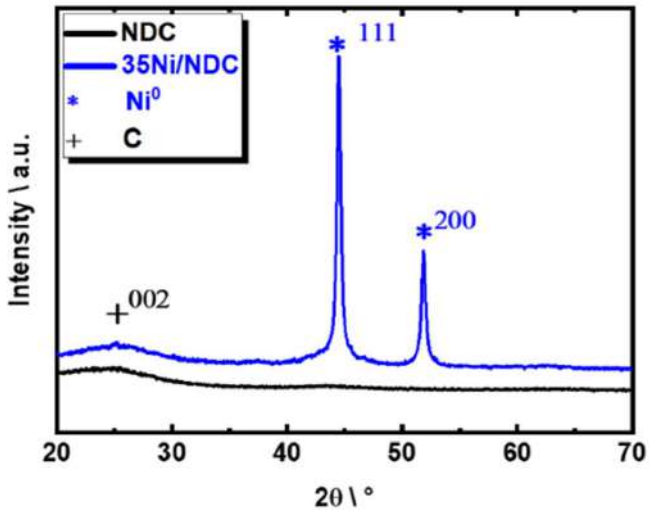

Figure 3.3. XRD patterns recorded for the parent NDC and freshly reduced 35Ni/NDC.

Images via high resolution scanning transmission electron microscopy (HR-STEM) and scanning electron microscopy (SEM) at **Figure 3.4** and **Figure C4-C5** in **Appendix**, show the support morphology and the Ni nanoparticles on the parent NDC and 35Ni/NDC. The comparison between NDC and 35Ni/NDC revealed that Ni nanoparticles are homogeneously dispersed on the surface of NDC with an average nanoparticle size of 25 nm. This is in good agreement with the crystallite diameter, calculated using the Scherrer equation from the XRD pattern. In addition, EDX mapping for C, N and Ni, *viz.* **Figure 3.4** and **C5** in **Appendix,** show that N is homogeneously distributed on the NDC support. The XRD results and microscopy imaging results are well-coupled to the results obtained from CO-TPD showing a high Ni surface area (21 m^2 g^{-1}) with crystallite size of 21 nm (**Table 3.1**).

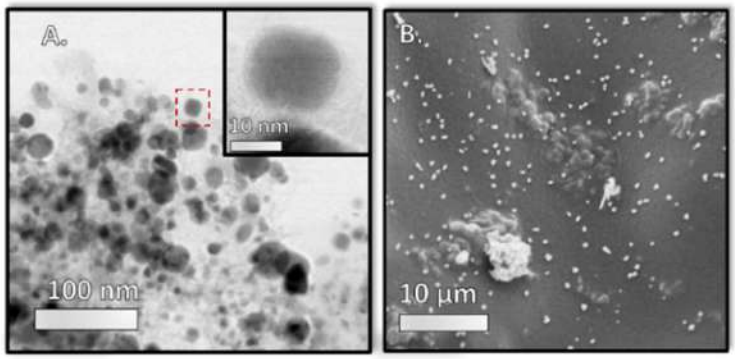

Figure 3.4. A) HR-STEM ; **B**) SEM picture of 35Ni/NDC.

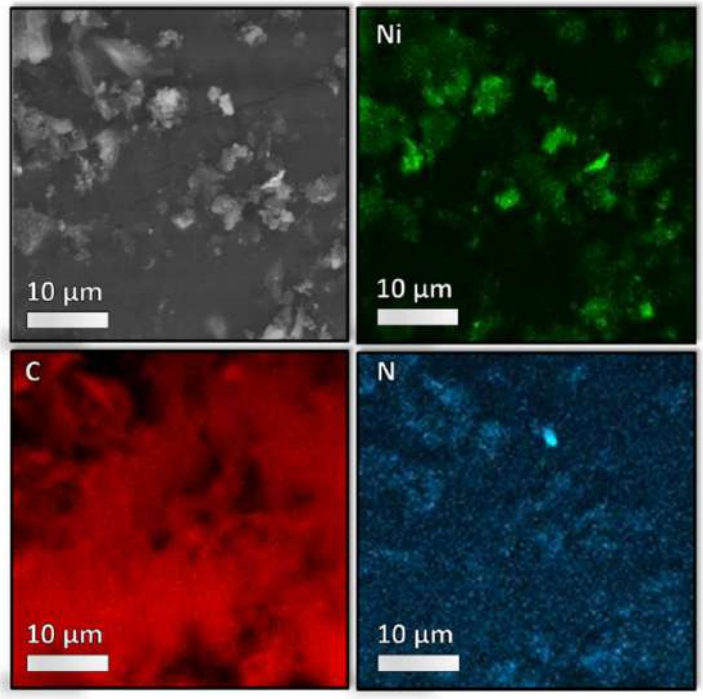

Figure 3.5. EDX mapping of 35Ni/NDC crashed pellets placed on conductive carbon tape. In black and white the selected area for mapping, in green, red, and blue respectively Ni, C and N. The black area in the C map are a shadowing effect due to the sample thickness.

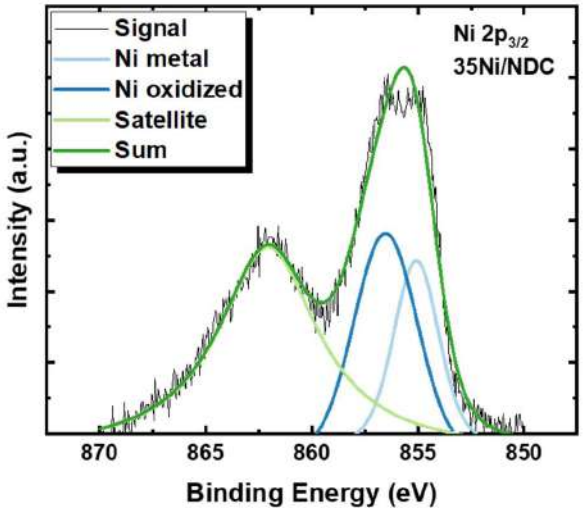

Figure 3.6. XPS spectra for Ni $2p_{3/2}$ from 35Ni/NDC catalyst.

Furthermore, X-rays photoelectron spectroscopy (XPS) results of the binding state of N (1s) bond for both parental NDC and 35Ni/NDC showed the presence of N-pyridinic, N-pyrrolic, N-graphitic and N-oxides species (**Figure C6** in **Appendix**).

However, due to the overlapping of the different N contributions, a clear quantitative deconvolution of these peaks was not possible. The XPS of Ni ($2p_{3/2}$) in the freshly reduced 35Ni/NDC exhibited the presence of Ni^0 and partly oxidized Ni (**Figure 3.6**). The presence of NiO on the outer layer of Ni^0 is attributed to the exposition of the catalyst to air after the reduction step. This assumption is in good agreement with HR-STEM coupled with EDX in which a low O amount (11 At.-%) was found on the core of Ni nanoparticle (*cf.* EDX quantification at **Table C1** in **Appendix**)**.** However, an accurate surface quantitative analysis of the Ni species by XPS was not possible due to signal interference from the different Ni species contributions. Nevertheless, NH_3-TPD showed weak acid sites at 550 K, which are attributed to the presence of NiO layer (**Figure C7** in **Appendix**).

3.4 Conclusions of Chapter 3

A simple, cheap, sustainable, scalable, and porous nitrogen-doped carbon (NDC) support was produced in pellet form. This simple approach requires only sustainable household starting products, a noodle machine, and an oven. In addition, the production of this NDC support was demonstrated at kg scale, paving the way for industrial utilization without additional re-shaping. Moreover, 35 wt.-% Ni was deposited as an active site for hydrogenation reactions, which has the potential to be applied to a wide range of hydrogenation and hydrodeoxygenation reactions within the context of biorefinery valorization in continuous flow systems.

Additionally, the NDC support can potentially be implemented with a wide range of metals rather than Ni, *e.g.* Cu, Fe, Pt, and Pd. Therefore, this NDC support has potential to pave the way for a fully new class of pelletized Mott-Schottky catalysts for biorefinery applications. For this purpose, the NDC support versatility has been proven by impregnating Pt instead of Ni for levulinic acid hydrogenation to γ-valerolactone.[260]

4. Catalytic valorization of lignocellulosic biomass-derived compounds in continuous flow systems: from single-step to integrated processes[2]

4.1 Introduction

In the context of biorefinery, several catalytic reactions have been applied for the valorization of lignocellulosic biomass (LCB) toward value-added chemicals, such as hydrogenations, hydrodeoxygenation, hydrogenolysis, decarboxylation, dehydration, and oxidation, *cf.* **Chapter 1.3.1.** Among these reactions, the focus of this thesis is on catalytic hydrogenation. Most of the reported hydrogenation studies use a noble metal-based catalyst in batch systems. However, non-noble metals, such as Ni, are considered a more sustainable alternative, cf. **Chapter 1.3.2.** Moreover, from a sustainability standpoint continuous flow systems should be preferred to batch, c*f.* **Chapter 1.2.3**. Accordingly, flow systems allow easier downstream processing, more efficient heating, as well as straightforward integration. However, to be practical and sustainable, LCB valorization in continuous flow system necessitates the catalyst being in pellet shape, based on non-noble metals, and have long-term stability in aqueous phase at temperatures above 373 K, *cf.* **Chapter 1.2.1**, **1.2.3** and **1.3.2**.

---

2 Part of this chapter is adapted from the original works:

1) F. Brandi, M. Bäumel, V. Molinari, I. Shekova, I. Lauermann, T. Heil, M. Antonietti, M. Al-Naji, Nickel on nitrogen-doped carbon pellets for continuous-flow hydrogenation of biomass-derived compounds in water, *Green Chem*. **2020**, 22,9, 2755-2766

2) F. Brandi, I. Khalil, M. Antonietti, M. Al-Naji, Continuous-Flow Production of Isosorbide from Aqueous-Cellulosic Derivable feed over Sustainable Heterogeneous Catalysts, *ACS Sustain. Chem. Eng.,* **2021,** 9, 2, 927-935.

The aim of this chapter is to present the first application of 35Ni/NDC pellet catalyst for hydrogenation of LCB-derived compounds in water. Herein, the catalytic performance of the prepared catalyst (35Ni/NDC) will be assessed for the hydrogenation of glucose (Glu) to sorbitol (Sor), xylose (Xyl) to xylit (Xyt), and vanillin (V) to 2-methoxy-3-methylphenol (MMP), respectively (**Chapter 4.3**). These compounds have been selected as valuable and already-commercialized LCB-derived chemicals representing every major LCB components: glucose for cellulose, xylose for hemicellulose, and vanillin for lignin, c*f.* **Chapter 1.3.1**. Similarly, the hydrogenated compounds, i.e., sorbitol, xylitol and MMP, are value-added chemicals with a wide range of applications, *e.g.* as sweeteners, flavors, polymer and resins precursors, and fuel additives c*f* **Chapter 1.3.1**. Therefore, in **Chapter 4.3,** the activity and stability over time on stream of the 35Ni/NDC will be investigated for the water-phase hydrogenation of Glu, Xyl and V toward Sor, Xyt and MMP.

Continuous flow systems facilitate process integration and intensification, c*f.* **Chapter 1.2.3.** Therefore, once the 35Ni/NDC catalytic performance in the single-step hydrogenation of Glu, Xyl and V is explored, there is the possibility to implement these processes into an integrated process. Among the single-step processes, the hydrogenation of Glu toward Sor has the potential to be further extended to isosorbide, c*f*. **Chapter 1.3.1**. Accordingly, 35Ni/NDC will be coupled with a commercially available catalyst, i.e., Beta zeolites, for the integrated process of glucose valorization toward isosorbide. This process consists of glucose hydrogenation toward sorbitol, catalyzed by 35Ni/NDC, followed by dehydration of sorbitol to isosorbide, catalyzed by Beta zeolites. The synthesis of isosorbide from sorbitol using Beta zeolite in aqueous media using continuous flow systems will be separately investigated in **Chapter 4.4.1** in both small and prototype-scale. Eventually, the optimum conditions obtained from glucose to sorbitol using 35Ni/NDC and sorbitol to isosorbide over Beta zeolite will be applied for the integrated process from glucose to isosorbide in prototype scale continuous flow reactors.

4.2 Procedure for continuous flow system investigation

The catalytic experiments were conducted in a homemade continuous flow fixed bed reactor, (**Figure S3**). This system consists of: (**A**) HPLC pump equipped with a pressure sensor (Knauer Azura P 4.1S Series), (**B**) mass-flow controller for $H_{2\,=}$ (Brooks Instruments, Model SLA5850SC1AF1B2A1) connected through a (**C**) "T" union for H_2-reactant mixing (Swagelok SS-400-30) before reaching the pre-heating unit and then to (**D**) a two-side opened heating unit equipped with a heat controller (Model # 4848 from the Parr Instrument Company) and (**E**) sampling unit equipped with proportional relief valves as a pressure regulator (Swagelok SS-RL4M8F8-EP), (**Figure B1** in **Appendix**). In order to ensure efficient heating an aluminum cylinder with three holes has been placed inside the heating unit, i.e., a preheating unit for the reactant before it comes in contact with the catalyst, a hole for the thermocouple (Model # A472E5 Parr Instrument Company) and a hole for the reactor (**Figure B2** in **Appendix**). The main investigations have been made using a stainless steel tubular reactor, i.e., the single-step hydrogenation of glucose to sorbitol, xylose to xylitol and vanillin to MMP as well as the dehydration of sorbitol to isosorbide, (inner diameter = 4.6 mm, outer diameter= 6.5 mm, length = 250 mm), (**right** reactor in **Figure B3** in **Appendix**). While isosorbide production from sorbitol scale-up experiment, as well as the integrated process for isosorbide production from glucose, have been conducted with a bigger stainless steel prototype-scale reactor (inner diameter = 21 mm, outer diameter = 25 mm, length = 280 mm), (**left** reactor in **Figure B3** in **Appendix**).

To conduct the integrated process for isosorbide production from glucose two fixed bed reactors have been coupled. The setup is similar to the above described with the difference of two coupled double two-side opened heating units equipped (**D1-D2**) rather than a single bed, (**Figure B4** in **Appendix**). The flow-charts of the single column and integrated process are reported in **Figure B5** and **B6** in **Appendix**, Respectively.

In a typical experiment, the aqueous reactant solution was fed via the HPLC pump at different flow rates (mostly 0.3 mL min^{-1}) and introduced into the preheating unit to the fixed bed reactor consisting of 35Ni/NDC and zeolite for hydrogenation and dehydration reaction, respectively, fixed between two layers of quartz wool. For the hydrogenation experiments the feed was mixed with an excess amount of H_2 (mostly Q_{H_2} = 15 mL min^{-1}) prior to the preheating unit. The temperature and pressure were kept constant at room conditions (298 K and atmospheric pressure) for 15 minutes. Afterwards, the system was pressurized to the desired pressure and the temperature was elevated to the reaction temperature. Samples (2.0 mL) were collected once the steady-state was reached, after *ca.* 30 min (1.5 h on prototype scale). The detailed description of the catalytic procedures are reported in **Section B4** and in **Appendix.**

Qualitative and quantitative analyses of the reactant and products were performed using HPLC/MS and HPLC, respectively. The detailed information about the reactants and product quantification procedures, as well as the calculation of the turnover frequency (TOF) can be found in **Section B5** of **Appendix**.

The batch experiment for sorbitol conversion into isosorbide was conducted in a stainless steel autoclave equipped with PTFE liners from Berghof (Model: BR-100). The batch catalytic experiments were performed at 503 K using 30 mL of aqueous solution of sorbitol ($c_{sorbitol}$ = 0.05 M) with 1.0 g of Beta(75) and 800 min^{-1} as stirring speed with autogenous pressure for 3 h. Prior the elevating the temperature to 503 K, the air was purged out using 1.0 MPa of N_2 for three times. The analysis of the reaction products followed the same protocol for the continuous flow system.

4.3 Hydrogenation of lignocellulosic biomass-derived compounds in water

Glucose hydrogenation to sorbitol

Based on the valorization of cellulosic biomass fraction, the hydrogenation of glucose (Glu) to sorbitol (Sor) is an essential reaction, (**Scheme 4**), *cf.* **Chapter 1.3.1**.[133-135] Industrially, Sor is synthesized from the hydrogenation of glucose utilizing skeletal Ni catalysts.[133, 136] Additionally, several noble metal-based catalytic systems have been reported for the Glu hydrogenation in water, such as Ru[135, 137-142] and Pt. [142-145], as well as non noble metals were used, such as Cu[146] and Ni[135, 137, 146], *cf.* **Chapter 1.3.1**. Furthermore, rapid deactivation of Ni catalysts was observed due to significant leaching of Ni under the reaction condition already in the first hours of reaction. [135, 137, 146] Also, 5.0 wt.-% Ru supported on MCM-48, carbon and TiO_2 each provided Glu conversion of 90-95% with 100% selectivity to Sor in a batch system at 493 K, 2.5 MPa of H_2 and 25 min of reaction time.[63, 141] Pan *et al*.[203] demonstrated that the Ru on multi-wall carbon nanotubes has a higher efficiency than Raney Ni catalyst in batch setup at 493 K, 4.0 MPa and 120 min of reaction time. Nevertheless, continuous flow investigation for Glu hydrogenation to Sor has been barely investigated in literature.

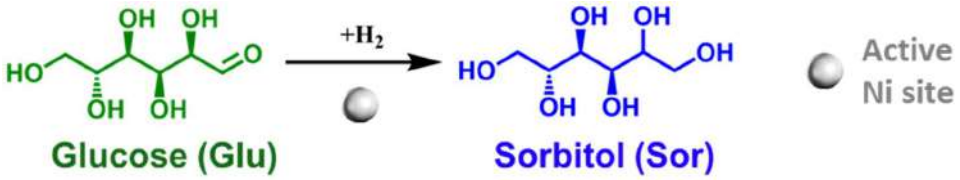

Scheme 4. The aqueous-phase hydrogenation of Glucose (Glu) into Sorbitol (Sor).

Thus, a continuous flow process for hydrogenation of Glu to Sor in water using 35Ni/NDC was designed and performed (**Scheme 4.1**). In this section, the influence of reaction temperatures and different space-time (**τ**) on the catalyst performance in the selective aqueous-phase hydrogenation of Glu to Sor were investigated. Additionally, evaluation of the catalytic activity as a function of time on stream (**TOS**) was studied. Firstly, a blank experiment with no catalyst at 423 K showed a low X_{Glu} (9.6 mol%), (**Figure C8** in **Appendix**). Additionally, fructose

(Fru) was the only detected product with Y_{Fru} of 5.3 mol%, which is formed via Glu isomerization in water at the utilized reaction conditions. The unidentified products (~4.3 mol%) can be correlated to the formation of insoluble humins in the presence of water under these reaction conditions.[261, 262] Furthermore, only the presence of the support (NDC) improved the X_{Glu} from 9.6 mol% to 29.3 mol% without significant change of Y_{Fru} (6.2 mol%), (**Figure C8** in **Appendix**), which is related to higher formation of insoluble humins (~23 mol%). Accordingly, the presence of porous NDC accelerates the dehydration and humification process of Glu even in the absence of the active Ni^0 hydrogenation sites.

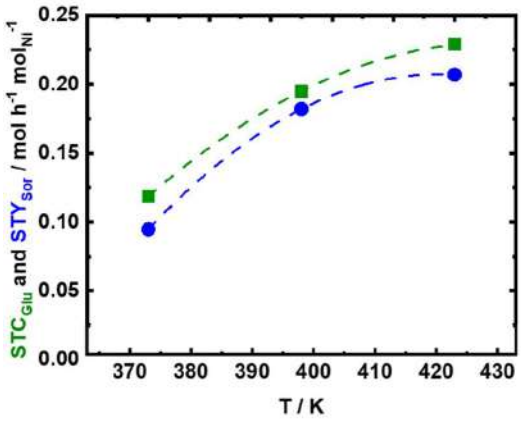

Figure 4.1. The space time conversion of Glu (STC_{Glu}) and yield of Sor (STY_{Sor}) as a function of reaction temperature (T), using 35Ni/NDC in the aqueous-phase hydrogenation of Glu to Sor, reaction conditions c_{Glu} = 56 mM (1.0 wt.-%) T = 373 K, 398 K and 423 K, , Q_{educt} = 0.3 mL min^{-1} (τ= 4.2 h mol_{Ni} mol_{Glu}^{-1}), Q_{H2} = 15 mL min^{-1} and p = 2.5 MPa.

The effect of the reaction temperature on the performance of 35Ni/NDC, as well as on the formation of insoluble humins was investigated using three different reaction temperatures, i.e., 373 K, 398 K and 423 K. As expected, the presence of 35Ni/NDC improved Glu conversion at 423 K with respect to the experiment conducted with no catalyst and with only the use of NDC (**Figure 4.1** and **Figure C8** in **Appendix**), yielding to a X_{Glu} of 97 mol% which correspond to a glucose space-time conversion **(STC_{Glu})** of 0.23 mol h^{-1} mol_{Ni}^{-1}. Also, in the presence of Ni^0 on NDC, Sor was the only identified product with a Sor space yield **(STY_{Sor})** of 0.21 mol h^{-1} mol_{Ni}^{-1} (Y_{sor} = 89 mol%). Moreover, the formation of insoluble humins was drastically reduced (from ~23 to ~8 mol%) in comparison with the experiments conducted in the absence of Ni (only NDC).

As expected the $\mathbf{STC_{Glu}}$ and $\mathbf{STY_{Sor}}$ increase with the temperature, elevating the reaction temperature from 373 K to 398 K and to 423 K is combined with an increase of $\mathbf{STC_{Glu}}$ from 0.11 mol h^{-1} mol_{Ni}^{-1} (X_{Glu} =51 mol%) to 0.19 mol h^{-1} mol_{Ni}^{-1} (X_{Glu} = 89 mol%) and to 0.23 mol h^{-1} mol_{Ni}^{-1} (X_{Glu} =97 mol%), respectively (**Figure 4.1**). Similarly, $\mathbf{STY_{Sor}}$ increased from 0.10 mol h^{-1} mol_{Ni}^{-1} (Y_{sor} = 46 mol%) to 0.18 mol h^{-1} mol_{Ni}^{-1} (Y_{sor} = 84 mol%) and to 0.21 mol h^{-1} mol_{Ni}^{-1} (Y_{sor} = 89 mol%), respectively (**Figure 4.1**). These results showed that at the lower reaction, i.e., 373 K, the conversion is very low and the hydrogenation does not proceed with high efficiency, while at 398 K there is an improvement of $\mathbf{STC_{Glu}}$, from 0.11 mol h^{-1} mol_{Ni}^{-1} to 0.19 mol h^{-1} mol_{Ni}^{-1}. A further increase of temperature to 423 K, leads to almost complete conversion (X_{Glu} =97 mol%), and to the highest $\mathbf{STY_{Sor}}$, 0.21 mol h^{-1} mol_{Ni}^{-1}. Nevertheless, at low temperatures, such as 373 and 398 K the formation of insoluble humins is very low (< 5mol%), while at 423 K the humification appears to be more pronounced (~8 mol%). However, this amount of insoluble humins that were formed using a space-time (τ) of 4.2 h mol_{Ni} mol_{Glu}^{-1}, i.e., a residence time of 15 min, is still very low in comparison to the reported data using a batch system (over 50 mol% at similar conditions)[262].

Table 4.1. Chemical composition obtained by elemental analysis and textural properties derived from N_2 sorption for the freshly reduced 35Ni/NDC_U_x and spent catalysts. The Ni specific surface area of 35Ni/NDC is determined via CO-TPD.

Catalyst	C / wt.-%	N / wt.-%	C/N ratio	Ni* / wt.-%	Zn* / wt.-%	A_{BET} / $m^2\,g^{-1}$	A_{meso} **/ $m^2\,g^{-1}$	V_{meso} **/ $cm^3\,g^{-1}$	V_p / $cm^3\,g^{-1}$	A_{Ni} † / $m^2\,g^{-1}$
35Ni/NDC	53	2.9	18	35	< 0.2	700	92	0.24	0.42	21
35Ni/NDC_U$_{Glu}$	56	2.8	20	31	< 0.2	730	90	0.25	0.51	14
35Ni/NDC_U$_{Xyl}$	52	2.7	19	29	< 0.2	799	113	0.26	0.55	14
35Ni/NDC_U$_{V}$	59	2.4	24	30¥	< 0.2	125	70	0.08	0.14	14

n.a.: Not applicable, *: Measured via ICP-OES, **: Calculated via QSDFT, †: Measured via CO-TPD and ¥: normalized to C.

Due to its high $\mathbf{STY_{Sor}}$ and $\mathbf{STC_{Glu}}$, reaction temperature of 423 K was selected for further investigation corresponding to aqueous-phase hydrogenation of Glu to Sor. These high $\mathbf{STY_{Sor}}$ and $\mathbf{STC_{Glu}}$ values using 35Ni/NDC are attributed to the high specific surface area (700 $m^2\,g^{-1}$) and specific pore volume (0.42 $cm^3\,g^{-1}$) of

the 35Ni/NDC catalyst, *cf.* **Chapter 3**. Moreover, it is correlated to the high amount of Ni (35 wt.-% proved by ICP-OES), which as well is homogenously and highly dispersed on the surface of NDC, with a high specific Ni surface area (A_{Ni}) of 20 m^2g^{-1} derived from CO-TPD (See the SEM, TEM and EDX images at **Figure 3.4** and **3.5** in **Chapter 3** and **Table 4.1**). Moreover, experiments were performed using 35Ni/NDC at 423 K and at different space-time (**τ**), i.e., 2.0 h, 2.8 and 4.2 h mol_{Ni} mol_{Glu}^{-1}, which correspond to a residence time of 6.4, 9.0 and 15 min, respectively (**Figure C9** and **C10** in **Appendix**). These experiments intend to demonstrate the key advantage of a continuous flow process, namely to control contact times which allows to avoid follow-up reactions, *e.g.* formation of humins, and to maximise the STC_{Glu} and STY_{Sor} as well as selectivity toward the desired product, i.e., Sor. Shortening the space-time from 4.2 to 2.8 and to 2.0 h mol_{Ni} mol_{Glu}^{-1}, the **STC_{Glu}** is drastically increasing from 0.22 to 0.34 and to 0.46 mol_{Glu} h^{-1} mol_{Ni}^{-1} (**Figure C9** in **Appendix**). Analogously resulted for **STY_{Sor}** from 0.21 to 0.31 and to 0.39 mol_{sor} h^{-1} mol_{Ni}^{-1}. Despite the higer **STC_{Glu}** and **STY_{Sor}**, the glucose conversion X_{Glu} slightly decrease from 97 mol% to 95 mol% and then to 84 mol% (**Figure C10** in **Appendix**).

This decrease X_{Glu} is attributed to the too short contact time between the reactant and the catalyst. A maximized X_{Glu} (97 mol%) and Y_{Sor} (89 mol%) were found at space-time (**τ**) of 4.2 h mol_{Ni} mol_{Glu}^{-1}. Shorter **τ**, i.e., 2.0 h mol_{Ni} mol_{Glu}^{-1} and 2.8 h mol_{Ni} mol_{Glu}^{-1}, showed only a linear decrease of X_{Glu} and Y_{Sor} (**Figure C10** in **Appendix**). Thus, it can be deduced that longer residence time can be applied to ensure efficient catalytic performance. Interestingly, we have observed only a little drop in selectivity toward sorbitol from 91%, to 89% and to 85%, when the residence time was shortened, from 4.2 to 2.8 and 2.0 h mol_{Ni} mol_{Glu}^{-1}, respectively. This is corresponded to the presence of traces unreacted Fru of ~1mol% and ~4 mol% at 2.8 and 2.0 h mol_{Ni} mol_{Glu}^{-1}, respectively.

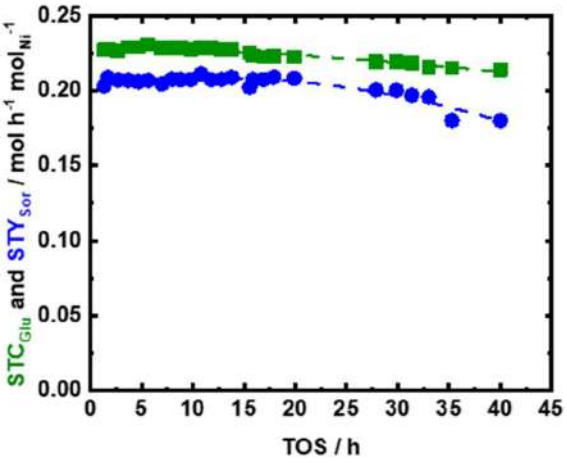

Figure 4.2. The space time conversion of Glu (STC_{Glu}) and yield of Sor (STY_{Sor}) as a function of time on stream (TOS) using 35Ni/NDC in the aqueous-phase hydrogenation of Glu to Sor; reaction conditions: c_{Glu} = 56 mM (1.0 wt-%), T = 423 K, , Q_{educt} = 0.3 mL min^{-1} (τ= 4.2 h mol_{Ni} mol_{Glu}^{-1}), Q_{H_2} = 15 mL min^{-1} and p = 2.5 MPa.

Therefore, the optimum reaction conditions namely (423 K, 4.2 h mol_{Ni} mol_{Glu}^{-1} of space time, 1.0 g of catalyst, H_2 flow of 15 mL min^{-1} and pressure of 2.5 MPa) were applied to study the catalyst performance as a function of time on stream (TOS) for conversion of Glu to Sor (**Figure 4.2**). The catalyst performance from the perspective of X_{Glu} retained without any change within 35 h of TOS (**STC_{Glu}** and **STY_{Sor}**>0.20 mol h^{-1} mol_{Ni}^{-1}). In addition, only a slight drop in the selectivity of Sor was observed after 35 h of TOS (**Figure 4.2**). Nevertheless, the **STY_{Sor}** persisted above 0.20 mol_{sor} h^{-1} mol_{Ni}^{-1} (Y_{Sor} >79 mol%) after 40 h of TOS (**Figure 4.2**). The observed decreases on **STY_{Sor}** can be correlated to the deposition of insoluble humins on the Ni active sites (~10 wt.-%, as derived from TGA, *viz.* on **Figure C11** in **Appendix** and elemental analysis in **Table 4.1**). Changing the work function of the carbon by introducing nitrogen to the framework intended to create a more stable catalyst under hydrothermal conditions. This promotes a charge transfer from the Ni to the carbon, which as a side effect strongly attracts the Ni to the surface of NDC (*cf.* **Chapter 1.3.2**). At the utilized reaction conditions and after 40 h on TOS, Ni amount decrease from 35 wt.-% to only 31 wt.-%, which is relatively low. The leaching of Ni could be explained that the loading of 35 wt.-% is relatively high in which slight amount of Ni^0 are weakly bonded to the NDC, i.e., not via Mott-Schottky transfer. However, It is a well-known phenomenon that Ni on other

support materials is completely and rapidly leached off, and consequently deactivated, along similar hydrothermal conditions. [135, 137, 146] We attribute this low amount of Ni leaching to the strong attraction of the Ni to the support caused by the introduction of nitrogen into the NDC framework.

The spent 35Ni/NDC_U_{Glu} system was studied using powder XRD to investigate the crystal structure (**Figure C12** in **Appendix**). Although the main reflections that typical of Ni^0, at 2θ of 44° and 51°, remain preserved. Also, an additional patterns showed reflections at 2θ of 19°, 33°, 38°, and 52°, which indicates a formation of hydroxides species as $Ni(OH)_2$ and NiOOH.[263] This oxidation of nickel is due to the exposure of catalyst to hot water within the washing process and cooling down the system after completing the reaction. Also, due to drying the catalytic system in air at 353 K before post characterization. The XPS analysis for Ni species of the spent catalyst, which is labelled as 35Ni/NDC_U_{Glu}, confirmed the presence of mostly oxidized species, on the surface of the catalyst (**Figure C13** in **Appendix**). This is attributed to the hydroxides formation. This is a common observation for Ni-supported catalyst that present in moisture conditions.[263] Additionally, it showed no change on the position of (N_{1s}) in the spent 35Ni/NDC with respect to (**Figure C14** in **Appendix**).

The spent catalyst shows similar morphology of the fresh catalyst (**Figure 3.4** in **Chapter 3** anf **Figure C15** in **Appendix**). In spite of humins formation, no significant changes on the textural properties were observed after 40 h of TOS with respect to the fresh catalyst (**Table 4.1** and **Figure C16** in **Appendix**). The Specific surface area $A_{BET,}$ slightly increased from 700 $m^2 g^{-1}$ to 730 $m^2 g^{-1,}$ but only among the micropores contribution. That can be correlated to higher availability of micropores due to the minimal leaching of Ni and/or to change in the material density. After 40 h of TOS, CO-TPD showed a slight reduction of Ni specific surface area from 21 $m^2 g^{-1}$ to 14 $m^2 g^{-1}$ that correlated to slight Ni leaching from 35 wt.-% to 31 wt.-%, deposition of carbonaceous species and agglomeration of non-strongly bonded Ni (**Table 4.1**). After 40 hours of TOS the XRD and XPS of the spent catalyst showed the presence of Ni oxidized species on the surface of NDC. Therefore, an attempt to regenerate Ni^0 in the spent catalyst was performed

(see the details reactivation procedure in **Section B** of **Appendix**). Indeed, the Ni0 was successfully restored via the regeneration procedure which is confirmed by XRD and HR-STEM. These characterization results showed that Ni^0 was the dominant phase on the surface of the catalyst (**Figure C17** and **C18** in **Appendix**). Along the manuscript the regenerated catalyst is given a code as (35Ni/NDC_R_x).

Finally, as a proof of concept the catalytic activity of 35Ni/NDC and synthesized 35 wt.-% Ni on commercially available carbon black (CB) in Glu hydrogenation to Sor under the optimum reaction conditions was compared. The results of using 35Ni/CB was worst with respect to 35Ni/NDC (**Figure C19** in **Appendix**). This can be a sign for the advantage of using Ni on heteroatom-doped carbon. This is consistent with the findings of Nie *et al.*[202] for aqueous-phase hydrogenation biomass-derived compounds.

Xylose hydrogenation

Similarly to Glu, Xylose (Xyl) is the major sugar in the hemicellulose fraction. Therefore, the hydrogenation of Xyl towards xylitol (Xyt) is an important reaction due to Xyt properties and applications, *cf.* **Chapter 1.3.1**.[153] These properties allow Xyt to be utilized in wide range of consumer products. In analogy to the process for Sor production, Xyt can be synthesized via hydrogenation of Xyl using supported Ni (Raney Ni, Ni/Al_2O_3, Ni/SiO_2) or Ru (Ru/Al_2O_3, Ru/C, Ru/TiO_2, Ru/ion exchange resins and Ru/HY zeolite catalysts).[153, 188-193] Most of these studies reported a high conversion of Xyl and Xyt yield in a batch system, temperature range from 393 K – 463 K, H_2 pressure of 2.0 MPa – 8.0 MPa at longer reaction times of 2 – 6 h.[188-193] Likewise the Glu hydrogenation, the activity of 35Ni/NDC was studied in hydrogenation of Xyl towards Xyt in water (**Scheme 4.2**).

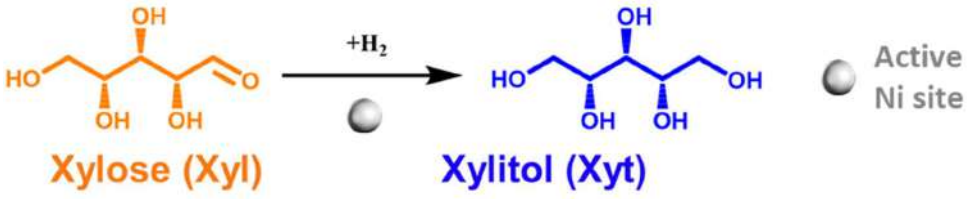

Scheme 4.2. Hydrogenation of xylose (Xyl) to xylitol (Xyt).

The influence of reaction temperature and space time (**τ**) on the performance at longer TOS was evaluated. Similarly to glucose experiment, a blank experiment was conducted at 423 K, without catalyst (**Figure C20** in **Appendix**) yielding 18 mol% loss of Xyl, and no Xit has been detected. This indicates the occurrences of a humification process. A higher conversion X_{Xyl} (40 mol%) was found using parent NDC, while no Xyt was formed. In this case, Xyl simply turned into insoluble humins, the process being catalyzed by the available high specific surface area in the parent NDC. The formed humins fractions are larger than in the glucose case (**Figure C8** and **Figure C20** at ESI). This is due to the fact that under hydrothermal conditions and at high temperature (423 K), Xyl is less stable than Glu. However, the humins formation in both cases in the continuous flow system remains lower than similar experiments conducted in batch system.[262] After adding 35 wt.-% of Ni to NDC, the catalytic hydrogenation performance improved drastically, yielding in a $\mathbf{STC_{Xyl}}$ of 0.28 mol_{Xyl} h^{-1} mol_{Ni}^{-1} and $\mathbf{STY_{Xyt}}$ 0.27 mol_{Xyt} h^{-1} mol_{Ni}^{-1} which correspond to X_{Xyl} = 99 mol% and Y_{Xit} = 97 mol%, respectively, (**Figure C20** in Appendix). In other words, we found mostly a quantitative conversion of Xyl to Xyt. The reaction temperature effect on the catalytic performance of 35Ni/NDC has been studied using 373 K, 398 K and 423 K (**Figure C21** in **Appendix**). A linear increase in $\mathbf{STC_{Xyl}}$ and $\mathbf{STY_{Xyt}}$ was found by increasing the reaction from 373 K, 398 K and 423 K (**Figure C21** in **Appendix**). The higher reactivity of Xyl with respect to glu, is attributed to its higher instability when exposed to high temperature.

Also, the space-time study confirmed the high activity of 35Ni/NDC for Xyl reduction to Xyt. In fact, even at short space-time (1.6 h mol_{Ni} mol_{Xyl}^{-1}), the X_{Xyl} was of 92 mol% and the Y_{Xyt} of 88 mol% (**Figure C22** in **Appendix**). Shortening the space time from 3.6 to 2.2 h mol_{Ni} mol_{Xyl}^{-1} did not affect the selectivity towards Xyt (>99%). Applying a shorter contact time (1.6 h mol_{Xyl} mol_{Ni}^{-1}), a negligible drop of Xyt yield from (>99mol%) to (95 mol%). This is attributed to traces of some undetected isomerization products, such as xylulose. Therefore, likewise for glucose the optimized condition were 423 K and 3.6 h mol_{Xyl} mol_{Ni}^{-1}, correspond to a residence time of 15 min.

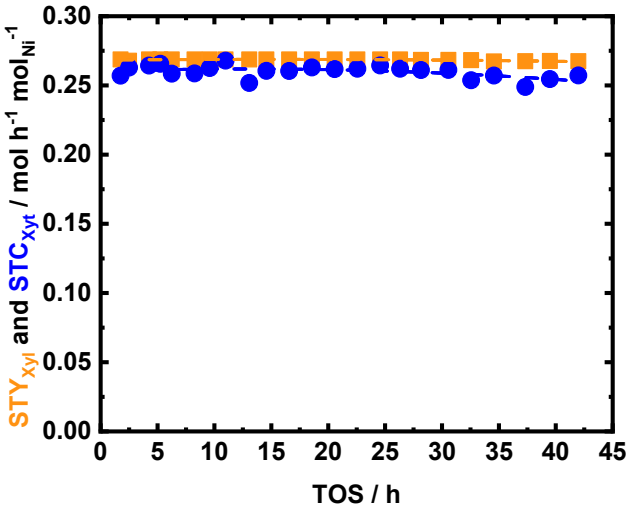

Figure 4.3. The space-time conversion of Xyl (STC_{Xyl}) and space-time yield of Xyt (STY_{Xyt}) as a function of time on stream (TOS) using 35Ni/NDC in the aqueous-phase hydrogenation of Xyl to Xyt; reaction conditions: c_{Xyl} = 64 mM (c_{Xyl}= 1 wt.-%), T = 423 K, Q_{educt} = 0.3, mL min^{-1} (τ= 3.6 h mol_{Ni} mol_{Xyl}^{-1}), Q_{H2} = 15 mL min^{-1} and p = 2.5 MPa.

The 35Ni/NDC has been exposed for 42 h of TOS, at the abovementioned optimum reaction conditions (**Figure 4.3**). The 35Ni/NDC showed a high catalytic performance with excellent stability. Similarly, this exceptional stability is attributed to the heterojunction effect due to the presence of N doping in the carbon. Identically to the reported characterization of the spent catalyst in Glu hydrogenation, the textural properties of the 35Ni/NDC_U_{Xyl} were preserved over the long TOS. Thus, only a little Ni leaching from 35 wt.-% to 29 wt.-% was found (**Table 1**). Additionally, the specific surface area showed a slight increase due to the deposition of a slight amount humin (> 4 wt.-% derived from TGA) on the surface of the catalyst (**Table 4.1**.and **Figure C11** in **Appendix**) . Also in this case the XRD pattern of the spent 35Ni/NDC_U_{Xyl} and the regenerate 35Ni/NDC_R_{Xyl} showed the formation of Ni-hydroxide species after reaction and their further reduction to Ni^0 (**Figure C12** and **C18** in **Appendix**). Moreover, the CO-TPD analysis showed a relatively low reduction of the specific Ni surface area A_{Ni} from 20 m^2 g^{-1} to 14 m^2 g^{-1} (**Table 4.1**) with preserved crystallite size (19 nm). This very similar behaviour of the two 35Ni/NDC_U_{Xyl} and 35Ni/NDC_U_{Glu} confirmed the robustness of 35Ni/NDC at such long TOS and over regeneration treatment.

Vanillin hydrogenation

Vanillin (V) is an important compound that can be derived from lignin, *cf.* **Chapter 1.3.1**.[23, 28, 87]. V hydrogenation products, 2-methoxy-4-methylphenol (MMP) and Vanillyl alcohol (VA) can be applied in food and polymer industries or ad fuel additive, *cf.* **Chapter 1.3.1**.[198] Typically, the hydrogenation of V towards vanillyl alcohol (VA) or MMP is conducted using supported precious metal (Pd, Pt, Ru and Rh) catalysts in batch systems and high pressure of H_2 (0.5 MPa – 10 MPa). Nevertheless, few studies have investigated the utilization of supported Ni or Cu as an active species. In this regards, Bindwal *et al*.[194] showed an efficient conversion of V to VA and MMP using Ru/C (complete V conversion with VA yield up to 90 mol % and MMP yield up to 10 mol% at 338 K and 2.1 MPa of H_2).[194] Furthermore, investigations about the performance of noble metals catalysts (Ru, Rh, Pd, Au and Pt) supported on C in aqueous phase hydrogenation of V in a batch system were reported.[200] All these catalysts showed a complete V conversion, whereas, Pd/C gave the highest yield of MMP (95%) H_2.[200] Moreover, bimetallic Cu-Pd catalysts anchored on organic porous polymer were found to be able to convert V to MMP (yield 93 mol%), in *i*-propanol as a solvent.[201] Nevertheless, few trails have been reported utilizing non-noble metal based catalysts for V hydrogenation. For instance, Nie *et al*.[202] obtained a V conversion of 90% and MMP yield of 66% using a 20 wt.-% Ni on nitrogen-doped carbon in a batch system at 423 K, 0.5 MPa of H_2 and 2 h of reaction time.[202]

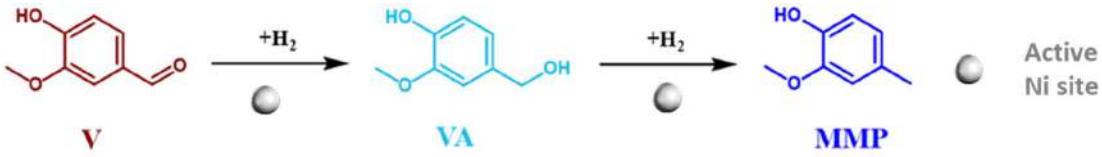

Scheme 4.. Hydrogenation of vanillin (V) toward 2-methoxy-4-methylphenol (MPP) through vanillyl alcohol (VA).

In this part, the selective aqueous-phase hydrogenation of vanillin (V) to 2-methoxy-4-methylphenol (MMP) via vanillyl alcohol (VA) will be addressed (**Scheme 4.3**). In contrast to the experiments conducted with aqueous solutions of sugars, i.e., Glu and Xyl, no conversion of V to any products were observed in the absence of catalyst and in the presence of the support (NDC) at 423 K, (**Figure C23** in **Appendix**). Moreover, under similar reaction conditions but in presence of

35Ni/NDC, a quantitative conversion of V towards MMP was obtained (**Figure C23** in **Appendix**). This conversion and yield are much higher when compared to literature experiments with a different Ni catalyst supported on carbon black and NDC in a batch system.[202]

The influence of reaction temperature on the space time conversion of V (**STC_V**) and on products distribution was investigated, by applying five different reaction temperatures (353 K, 373 K, 398 K, 408 K and 423 K). The complete **STC_V** to VA and MMP was obtained over 373 K (**Figure 4.4**). It can be clearly seen that from the reaction temperature of 398 K and above, the reaction equilibrium is shifted towards the formation of MMP, which is the consecutive product of VA hydrogenation (**Scheme 4.3**). Interestingly, the experiment utilized low reaction temperature (353 K) resulted in high space time yield of VA (**STY_{VA}**) of 0.22 mol_{VA} h^{-1} mol_{Ni}^{-1} (Y_{VA} = 77 mol%) and low **STY_{MMP}** of 0.04 mol_{MMP} h^{-1} mol_{Ni}^{-1} (Y_{MMP} = 16.9 mol%), (**Figure 4.4**). A similar interplay between VA and MMP is in agreement with similar studies reported in batch system using Ni, Pd and Ru catalyst by altering the reaction time.[199, 202, 264] Therefore, it can be deduced that the prepared catalyst exhibited a high efficiency on V hydrogenation towards VA and/or MMP. Since varying the temperature has been reported a change in the main product from MMP to VA, the same has been researched varying the space time at 423 K (**Figure C24** in **Appendix**). In this context, the space time was found to be less effective in tuning the reaction products with respect to reaction temperature. However, it is possible to see that altering the space time of one order of magnitude, i.e., from 3.4 h mol_{Ni} mol_V^{-1} which is equal to 15 min of residence time to 0.35 h mol_{Ni} mol_V^{-1} that correspond to 1 min of residence time, the **STY_{VA}** increased from to 0.95 mol_{VA} h^{-1} mol_{Ni}^{-1} (Y_{VA} from 0 to 33 mol%), (**Figure C24** in **Appendix**). These results showed that the tunability of reaction products is also possible by reducing the residence time from minutes to potentially seconds scale at low reaction temperature range. Additionally, this indicate that using a flow system also allows optimization and potential isolation of the intermediate products.

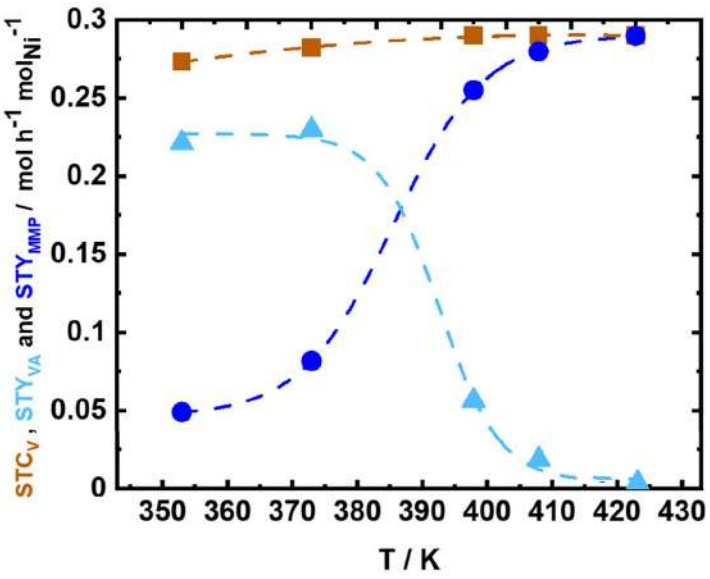

Figure 4.4. The space time conversion of V (STC_V), the space time yield of VA (STY_{VA}) and space time yield of MMP (STY_{MMP}) as a function of temperature (T) using 35 Ni/NDC in the aqueous-phase hydrogenation of V to VA and MMP; reaction conditions: c_V = 72 mM (1.0 wt.-%), T = 353 K, 373 K, 398 K, 408 K and 423 K, Q_{educt} = 0.3 mL min^{-1} (τ= 3.4 h mol_{Ni} mol_V^{-1}), Q_{H_2} = 15 mL min^{-1} and p = 2.5 MPa.

The stability of the catalyst has been investigated using the optimized reaction conditions, in which V is quantitatively converted to MMP. Similarly to Glu and Xyl hydrogenations, in this case the catalyst survived after 40 h of time of stream (**Figure 4.5**). In fact, the utilized catalyst showed better catalytic performances, i.e., **STCv** of 0.29 mol_V h^{-1} mol_{Ni}^{-1} (X_V = 100 Mol%) and **STY_{MMP}** of 0.28 mol_V h^{-1} mol_{Ni}^{-1} Y_{MMP} > 98 mol%, after 40 h of TOS. Contrarily to what observed in the case of Glu and Xyl revealed a significant decrease of the specific surface area (A_{BET}), from 700 m^2g^{-1} to 125 m^2g^{-1}. This reduction is mainly attributed to a drop in the micropores, (**Figure C16** in **Appendix**). This is common phenomenon for porous carbon in the presence of aromatic species.[32] Therefore, the decrease in the specific surface area can be explained as pore blocking due to the strong interaction between the aromatics and the NDC surface. This confirmed from the elemental analysis of the spent catalyst in which increasing of C from 53 wt.-% to 59wt.-% when compared to the fresh 35Ni/NDC (*c.f.* **Table** 4.**1**). However, this deposition did not affect the catalyst performances, since the **STCv** and **STY_{MMP}** were extremely stable over 40h of TOS. This constant activity correlated to the presence of highly dispersed Ni and the remaining

efficient mesoporous that allows this reaction to proceeds without noticeable deactivation.

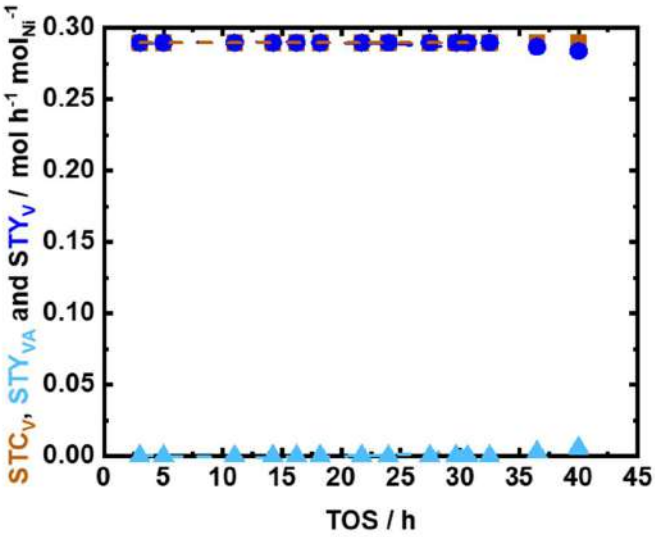

Figure 4.5. The space time conversion of V (STC_V), the space time yield of VA (STY_{VA}) and space time yield of MMP (STY_{MMP}) as a function of time on stream (TOS) using 35Ni/NDC in the aqueous-phase hydrogenation of V to MMP; reaction conditions: c_V = 72 mM (1.0 wt.-%), T = 423 K, Q_{educt} = 0.3 mL min^{-1} (τ = 3.4 h mol_{Ni} mol_V^{-1}), Q_{H_2} = 15 mL min^{-1} and p = 2.5 MPa.

Moreover, Ni leaching was minimal and found to be 30% after 40 h TOS which is similar the values reported for 35Ni/NDC_U_{Glu} and 35Ni/NDC_U_{Xyl} (**Table 4.1**). In agreement with the results obtained with the spent catalyst in Glu and Xyl hydrogenation, a slight reduction of Ni specific surface area from 21 m^2 g^{-1} to 14 m^2 g^{-1} that is attributed to slight Ni leaching from 35 wt.-% to 31 wt.-%, deposition of carbonaceous species and agglomeration of non-strongly bonded Ni (**Table 4.1**). Again, the successful regeneration procedure was confirmed by the XRD reflections, which showed the re-reduction of Ni from (**Figure C17** and **C18** in **Appendix**). Additionally, both XRD and CO-TPD of the regenerated sample showed similar Ni crystallite size of ~20 nm.

Finally, the robustness of this catalyst has been confirmed one more time, extending its usage from the valorization of sugar fraction of biomass to the aromatics fraction. In all these cases the catalyst showed high catalytic performance after 40 h of TOS with and was successfully regenerated. Therefore, the 35Ni/NDC catalyst has the potential to be implemented into

multi-step valorisation using others commercially available catalysts. To this aim, in the following chapter, 35Ni/NDC will be used in combination with zeolites for integrated processes, such as glucose to isosorbide.

4.4 Integrated process for isosorbide production from glucose

4.4.1 Sorbitol dehydration to Isosorbide over Beta zeolites

In the previous chapter, Glu to Sor has been reported using 35Ni/NDC catalyst. Although Sor is a valuable compounds, it can be upgraded via acid-catalyzed hydrolysis to a high valuable building block such as Isosorbide, *cf.* **Chapter 1.3.1**. Despite its value, Isosorbide is produced nowadays with non-sustainable and economically inefficient homogenous catalyst, *cf.* **Chapter 1.3.1**. Seeking for heterogenous alternatives, several solid acid catalysts, i.e., zeolites, mixed oxides and resins, have been proposed for isosorbide production from sorbitol.[148, 163-176] These trials used a molten bulk phase in small quantities (the solid phase consists of sorbitol and catalyst), i.e., they cannot be largely scaled. Of these catalysts, zeolite was found to be the optimum choice for dehydration of sorbitol to isosorbide, and Beta zeolite showed the highest catalytic performance (isosorbide yield ~ 80 mol%), as it possesses suitable textural properties, i.e., pore size distribution of (5-7 Å) and acid side density above 300 µmol g^{-1}.[177, 178] However, to date, isosorbide synthesis in flow systems has been reported only using water steam, i.e., gas-phase reactions.[172, 180-182] The group of Huang tested various solid acids such as sulfated copper oxide,[181] metal phosphate,[180] supported tungstophosphoric acid [172] and modified tantalum oxide by phosphoric acid in the gas-phase dehydration of sorbitol to isosorbide. [182] The highest isosorbide yield using these solid acids in gas-phase reaction was 68 mol% at 473 K.[181] All those above-mentioned approaches rely on the usage of gas-phase reaction, using N_2 as carrier and inert gas. Also, Xi *et al.*[265] reported a sequential process for isosorbide production from cellulose, composed by cellulose depolymerization/hydrogenation toward sorbitol using Ru/$NbOPO_4$-pH_2 in batch system. In a separated second step a steam of the

formed sorbitol was flown over $NbOPO_4$-pH_2 for isosorbide production, with an isosorbide yield of 57 mol%.[265] When compared to water in liquid-phase, the use of vapor phase reaction presents additional costs such as the gas-supply and gas-liquid separation.

In these terms, it is surprisingly that the isosorbide synthesis from sorbitol in liquid aqueous-phase has not been reported yet. Therefore, to establish an integrated process from glucose to isosorbide, is necessary to conduct the sorbitol dehydration in continuous flow systems over solid acid catalyst first.

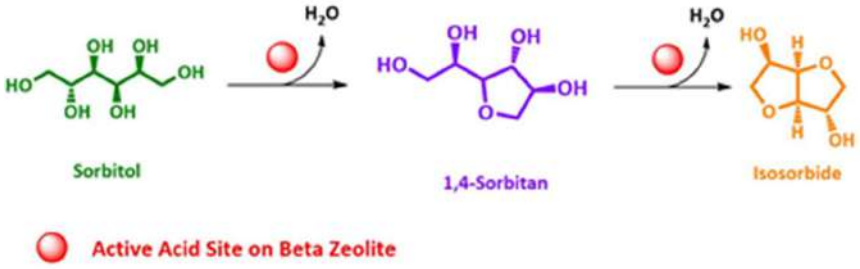

Scheme 4.4. Synthesis by sorbitol dehydration to 1,4-sorbitan and finally to isosorbide over Beta zeolite.

Based on the literature, Beta zeolite was selected as a catalyst for sorbitol dehydration to isosorbide.[177] Beta zeolite has a 3D pore architecture and offers sufficient specific surface area (400 – 600 $m^2\ g^{-1}$) and total acid site densities (200 – 600 µmol g^{-1}) to perform efficiently the bimolecular dehydration of sorbitol to isosorbide. In addition, it allows quick diffusion to/from the pores since its pore size (6.6 x 6.7 Å) is larger than the cross section of both sorbitol (5.7 x 5.9 Å) and isosorbide (5.9 x 6.2 Å). As an attempt to maximize isosorbide yield from an aqueous solution of sorbitol in a flow system, the reaction temperature, acid sites density of Beta zeolite, and catalyst contact time were varied.

The textural properties of all the used Beta zeolites, i.e., Beta(12.5), Beta(75) and Beta(150), were characterized via N_2-sorption, XRD, SEM and Pyr-IR. The specific surface area (A_{BET}), the pore volume (V_p) and the average pore-diameter (D_p) were deduced from N_2-sorption, (**Table C2** and **Section C2.2.1** in **Appendix**). Moreover, the XRD patterns of fresh Beta zeolites used in this work exhibited the

typical reflection of zeolites (**Figure C25** in **Appendix**). Similarly, the SEM images showed typical zeolite morphology, (**Figure C26** in **Appendix**).

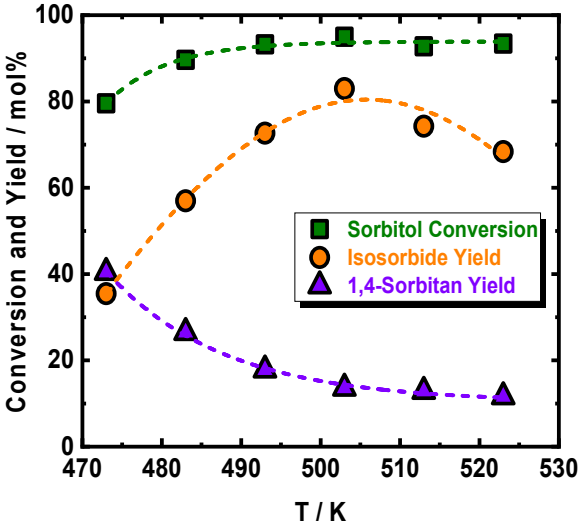

Figure 4.6. The conversion of sorbitol and the yield of isosorbide and 1,4-sorbitan as a function of reaction temperature; Reaction conditions: $c_{sorbitol}$ = 0.05 M, $Q_{solution}$ = 0.3 mL min^{-1}, T = 473 K, 483 K, 493 K, 503 K, 513 K and 523 K, p_{system} = 4.0 MPa, $m_{catalyst}$ = 2.5 g and τ = 3.0 h kg mol^{-1}.

Initially, Beta zeolite with a Si/Al molar ratio of 75 has been selected to perform a temperature studies, as it showed optimum catalytic performance in molten bulk phase.[177] Therefore, increasing the reaction temperature from 473 to 503 K was found coupled with gradual increase of sorbitol conversion from 80 – 95 mol% and isosorbide yield from 38 - 83 mol% (**Figure 4.6**). A lower reaction temperature resulted in the formation of higher amounts of 1,4-sorbitan instead of isosorbide due to insufficient amount of energy to enable an efficient performance of the second dehydration from 1,4-sorbitan to isosorbide (**Figure 4.6**). The conversion of sorbitol (95 mol%) remained constant throughout further increase of reaction temperature to 523 K. However, isosorbide yield was found to decrease from 83 mol% at 503 K to 76 mol% at 513 K and subsequently to 68 mol% at 523 K without any identified byproducts. This gradual decrease of isosorbide yield at temperature above 503 K is due to the formation of high condensed humic species (dark brown colored solution) that also deposit on the catalyst. TGA analysis for the spent catalyst showed a weight loss of around 3.0 wt.-%, reflecting this deposition. This

indicates that isosorbide is not stable at temperature higher than 503 K. Moreover, the blank experiment with absence of catalyst at 503 K showed no conversion of sorbitol, which is stable under this reaction conditions. This indicate that the presence of solid acid catalyst is essential to enable the dehydration of sorbitol to isosorbide. Furthermore, these findings indicate the degradation of the products as the major limitation for further temperature increasing. In these regards, the removal of products from the hot reaction environment guaranteed by of continuous flow systems can be beneficial for selectively perform the dehydration of sorbitol to isosorbide, i.e., by using the continuous flow system sorbitol is converted selectivity to 1,4-sorbitan and isosorbide with no additional by-products such as the isomers of 1,4-sorbitan.

To gain more insight of the reaction kinetics, the apparent activation energy (E_a) for the 1st dehydration (sorbitol to 1,4-sorbitan) and 2nd dehydration (sorbitol to isosorbide) reactions were calculated from Arrhenius plot assuming first order kinetics (**Figure C27** in **Appendix**). The calculated values are 55 kJ mol^{-1} and 125 kJ mol^{-1}, respectively. These calculated E_a values are lower than the one reported in literature for sorbitol dehydration over heterogeneous catalysts in molten phase batch system, i.e., silicotungstic acid (140.3 kJ mol^{-1})[266], sulfonated ZrO_2 (87 kJ mol^{-1})[174] and Beta zeolite (89 kJ mol^{-1})[177]. Our 55 kJ mol^{-1} for sorbitol dehydration to 1,4-sorbitan was comparable to the value calculated of homogenous catalysts (48 kJ mol^{-1} for H_2SO_4).[161, 162] In addition, the calculated E_a for 1,4-sorbitan dehydration to isosorbide is comparable to the reported value for silicotungstic acid (104.17 kJ mol^{-1}).[169] All these results indicated that the second dehydration of 1,4-sorbitan to isosorbide is the rate-determining step while the reaction at the operation conditions was not limited by transport phenomena. Furthermore, the turnover frequency (TOF) for isosorbide production was found to be 0.64 h^{-1} at 503 K. These results emphasize the advantages of operating this reaction in continuous-flow system which will improve the isosorbide formation.

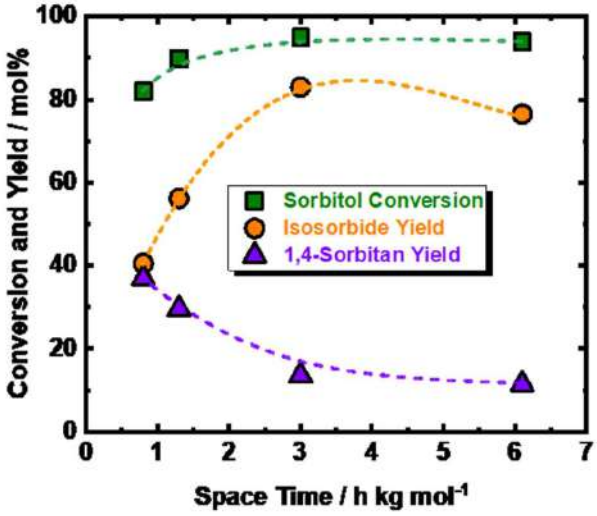

Figure 4.7. The conversion of sorbitol and the yield of isosorbide and 1,4-sorbitan as a function of space time; Reaction conditions: $c_{sorbitol}$ = 0.05 M, $Q_{solution}$ = 0.15, 0.3. 0.7, 1.0 mL min^{-1}, T = 503 K, p_{system} = 4.0 MPa, $m_{catalyst}$ = 2.5 g and **τ**= 6.1, 3.0, 1.3 and 0.8 h kg mol^{-1}.

The effect of contact time was also investigated using Beta(75) and 503 K as reaction conditions. As expected, below 3.0 h kg mol^{-1}, the reaction turns incomplete and sorbitol conversion decreased from 95 mol% to 81 mol% (**Figure 4.7**), as well as Isosorbide yield dropped from 83 mol% to 56 mol%. Insignificant influence of space time above 3.0 h kg mol^{-1} was found on all the sorbitol conversion and 1,4-sorbitan yields (**Figure 4.7**), whereas isosorbide yield slightly decrease from 83 mol% to 76 mol%. This latter decrease is attributed to the longer residence time, which leads to isosorbide decomposition and consequent humification. Accordingly, the use of flow system allows a fast quenching of metastable products to form high isosorbide yield. An experiment at low space time, of 0.8 h kg mol^{-1} at 503 K, was performed to ensure that isosorbide and 1,4-sorbitan is the only reaction products by operating the reaction where the sorbitol conversion was not at its maximum (< 94 mol%), (**Figure C28** in **Appendix**). After 3.5 h of time on stream (TOS), isosorbide and 1,4-sorbitan were the only detected products with yields of 50 mol% and 40 mol%, respectively. With the progress of the reaction, the conversion of sorbitol and the yield of isosorbide gradually decreasing respectively to 60 mol% and 10 mol% after 12 h of TOS. At this TOS

value, 1,4-sorbitan was the dominant product (yield around 40 mol%). This finding is a further evidence that the dehydration of sorbitol in continuous flow system resulted on 1,4-sorbitan and isosorbide. Also, it emphasizes that the dehydration of 1,4-sorbitan to isosorbide is the rate determining step. On the other hand, the gradual drop of sorbitol conversion and isosorbide yield is attributed to the hydrothermal instability of Beta (75) under these harsh reaction conditions (**Figure C25** and **C28** at ESI). In this term, the hydrothermal stability of the zeolite catalyst represents the central drawback of such catalyst for industrial applications.

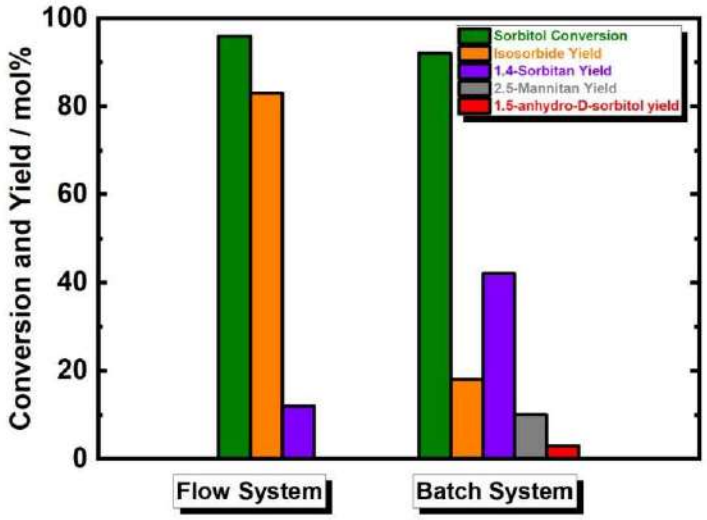

Figure 4.8. The conversion of sorbitol and isosorbide yield in aqueous liquid phase dehydration in continuous flow reactor and batch system over Beta(75); reaction conditions in continuous flow reactor: $c_{sorbitol}$ = 0.05 M, $Q_{solution}$ = 0.3 mL min^{-1}, T = 503 K, p_{system} = 4.0 MPa, $m_{catalyst}$ = 2.5 g and τ = 3.0 h kg mol^{-1}; reaction conditions in batch system: $c_{sorbitol}$ = 0.05 M, T = 503 K, V_{educt} = 30 mL, $m_{catalyst}$ = 1.0 g, n = 800 min^{-1} $t_{reaction}$ = 2 h and autogenous pressure.

For a comparison purpose and deep understanding of the reaction pathway and products distribution, experiments in batch system was performed in absence and presence of Beta(75) at 503 K (**Figure C34**). The blank experiment (without catalyst) showed no conversion of sorbitol. This is in an agreement with the one that performed at continuous flow system, as well as show that the presence of solid acid catalyst is essential for this reaction. Interestingly, the presence of Beta(75) led to 92 mol% conversion of sorbitol to 42 mol% of 1,4-sorbitan as a major product (**Figure C34**), as well as isosorbide of 18 mol%, 2,5-mannitan of 10

mol% and 1,5-anhydro-D-sorbitol of 3 mol% (the side product was confirmed using HPLC/MS equipped with hypercarb column and evaporative light scattering detector (ELSD). The low yield of isosorbide is due to the deposition of humificated products on the surface of the catalyst which blocked the accessibility to the active acid side (BAS), as well as the absence of removal of the formed product in comparison to continuous flow system. This result clearly showing the advantageous of using a continuous flow system with respect to batch reactor as it is efficient and led to high selectivity toward isosorbide.

In addition, aiming to fully understand the role of the acid sites for isosorbide production from sorbitol, we investigated Beta zeolites with different Si/Al molar ratios (12.5, 75 and 150) under the optimum reaction conditions, *cf.* **Section 4.2.2** in **Appendix**. The experiment showed that the Beta(75) zeolites present the more suitable acitidy, owing to Brønsted (BAS) and Lewis (LAS) acid site densities of 69 μmol g^{-1} and 14 μmol g^{-1} at 523 K, respectively. Similarly, an experiment using Beta(75) in batch systems was conducted for comparison purpose

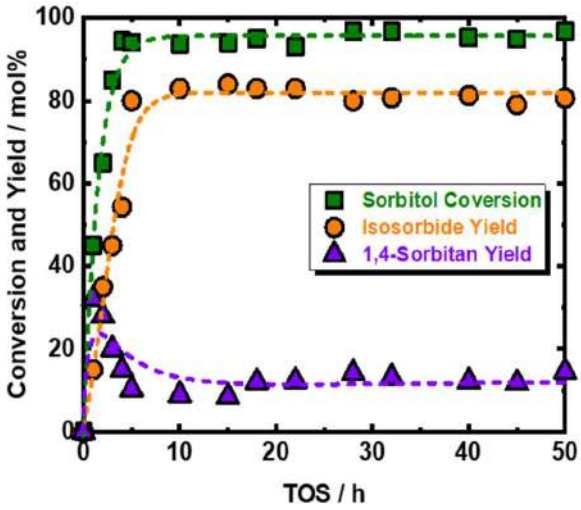

Figure 4.9. The conversion of sorbitol and the yield of isosorbide and 1,4-sorbitan as a function of time on stream (TOS) using Beta(75); Reaction conditions: $c_{sorbitol}$ = 0.05 M, $Q_{solution}$ = 0.7 mL min^{-1}, T = 503 K, p_{system} = 4.0 MPa, $m_{catalyst}$ = 30 g and τ = 14.8 h kg mol^{-1}.

To investigate this process on a larger scale and analyzing process stability at higher space time, Beta(75) in pellet form, and reaction conditions of 503 K, 14.8

h kg mol^{-1} and a larger prototype set-up were used (the experimental details are shown in **Section B** in **Appendix**). Under these reaction conditions and after reaching the steady state, the conversion of sorbitol (94 mol%) and the yield of isosorbide (83 mol%) were maximized, (**Figure 4.9**). Also, by using this prototype tubular reactor, an isosorbide TOF of 0.12 h^{-1} was calculated. This process was conducted for 50 h of TOS and the catalysts performance appeared to be stable. These results clearly showed the advantages of using a continuous flow system for isosorbide synthesis with respect to a batch system in which the catalyst suffers from a rapid deactivation, as continuous removal of the products is absent. The post characterization of Beta(75) showed a reduction in the specific surface area from 520 m^2 g^{-1} to 290 m^2 g^{-1} combined with decrease of in crystallinity (**Table C2** and **Figure C25** in **Appendix**). SEM images of the fresh and spent catalysts showed no differences (**Figure C26** in **Appendix**). The changes in the textural properties are both due to the deposition of carbonaceous species and the known instability of zeolites in hot aqueous media (**Figure C29** in **Appendix**), and are in good agreement with previous literature reports.[267, 268]

4.4.2 Glucose to isosorbide integrated process using 35Ni/NDC coupled with Beta zeolites

To date, very few studies on literature have reported Isosorbide synthesis from glucose. Uniquely, the Sels group showed that isosorbide (> 60 mol%) can be straightforwardly produced from cellulose using two different catalysts (heteropoly acids for the dehydration reactions and Ru on carbon for the hydrogenation reaction) at 503 K and under 5 MPa of H_2.[269] Similarly, the direct complete conversion of aqueous glucose solution to isosorbide (yield = 79 mol%) was reported using Ru/Dowex at 463 K after 24 h.[154] However, these studies rely on the usage of batch systems, while one of major advantage of using continuous flow systems consists in straightforward integration for industrial application, cf. **Chapter 1.2.3**. Accordingly, in the two previous section, i.e., **Chapter 4.3** and **Chapter 4.4.1**, are distinctly reported the continuous flow synthesis of Sorbitol from Glucose over 35Ni/NDC catalyst and of Isosorbide from Sorbitol over Beta zeolites. Since the two reaction are conducted in the same solvent, i.e., water, the two reaction can be straightforward implemented in an integrated process for

isosorbide production from glucose, without isolating the in-situ formed sorbitol (**Scheme 4.4**).

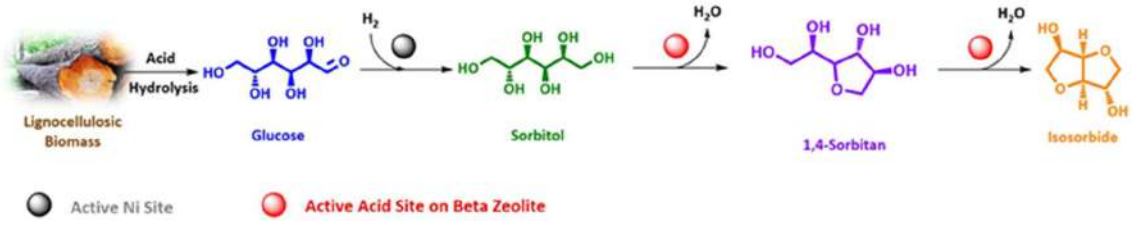

Scheme 4.4. Presented synthesis of isosorbide by hydrogenation of glucose to sorbitol over 35Ni/NDC, followed by sorbitol dehydration to 1,4-sorbitan and finally to isosorbide over Beta zeolite.

In addition, to prove the scalability of the proposed integrated process, were used the prototype-scale reactors. Therefore, to perform this experiment, the prototype scale setup for sorbitol dehydration to isosorbide has been coupled to a similar scale setup for aqueous-phase hydrogenation of glucose to sorbitol using 35Ni/NDC catalyst, analogously to what reported in smaller scale in **Chapter 4.3** (the experimental details of the integrated process are describe in details in **Section B4** in **Appendix**).

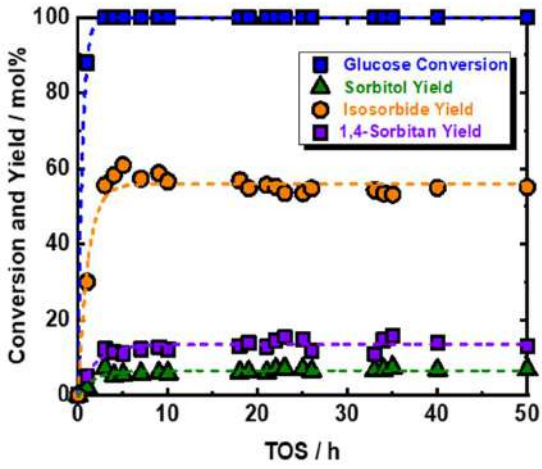

Figure 4.9. The conversion of glucose and the yield of sorbitol, isosorbide and 1,4-sorbitan as a function of time on stream (TOS) using Beta(75) and 35Ni/NDC; Reaction conditions: $c_{glucose}$ = 0.05 M, $Q_{solution}$ = 0.7 mL min^{-1}, T_1 = 423 K and T_2 = 503 K, p_{system} = 4.0 MPa, $m_{35Ni/NDC}$ = 10 g and $m_{Beta(75)}$ = 30 g and $\tau_{35Ni/NDC}$ = 4.9 h kg mol^{-1} and $m_{Beta(75)}$ = 14.8 h kg mol^{-1}.

In this integrated experiment, the aqueous glucose solution has been fed at the same flow rate, i.e., 0.7 mL min^{-1}, over 35Ni/NDC at 423 K (Reactor 1), followed by bimolecular dehydration of the formed sorbitol to isosorbide (Reactor 2) on Beta(75) at 503 K. After reaching the steady state, a complete glucose conversion was found (**Figure 4.9**). Furthermore, an isosorbide yield of 54 mol%, together with 14 mol% of 1,4-sorbitan and 10 mol% of sorbitol that did not undergo dehydration were calculated. Interestingly, traces of isomannide (< 5 mol%) was observed as a result of the hydrogenation of fructose (formed by glucose isomerization) to mannitol followed by dehydration of the intermediates, i.e., mannitol, 2,5-mannitan (**Scheme C1** in **Appendix**). These yields of 1,4-sorbitan and isosorbide are comparable to the reported data obtained from the one pot hydrogenation/dehydration of glucose in water over Ru/Dowex at 463 K after 24 h of reaction time in batch system.[154] The performance of the catalysts, i.e., 35Ni/NDC at glucose hydrogenation and Beta(75) at dehydration of the formed sorbitol to isosorbide, remained constant for 50 h of TOS. A similar experiment analyzing only the products after Reactor 1, gave a 95 mol% conversion of glucose with yields of 88 mol% of sorbitol and 5 mol% of fructose (**Scheme C1** and **Figure C30** in **Appendix**). These findings are in agreement to the previous studies conducted in a smaller scale, cf. **Chapter 4.3**. This makes the overall 54 mol% isosorbide yield in the integrated experiment up to 78 mol% when correlated to sorbitol yield that formed from glucose after the first reactor. As expected, the founded isosorbide yield is in accordance with the one reported with similar condition, i.e., 83 mol% (**Figure 4.6**). This agreement is an evidence that isosorbide production from Beta (75) in these conditions is a robust procedure, whose activity is not affected by minor changes in the reactant educts.

4.5 Conclusions of Chapter 4

The 35Ni/NDC catalyst exhibited high catalytic performance in aqueous-phase hydrogenation of glucose, xylose, and vanillin in a continuous-flow system. The utilization of a continuous-flow system allows high control of reactant conversion and product selectivity. For aqueous-phase sugar hydrogenation, reaction temperature is the most important factor to moderate undesired humification. In vanillin hydrogenation, reaction temperature and residence time are the key factors for well-controlled product selectivity, between either vanillyl alcohol or 2-methoxy-4-methylphenol. In all presented reactions under optimized conditions, the catalyst system was stable for 40 h on flow, with no practical loss in catalytic performance, which corresponds to 120 batch cycles with direct catalyst reuse demonstrating this in a space-time yield concept: a kilo of our catalyst can produce in a day 7.7 kg of the product (Sor, Xyt, or MMP). The phenomenon of rapid Ni leaching in water was hindered by changing the electron density of the carbon by introducing nitrogen to the system, which enhanced catalytic performance for longer time on stream. Nevertheless, further development for long-term operation of the catalyst are required, i.e., optimizing support synthesis to increase the N content on the support and the stabilization of Ni on the support.

Additionally, continuous flow dehydration of sorbitol to isosorbide in liquid water over Beta zeolite was reported. Isosorbide yield of 83 mol% is the highest yield yet reported in literature for both batch and continuous flow systems using heterogeneous catalysts. From these observations, the combination of Brønsted acid sites and a high specific surface area are crucial factors for a highly active catalyst design, targeted for isosorbide production from sorbitol in liquid aqueous-phase utilizing a continuous flow system. The calculated apparent activation energies suggest that the first dehydration step of sorbitol to 1,4-sorbitan is very fast, while the removal of the second water molecule to form isosorbide is the rate-determining step. In this context, the capability of a continuous flow system to rapidly quench the reaction products has been found beneficial to obtain high isosorbide yield. Moreover, the dehydration to isosorbide in water was performed in a medium size prototype reactor, which gave efficient and stable performance up to 50 h of time on stream.

Finally, the integrated aqueous-phase glucose hydrogenation to sorbitol, followed by the bimolecular dehydration to isosorbide was investigated at prototype scale. The positive result of this benign process offer a more efficient route for isosorbide production and, could make isosorbide an economically feasible replacement for bisphenol A in polycarbonates and polyesters. The missing hydrothermal stability of standard zeolites in aqueous media at elevated temperature remains the central drawback for the application of standard zeolites at a viable biorefinery scale. Therefore, the development of new, hydrothermally stable, heterogeneous acid catalysts is eagerly required. Eventually, investigation of this process on large scale (pilot plant level) should be considered to elucidate the industrial relevance of this approach.

5. Valorization of waste raw materials

5.1 Introduction

The development of a circular bio-economy, and sustainable society depends on the effective valorization of feedstocks, as well as industrial process design aimed at waste minimization.[36, 38] In this context, the valorization of waste LCB products from established industries such as agro-forestry, or paper and pulp is a major opportunity for sustainable biorefinery.[39] One of the major bottleneck for the development of modern biorefinery is the pre-treatment of LCB feedstock, *cf.* **Chapter 1.2.1.** The pulp and paper industry alone processes ~1 Gton of LCB as feedstock every year. [14, 75] From this perspective, only the fraction of sugar is valorized as pulp, whereas the remaining lignin is isolated as by-products during the pretreatment. The isolated lignin is used in some product streams with low capacity, but mostly converted in energy and heat via combustion. However, moving toward a more sustainable and mature biorefinery is a broadly proclaimed and targeted goal, which is based on efficiently valorizing all LCB components, including lignin. Therefore, the aim of this chapter is to provide a continuous flow process design for lignin valorization starting from waste materials such as sodium lignosulfonate (LS), as well as waste beech wood sawdust (BWS) from the paper and pulp industry.

The reductive catalytic treatment of lignin has emerged as one of the most promising strategies for lignin valorization via catalytic depolymerization, to obtain valuable dimers and monomers. Therefore, in this chapter, 35Ni/NDC will be applied in the context of catalytic valorization of the industrial waste stream. Among industrial waste, sodium lignosulfonate (LS) is the major waste of paper and pulp industry, with only few low-value applications.[270] Therefore, LS valorization toward monomers was investigated, combining solvothermal fragmentation (SF) using water/alcohol mixtures with a catalytic hydrogenolysis/hydrogenation using 35Ni/NDC (SHF).

Moreover, alternative LCB pretreatments for pulp processes are necessary to valorize lignin and reduce the byproducts. In this context, reductive catalytic fractionation (RCF) of lignin is one of the most promising avenues for the valorization of lignin toward monomers and dimers *cf.* **Chapter 1.3.** Therefore, in **Chapter 5.3,** 35Ni/NDC will be applied for the reductive catalytic fractionation (RCF) of lignin in a continuous flow system, using beech wood sawdust (BWS) as feedstock. Herein, two distinct reactors will be used, one for extraction and solvothermal fractionation of lignin (SF) from BWS coupled with a 35Ni/NDC packed reactor for RCF (SF-RCF). Therefore, SF-RCF will be applied for the first time in prototype-scale which will exceed the mg-scale in favor of a more practical gram scale production. This will facilitate the analysis of SF-RCF products, to study the mechanism and actual practicality of the approach for biorefinery.

5.2 Valorization of waste sodium lignosulfonate in continuous flow system

5.2.1 Background and state of the art

Lignin is a complex three-dimensional network of cross-linked phenylpropanoid units connected through different types of ether bonds, i.e., β-O-4, 4-O-5, γ-O-α, and carbon-carbon bonds, e.g., 5-5, β-β linkages, viz. **Figure 1**.[8, 22, 23, 116] Some of the big challenges in lignin valorization are its heterogeneity, its recalcitrance against treatments, as well as the mandatory use of mild conditions, such as low temperature and pressure as lignin monomers are very sensitive to follow up condensation reaction.[23, 71]

Currently, in pulp and paper industries, four main technologies are used to separate lignin from the other biomass components, i.e., the Kraft, Soda, Organosolv, and Sulfite processes.[23, 270-272] These processes rely on the lignin separation from the LCB matrix via solubilization by applying harsh conditions such as low pH (1-5) and high temperature (433-493 K).[205, 270] The resulting lignin is named technical lignin and indeed different from the primary plant product.[205, 270]

Every year, from the principal 250 Mton about ~70 Mton of technical lignin are separated, of which an estimated 95 % are burned to produce energy.[76, 77] Among this quantity, approximately 2 Mton/y are only by sulfite process.[76, 270]

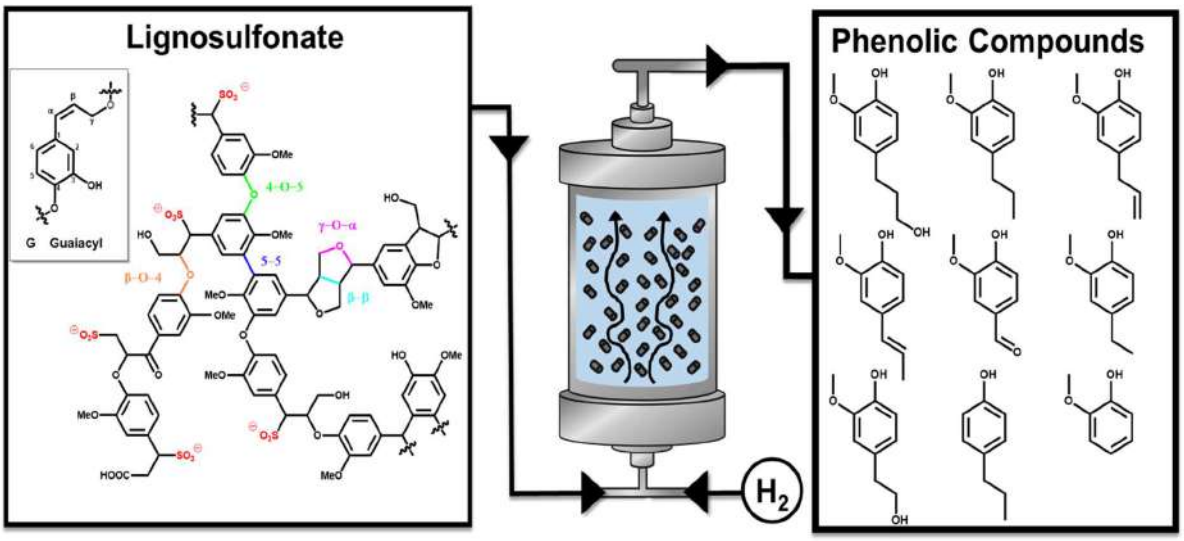

Figure 5.1. Route for sodium lignosulfonate valorization towards monomers using a continuous flow system.

In the sulfite pulping, debarked wood chips are treated with sulfite and bisulfite salts solution (Na is the major counter-ions to bisulfite) in acidic aqueous media (pH 1-5) at temperatures ranging from 398 to 463 K.[270, 273] During the process, the lignin's ether bonds undergo partial hydrolysis followed either by sulfonation, introducing SO_3^- functionality, or by oxidative coupling, forming parasitic C-C bonds.[270, 274] Consequently, the resulting technical lignin is named sodium lignosulfonate (LS). It possesses a wide range of molecular weight (M_w) from 1000 to 100000 g mol^{-1}, the obtained M_w values depending on process severity.[270] LS contains a large amount of sulfur (3 to 8 wt.-%) and a reduced amount of C-O bonds (**Figure 5.1**) when compared to the native lignin in wood.[23] Uniquely, LS is highly water-soluble due to the presence of SO_3^- groups. The sulfonate gives LS the surfactant properties and it is used in a wide class of applications, *e.g.*, as superplasticizer in cements and clays [275], dispersant agent for polymeric foams [276, 277], dyes,[278] and colloidal dispersions.[279, 280] Additionally, LS has been used to create wholly new lignin-based material, *e.g.*, bio-composites for fire-retardant thermal insulators [281, 282] or S-doped carbonaceous materials for high-

performance electrochemical devices such as batteries and supercapacitors.[281, 283, 284] All the above-mentioned applications have been reported to depend strongly on the molecular weight distribution (M_w).[282, 285, 286]

As LS has a high phenolic content, it also shows great potential for the production of bio-based aromatics via oxidative or reductive catalytic fractionation (O or RCF).[279, 287-291] In the last decade, RCF that was pioneered by the Sels group, has been reported as one of the methods with the highest potential for lignin valorization towards phenolic single units, mostly starting directly from wood.[16, 21, 28, 71, 78, 80, 81, 207, 211] Despite the potential of RCF, few studies have been reported using LS solutions. To this end, Shu *et. al* [288] reported LS hydrogenolysis using a Pt on carbon catalyst and $CrCl_3$ homogenous co-catalyst at 553 K, 3 MPa of H_2, in batch systems. Additionally, the effect of a Ni and Mo bimetallic catalyst on Al_2O_3 was studied in ethylene glycol and supercritical ethanol at 583 K and 2.6 MPa of H_2 in batch systems. [292, 293] This approach led to LS fragmentation mostly towards dimers and oligomers resulting in an optimized 88 wt.-% oil yield, while the minor fraction of monomers was only qualitatively studied.[292, 293] All these studies were performed in batch systems, which presents disadvantages when compared to continuous flow systems, such as more complicated product-catalyst separation as well as the time and energy-consuming discontinuous steps such as reactor heating/cooling procedures and its loading/unloading.[71, 80, 212] Horáček *et al.* [287] only reported the LS fragmentation in a continuous flow system at a very high reaction temperature (593 K) over bimetallic Ni and Mo catalyst supported on Al_2O_3. In this study and due to over hydrogenation, guaiacol was found the major product of LS catalytic fragmentation (yield higher than 1.8 wt.-%). The major challenge of all the trials dealing with LS is metal catalyst poisoning due to the included sulfur, which led to rapid catalyst deactivation and limited reusability.[287-289, 292, 293] In these regards, the advantages of metal-supported nitrogen-doped carbon (NDC), such the 35 wt.-% Ni on NDC (35Ni/NDC), described in **Chapter 4**,has the potential to positevly influence the catalytic performances.

In this chapter, the LS depolymerization in a continuous flow system at mild reaction conditions is investigated using water/alcohol solvent system. In addition, the effect of catalyst-free solvothermal fragmentation (SF) of LS to low M_w fractions and phenolic monomers was explored. Furthermore, the latter step was coupled to

hydrogenolysis/hydrogenation fragmentation (SHF)in a continuous flow system using water/alcohol solvent and 35 wt.-% Ni supported on nitrogen-doped carbon (35Ni/NDC) as a catalyst. Finally, the advantage of operating the catalytic depolymerization of LS in a continuous flow system was highlighted with respect to batch system.

5.2.2 Experimental procedures

Materials

All the materials, including sodium lignosulfonate (LS), were utilized as received without further purification. The complete list of used chemicals, suppliers, purities is found in **Section A** of the **Appendix**.

Continuous flow setup

The liquid-phase LS depolymerization using water/alcohols solvent mixtures was conducted in a continuous flow system, similar to what reported in **Chapter 4.2** and in **Section B3** of **Appendix**. In this case the prototype-scale reactor has been used (**Figure B3** in **Appendix**). The set-up experiment using two consecutive fixed bed reactors filled with 10 g each of 35Ni/NDC has been performed with a setup analogous to the one used for the integrated process from glucose to isosorbide, described in **Chapter 4.2** and visualizes in **Figure B4** in **Appendix**. The flow chart of the setup are displayed in **Figure B5** and **Figure B6** in **Appendix**.

LS depolymerization experiment

Prior to each experiment, the LS solution (c_{LS} = 1.0 wt.-% or 2.5 wt.-%) was filtrated through a paper filter (Whatman™ grade 40, 8µm) to remove eventual solid residues that could cause clogging of the continuous flow system. In a typical experiment, the solution of LS was fed by the HPLC pump at 1.0 mL min^{-1}, then mixed with H_2 (20 mL min^{-1}) and passed through the preheating unit and the tubular reactor. The temperature and pressure were kept constant at ambient conditions (398 K and atmospheric pressure) for 30 minutes at this steady-state. Afterwards,

the system has been pressurized to 7.0 MPa to ensure the presence of water/alcohol solvent system in liquid state. Later, the system was heated to the desired reaction temperature (423 K, 473 K, and 523 K). 10 g of catalyst mass was used in each catalytic experiment. Samples (30 mL) were collected once the steady-state was reached (*ca*. 60 min). In the case of the two coupled reactors, a second, similarly filled reactor was mounted after the first reactor, and the same conditions were used as in the single reactor experiments. Samples were collected once both systems reached the steady-state (*ca.* 120 min).

The collected sample has been injected in SEC without further processing, while a product analysis procedure has been established to separate the residual LS from the reaction mixture, and therefore analyze the separated mixtures in GC-MS, GC-FID, 2D HSQC NMR, FTIR, elemental analysis and EDS. All the detailed descriptions of the applied analytical methods are reported in **Section B2** in **Appendix** . The established products analysis procedure are described in detail in **section B5** in **Appendix**.

The batch experiment was conducted in a stainless steel autoclave equipped with PTFE liners and a magnetic stirrer from Berghof (Model: BR-100). The batch catalytic experiments were performed at 523 K using 30 mL of LS solution in MeOH/H_2O solvent mixture (c_{LS}= 2.5 wt.-%) with 1.0 g of 35Ni/NDC and 7.0 MPa of external H_2 pressure for 1 and 3 h. Prior to heating to 523 K, the air was purged out using 1.0 MPa of N_2 three times. The analysis of the reaction products followed the same protocol that was established for the continuous flow experiments.

5.2.3 Results and discussion

Compositional analysis of sodium lignosulfonate

Initially, the chemical composition of the utilized commercially available sodium lignosulfonate (LS) has been investigated via elemental analysis, **(Table 5.1)**. The LS was found to contain 7.0 wt.-% of sulfur (**Table 5.1**). This finding indicates a high sulfonation degree, and consequentially high content of counter ions (Na, Ca, and Mg). Na was found to be the major sulfonate counter ion with 10 wt.-%,

combined with the presence of Ca and Mg traces (**Table 5.1**). The presence of these Ca and Mg ions points to the usage of mixed sulfite salts containing Na, Ca and Mg in the industrial sulfate process.[270] Moreover, the TGA analysis of LS showed a relatively high residual mass at 973 K of 56 wt.-%, confirming the high sulfonation degree (**Figure C34** in **Appendix**). Finally, the moisture content was found to be 4.5 wt.-%, as derived from TGA analysis (see **Table 5.1** and **Figure C34** in **Appendix**).

Table 5.1. Chemical composition, textural and size properties of LS.

	C[a] / wt.-%	S[b] / wt.-%	O[a] / wt.-%	H[a] / wt.-%	Na[c] / wt.-%	Ca[c] / wt.-%	Mg[c] / wt.-%	M_w [d] / g mol^{-1}	Đ[d]
LS	40	7.0	36	4.0	10	1.0	0.10	12390	9.1
SHF-LS[e]	39	5.0	34	4.6	9.4	0.8	0.10	433	1.2

[a]Measured via EA analysis, [b]measured with EDS, [e]measured via ICP-OES, [d]calculated from SEC.[e] referred to SHF-MeOH/H_2O experiment.

The SEC analysis of an aqueous LS solution (1 wt.-%) showed a weight average molecular weight (M_w) of 12390 g mol^{-1} with a dispersity (Đ) of 9.1 (**Figure C35** in **Appendix**). This high Đ value indicates that LS presents a polydisperse distribution of molecular weight. The 2D HSQC NRM spectra of the LS showed the absence of syringyl units, and only guaiacyl units have been found in the typical aromatic region (δ_C/δ_H 100-150/6.2-7.5), (**Figure C36** in **Appendix**).[294, 295] This indicates that the utilized LS has been produced from softwood, in which the syringyl to guaiacyl molar ratio (S/G) is zero. Generally, lignin-rich in guaiacyl units is favorable for certain applications such as additives for polymers and resins. This is due to the reactive ortho-position of the phenolic rings, which promotes radical-initiated crosslinking.[296] 2D HSQC NMR of LS showed the presence of Sulfo-groups in α position (α-$SA_{\alpha,\beta,\gamma}$) at δ_C/δ_H 66-68/4.5-4.7, 79-82/4.7-5.1 and 60-62/3.9-4.0 respectively, which is typical for LS, (**Figure C36** in **Appendix**).[294, 295] Moreover and as expected, FTIR analysis showed the typical O-H band at around 3400 cm^{-1}, the asymmetric and symmetric O=S=O stretching at 1150-1200 cm^{-1} and 1036 cm^{-1} and the typical signals of the aromatic ring vibration at around 1400 cm^{-1}respectively, (**Figure C36** and **Table C4** in **Appendix**). [297]

Solvothermal fragmentation (SF) of sodium lignosulfonate

The usage of short-chain bio-derivable alcohol such as ethanol (EtOH) and methanol (MeOH), as well as their mixture with water, have been reported as an efficient solvent mixtures for both lignin extraction and valorization processes.[209, 211, 298, 299] Due to the low solubility of LS-salts in organic solvents, an aqueous solvent mixture, i.e., MeOH/H_2O and EtOH/H_2O, is necessary.[77] Therefore, the efficiency of water/alcohol mixtures (MeOH/H_2O and EtOH/H_2O with 1:1 wt.-% ratio) as a solvent was studied for the catalyst-free solvothermal (SF) LS fragmentation of LS.

The solvothermal fragmentation reactions (SF) were performed at 423 K, 473 K and 523 K in absence of the catalyst. In both cases, i.e., using MeOH/H_2O and EtOH/H_2O as a solvent mixture, the (SEC) elugrams exibithed the successive disappearance of the peak at low retention times (<10 min), corresponding to the high molecular weight fraction, (**Figure 5.2** and **Figure C38** in **Appendix**). For the MeOH/H_2O solvent mixture, the derived mass average molecular weight (M_w) was decreased from 12390 g mol^{-1} of untreated LS over 9132 g mol^{-1} and 6093 g mol^{-1} to 3856 g mol^{-1}, following the increase of reaction temperature from 423 K, to 473 K and to 523 K, respectively (**Figure 5.2**, **Table C5** and **Figure C39** in **Appendix**). Similarly, EtOH/H_2O solvent mixture showed a decrease of M_w with the increase of temperatures, i.e., from 423 K to 473 K and to 523 K, giving the at 523 K the M_w lowest value of 3000 g mol^{-1} (**Figure 5.3**, **Table C5** and **Figure C39** in **Appendix**). Analogously to M_w, the number averaged molecular weight distribution (M_n) decreased with the increase of reaction temperature, giving the minimum at 523 K, with M_n of 586 g mol^{-1} and 556 g mol^{-1} for MeOH/H_2O and EtOH/H_2O, respectively (**Figure C39** and **Table C5** in **Appendix**).

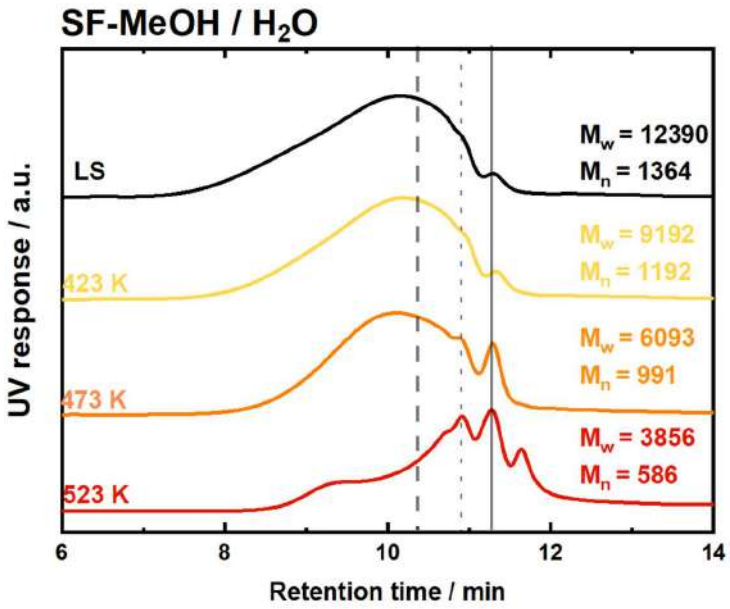

Figure 5.2. SEC chromatograms of the solvothermal fragmentation (SF) of LS in MeOH/H_2O (1:1 wt.-% Ratio). Reaction conditions: c_{LS} = 1.0 wt.-%, T = 423 K, 473 K and 523 K, p = 7.0 MPa, Q_{educt} = 1.0 mL min^{-1},Q_{H_2} = 20 mL $min^{-1}$and $t_{residence}$ = 50 min. The straight line indicates the eluents buffer reference peaks ($NaHPO_3$), dotted and dashed lines show the analytical standard peak (sodium poly-(styrene sulfonate)) with M_w of 246 g mol^{-1} (RT = 10.9 min) and with M_w of 891 g mol^{-1} (RT= 10.4 min), respectively.

The significant drop in molecular weights in both cases indicates that the cleavage of the weaker linkages of LS (mostly phenyl ether bonds) occurs already at the lower reaction temperatures, i.e., 423 K and 473 K. Rather expectedly, this fragmentation is getting most effective at the highest applied temperature, i.e,. 523 K. However, the molecular weight dispersity (Đ) was found higher than 5.0 at all of the investigated temperatures using both solvent systems (**Table C5** in **Appendix**). This indicates that fragmentation occurred only partially, resulting in a heterogeneous mixture with different size of oligomers, mostly tri-, tetra- and pentamers. An additional explanation for such heterogeneous molar mass distribution could also be in-situ re-polymerization (side reactions) of the cleaved intermediates due or radical polymerizations.

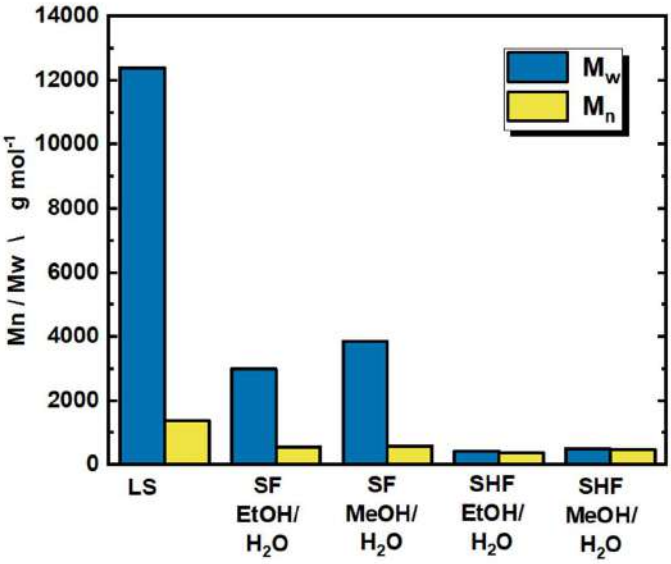

Figure 5.3. Mass-average (M_w) and number-average (M_n) molar mass calculated from SEC curves for the thermal LS fragmentation (SF) and solvothermal assisted by catalytic Hydrogenolysis/hydrogenation (SHF) using EtOH/H_2O and MeOH/H_2O solvent systems; Reaction conditions: c_{LS} = 1.0 wt.-%, T = 423 K, 473 K and 523 K, m_{cat}= 10 g, p = 7.0 MPa, Q_{educt} = 1.0 mL min^{-1},Q_{H_2} = 20 mL$min^{-1}$and $t_{residence}$ = 50 min.

Based on this, MeOH/H_2O sample was selected in order to qualitatively analyze the monomers and dimers using GC-MS, (**Figure C39** and **C40** in **Appendix**). From this chromatogram, a wide range of phenolic molecules (16 compounds) has been identified and reported in **Table C6** in **Appendix**. Moreover, the GC-MS chromatogram exhibited peaks at high retention time region (>20 min), which can be attributed to dimers. However, these dimers were not identified and recognized by the compounds database of the GC (NIST_17 Mass Library). Among the identified compounds, 4-propyl guaiacol (G1), 4-ethyl guaiacol (G2), homovanillic alcohol (G3), dehydroconyferyl alcohol (G4), guaiacol (G5) and creosol (G6) were quantified with GC-FID, and a cumulative monomer yield of 4.6 mg g_{LS}^{-1} was calculated (**Figure C41** in **Appendix**). It is interesting to resume that already solvothermal fragmentation in continuous flow systems produced partially depolymerized LS. Within this simple approach, the molecular weight distribution has been found to depend directly on the reaction temperature. This finding can be attributed to the thermal elimination of single phenol units from LS. This is a typical behavior of a thermodynamically unstable polymer that undergoes reversible addition-fragmentation reactions. Moreover, the derived dispersity values (Đ=6.5)

indicates that this equilibrium is perturbed by a side reactions such as condensation of the cleaved fragments. Such phenomenon is a clear evidence of the presence of a ceiling temperature, above which the polymer is spontaneously depolymerized into smaller units. Interestingly, the ceiling temperature is a general phenomenon in polymer science but was mostly not reported in the community of lignin biorefinery.[300]

Sodium lignosulfonate (LS) catalytic assisted solvothermal fragmentation hydrogenloysis/hydrogenation (SHF)

In this part, the influence of coupling a catalytic hydrogenolysis/hydrogenation step with the abovementioned solvothermal treatment on LS depolymerization was investigated. Herein, the presence of a redox catalyst (35Ni/NDC) facilitates LS depolymerization through hydrogenolysis of LS fragments ether bonds, mostly β-O-4, β-O-5, and 4-O-5. Simultaneously, the formed unsaturated fragments are reduced, i.e., hydrogenated, which prevent the recondensation of the formed unsaturated fragments. For these purposes, set of experiments were performed at three different reaction temperatures, i.e., 423 K, 473 K, and 523 K, using water/alcohol with weight ratio (1:1) as a solvent mixture, i.e., EtOH/H_2O and MeOH/H_2O. These experiments are noted as SHF-MeOH/H_2O and SHF-EtOH/H_2O.

The dependence of the molecular weight distribution on reaction temperature in these experiments is shown in **Figure 5.4**. Increasing the reaction temperature from 423 K to 473 K and to 523 K, the SEC elugrams showed a disappearing of the peak at low retention time (RT< 9 min), which corresponds to high molecular weight fraction, in both solvent systems. Similarly, M_w and M_n exhibited a significant decay when the temperature was increased from 423 K to 473 K and to 523 K for both SHF-MeOH/H_2O and SHF-MeOH/H_2O, (**Figure 5.3** and **Figure C42** in **Appendix**). The M_w has been found to be decreased to 433 g mol^{-1} and to 502 g mol^{-1} at 523 K for SHF-MeOH/H_2O and SHF-EtOH/H_2O, respectively (**Figure 5.4** and **Table C5** in **Appendix**).

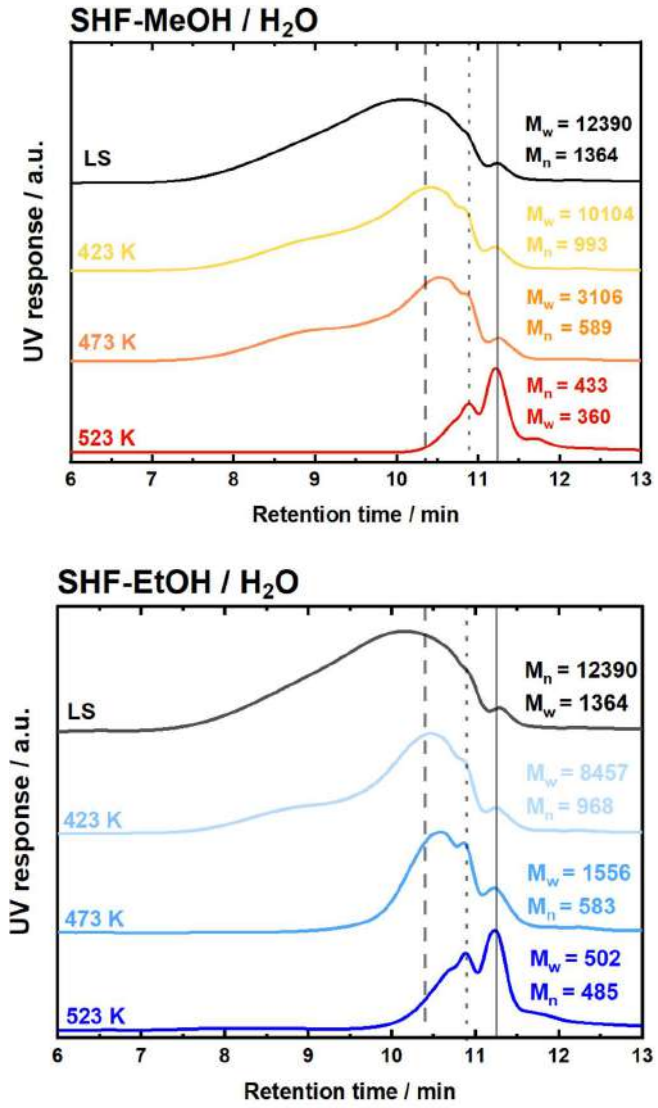

Figure 5.4. SEC chromatograms of LS SHF-MeOH/H_2O (top) and SHF-EtOH/H_2O (bottom). Reaction conditions: c_{LS} = 1.0 wt.-%, T = 423 K, 473 K and 523 K, p = 7.0 MPa, Q_{educt} = 1.0 mL min^{-1},Q_{H_2} = 20 mL $min^{-1}$and $t_{residence}$ = 50 min. solvent system: MeOH/H_2O and EtOH/H_2O with weight ratio (1:1).m_{cat} = 10.0 g. The straight line indicates the eluents buffer reference peak ($NaHPO_3$), dotted and dashed lines show the analytical standard peak (sodium poly-(styrene sulfonate)) with Mw of 246 g mol^{-1} (RT = 10.9 min) and with M_w of 891 g mol^{-1} (RT= 10.4 min), respectively.

All the values are smaller than those for SF (**Table S2** in ESI). Most interestingly, Đ has substantially decreased from 6.5 to 1.2, i.e., from a highly disperse to a relatively monodisperse distribution (**Table C5** in **Appendix**). This decrease of both Đ and M_w clearly characterizes the role of SHF in LS fragmentation, which occurred to a higher and in a more controlled extent with respect to SF. These observations

are in good agreement with the proposed mechanism of stabilization of the formed monomers via hydrogenolysis/hydrogenation, where the presence of both H_2 and redox catalyst behaves as a protective factor to prevent recondensation.[80, 85]

For detailed insights about the structure of the sample taken from SHF-MeOH/H_2O at 523 K, characterizations of the freeze-dried solid residue (denoted as SHF-LS) were performed via elemental analysis (EA) including analysis of Na, Ca, Mg via ICP-OES, FTIR, and 2D HSQC NMR. The EA showed a drop of the S content from 7.0 wt.-% to 5.0 wt.-%, while the O content dropped slightly from 36 wt.-% to 34 wt.-%,(**Table 5.1**). Differently, Na, Ca, and Mg amount in the freeze-dried solid residue remained constant before and after the experiment. The difference in S content is attributed to elimination of sodium sulfate and sodium sulfide as a result of sulfonate hydrolysis and reduction. We also found a slightly higher acidity of the product solution (pH = 5.5) when compared to the reactant solution (pH = 6.3). It is important to note that at this pH the water soluble phenolates are not formed with no subsequent loss of aromatics in water phase. The 2D HSQC NMR spectra for SHF-LS showed the disappearance of the sulfo-group signals (α-$S_{\alpha,\beta,\gamma}$ at δ_C/δ_H 66-68/4.5-4.7, 79-82/4.7-5.1 and 60-62/3.9-4.0), which is an indication of the sulfonate group removal from LS (**Figure C43** in **Appendix**). In addition, low intensity of Ni_2S_3 reflections with respect to Ni^0 were found in XRD pattern of spent catalyst indicating a small amount of S^{2-} reacting on the catalyst surface (**Figure C44** in **Appendix**), which however does not influence the catalyst performance, as proven by SEC and monomers yield. Furthermore, FTIR analysis of SHF samples showed a decrease of the O=S=O stretching bands at 1036 cm^{-1} and at around 1200 cm^{-1}, when compared to the original FTIR spectrum of LS, (**Figure C37** and **Table C4** in **Appendix)**. Moreover, FTIR showed that the C-H stretching modes at 2954 and 2937 cm^{-1} exhibited higher peak intensity in SHF samples than in the original LS. This suggest a higher concentration of alkyl chains in the SHF sample due to the LS hydrogenolysis/hydrogenation.

In order to evaluate the depolymerization efficiency at different temperatures, the SHF product has been qualitatively and quantitatively analyzed using GC-MS and GC-FID, respectively**.** From the GC-MS it was possible to identify a wide range of

compounds (18 compounds), reported in **Table C7** in **Appendix**. Among the identified compounds, 4-propyl guaiacol (G1), 4-ethyl guaiacol (G2), homovanillic alcohol (G3), dehydroconyferyl alcohol (G4), guaiacol (G5), Creosol (G6), 4-propyl phenol (H1) were the predominant ones, and have been quantified from GC-FID chromatograms (**Table C8** and **Figure C40** and **C45** in **Appendix**). At a reaction temperature of 423 K, the cumulative monomers yield was found to be 9.1 mg g_{LS}^{-1} and 1.8 mg g_{LS}^{-1} for MeOH/H_2O and EtOH/H_2O solvent mixture respectively (**Figure 5.4** and **Figure C46** in **Appendix**). Increasing the temperature from 423 K to 473 K and 523 K corresponded to an increase in the monomers yield from 9.1 mg g_{LS}^{-1} to 16 mg g_{LS}^{-1} and to 34 mg g_{LS}^{-1} for SHF-MeOH/H_2O mixtures and from 1.8 mg g_{LS}^{-1} to 6.3 mg g_{LS}^{-1} and to 31 mg g_{LS}^{-1} for SHF-EtOH/H_2O. The values of monomers yield in both solvent systems at low temperature, i.e., at 423 K and 473 K, are in-line with the maximum theoretical yield (~10 mg g_{LS}^{-1}) that Rinaldi *et al.* reported only for β-O-4 linkages of LS, indicating the complete cleavage of these linkages type.[23] Nevertheless, at 523 K, the cumulative monomer yield was found three times higher than the maximum theoretical yield, indicating the cleavage of others linkages in addition to β-O-4. In all the cases except EtOH/H_2O at 423 K, the monomers were similarly distributed with propyl-guaiacol (**G1**) and dihydroconyferyl alcohol (**G4**) as the major products, *viz.* in **Figure 5**. However, the prevalence of phenolic monomers with reduced tail, such as G1-G6 and H1, indicates the effective hydrogenlysis/hydrogenatin of LS fragments in SHF process by the 35Ni/NDC catalyst.

In the studied system, SHF-MeOH/H_2O solvent mixture showed higher monomer yield over all the temperature range than SHF-EtOH/H_2O. The higher activity of MeOH/H_2O then EtOH/H_2O in SHF experiments is attributed to the higher polarity of such mixture that allows a better solubility of LS, which led to higher diffusion of LS through the 35Ni/NDC catalyst and higher LS hydrogenolysis/hydrogenation rates. These findings is in agreement with other studies conducted with MeOH on catalytic lignin depolymerization reported by the Sels group.[299, 301] This demonstrated the crucial role of a polar solvent in lignin solubilization, which could lead to improve process efficiency.

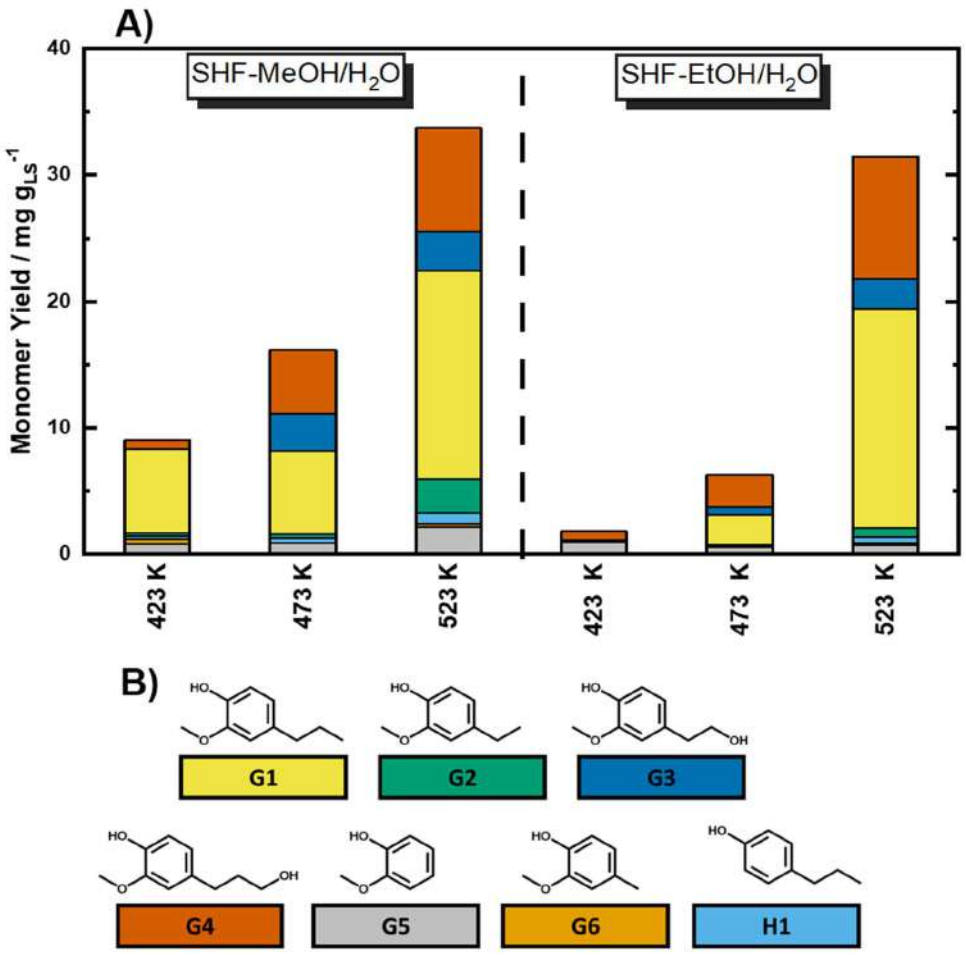

Figure 5.5. A) Monomer yield for the SHF-MeOH/H_2O and SHF-EtOH/H_2O as function of temperature. Reaction conditions: c_{LS} = 1.0 wt.-%, T = 423 K, 473 K and 523 K, p = 7.0 MPa, Q_{educt} = 1.0 mL min^{-1},Q_{H_2} = 20 mL $min^{-1}$and $t_{residence}$ = 50 min. solvent system: MeOH/H_2O and EtOH/H_2O with weight ratio (1:1), m_{cat}= 10.0 g. **B)** Structure of the identified compounds.

Process optimization

In order to maximize the efficiency of the LS depolymerization toward monomers, a further experiment has been performed with a higher LS concentration than the previous SF and SHF experiments (2.5 wt.-% of LS solution) at 523 K. This LS concentration represents the solubility limit of LS in the MeOH/H_2O solvent mixture. Herein, M_w and M_n were found of 430 and 391 g mol^{-1} with Đ of 1.1, respectively (see **Table C9** in **Appendix**). These values are almost identical to the one obtained

from the experiment conducted using 1 wt.-% LS solution (**Table C9** in **Appendix**). Also, the cumulative monomer yield was found to be similar in both cases. One of the advantages of operation in continuous flow systems is the possibility to couple multiple reactors together. Herein, two identical packed reactors with 35Ni/NDC have been coupled in series, in order to prolong the contact time between the LS solution and the catalyst and consequently optimize the monomer yield (**Figure 5.6** and **Figure B4** in **Appendix)**. Therein, the concentrated 2.5 wt.-% LS solution has been continuously fed through the two coupled reactors packed with 35Ni/NDC (referred as dual column experiment.). The molecular weight distributions in the two reactors experiment showed a slight decrease when compared with the sole reactor experiment using 2.5 wt.-% (**Table C9** in **Appendix**). In contrast, the cumulative monomer yield increased from 27 to 42 mg g_{LS}^{-1} when compared to the single column experiment (**Figure 5.6)**, i.e., prolonging the residence time resulted in improved monomer yield. In addition, this monomers yield (42 mg g_{LS}^{-1}) is four times higher than the maximum theoretical monomers yield (~10 mg g_{LS}^{-1}) that was reported by Rinaldi *et al.* based on the cleavage of LS β-O-4 linkages.[23]

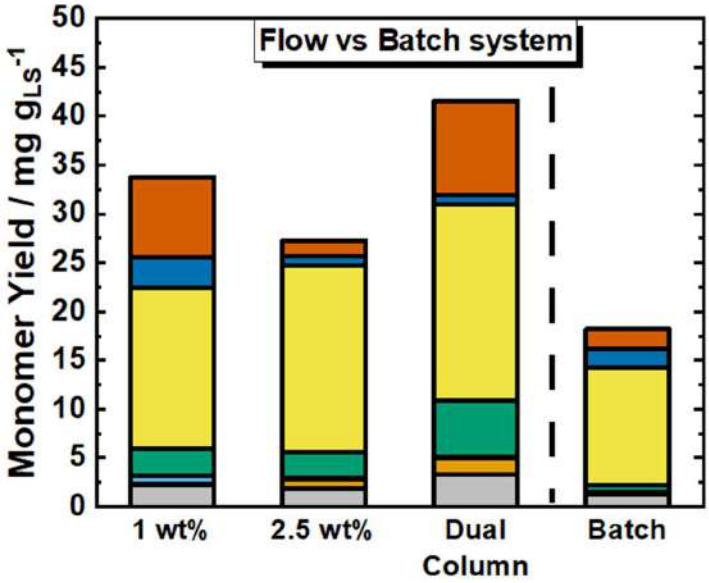

Figure 5.6. Monomers yield derived from the SHF-MeOH/H_2O in continuous flow system and batch reactor; Reaction Conditions in **continuous flow system**: c_{LS} = 1.0 and 2.5 wt.-%, T = 523 K, p = 7.0 MPa, Q_{educt} = 1.0 mL min^{-1}, Q_{H_2} = 20 mL $min^{-1}$and $t_{residence}$ = 50 min. solvent system: MeOH/H_2O with weight ratio (1:1). M_{cat} = 10g. Reaction conditions in **dual column continuous flow system**: c_{LS} = 2.5 wt.-%, T1 and T2 = 523 K, p = 7.0 MPa, Q_{educt} = 1.0 mL min^{-1},Q_{H_2} = 20 mL $min^{-1}$and $\tau_{residence}$ = 100min. solvent system: MeOH/H_2O with

weight ratio (1:1). m_{cat} = 20g.Reaction conditions in **batch system**: c_{LS} = 2.5 wt.-%, V_{educt} = 30 mL, T = 523 K, p_{H_2} = 7.0 MPa, n = 400 rpm, and $t_{reaction}$ = 60 min. solvent system: MeOH/H_2O with weight ratio (1:1). The quantified compounds (G1-G6 and H1) are reported in **Figure 5.5B.**

Comparison between batch and flow

To identify the assumed advantages of continuous flow over batch systems, the catalytic LS depolymerization was performed in a batch system using MeOH/H_2O solvent system. 1 h reaction time was set to be comparable to the one in flow system, yielding an M_w of 1615 g mol^{-1} and a Đ of 3.3 (**Table C9** in **Appendix**). These values are considerably higher than the ones of the flow systems experiment. In addition, the cumulative monomers yield was found to be 18 mg g_{LS}^{-1}, which is lower than that for continuous flow system (27 mg g_{LS}^{-1}). We attribute these findings to the re-polymerization of the phenolic intermediates in batch system due to deposition of LS and char formation on the catalyst, which is typical of batch system. [240] Increasing the reaction time from 1h to 3h, corresponded to an increase of M_w from 1615 g mol^{-1} to 6942 g mol^{-1}, combined with Đ increase from 3.3 to 10. This is attributed to the fragments re-polymerization in batch system that also leads to catalyst deactivation due to longer contact times between reactants and products.[302]

5.3 Beech wood sawdust valorization

5.3.1 Background and state of the art

Wood sawdust is a waste material from the primary physical treatment of LCB in the lumber industry, such as sawing and shaving.[303] In Europe, beech (or *Fagus sylvatica*) is the most common deciduous tree and the most economically relevant wood in Europe, with a production 160 kton per year.[304] Nevertheless, beech wood sawdust (BWS) has a low commercial value and is generally used as fuel, livestock bedding, adsorbent materials, or particleboard panels.[303, 305] However,

BWS has the potential to be implemented into biorefinery to produce value-added compounds.

Traditionally, wood can be treated with pulp processes, i.e., with alkali treatments to separate the cellulosic pulp from lignin, such as the Kraft process, or Sulfite and Soda pulping. In these approaches, sugars are valorized within the pulp, and lignin is separated as a low valuable by-product, *cf.* **Chapter 5.2**. Recently, to avoid waste production several alternative methodologies have been proposed based on the lignin-first paradigm, *cf.* **Chapter 1.3.1.** Lignin first is an integral approach to derive a valuable and treatable LCB fraction from polysaccharides and lignin.[71] Moreover, this approach is based on the simultaneous extraction, fragmentation, and active stabilization of lignin from the LCB matrix as the initial step to obtain pulp.[80, 205, 306] One of the most promising lignin-first methodologies is the reductive catalytic fractionation (RCF).[21, 80, 211, 212] A typical RCF process consists of two steps, the extraction of lignin from LCB (with by partial solvothermal fragmentation) followed by the catalytic depolymerization (hydrogenolysis) and stabilization of unsaturated fragments via hydrogenation.[71, 80] To date, the majority of RCF processes have been conducted in batch systems, yielding more than to 50 wt.-% of cumulative monomer yield.[16, 71, 80, 207, 208] However, in a batch system the RCF catalyst and biomass bed are placed in the same vessel, which lead to difficulty to investigate separately the lignin extraction and the catalytic process as well as requires separation steps after reaction.[80, 81] To overcome these drawbacks, continuous flow systems are a suitable alternative.[211, 307] Ideally, a continuous flow RCF presents the two typical process steps physically separated in two distinct packed reactors connected together. Accordingly, in the first reactor (packed with BWS) occurs the extraction and partial solvothermal fragmentation of lignin (SF) while in the second reactor (packed with 35Ni/NDC catalyst) the catalytic fragmentation (hydrogenolysis) and stabilization via hydrogenation (RCF), (**Figure 5.7** and *cf*. **Chapter 1.2.3**).[81, 298] This process allows the investigation and optimization of the two process distinctly. Additionally, it provides better time-resolved data when compared to batch.[80] Moreover, operating in continuous flow mode guarantees high control over residence time and efficient heating, which can reduce unwanted recondensation of the products.

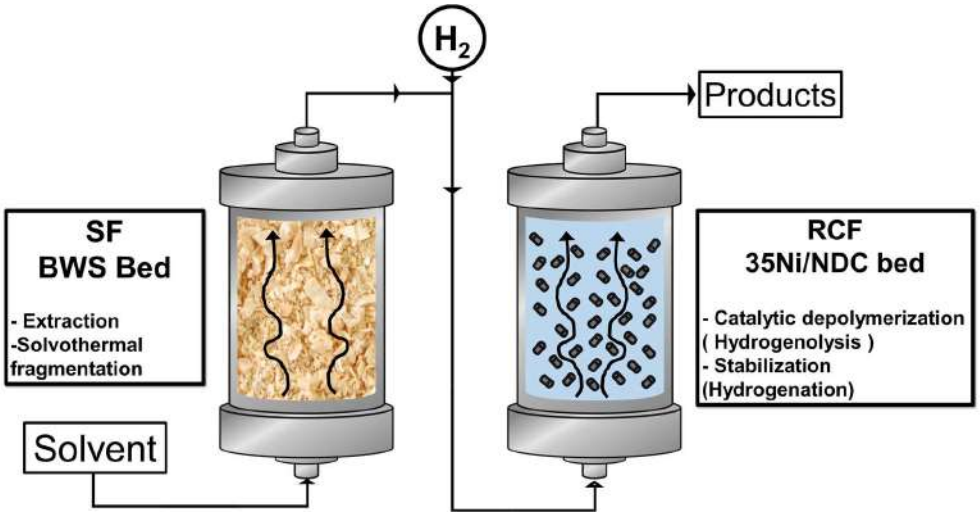

Figure 5.7. Scheme of SF-RCF in continuous flow mode. In the first reactor, the lignin is extracted from the bed and solvothermally fragmented (SF). In the second reactor, the partially fragmented lignin undergoes reductive catalytic fractionation (RCF) hydrogenolysis and stabilized via hydrogenation.

However, the continuous flow SF-RCF of biomass has yet been adequately investigated. Firstly, Samec *et al.* reported the lignin transfer-hydrogenolysis depolymerization with two coupled reactors (extraction and hydrogenation reactors) using MeOH/H_2O (7:3 wt.-% ratio) as a solvent mixture and H-donor, with 5 wt.-% Pd/C (150 mg) as catalyst and birch wood (150 mg) as feedstock. This work reported a maximum of 27 wt.-% of monomer yield with 0.1 mL min^{-1} of educt flow, an extraction temperature of 473 K, and a reduction temperature of 453 K. The Luterbacher's group designed a two step semi-continuous flow process, feeding a solution of acetal-stabilized birch wood lignin previously extracted in batch (solvent MeOH/dioxane 8:2 wt. ratio) over a packed-bed reactor (500 mg of 5% Ni/C or 5% Ru/C).[308] In this process, a high monomer yield (~40 wt.-%) was obtained at 453 K, with an educt flow rate of 0.1 mL min^{-1} and H_2 flow rate of 50 mL min^{-1} at 6.0 MPa. Uniquely, the Beckham and Roman Leshkov groups designed a continuous flow process coupling a catalyst-packed bed reactor with a dual bed "switchable" LCB-packed bed reactor.[298] In this study, the extraction bed was filled with 1 g of poplar wood while the catalyst was filled with 600 mg of pelletized Ni/C catalyst (15% Ni on C and SiO_2 50/50 wt. ratio), yielding a maximum of 15 wt.-% monomer yield at a temperature of 463 K, MeOH as solvent (flow rate

0.5 mL min^{-1}) and 50 mL min^{-1} of H_2 flow rate at 6 MPa.[298] However, the above-mentioned flow systems rely on the usage of a low mass of wood bed (mg scale), which represents a bottleneck for accurate investigation and analysis of the products.

In this chapter the solvothermal fragmentation (SF) coupled with the reductive catalytic fractionation (SF-RCF) of beech wood sawdust (BWS) using the double-column prototype scale reactor (10 g) in continuous flow systems using 35Ni/NDC catalyst (10 g) is presented. The SF-RCF will be conducted using biomass derivable organic solvents, i.e., MeOH and MeTHF. The efficiency of the SF-RCF process will be evaluated in terms of cumulative yield of phenolic monomers. In addition, the RCF efficiency will be evaluated at different time reaction times.

5.3.2 Experimental procedures

Materials

All the materials, including beech wood sawdust (BWS), were utilized as received without further purification. The complete list of used chemicals, suppliers and purities can be found in **Section A** of the **Appendix**.

Continuous flow experiments

The lignin extraction and solvothermal fragmentation (SF) experiment was conducted in a continuous flow system, similar to what was reported in **Chapter 4.2** and in **Section B3** of **Appendix**. In this case, the prototype-scale reactor (**Figure B3** in **Appendix**) was packed with 10 g of BWS (diameter 1.0-0.5 mm), sandwiched between ~1 g of glass wool to ensure efficient heating and to prevent clogging of the system. Then, the solvent solution (i.e., MeOH or MeTHF) was fed via HPLC pump at 1.0 mL min^{-1} and passed through the preheating unit and tubular reactor. The temperature and pressure were kept constant at ambient conditions (298 K and atmospheric pressure) for 30 minutes at this steady-state. Afterwards, the system was pressurized to 7.0 MPa to ensure the presence of the solvent system in liquid state. Later, the system was heated to the desired reaction temperature (498 K and 508 K).

For solvothermal coupled with reductive catalytic fractionation (SF-RCF), two prototype-scale reactors, one filled with 10 g of BWS followed by the other with 10 g on 35Ni/NDC, were coupled analogously to the setup used for the integrated process from glucose to isosorbide, described in **Chapter 4.2** and visualizes in **Figure B4** and **Figure B7** in **Appendix**. Then, the solvent solution (i.e., MeOH or MeTHF) was fed via HPLC pump at 1.0 mL min^{-1} with the addition of 40 mL min^{-1} of H_2 at 7.0 MPa.

Samples (30 mL) were collected once the steady-state was reached (*ca*. 120 min) once per hour. The collected sample were injected in SEC without further processing, while a product analysis procedure was established to analyze the separated mixtures with GC-MS and GC-FID. In both cases, the residual BWS analysis was conducted after drying the BWS at 363 K for 12 h. All the detailed descriptions of the applied analytical methods are reported in **Section B2** in **Appendix** . The established products analysis procedure are described in detail in **section B5** in **Appendix**.

5.3.3 Results and discussion

Firstly, the elemental composition and the amount of Klason lignin (K_L) of the beech wood sawdust (BWS) have been investigated to ensure an accurate product quantitative analysis. The chemical composition was evaluated using elemental analysis for C, O and H, giving content of 46 wt.-%, 44 wt.-% and 5.6 wt.-%(**Table 5.2**), which correspond to a C/O ratio of 1:1.The K_L was found of 21 wt.-%, which is the expected value according to literature.[85] Additionally, the moisture content in the BWS was calculated to be 4.7 wt.-% (**Figure C47** in **Appendix**). Elemental analysis, as well as KL values, are in good agreement with the typical beech wood composition.[206] Moreover, acid soluble lignin (ASL), cellulose, and hemicellulose content in beech wood was taken from literature as 3.4 wt.%, 35 wt.-% and 20 wt.-%, respectively (**Table 5.2**).[85] Furthermore, the BWS crystallinity was investigated with XRD, showing two broad peaks at 2θ of 15° and 22°, which are typical attributed to cellulose in the LCB matrix (**Figure 5.8**).[309]

Table 5.2. Chemical composition obtained by elemental analysis of and the K_L content in original beech wood sawdust (BWS).

	Moisture / wt.-%	K_L / wt.-%	ASL wt.-%**	Cellulose / wt.-%*	Hemicellulose / wt.-%*	O / wt.-%	C / wt.-%	H / wt.-%	C/O Ratio
BWS	4.7	21	3.4	39	20	44	46	5.6	1.1

*These values are taken from reference [85]and [310] while ** from reference [310].

To investigate lignin extraction and solvothermal fragmentation in the first reactor, a study was conducted in a single BWS-packed reactor, *cf.* **Section B3** of **Appendix**. Accordingly, the effect of temperature and time on stream (TOS) have been studied using methanol (MeOH) and 2-methyltetrahydrofuran (MeTHF) as a solvent. MeOH is well known as an efficient solvent for lignin extraction,[209, 211, 298, 311] while MeTHF was scarcely investigated and can be alternatively used with the aim to simplify the separation of sugars from lignin *via* water-MeTHF extraction. In addition, both solvents, i.e., MeOH and MeTHF, can be derived from LCB within a biorefinery process.

Initially, the effect of temperature on the efficiency of lignin extraction and solvothermal fragmentation was evaluated in terms of residual BWS mass, residual wood crystallinity (XRD), and molecular weight distributions of extracted products from size exclusion chromatography (SEC). Firstly, MeTHF was used as solvent at 448 K, 473 K, 498 K, and 523 K. Therefore, increasing the temperature from 448 K to 473 K and 498 K corresponded to a decrease in residual mass from 9.4 g, to 8.6 g, and to 6.5 g respectively (**Figure C48** in **Appendix**). Low residual mass at 473 K and 498 K suggest removal of lignin combined with partial removal of the sugar fractions. Accordingly, the XRD of the residual wood displayed more intense and sharper cellulose peaks at 2θ of 15° and 22° when compared to initial BWS (**Figure 5.8**). This indicates the extraction from the BWS of the amorphous components, i.e., lignin and hemicellulose, combined with the preserved crystallinity of cellulose.

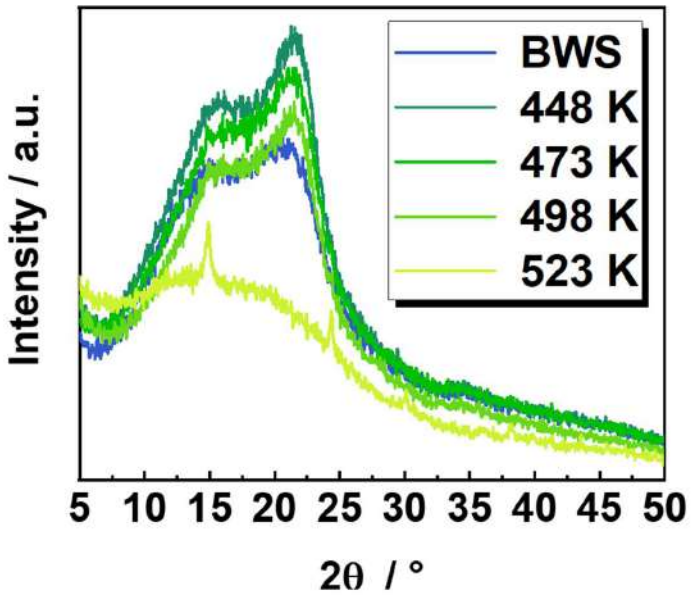

Figure 5.8. XRD reflection patterns for the initial BWS and the residual wood at different temperature using MeTHF as solvent. **Reaction conditions**: m_{BWS} = 10 g, $T_{extraction}$= 498 K, p= 7.0 MPa, Q_{educt} = 1.0 mL min^{-1}, $t_{residence1}$ = 50 min. **Caution** the low-intensity peaks in the 524 K peaks at 2θ~14° and ~25° are typical glass wool signals, herein caused by glass wool impurities.

A further increase of temperature from 498 K to 523 K correspond to the almost complete liquefaction of BWS (residual mass of 0.3 g), (**Figure C48** in **Appendix**). This finding is combined with the complete loss of crystallinity of the residual wood displayed by XRD (**Figure 5.8**). This indicates that at 523 K the lignin extraction is not selective, with loss of all LCB components, i.e., hemicellulose and cellulose in addition to lignin. Therefore, the sample at 498 K was selected for further analysis and investigation. Firstly, the molecular weight distributions were analyzed with SEC, resulting in a weight average molecular weight (M_w) of 1160 g mol^{-1} and a number average molecular weight (M_n) of 896 g mol^{-1} (corresponding to a dispersity Đ of 1.3). These findings indicate the presence of relatively small fragments of polymer in the extracted solution, which are attributed to lignin. Moreover, these low M_w and M_n indicates that the lignin depolymerization occurs solvothermally in absence of catalyst. These findings are attributed to the fast product quenching guaranteed from continuous flow system, which prevent product recondensation.

Based on the aforementioned results, MeOH was used for extraction at 498 K for 6 hours of TOS. In this case, the residual mass of BWS was found to be slightly lower (6.3 g) than using MeTHF (6.5 g), indicating a more effective extraction

process (**Table C10** and **Figure C50** in **Appendix)**. Similarly to the MeTHF experiment, the SEC of MeOH extraction sample after 2 h TOS showed a M_w of 1239 g mol^{-1} and a M_n of 903 g mol^{-1} (**Table C10** in **Appendix**).

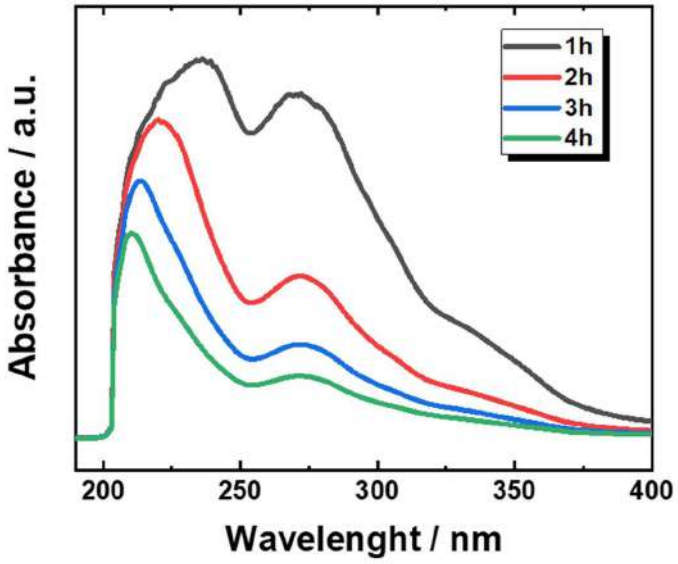

Figure 5.9. UV-Vis spectra of SF samples using MeOH as solvent at different time. **Reaction conditions**: m_{BWS} = 10 g, $T_{extraction}$= 498 K, p= 7.0 MPa, Q_{educt} = 1.0 mL min^{-1}, $t_{residence1}$ = 50 min.

One of the advantages of SF-RCF in continuous flow systems is the possibility to provide precise time-resolved investigations. Therefore, the UV-Vis spectra of the extracted solution was recorded once every hour. Accordingly, the first sample, at 1 h of TOS, using MeOH showed the two typical lignin maxima at wavelength of 208 nm and 250 nm corresponding to the π → π* electronic transition in the aromatic ring and to the conjugated methoxyphenyl group, respectively (**Figure 5.9**).[312, 313] However, the presence of the UV-inhibitor, BHT, as a stabilizer in MeTHF strongly interfered with the measurement, hampering a precise peak attribution (**Figure C50** in **Appendix**). Nevertheless, in both cases by increasing the TOS from 1h, to 2h, 3h and 4h, corresponded to a progressive decrease in the absorbance intensity of the identified peaks (**Figure 5.9** and **C50** in **Appendix**). This is attributed to the progressive decrease of aromatic chromophore concentration, i.e., of lignin concentration, in the extracted solution. Thus, the efficiency of lignin extraction is maximized at the beginning of the process and decrease with TOS increasing. Alternatively, the presence of lignin even after 4h

indicates an incomplete lignin extraction process, which is attributed to non-accessible lignin.

Based on the above-mentioned results, a temperature of 498 K, solvent flow rate of 1 mL min^{-1}, and system pressure of 7.0 MPa were selected as reaction conditions to perform the lignin extraction and solvothermal fragmentation combined with catalytic hydrogenolysis and hydrogenation using 35Ni/NDC as catalyst. For this purpose two reactors were coupled, one for lignin extraction and solvothermal fragmentation, and the other for catalytic reduction. The experimental setup and procedure of these experiments are described in detail in **section B3** and **B4** in **Appendix**.

Initially, the efficiency of SF-RCF over time on stream was evaluated using MeTHF and MeOH as solvents, (**Figure 5.10 A** and **5.10B**) .The SF-RCF samples were analyzed with SEC to investigate the presence and size of polymers. However, resulting M_w below the quantification limit of the applied calibration (<600 g mol^{-1}), indicate an efficient depolymerization of extracted lignin. Therefore, the evaluation of the process was based on the quantification of lignin-derived monomers. In this regard, 15 compounds were identified via GC-MS and quantified with GC-FID (**Figure 5.10C** and **Table C11** in **Appendix**). Furthermore, the GC-MS chromatogram displayed peaks at high retention time region (>20 min), typically attributed to dimers and trimers. However, were not possible to identify these compounds according the used GC database (NIST 17).

The identified compounds present both guaiacyl and syrginyl units, which is expected as a result of the typical beech wood S/G ratio of 3.36.[314]. In the case of MeTHF, the cumulative monomer yield was found to progressively decrease during the first 4 h of TOS, from 11.0 mg g_{KL}^{-1} after 1 h to 9.5 mg g_{KL}^{-1} after 2 h and to 6.8 mg g_{KL}^{-1} after 3h. Moreover, extending the TOS to 4, 8, and 10 h correspond to a decrease of cumulative monomer yield from 4.7 mg g_{KL}^{-1} to 2.8 mg g_{KL}^{-1} and to 2.7 mg g_{KL}^{-1}, respectively (**Figure 5.10 B**). These findings indicate that the combination of lignin extraction in SF and RCF is maximized in the first 4 h pf TOS, which is correlated to the decay in lignin extraction from BWS. This is in good agreement with the findings of Beckham and Roman Leshkov groups, which reported a similar decrease after the first 4 hours of TOS.[298] The same progressive decrease in

cumulative monomer yield was found using MeOH as a solvent, namely from from 22.2 mg g_{KL}^{-1} at 1h to 14 mg g_{KL}^{-1} at 2 h of TOS, to 7.6 mg g_{KL}^{-1} at 3h and 4.99 mg g_{KL}^{-1} at 4 h of TOS (**Figure 5.10 A**). Extending the TOS to 8 and 10 h yielded in a cumulative monomer yield of 2.97 and 2.78 mg g_{KL}^{-1}, respectively.

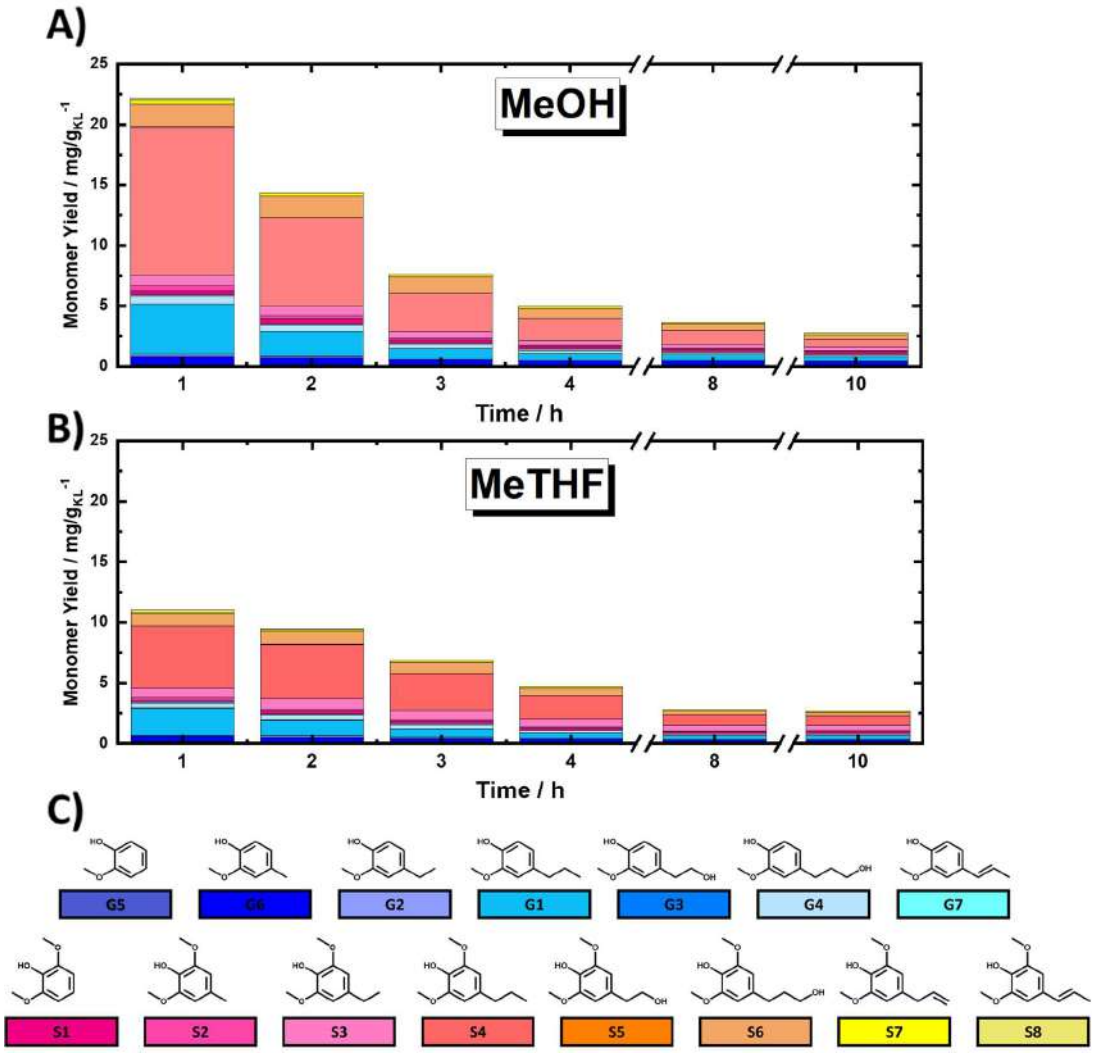

Figure 5.10. Monomer yield of SF-RCF process as a function of time on stream (TOS) using **A)** MeTHF and **B)** MeOH and as solvent.**C)** Structure of quantified monomers. **Reaction conditions**: $m_{35Ni/NDC}$ = 10 g, M_{BWS} = 10 g, $T_{extraction}$= 498 K $T_{reduction}$ = 498 K, p= 7.0 MPa, Q_{educt} = 1.0 mL min^{-1}, Q_{H2} = 48 mL min^{-1}, $t_{residence1}$= $t_{residence2}$ = 50 min.

In the first 2 h of TOS, the cumulative monomer yield using MeOH as a solvent was found to be double in comparison to MeTHF, (22.2 and 11.0 mg g_{KL}^{-1}, respectively). Increasing the TOS from 2 to 10 h corresponded to a progressive decrease in cumulative monomer yield until 2.7 mg g_{KL}^{-1} for both solvents (**Figure 5.10 A-B**). Nevertheless, both solvents displayed similar monomer distribution all

over the investigated TOS, with 4-propyl syringol and 4-propyl guaiacol (G1and S4) as the most abundant quantified monomer (**Figure 5.11**). It is noteworthy to mentioned that the selectivity to predominant monomers remains without change in reaction time (after 10 hours), which allows the exclusion of catalyst deactivation as a reason for lowering rate of extraction. Moreover, for the investigated TOS, the syringyl to guacyl ratio (S/G) of ~3 was found, which is expected with respect to the initial BWS S/G ratio (3.36). The constant S/G ratio indicates a near-homogenous extraction process of lignin from the LCB matrix.

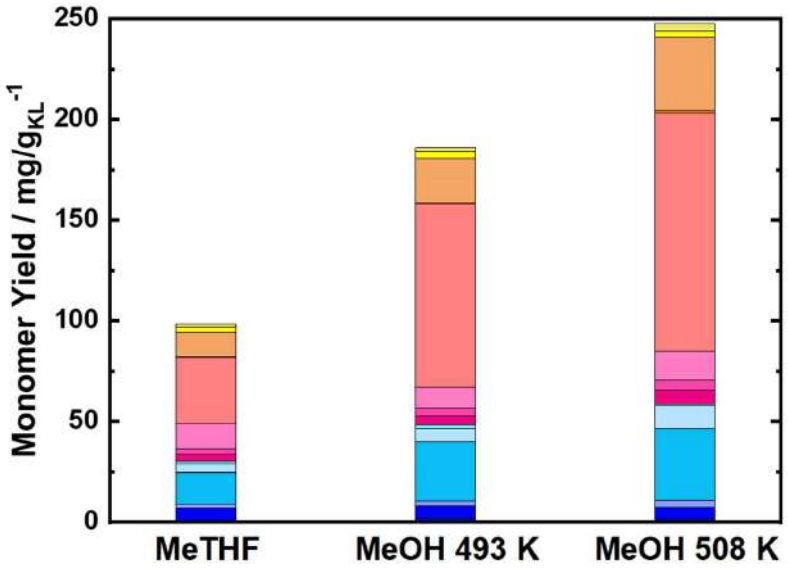

Figure 5.11. Monomer yield of SF-RCF process after 10 h of TOS in function of the used solvent, i.e., MeTHF MeOH. **Reaction conditions**: $m_{35Ni/NDC}$ = 10 g, m_{BWS} = 10 g, $T_{extraction}$= 498 K $T_{reduction}$ = 498 K and 508 K, p= 7.0 MPa, Q_{educt} = 1.0 mL min^{-1}, Q_{H2} = 48 mL min^{-1}, $t_{residence1}$= $t_{residence2}$ = 50 min, TOS= 10 h. The colors are referred to the compounds listed in **Figure 5.10.C.**

To achieve a complete quantification of the total monomer yield over all the TOS, the reaction products was collected from the beginning to the end of the reaction (after 10 of TOS, around 600 mL) were collected using both MeOH and MeTHF as solvents (**Figure 5.11**). As expected, the total monomer yield using MeOH as a solvent was found double with respect to MeTHF, i.e., 186 mg g_{KL}^{-1} and 98.3 mg g_{KL}^{-1} respectively. These results are in good agreement with the samples after 1h, and strongly indicates that lignin extraction takes place mainly at the first hours (around 4 h) of the experiments. Additionally, the higher total monomer yield shows a clear advantage of MeOH over MeTHF as a solvent. This is in agreement with

the findings of the Sels group, which reported the efficiency of MeOH as a solvent in batch systems. [209, 315] This higher MeOH efficiency is attributed to a higher polarity (and Lewid acidity) with respect to MeTHF, which allows deeper penetration of the solvent inside the LCB matrix and higher lignin accessibility. [315] The total monomer yield of 185 mg g_{KL}^{-1} is lower than the reported values for batch systems using hardwood (400-550 mg g_{KL}^{-1}), which is attributed to the lack of accessibility of lignin due to large BWS size.[21] Nonetheless, a total monomer yield of 185 mg g_{KL}^{-1} is higher than the maximum yet reported for flow systems of 172 mg g_{KL}^{-1} from the Beckham and Roman Leshkov groups, using Ni catalyst poplar wood.[298] This higher monomer yield is attributed to a long TOS of 10 h, as well as to the usage of pellet shaped NDC support rather than mixed Ni/C with SiO_2. Moreover, using 10 g of BWS allowed to quantify a bigger number of compounds (15 with respect to 8). However, after 10 h of TOS, a residual wood mass of 6.3 and 6.6 g was found for MeOH and MeTHF, respectively. This low residual mass indicates the extraction of carbohydrates in addition to lignin from the BWS. This is in agreement, to what found for the non-catalytic extraction after 6 h of TOS. In addition, GC-MS exhibited the presence of furanic compounds derived from the sugar fraction. However, it is noteworthy to be mentioned here that in this work the sugars derivatives from BWS were not quantified, as the scope of this chapter was mainly on lignin valorization. Nevertheless, currently investigations aiming to reach the highest possible carbon mass balance are ongoing.

In order to maximize the cumulative monomer yield, a further experiment using MeOH as a solvent was performed, increasing the temperature for the first reactor (SF) from 498 K to 508 K, while the second reactor (RCF) was kept constant at 398 K. Similar to the experiment at 498 K, a time-resolved study was conducted for the SF-RCF with 508 K as the extraction temperature. The cumulative monomer yield of this experiment for the first 4 h of TOS was found to be higher than that with 498 K as the extraction temperature, yielding 34.1 mg g_{KL}^{-1} at 1 h of TOS, 19.7 mg g_{KL}^{-1} at 2 h of TOS, 10.4 mg g_{KL}^{-1} at 3h of TOS, and 6.4 mg g_{KL}^{-1} at 4h of TOS (**Figure 5.12** and **Table C14** in **Appendix**).

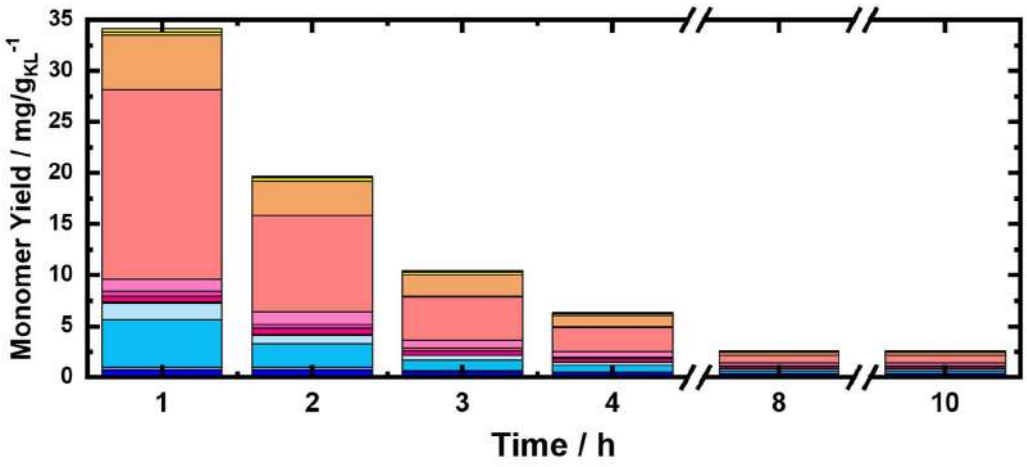

Figure 5.12. Monomer yield of SF-RCF process as a function of time on stream (TOS) using MeOH as solvent and **Reaction conditions**: $m_{35Ni/NDC}$ = 10 g, m_{BWS} = 10 g, $T_{extraction}$= 508 K $T_{reduction}$ = 498 K, p= 7.0 MPa, Q_{educt} = 1.0 mL min^{-1}, Q_{H2} = 48 mL min^{-1}, $t_{residence1}$= $t_{residence2}$ = 50 min. The colors are referred to the compounds listed in **Figure 5.10.C.**

Interestingly, at 8 and 10 h of TOS the monomer yield of at an extraction temperature of 498 K and 508 K were found with a similar value of around 2.8 mg g_{KL}^{-1}, indicating a minimized extraction efficiency at such TOS. These findings confirmed that the higher extraction efficiency occurs during the first 4 h of the reaction. Furthermore, the total monomer yield after 10 h increased from 185 mg g_{KL}^{-1} to 247 mg g_{KL}^{-1} (**Figure 5.11** and **Figure C51** in **Appendix**). The higher total monomer yield at 508 K is attributed to more accessible lignin with respect to 498 K. However, the residual BWS mass was found to decrease from 6.4 g to 5.9 g, with the increased extraction temperature of 498 K to 508 K, which indicates that a higher amount of sugars is extracted at 508 K.

5.4 Conclusions of Chapter 5

In summary, in this chapter the 35Ni/NDC catalyst have been successfully applied for the valorization of lignin in two rather distinct approaches, for LS and BWS valorization in continuous flow systems.

In **Chapter 5.2**, industrial LS was successfully valorized using solvothermal fragmentation independently, and combined with catalytic

hydrogenolysis/hydrogenation in a continuous flow system. The depolymerization was found to occur thermally in absence of catalyst, rather independent of the solvent mixture. The decrease in molecular weight was found to depend on the reaction temperature, whereas LS at those temperatures is unstable, and displayed a ceiling behavior. This allows a direct and simple tuning of molecular weight for the formed fractions based on reaction temperature.

To obtain monomers and lower molecular weight fraction, solvothermal fragmentation should be coupled with a catalytic hydrogenolysis/hydrogenation step (SHF). An optimum cumulative monomer yield of 32 mg g_{LS}^{-1} was obtained at 523 K using MeOH/H_2O as solvent using 35Ni/NDC as catalyst. Moreover, the SHF allowed a higher degree of depolymerization, even at lower temperatures. This clearly displayed the vital role of 35Ni/NDC in this approach, as it is responsible for further fragmentation through hydrogenolysis/hydrogenation steps as well as due to its protective effect against product recondensation. Extending the residence time by coupling two reactors yielded an even higher cumulative monomer yield of 42 mg g_{LS}^{-1}, with respect to the experiment in a single tubular reactor, pointing to possible further improvement.

In chapter **Chapter 5.3,** the valorization of BWS was conducted by coupling two reactors, one packed with BWS for SF, followed by a 35Ni/NDC catalyst-packed reactor for SF-RCF with MeOH and MeTHF as solvents. The extraction was found to be effective at 498 K for both solvents, yielding 185 mg g_{KL}^{-1} using MeOH as the solvent. Moreover, the extraction power of the solvent was maximized in the first few hours of TOS, and decreased progressively with increasing TOS. Furthermore, the cumulative monomer yield was optimized to 247 mg g_{KL}^{-1} applying an extraction temperature of 508 K. To date, this value represents the highest cumulative monomer yield for continuous flow SF-RCF. However, there are ongoing investigations to optimize the system, such as the effect of temperature over the hydrogenation reaction and flow rate of the solvent. Additionally, experiments are ongoing for evaluating the influence over the SF-RCF of removing water-soluble hemicellulose prior to the treatment using hot liquid water as a solvent.

Furthermore, the analysis of carbohydrates in residual BWS would assess the process selectivity. In addition, the analysis of sugar-derived compounds in the

products could determine the effect of simultaneous feed of sugar and lignin through 35Ni/NDC in continuous flow. Nevertheless, to date, these experiments represent the only study in literature that exceed the mg scale of wood and catalyst, and demonstrate the feasibility of 35Ni/NDC for BWS valorization.

It is important to underline that all presented results were made using industrial waste as received, i.e., LS containing 7.0 wt.-% of sulfur and 10 wt.-% sodium, or not-sieved BWS. Nevertheless, giving value to industrial waste will increase the sustainability of already established biorefinery processes and accelerate the transition toward a sustainable and circular bio-economy.

6. Conclusions and outlooks

The central motivation of this thesis is to contribute to the development of sustainable and integrated biorefinery processes, using heterogeneous catalysts in continuous flow systems. Therefore, the synthesis of a 35 wt.-% Ni on nitrogen-doped carbon catalyst (35Ni/NDC) served as a starting point to establish a framework of catalytic continuous flow processes for lignocellulosic biomass-derived compound valorization. Furthermore, the 35Ni/NDC catalyst was successfully applied to the valorization of industrial LCB-waste, namely, sodium lignosulfonate (Ls) and beech wood sawdust (BWS). Prototype-scale reactors provided an insight into the great potential to scale-up the reported process from laboratory to pilot scale.

The synthesis of a simple, scalable, cheap, and highly porous 35Ni/NDC support in pellet shape was successfully achieved. Then, the 35Ni/NDC catalyst was applied for aqueous-phase hydrogenation reactions, namely: glucose to sorbitol, xylose to xylitol, and vanillin to 2-methoxy-4-methylphenol, exhibiting high catalytic performances over a long time on stream. The high catalytic performances were attributed to the high specific surface area of 35Ni/NDC and to the heterojunction effects stabilizing and adjusting the dispersity of Ni nanoparticles onto NDC. Thus, 35Ni/NDC catalyst has the potential to provide a safer and more sustainable alternative to Raney Nickel. Additionally, continuous flow systems allowed high control over reactant conversion and product selectivity. Notwithstanding, there are still perspectives for improving the 35Ni/NDC catalyst. This could be accomplished by varying the carbon precursor with respect to semolina, or other sustainable materials can be used such as more protein-rich wheat or wheat-derived waste, e.g. dry bread. Furthermore, to verify the industrial viability, the activity of 35Ni/NDC should be evaluated on a larger scale and in combination with other catalysts in integrated processes.

To that end, 35Ni/NDC catalyst was combined with commercial Beta zeolite in a dual column integrated process for isosorbide production from glucose. Accordingly, Isosorbide was obtained with high yield over a long time on stream in both the single column sorbitol dehydration over Beta zeolite and in the dual

column experiment from glucose over 35Ni/NDC and Beta zeolite. This high yield was attributed to the combination of high surface area and acid site density of Beta zeolite for sorbitol to isosorbide dehydration as well as to the high catalytic efficiency of 35Ni/NDC in the glucose hydrogenation to Sorbitol. In addition, the capability of continuous-flow systems to rapidly quench the products was found to play a crucial role to obtain isosorbide in high yields. Hence, the reported catalytic strategy has the potential to provide a more efficient and economically viable route for isosorbide production. Moreover, these results demonstrated the possibility of integrating this system by coupling two packed bed reactors in continuous flow. However, the missing hydrothermal stability of zeolite at high temperatures represents the main drawbacks of this approach. This could be overcome with the development of hydrothermally stable heterogeneous catalysts, e.g. acidic carbon pellets. Moreover, the system integration should not be limited to only two coupled reactors but rather expanded in a more complex design embracing multiple steps and separation processes, e.g., the production of isosorbide from cellulose.

Beyond the upgrading of LCB-derived compounds, 35Ni/NDC was successfully applied for lignin valorization from waste LCB materials, i.e., sodium lignosulfonate (LS) and beech wood sawdust (BWS). The LS depolymerization was found to occur solvothermally in the absence of catalyst, with tunable molecular weight by varying temperature. These findings were attributed to the instability of LS as a polymer that presents ceiling behavior. Nevertheless, the presence of a catalyst (35Ni/NDC) emerged to be essential to obtain a high monomer yield due to the hydrogenation/hydrogenolysis reactions of the cleaved LS fragments. Furthermore, the usage of continuous flow system guaranteed optimum control over molecular weight and monomer yield.

Similarly, the BWS valorization was conducted by combining solvothermal and catalytic reductive fractionation in a dual-column experiment. The efficiency of 35Ni/NDC for the reductive catalytic fractionation of wood was successfully demonstrated with a comparably high monomer yield. The high yield was attributed to the efficiency of 35Ni/NDC on the hydrogenation of fragmented lignin as well as to the fast product quenching guaranteed by continuous flow systems. Moreover, the usage of large BWS mass (10 g) can potentially give more reliable data for deeper insight into product analysis and reaction mechanism, as well as pave the way for a process scale-up. However, there are ongoing investigations on this

project, such as the effect of varying flow rate and hydrogenation temperature over the monomer yield, the carbohydrate fraction, as well as the effect of removing at first water-soluble hemicellulose over the process selectivity.

Overall, this thesis provided insight for all main aspects regarding the development of an integrated biorefinery, in terms of: catalyst design, process design, process integration, and process intensification. Furthermore, the flexibility of a continuous flow system based on a packed bed reactor was demonstrated over a broad framework of targeted chemical transformation comprising cellulose-derived feedstocks, hemicellulose-derived feedstocks, lignin-derived feedstocks, technical lignin, and waste wood. Moreover, the scalability of catalyst and process was demonstrated, bridging the gap between a laboratory (mg-scale) to a pilot plan scale (kg). Furthermore, the scalability of the 35Ni/NDC catalyst on an industrial scale should be determined with a specific techno-economic assessment. Finally, this work provided a step further to drive biorefinery processes from small laboratory scale into big industrial scale.

Appendix

A Materials

List of used chemicals

D-(+) Glucose Anhydrous (>99,5%), D-(-) fructose (>99%), D-(+) xylose (>99%), D-sorbitol (>98%), vanillin (>99%), 1,2,6 hexanetriol (96%), dianhydro-D-glucitol, sulfuric acid (95-97%) ,L-iditol (≥ 98%) 4-propyl-guaiacol (99%), homovanyllyl alcohol (99%) 4-eethyl-2,6-dimethoxyphenol (99%), 4-ethyl guaiacol (99%), methanol (>99.5%) and sulfuric acid (95-97%) were delivered from Sigma-Aldrich. Xylitol was provided by Laguma. Isosorbide (98%) and hydrochloric acid (0.1 M in water) was obtained from Merk. Vanillyl alcohol, 2-methoxy-4-methylphenol (99%) and 1,5-anhydro-D-sorbitol (97%) were purchased from Acros Organics. Urea and nickel nitrate hexahydrate (>99%) and 2-methyltetrahydrofuran (MeTHF) were supplied from Carl Roth. Guaiacol (99%) has been provided by Sigma. Homovanillyc alcohol (99%) syringol (99%) and 4-propyl phenol (99%) were supplied from Aldrich. Dhydroconyferyl alcohol (97%) was supplied from AmBeed. Zinc oxide nanoparticles (d = 20 nm) were ordered from Nanostructured and Amorphous inc. Semolina (type durum wheat) was purchased from the commercial brand Divella. The forming gas bottle (95/5) and H_2 bottle were purchased from Westfalia. Carbon black grains - Vulcan©-XC72R were furnished by Cabot. H-form Beta(12.5) in powder form and H-form Beta(75) in pellet form were supplied by Clariant. Whereas, H-form Beta(150) in powder form were obtained by Zeolyst. All Beta zeolites that have been used in this thesis are coded as the following: Beta(Si/Al molar Ratio). 1,4-Sorbitan (98%), 2,5-mannitan (98%) and 2,5-anhydro-d-gluctiol (98%) were purchased from BIOZOL Diagnostica Vertrieb GmbH. Industrial residues of Sodium lignosulfonate (LS) have been provided from Domsjö-Fabriker. The sodium poly-(styrene sulfonate) SEC standards (Mw of 29500 g mol^{-1}, 15800 g mol^{-1}, 13500 g mol^{-1}, 9740 g mol^{-1}, 3800 g mol^{-1}, 1670 g mol^{-1}, 891 g mol^{-1} and 246 g mol^{-1}) have been provided by Polymer Standard Service-USA inc. (PSS). $MgSO_3$ anhydrous has been purchased by J.T. Baker. Saw dust beech wood

(BWS) was supplied by GOLDSPAN®. All the chemicals were used as received without any further purification.

B Methods

B.1 Catalyst synthesis

Incipient wetness impregnation of 35 wt.-% Ni on NDC

A 35 wt.-% Ni catalyst supported on NDC pellet is prepared *via* incipient wetness impregnation. Before Ni impregnation, the washed and dried NDC pellets were dried under vacuum at 363 K for 12 h. To obtain the target metal loading, i.e., 35 wt.-%, the appropriate amount (170 g) of Nickel nitrate hexahydrate ($Ni(NO_3)_4 \cdot 6H_2O$) was dissolved in (110 mL) of millipore water, followed by dropwise addition with continuous stirring of the aqueous Ni solution on the NDC dried pellets until complete saturation of the support pores. Subsequently, the impregnated pellets were dried again at 333 K in air for 12 h. Afterwards, the catalyst was calcined under N_2 atmosphere at 723 K. The temperature program of the calcination process consists of two steps: i) purging with N_2 at room temperature for 30 min; ii) increasing the temperature to 723 K with a heating rate of 3 K min^{-1} and maintained for 2 h. Prior the catalytic experiments, the catalyst was reduced in forming gas (5 wt.-% H_2 and 95 wt.-% N_2) using the following program: i) 30 min of purging at room temperature, ii) increasing the temperature to 723 K with a heating rate of 3 K min^{-1} and maintained for 5 h.

For the experiments conducted in **chapter 4**, the used catalysts will be annotated with 35Ni/NDC_U_{Glu}, 35Ni/NDC_U_{Xyl} and 35Ni/NDC_U_V which refers to their use in Glu, Xyl and V hydrogenation, respectively.

Methodology for regeneration of Ni^0 at spent catalyst

After the reaction, Ni^0 at spent catalyst was regenerated through calcination procedure under air increasing the temperature to 573 K with a heating rate of 3 Kmin^{-1} and maintained 3 h, followed by reduction step under forming gas (5 wt.-% H_2 and 95 wt.-% N_2) using the following program: i) 30 min of purging at room temperature, ii) increasing the temperature to 723 K with a heating rate of 3 K min^{-1} and maintained for 5 h.

Pelletization of zeolite

All the used zeolite were used without any further chemical modification. Prior the reaction, the used zeolites in powder form were pressed up to 10 metric ton using hydraulics press (CARVER 3851CE). Afterwards, the zeolite has been crushed and sieved in the range 250-500 μm to ensure a homogeneous flow of the reactant through the catalyst bed during the experiment, as well to avoid the pressure drop and clogging of the system

B.2 Characterization methods

Combustion elemental analysis (EA)

Elemental analysis of C, N, O and S was performed with a Vario-MICRO cube CHNOS Elemental Analyzer (Elementar Analysensysteme GmbH, Langenselbold) in the CHNS mode. Prior to the analysis the samples were finely ground.

Inductively coupled plasma optical emission spectroscopy elemental analysis (ICP)

The Ni, Zn, Na, Ca and Mg content was determined by inductively coupled plasma optical emission spectroscopy (ICP-OES) using an Optima 8000 ICP-OES from PerkinElmer. Prior to the analysis, the samples (0.1 mg) were finely grinded and digested for 13 hours in 500 µL of Aqua regia solution (3:1 molar ratio of HCl and HNO_3, respectively).

Thermogravimetric analysis (TGA)

TGA measurement was performed using a Thermo Microbalance TG 209 F1 Libra (Netzsch, Selb, Germany). In a typical experiment, 0.01 g of sample were placed on a Pt crucible, dried at 423 K C for 2 h and then heat to 1273 K with a heating rate of 10 K min^{-1}. The heating has been performed under a synthetic air flow of 20 mL min^{-1}. Previous to the analysis the samples has been dried for 6h at 363 K under vacuum.

X-ray diffraction (XRD)

Powder XRD measurement were performed on a Bruker D8 diffractometer equipped with a CuK_α source (λ = 0.154 nm) and a NaI scintillation counter-Scinti-Detector. The diffraction pattern was recorded in the *2θ* range between 4-70° with steps of 0.05° and acquisition time of 2 sec per step.

The Ni^0 crystallites size has been calculated applying the Scherrer equation at the reflection at 44° θ.

$$B(\theta) = K\lambda / L \cos\theta$$

Where B is the size of the crystallites, L is the full width at half max (FWHM) calculated for the main reflection at the Bragg angle of 44°θ. K is the shape factor of crystallites, herein, a spherical assumption has been made, with K = 0.9.

N_2 sorption

N_2 sorption measurements were accomplished with N_2 at 77 K, after degassing the sample at 423 K for 20 hours under vacuum, using a Quantachrome Quadrasorb SI porosimeter. The specific surface area was calculated by applying the Brunauer-Emmet-Teller model in the relative pressure region of (0-0.05) for the adsorption branch (A_{BET}). The pore volume, the pore size distribution and the average pore size were determined using the desorption branch via Barrett-Joyner-Halenda (BJH) for Zeolites, as well the quenched solid functional theory (QSDFT) calculation of the desorption branch using the QuadraWin program for slit/cylindral pores for NDC and Ni/NDC.

Scanning electron microscopy (SEM) and transmission electron microscopy (TEM)

The surface morphology and structure of the support and catalyst were investigated using SEM. The SEM images were taken using a Zeiss Lei Gemini 1550 microscope. Information about the dispersion of the Ni nanoparticles was obtained using transmission electron microscopy (TEM). The sample was

prepared by dispersing (0.05 g) in ethanol in an ultrasonic bath for 10 min. Finally, the sample was placed onto a carbon-coated copper grid and dried at room temperature. The images were taken using an EM 912 microscopy (Omega/Carl-Zeiss Oberkochen) operating at 120 kV.

High-resolution scanning transmission electron microscopy (HR-STEM)

The HR-STEM images were acquired using a double-Cs-corrected JEOL ARM200F, equipped with a cold field emission gun and an energy-dispersive X-ray (EDX) filter. The acceleration voltage was set to 80 kV for the investigation.

Energy-dispersive X-ray spectrometry (EDS)

The EDS investigation of LS and SHF-LS has been conducted on a Scanning electron microscope (SEM) – Gemini Leo 1550 equipped. Prior to the analysis, the detector has been calibrated with a standard copper sample, the measure was conducted at 15 keV.

X-ray photoelectron spectroscopy (XPS)

XPS measurements were conducted under ultrahigh vacuum (UHV) $1.5x10^{-8}$ Pa (CISSY equipment) equipped with a SPECS XR 50 X-ray gun with AlK_{α} (1486 eV) and Mg K_{α} (1254 eV) radiation source and combined with a lens analyzer module (CLAM). The binding energy was calibrated with $Au4f_{7/2}$ as reference. The binding energy determination and the peak deconvolution has been made using “Igor” and “CasaXPS” software, for the background a Shirley function was used, while for the peak deconvolution a Voight function has been selected. Previous to the analysis the sample where grinded finely and dispersed on a top of a conducting tape and evacuate in UHV for 40 min.[316]

Carbon monoxide temperature programmed desorption (CO-TPD)

CO-TPD measurements was performed using AMI-300 equipped with thermal conductivity detector (TCD) from Altamira Instrument. In each measurement, 0.05 g of catalyst was placed between two layer of quartz wool in the measurement cell (quartz U-tube). primarily, the sample was treated at 393 K in a flow He for 1 h. Afterwards, the sample was reduced by increasing the temperature to 723 K in the presence of a mixture of H_2 (20%) in He (80%) with a dwell of 4 h. Later, saturation of the catalyst with CO at 303 K was applied by flowing CO (20%) over the sample for 5 h. Then, the non-adsorbed CO was removed by flowing He (100%) over the sample for 30 min. To ensure a complete saturation of the samples, 20 pulses (509 µL each) of CO (20%) in He (80%) over the sample at 303 K. Finally, the CO desorption profile was recorded by increasing the temperature from 303 to 823 K with K min^{-1} with dwell of 30 min at 823 K.

Temperature programmed desorption of ammonia (NH_3-TPD)

The total acid sites density for NDC and 35Ni/NDC was characterized via ammonia temperature-programmed desorption (NH3-TPD). All measurements were performed using AMI-300 equipped with thermal conductivity detector (TCD) from Altamira Instrument. In each measurement, 0.05 g of catalyst was placed between two layers of quartz wool in the measurement cell (quartz U-tube). primarily, the sample was treated at 393 K in a flow He for 1 h. Afterwards, saturation of the catalyst with NH_3 at 323 K was applied by flowing NH_3 (20%) over the sample for 5 h. Then, the non-adsorbed NH_3 was removed by flowing He (100%) over the sample for 30 min. To ensure a complete saturation of the samples, 20 pulses (509 µL each) of NH_3 (20%) in He (80%) over the sample at 323 K was pulsed. Finally, the NH_3 desorption profile was recorded by increasing the temperature from 323 K to 923 K with 10 K min^{-1} with dwell of 30 min at 923 K.

Pyridine-probed infrared spectroscopy (Pyr-IR)

The amount of silanol groups and acidic sites were quantified by Fourier-transform infrared spectroscopy (FT-IR) using a Nicolet 6700 Spectrometer

equipped with a deuterated triglycine sulfate (DTGS) detector. Prior to analysis, samples were pressed, under a pressure of 10^7 Pa, into precisely weighted self-supported wafers of 5-10 mg/cm^2, and degassed *in-situ* at 673 K (5 K/min) for 1 h under vacuum (< $0{,}1 \cdot 10^{-3}$ MPa). After cooling to 423 K, spectra of the materials were recorded as a reference with an accumulation of 64 scans at a resolution of 2 cm^{-1}. Note that the graphical resolution is greater than the spectral resolution and is close to 0.5 cm^{-1}. All spectra were normalized to a constant disc mass (5 mg/cm^2 of dry catalyst). For acid sites quantification by pyridine adsorption, the samples were then subjected to $2{,}5 \cdot 10^{-3}$ MPa pyridine until saturation at 323 K . Spectra were recorded at 423 K after 20 min of thermal desorption under vacuum (<$0{,}1 \cdot 10^{-3}$ MPa) at 423 K, 523 K, and 623 K.[317] The amount of Brønsted and Lewis acid sites were determined by integrating the area of the characteristic bands: v8a of the pyridinium ions (PyH^+) at 1545 cm^{-1} and *v*19b band of the coordinated pyridine species (PyL) at ~1445 cm^{-1}, and using their corresponding molar absorption coefficient: εPyH^+) = 1.67 cm/µmol and ε (PyL) = 2.22 cm/µmol, respectively.[318]

To quantify the total amount of silanols of the BEA zeolite samples, the combination band (v+δ)OH located at around 4600 cm^{-1} that refers to silanol groups was used instead of the fundamental v(OH) at ~3740 cm$^{-1,}$ due to the high dependence of the molar absorption coefficient of this latter "$\varepsilon(\nu_{Si\text{-}OH})$" on H-bonding interactions[319], making the area of the whole v(SiOH) massif not proportional to the Si-OH concentration. By contrast, it is possible to accurately calculate the amount of silanol groups using the sharp (v+δ)OH combination band located at about 4600 cm^{-1} with the molar extinction coefficient determined by Gallas *et al.*[320], $\varepsilon_{(v+\delta)OH}$ = 0.16 cm/µmol.

Size-exclusion gel permeation chromatography (SEC)

Size exclusion chromatography (SEC) of sodium lignosulfonate (LS) and depolymerized LS was conducted in a PSS Thermo Separation Products (TPS) equipped with a PSS SECurity^2 UV-1000\2000 detector and a two columns systems composed by: i) precolumn PSS-MCX 5 µm and ii) main column PSS-MCX-analytical 5 µm. The injection volume has been set to 100 µL, with an elution flow of 1.0 mL min^{-1} using Na_2HPO_4 0.084 M aqueous buffer as eluent and column

temperature of 298 K. Prior to the analysis the sample has been diluted 1:10 in the Na_2HPO_4 and the salt peak at 298 K has been used as the internal standard.

Size exclusion chromatography (SEC) of depolymerized lignin from BWS was conducted with a similar PSS-TPS device equipped a PSS-GRAM VS pre-column followed by two columns (PSS GRAM 7µm, 100 Å and PSS GRAM 7 mm, 1000 Å). The injection volume has been set to 100 µL, with an elution flow of 0.8 mL min^{-1} using N-methylpyrrolidone (NMP) + 0.5 g L^{-1} of LiBr.

The molecular weight distributions quantification (M_w, M_n and Đ) has been performed using the PSS – WinGPC UniChrom software and sodium poly-(styrene sulfonate) standards. Accordingly, eight different standard have been used with a M_w of 29500 g mol^{-1} (RT 8.63 min), M_w of 15800 g mol^{-1} (RT 9.14 min), M_w of 13500 g mol^{-1} (RT 9.25 min), M_w of 9740 g mol^{-1} (RT 9.47 min), M_w of 3800 g mol^{-1} (RT 9.88 min), M_w of 1670 g mol^{-1} (RT 10.23 min), M_w of 891 g mol^{-1} (RT 10.44 min) and M_w of 246 g mol^{-1} (RT 10.9 min). The standards have been fit with a calibration curve applying a polynomial function of the seventh order (PSS –poly 7).

Two Dimensional ^{1}H-^{13}C heteronuclear single quantum coherence nuclear magnetic resonance (2D HSQC- NMR)

NMR spectra were recorded on a Bruker Ascend 400 MHz spectrometer. A sample of the sodium lignosulfonate (50 mg) was dissolved in 0.6 mL of DMSO-d6. HSQC experiments had the following parameters: standard Bruker pulse sequence ‘hsqc’, spectral width of 8.6 ppm in F2 (1H dimension) by using 2048 data points for an acquisition time (AQ) of 159 ms, spectral width of 149 ppm in F1 (^{13}C dimension). The number of scans was 64 with an interscan delay of 1.5 s (D1).

Freeze-drying

The freeze-drying of the SHF-LS sample has been conducted using a Christ Alpha 1-4 LSC-basic device. Prior to the freeze-drying, the sample has been placed in a falcon tube and frozen at -263 K for 10 h. Afterwards, a further cooling step has been conducted in liquid nitrogen (77 K) for 5 minutes. Then, the sample

has been freeze-dried for 10 h at a pressure of around 4 kPa followed by 10 h at 0.5 kPa for complete drying.

pH-analysis

The pH of the reactant LS solution and the SHF-LS collected solution has been measured using a WTW Multilab 540 pH meter equipped with a KCL. Prior to the analysis, the pH meter has been calibrated using the Burkett standard buffer solution for pH of 4.0, 7.0 and 8.0. The pH has been measured while the sample has been kept under continuous stirring.

Gas Chromatography equipped with mass spectrometer detector (GC-MS) and with flame ionization detector (GC-FID)

The qualitative and quantitative product analysis has been performed using a Gas chromatography (Agilent 8890 GC) equipped with a HP-5MS Ultra Inert column from Agilent (model: USR577054H), a split-splittles liner (Agilent 5190-2295) and coupled with both mass spectrometer detector, i.e., GC-MS configuration, (Agilent 5975 MSD) and flame ionization detector (Agilent), i.e,. GC-FID configuration,.

For qualitative analysis the GC-MS configuration was used. The MS method has been set with a run time of 32 min, injection volumes of 1.0 µL, and He as carrier gas with a flow of 1 mL min^{-1}. The injection has been set in Split mode with a split ratio of 10 while the inlet has been kept at 553 K to evaporate the injection. The temperature program for the column oven has been set as following: start at 323 K and maintaining for 1 min, then increasing to 573 K with a heating rate of 10 K min^{-1} and maintaining at 573 K for 6 min. The MS detector has been set to scan between 50 and 250 m/z with a gain factor of 1.1. The solvent delay has been set at 2.6 min, while the MS detector and the quadrupole has been kept at 503 K and 423 K, respectively. The mass spectra of the compounds were analyzed integrating the peak area using the Agilent MassHunter Qualitative Analysisi 10.0 software from and comparing with the NIST 17 mass spectral database.

For the quantitative analysis GC-FID configuration has been used. The injection and the oven methods has been set identically to the GC-MS analysis above

described. During the analysis the FID detector has been fed with H_2 flow of 30 mL min^{-1} as fuel gas while the heater has been kept at 623 K to avoid product condensation at the GC/FID interface. The quantification of the peak has been conducted using the Agilent MassHunter Qualitative Analysis 10.0 using the ChemStation integrator.

Uv-vis Analysis

UV-vis measurements of the extracted lignin solution for BWS have been performed using a high-performance split beam T70+ UV-vis spectrophotometer from PG Instruments. Prior to the experiment, 100 µL of each sample were diluted in 2.5 mL of solvent, i.e., MeOH, MeTHF (according to the solvent used for the reaction), in a high-precision quartz cuvette, type 100-QS (10 mm size). For every measure, the spectrum has been recorded between wavelengths of 1110 nm and 190 nm with 1nm steps. The spectrophotometer is interfaced to a PC using the UV-Win software used for the determination of absorbance spectra.

Klaison lignin quantification

The acid-insoluble lignin, called Klason Lignin (KL) of the beach wood sawdust (BWS) was determined based on the procedure reported by Nakano and Meshitsuka.[321] Accordingly, 1g of BWS was transferred to 50 mL flask with 15 mL of H_2SO_4 solution (72 wt.-%). The mixture was left at room temperature for 2 h under continuous stirring. Afterwards, the solution has been transferred in a round-bottom flask containing 360 mL of water. Then, the solution was boiled for 4 h under reflux conditions. Afterwards, the solution was directly filtrated without cooling. After filtration, a brown sludge was retained. The precipitate was washed with hot water to remove any leftover acid and the obtained residue was dried at 353 K for 12 h. The mass of the KL has been determined gravimetrically from the weight of the dried residue. Therefore the KL content has been quantified in wt.-% with respect of the initial BWS mass.

B.3 Continuous flow systems setup

Figure B1. The reaction set up consists of **A**) HPLC pump equipped with pressure control **B**) "T" unit for gas-liquid mixing **C**) Mass flow controller for H_2 **D**) heating unit (see the inner part of it at Figure S4) **E**) relief valve used for pressure controlling, connected with **s**ample collector.

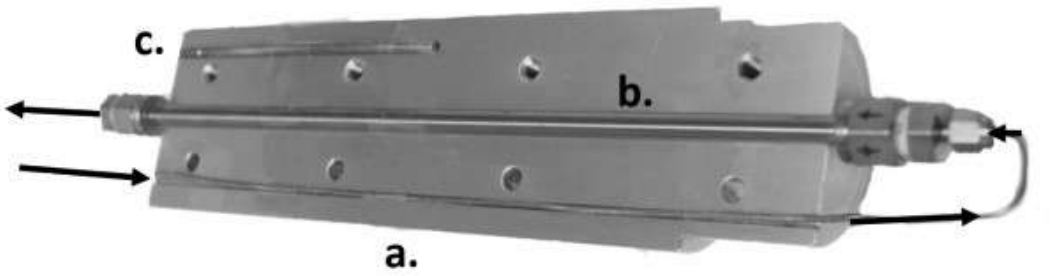

Figure B2. Customized aluminum cylinder used for ensure efficient heat consisting of three holes, **A**) pre-heating unit, **B**) tubular reactor place and **C**) thermocouple location for temperature control. In this case the reactor has an outer diameter of 6.5 mm, a similar cylinder has been made for the bigger tubular reactor (outer diameter of 25 mm).

Figure B3. The used stainless steel tubular reactors: **Left)** the prototype scale reactor , with inner diameter 21 mm, outer diameter 25mm and length 280 mm. **Right)** reactor with inner diameter of 4.6 mm, outer diameter of 6.5 mm and length of 250 mm.

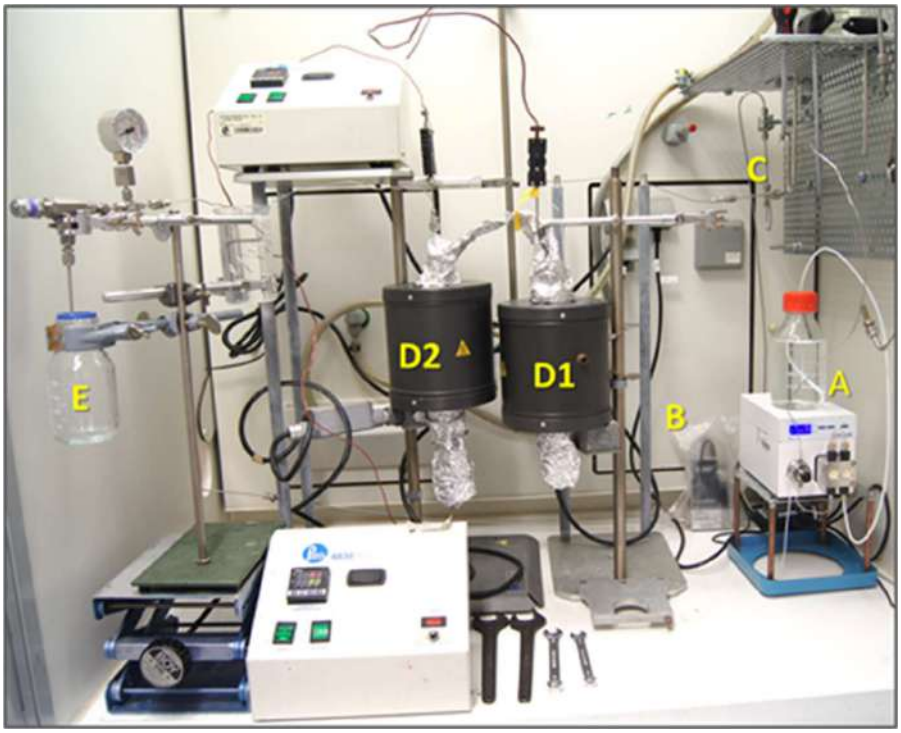

Figure B4. Integrated process of glucose conversion to isosorbide in continuous flow setup, the setup consists of **A**) HPLC pump equipped with pressure control, **B**) Mass flow controller for controlling the flow of H_2, **C**) tee union for gas–liquid mixer, **D1**) and **D2**) independents heating units and **E**) sampling unit equipped with proportional relief valve.

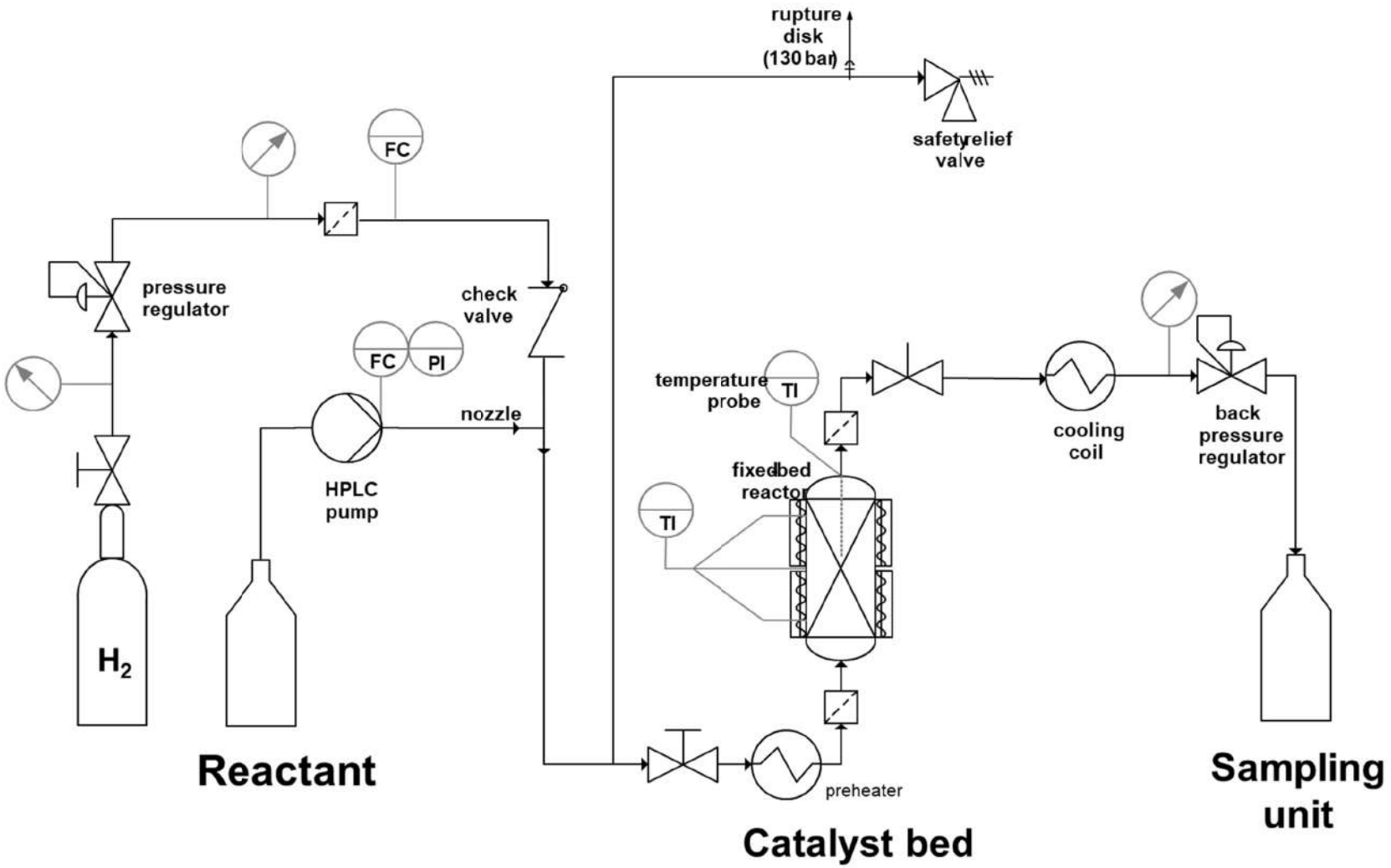

Figure B5. Flowchart of the single column setup.

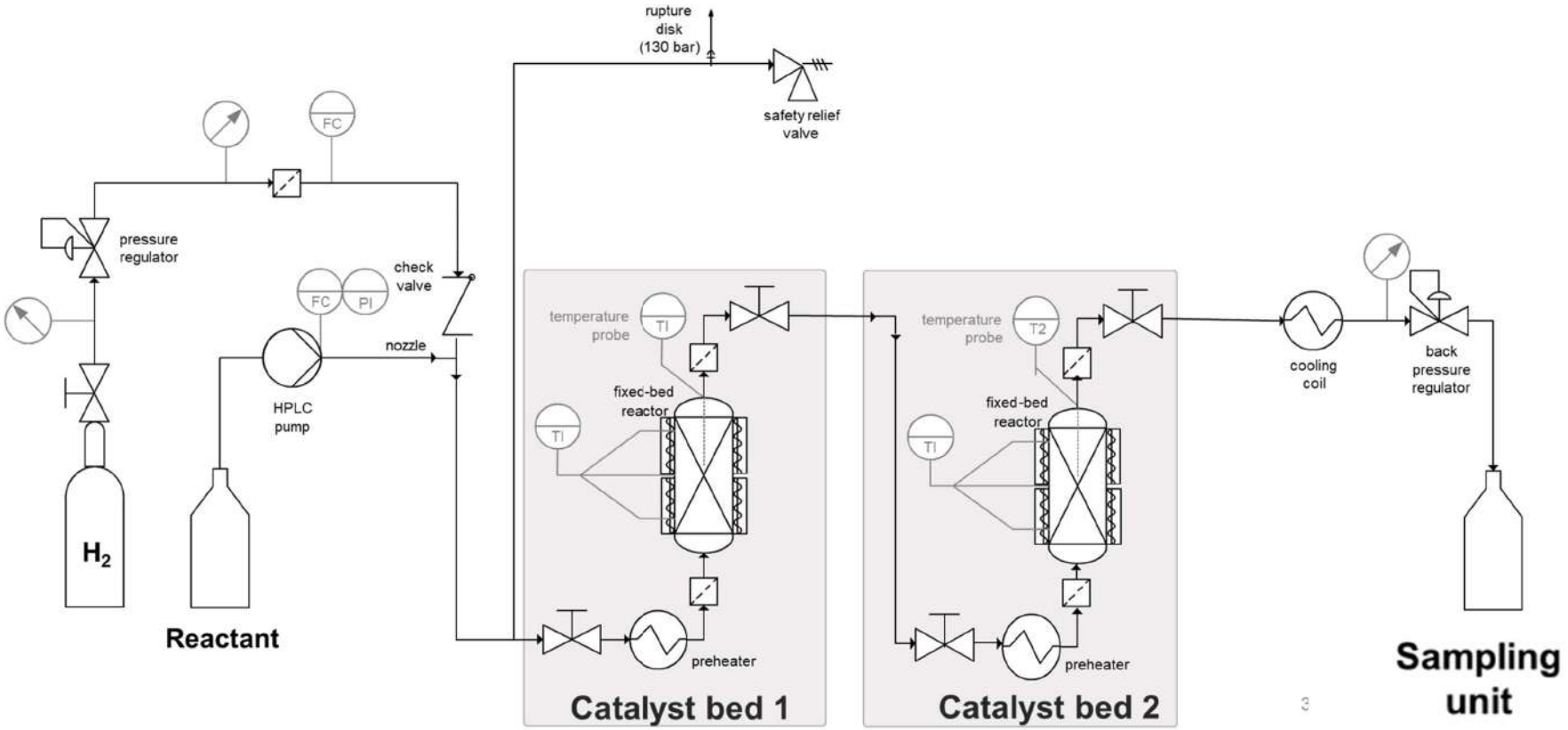

Figure B6. Flowchart of the dual column column setup.

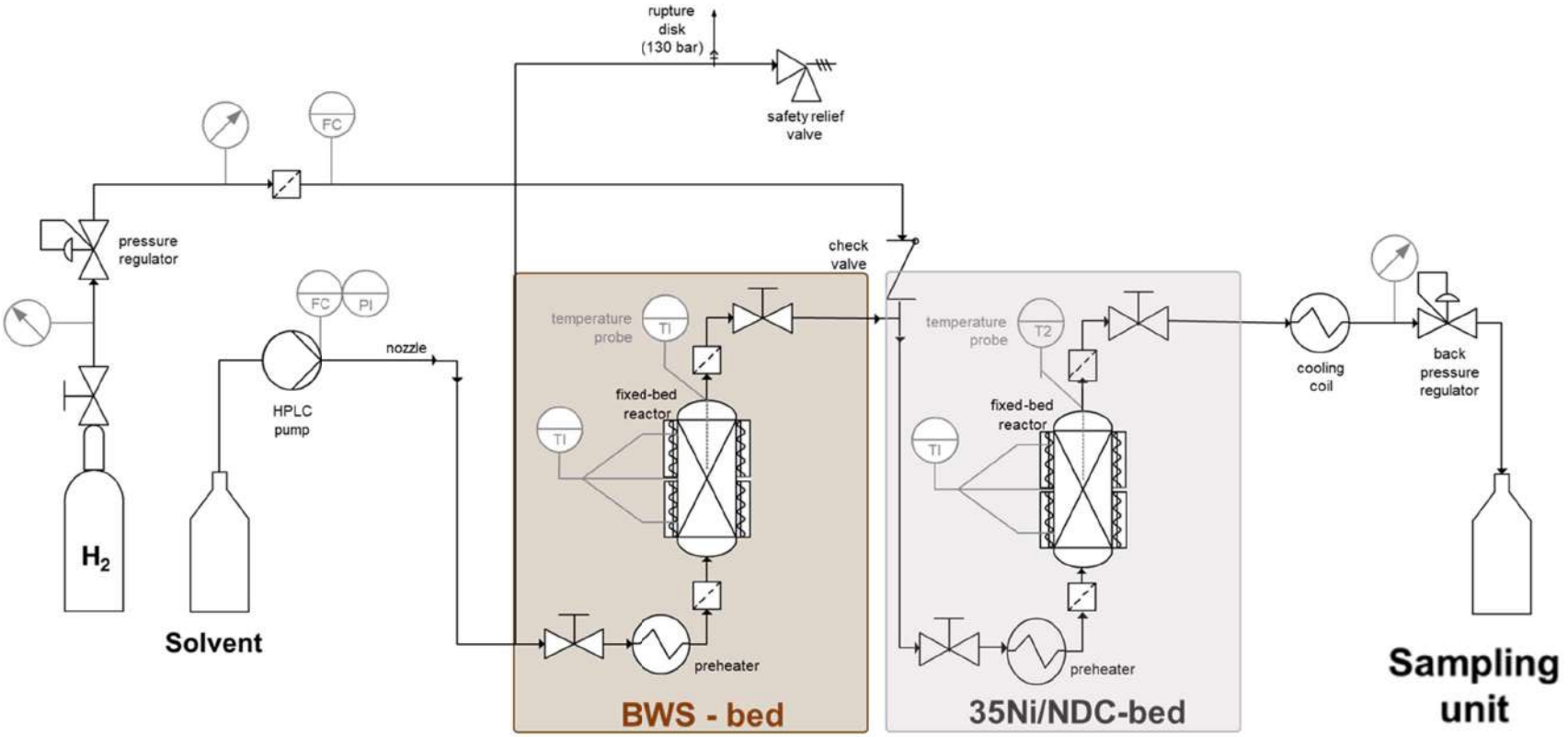

Figure B7. Flowchart of the SF-RCF dual column setup.

B4 Catalytic experiments procedures

Single-step valorization of Glucose to Sorbitol, Xylose to Xylitol and Vanillin to MMP.

In a typical experiment 1 wt.-% of an aqueous solution of glucose (c_{Glu} = 56 mM), xylose (c_{Xyl} = 64 mM) or Vanillin (c_V = 72 mM) were fed *via* HPLC pump at different liquid flow rates of 0.3, 0.5, 0.7, 1.0 or 3.0 mL min^{-1}, mixed with an excess amount of H_2 (Q_{H_2} = 15 mL min^{-1} at a pressure of 2.5 MPa) and introduced into the preheating unit prior to the fixed bed reactor. 1 g of catalyst pellets were fixed between 0.1 g of quartz wool. The reactor temperature and pressure were kept at ambient values for 15 min. Later, the system pressure was adjusted to 2.5 MPa and the temperature was increased to the targeted values, i.e., 353 K, 373 K, 398 K, 408 K and 423 K. Samples (ca. 2 mL) were collected once the steady state was reached after *ca*. 30 min.**Caution**: Each time of stream (TOS) experiment was conducted in 4 consecutive days (*ca*. 10 hours each days) without removing the catalyst from tubular reactor and applying any post treatment on the catalyst.

Products analysis was performed using HPLC Agilent 1200 series equipped with a quaternary pump, diode array detector (DAD) and refractive index detector (RID). The analysis procedure and quantification of the reaction products are described in details in **Section B5**.

Sorbitol to isosorbide dehydration and integrated process for isosorbide production from glucose

In a typical experiment of isosorbide production from sorbitol, an aqueous solution of sorbitol ($c_{sorbitol}$ = 0.05 M) was fed with HPLC pump at 0.3 mL min^{-1} and introduced into the preheating unit to the fixed bed reactor consisting of 2.5 g of zeolite fixed between two layers of quartz wool (30 g of Beta(75) was used for the experiment in prototype tubular reactor scale). The temperature and pressure were kept constant at room conditions (298 K and atmospheric pressure) for 15 minutes. Afterwards, the system was pressurized to 4.0 MPa to ensure the presence of the reactant solution in the liquid phase and the temperature was elevated to 503 K.

Samples (2.0 mL) were collected once the steady state was reached, after *ca.* 30 min (1.5 h on prototype scale).

In the case of the integrated process, an aqueous solution of glucose ($c_{glucose}$ = 0.05 M) were fed with the HPLC pump at 0.7 mL min^{-1} and mixed with an excess of H_2 (25 mL min^{-1} at the pressure of 4.0 MPa) and introduced into the two consecutive tubular reactors, the first one set to a temperature of 423 K and the second at the temperature of 503 K. In this experiments, catalyst mass of 10 g of 35Ni/NDC (the first tubular reactor for hydrogenation of glucose to sorbitol), and 30 g of Beta(75) at the second tubular reactor (for dehydration of the formed sorbitol from the first reaction to isosorbide)were used. Similar to the above-mentioned investigation (dehydration of sorbitol to isosorbide), the system was kept at room condition for 15 minutes and then set to the targeted pressure and temperatures. Samples were collected once both systems reached the steady state, i.e., after *ca* 3 h.

Qualitative and quantitative analysis of the reactant and products were performed using HPLC/MS and HPLC, respectively. Detailed information about the reactants and product quantification, as well as the calculation of the turnover frequency (TOF) can be found at the ESI.

B5. Products analysis and quantification

Single-step valorization of Glucose to Sorbitol, Xylose to Xylitol and Vanillin to MMP.

Reactants and products of the catalytic hydrogenation reactions were analyzed using HPLC Agilent 1200 series equipped with a quaternary pump, diode array detector (DAD), and refractive index detector (RID). For the analysis of the products that were derived from Glu and Xyl hydrogenation reaction, the HPLC system was equipped with Phenomenex Rezex ROA Organic Acid column (length 300 mm, 7.8 mm inner diameter) and RID was used as a detector. The analysis program was set to 45 min at 348 K using 0.1 wt.-% aqueous solution of formic

acid as eluent with flow of 0.35 mL min^{-1} and 3 µL as an injection volume. The retention time for the Glu, Sor, Fru, Xyl and Xyt was 18.0 min, 19.1 min, 19.9 min, 19.1 min and 21.4 min, respectively.

For V hydrogenation the HPLC was equipped with a C18 column (Hypersil GOLD C18 Selectivity LC Series) column and DAD was used as a detector. The DAD detector was used to ensure a complete separation of the reactant and products due to the presence of characteristic chromophores. All measurements were conducted using a wavelength of 280 nm. The HPLC program included an injection volume of 3.0 µm at 308 K. The retention time was 15 min with an eluent flow of 1.2 mL min^{-1}. The eluent phase consists of an isocratic mixture of acetonitrile and water (50:50 vol.-%) has been used in the first 8 minutes.Then, the column was washed with a non-isocratic solution of 100 % acetonitrile between the 8^{th} and 12^{th} minutes. Finally, the eluent composition has been reset to the initial isocratic phase at 15^{th} minute. Prior the analysis, each sample was diluted with water (0.1 mL in 1 mL) to avoid saturation of the DAD with high concentrated solution (1 wt.-%). The retention time for the V, VA and MMP was 3.0 min, 2.7 min and 3.8 min, respectively.

The products were identified comparing the retention time with standards substances. The molar concentration (c_i) of the reactant and products was calculated from the integrated area of peaks and referred to calibration curve conducted with standard compounds. The conversion and yield of the i-th compound (X_i, and Y_j) were calculated as reported the following equations:

$$X_i = \frac{c_i^0 - c_i^t}{c_i^0} \cdot 100\%$$

$$Y_j = \frac{c_j^t}{c_i^0} \cdot 100\%$$

where c^0_i and c^t_i indicates respectively the initial reactant concentration and the reactant concentration at a distinct time.

Space time conversion (**STCi**) and space time yield (**STYi**) normalized to Ni content were calculated as following:

$$STC_i(mol_i h^{-1} mol_{Ni}^{-1}) = \frac{c_i^0 - c_i^t}{n_{Ni} \cdot N_i^t}$$

$$STY_j(mol_j h^{-1} mol_{Ni}^{-1}) = \frac{c_j^t}{n_{Ni} \cdot N_i^t}$$

$$\tau\left(h\ mol_{Ni}\ mol_i^{-1}\right) = \frac{n_{Ni} \cdot N_i^t}{c_i^0}$$

Where n_{Ni} indicates the moles of Ni inside the reactor and N_i molar flow used (L h^{-1}).

Sorbitol to isosorbide dehydration and integrated process for isosorbide production from glucose

Qualitative analysis of the reaction products was performed using reverse phase HPLC with Agilent 1200 series equipped with an ELSD detector and Hypercarb column (150 mm x 4.6 mm, 3 µm). The analysis method performed using flow rate of 0.7 mL min^{-1} with bidistilled H_2O (0.1% formic acid) as isocratic eluent (5 min), followed by linear gradient to 10% ACN (25 min), linear gradient to 100% ACN (5 min).

Quantitative product analysis was conducted using HPLC Agilent 1200 series equipped with Phenomenex Rezex ROA Organic Acid column (length 300 mm, 7.8 mm inner diameter), a quaternary pump and RID detector. The analysis program was set to 20 min at 353 K using 0.005 N of H_2SO_4 as eluent with flow of 0.7 mL min^{-1} and 2.0 µL as an injection volume. The retention time for the glucose, sorbitol, 1,4-sorbitan, 2,5-anhydro-D-Glucitol and isosorbide was 9.2, 10.2, 10.6, 11.3 and 12.7 min, respectively. The conversion and yield of the *i*-th compound (X_i and Y_j) were calculated as reported in the following equations:

$$X_i = \frac{c_i^0 - c_i^t}{c_i^0} \cdot 100\%$$

$$Y_j = \frac{c_j^t}{c_i^0} \cdot 100\%$$

Were c^0_i and represent the initial reactant concentration, while c_i/c_j the reactant/product concentration at the given condition. The turnover frequency of

isosorbide production (TOF), expressed in h^{-1}, has been calculated from the turnover number (TON) as follow:

$$\mathrm{TON} = \frac{\mathrm{N}_{isosorbide}}{\mathrm{N}_{\mathrm{Acid\ sites}}} = \frac{C_{isosorbide} \cdot V_{React}}{H^{+}_{Density} \cdot M_{Cat}}$$

$$\mathrm{TOF} = \frac{TON}{t_r}$$

Where $N_{isosorbide}$ indicates the mole number of isosorbide calculated from the measured isosorbide concentration $C_{isosorbide}$ and the reactor volume V_{React}. Similarly, $N_{Acid\ sites}$ indicates the atomic mole number of acidic site, calculated from the acidic site density , $H^{+}_{Density}$, from NH_3-TPD and the catalyst mass, M_{cat}. The TOF has been calculating using the residence time inside the reactor, t_r , expressed in h.

Analytical procedure and product analysis for LS valorization

An analytical procedure has been established to meets the requirement for each analytical techniques, i.e., solid specimen for EA, ICP, 2D HSQC NMR XRD, and FTIR) and liquid with minimized water content for GC analysis (GC-MS and GC-FID), see **Figure B6**. The used procedures for these methods are reported in detail in **Section B2** For every experiment, a sample of around 30 g has been collected. Initially, the alcohol solvent, i.e., MeOH and EtOH, have been removed with rotary evaporation. In the case of EtOH, where the water-EtOH azeotrope is formed, the rotary evaporation has been interrupted when the half of initial sample has been evaporated.

After the first step, the resulting liquid has been separated into two equals fractions of around 7.5 gram in order to be further treated for solid and liquid analysis separately.

In the case of solid analysis, the water solvent has been removed via freeze-drying. The resulting solid has been used for EA, ICP, 2D HSQC NMR, and FTIR analysis.

The other portion has been treated in order to perform GC analysis. Accordingly, to separate the residual sulfonate fragments and to extract the monomer from the

aqueous phase the sample has been extracted using MeTHF as extractive solvent.. thus, almost 5 g of water sample have been extracted with 50 mL of MeTHF, with 5 iterative extractions of 10 mL each. Afterwards, eventual water residuals in the solution have been dried adding almost 5g of $MgSO_3$ anhydrous. The $MgSO_3$ slurry has been removed via filtration. Finally, the MeTHF solution has been concentrated with rotary evaporation until an exact mass of almost 2.5 g has been reached.

The quantification has been conducted in comparison of the calibration curve with standard compounds using GC-FID as the detector. The single monomer yield and the cumulative monomers yield expressed in mg g_{LS}^{-1} have been calculated as follow:

$$y_i = \left(C_i \cdot \frac{M_0}{M_f}\right) \cdot \frac{1}{C_{LS}} \cdot 1000$$

$$Y_i = \sum_{n=1}^{N} (y_i)$$

Where C_i indicates the measured concentration of the *i*-th compounds expressed in wt.-%, M_0 indicates the Mass of the collected sample before the analytical procedure, M_f represents the mass of the sample after the final step of the concentration and c_{LS} represents the LS concentration in the reactant solution.

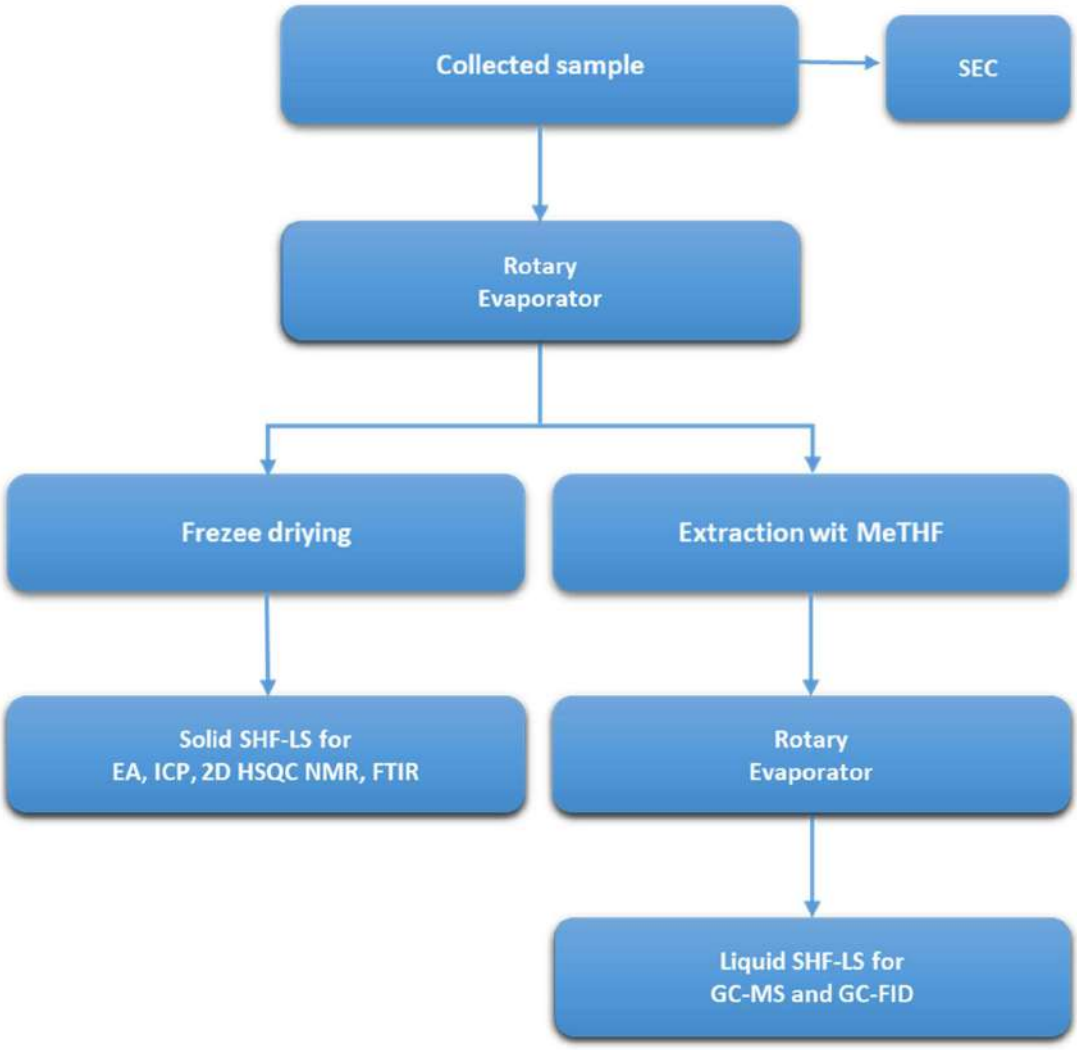

Figure B6. Analytical procedure scheme for solid SHF-LS and liquid SHF-LS analysis.

Analytical procedure and product analysis for BWS valorization

The analysis of the BWS valorization products was conducted using GC-MS and GC-FID for qualitative and quantitative analysis, respectively. The detailed description of the applied methods is reported in **Section B4.** In order to obtain higher intensity signals, prior to the analysis, 5 g of the collected samples have been concentrated with rotary evaporator until an exact mass of 1g was reached. Afterwards, the concentrated samples have been injected in GC-FID

The quantification has been conducted in comparison of the calibration curve with standard compounds using GC-FID as the detector. The monomer yield and were reported based on the Klason lignin content (mg g_{KL}^{-1}) and have been calculated as follow:

$$y_i = C_i \cdot \frac{M_i}{M_0} \cdot \frac{1}{M_{KL}} 1000$$

Where C_i indicates the measured concentration of the *i*-th compounds expressed in wt.-%, M_0 indicates the Mass of the collected sample before the rotary evaporation (genrally 5.0 g), M_f represents the mass of the sample after the rotary evaporation (generally 1.0 g) and M_{KL} represents the Klason Lignin content. However, the sensitivity factor of the remaining non-commercially available monomers (4-ethyl syringol, propyl syringol, syringyl ethyl alcohol, dihydro sinapyl alcohol, allyl syringol, and isoallyl syringol) were deduced by appling the effective carbon number (ECN) principles on the sensitivity factor of analogous compounds.[331]

C. Supporting information (SI)

C.1 Supporting information chapter 3

Figure C1. The extrusion machine from La Monferrina P3

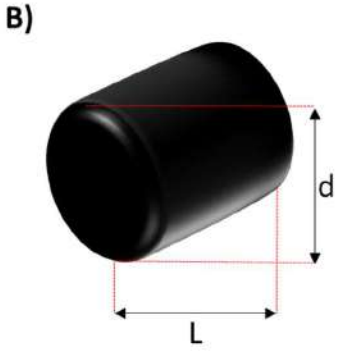

d / mm	L / mm
0.7±0.1	1.2±0.3

Figure C2. A) The raw carbon pellets after extrusion and the carbonized pellets. **Caution:** the pellets in this image has been extruded with bigger dye (0.5 cm) for representation purposes.[322] **B**) Illustration representing a single pellet dimension, diameter (d) and length (L).

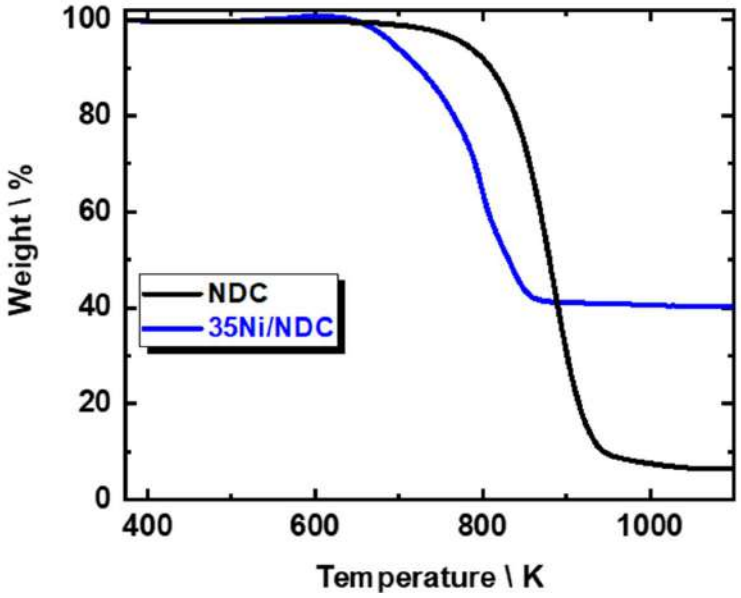

Figure C3. TGA in synthetic air, of the pristine NDC support and 35Ni/NDC.

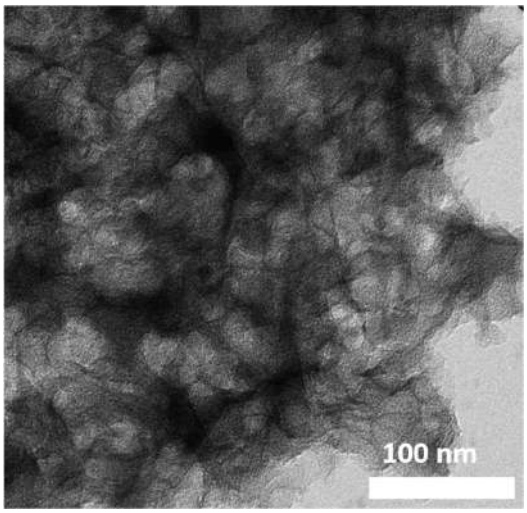

Figure C4. TEM pictures of NDC support. In the picture is visible the highly porous structure of NDC.

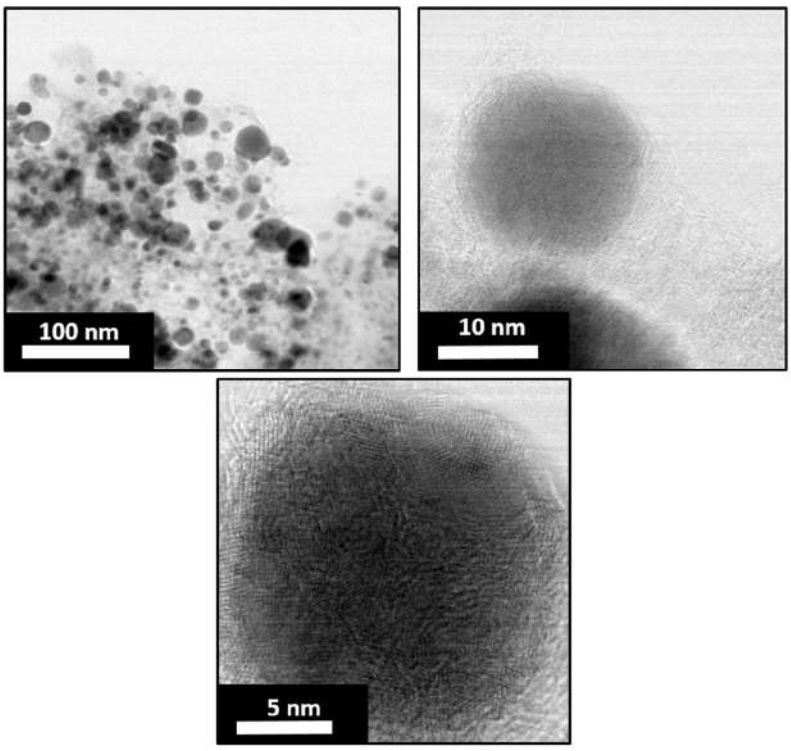

Figure C5. HR-STEM of the 35Ni/NDC catalyst.

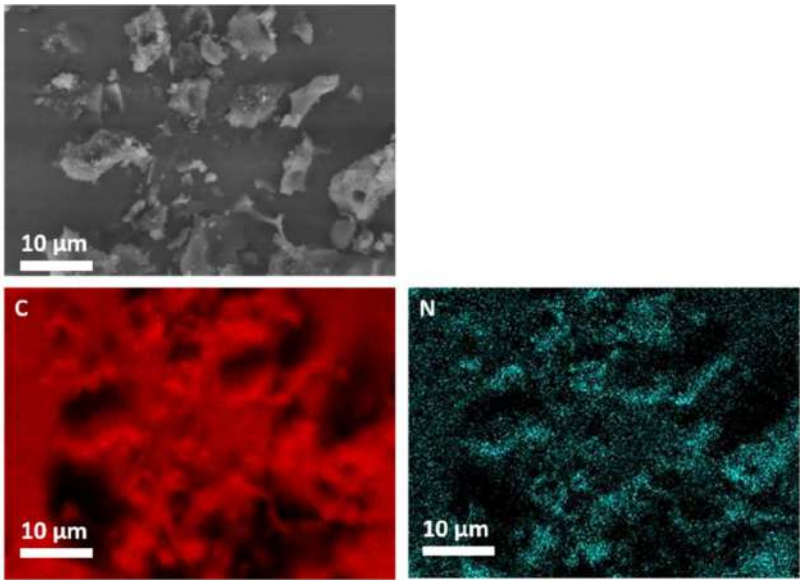

Figure C5. EDX mapping of the pristine NDC support. The upper left picture is the selected SEM area, while the EDX mapping is presented for C (red) and N (blue). The Black region in the C spectra represent a *shadowing effect* due to the thickness of the crashed pellets.

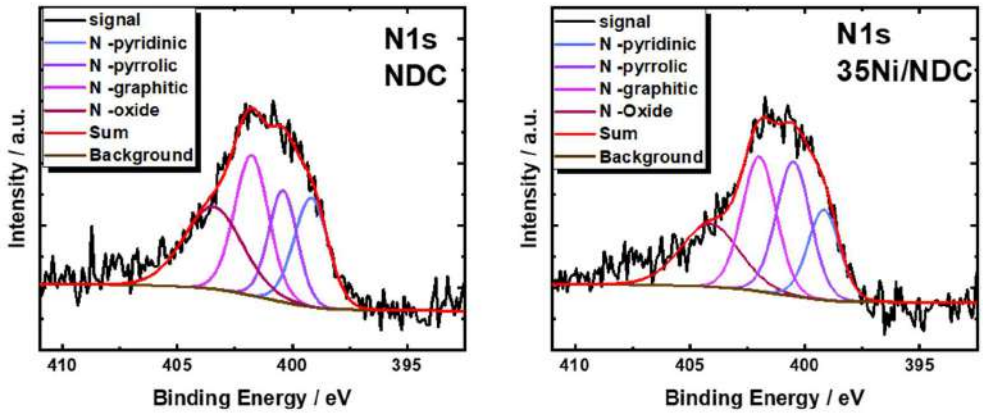

Figure C6. N1s XPS profile of the NDC support and 35Ni/NDC catalyst.

Table C. Elemental composition of fresh 35Ni/NDC quantified via EDX that linked to HR-STEM.

Catalyst	C - K/ At.-%	Ni-K / At.-%	O-K / At.-%
35Ni/NDC- nanoparticle region	20	67	11
35NiNDC- support region	94	3.8	1.7

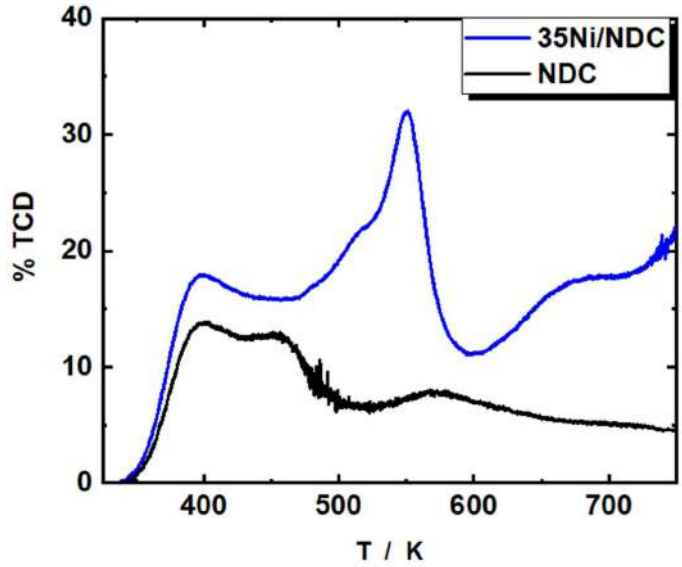

Figure C7. NH_3-TPD of NDC (black line) and 35Ni/NDC (blue line).

C.2 Supporting information chapter 4

Supporting information chapter 4.4.2

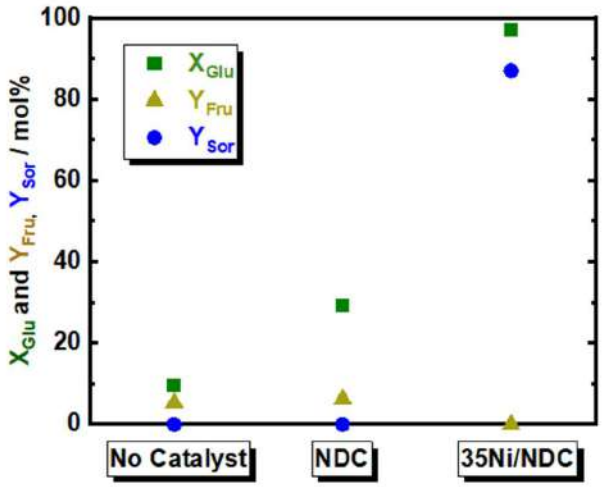

Figure C8. The conversion of glucose (X_{Glu}) and the yield of fructose and sorbitol ($Y_{Fru,}$ and Y_{sor}) in the absence of catalyst, in the presence of NDC and using 35Ni/NDC in the aqueous-phase hydrogenation of Glu to Sor; reaction conditions: c_{Glu} = 56 mM (1.0 wt.-%), T = 423 K, $m_{catalyst}$ = 1.0 g, Q_{educt} = 0.3 mL min^{-1} (τ = 4.2 h mol_{Ni} mol_{Glu}^{-1}), Q_{H_2} = 15 mL min^{-1}, p = 2.5 MPa.

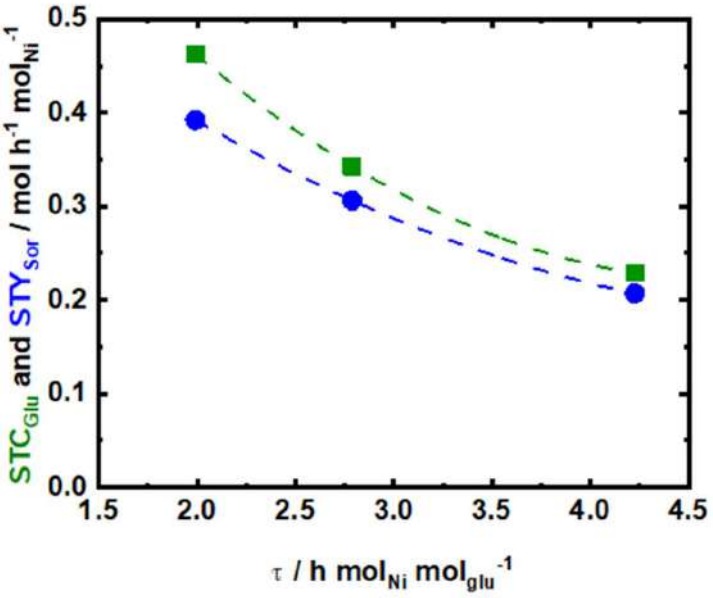

Figure C9. Space time conversion of Glu (STC_{Glu}) and space tiem yield of Sor (STY_{Sor}) as a function of space time "τ" using 35Ni/NDC in the aqueous-phase hydrogenation of Glu to Sor; reaction conditions: c_{Glu} = 56 mM (1.0 wt.-%) , T = 423 K, Q_{educt} = 0.3, 0.5 and 0.7 mL min^{-1} (τ = 2.0, 2.8 and 4.2 h mol_{Ni} mol_{Glu}^{-1}), Q_{H_2} = 15 mL min^{-1} and p = 2.5 MPa.

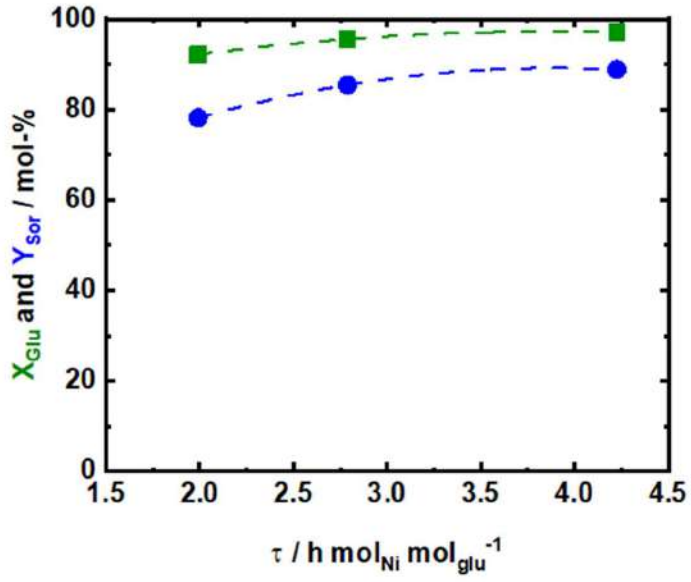

Figure C10. The conversion of Glu (X_{Glu}) and yield of Sor (Y_{Sor}) as a function of space time "τ" using 35Ni/NDC in the aqueous-phase hydrogenation of Glu to Sor; reaction conditions: c_{Glu} = 56 mM (1.0 wt.-%) , T = 423 K, $m_{catalyst}$ = 1.0 g, Q_{educt} = 0.3, 0.5 and 0.7 mL min^{-1} (τ= 2.0, 2.8 and 4.2 h mol_{Ni} mol_{Glu}^{-1}), Q_{H_2} = 15 mL min^{-1} and p = 2.5 MPa.

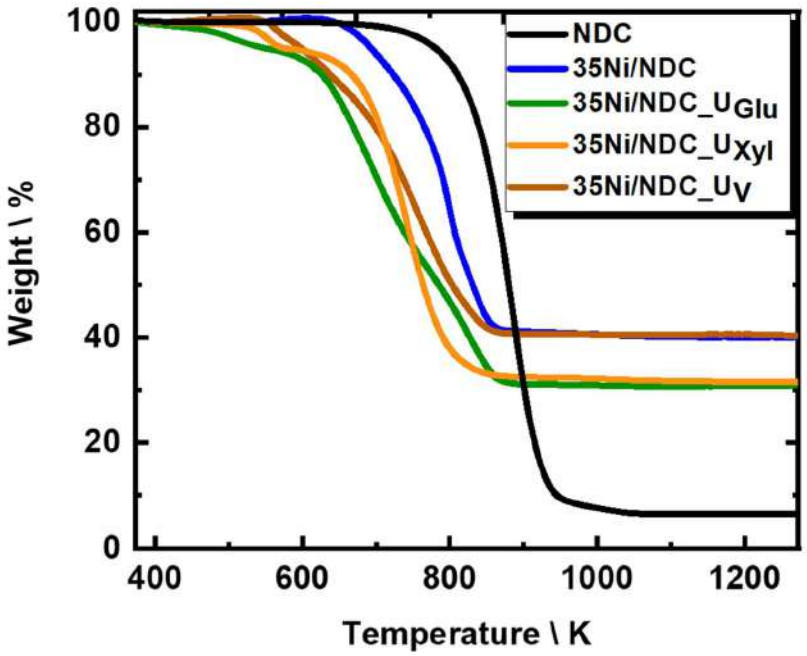

Figure C11. TGA in synthetic air, of the pristine NDC support, the fresh catalyst, 35Ni/NDC and the used ones, 35Ni/NDC_U_{Glu}, 35Ni/NDC_U_{Xyl} and 35Ni/NDC_U_V.

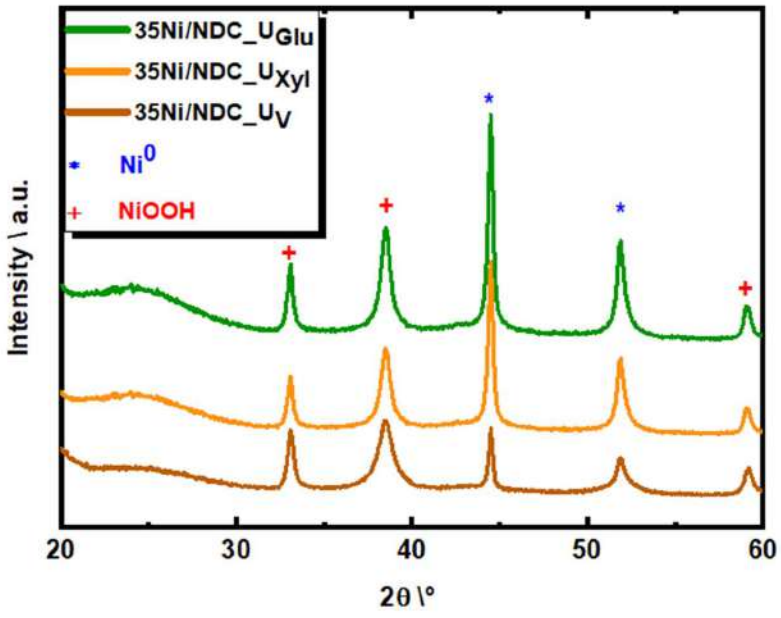

Figure C12. XRD diffraction patterns of spent catalysts 35Ni/NDC_U_{Glu}, 35Ni/NDC_U_{Xyl} and 35Ni/NDC_U_V.

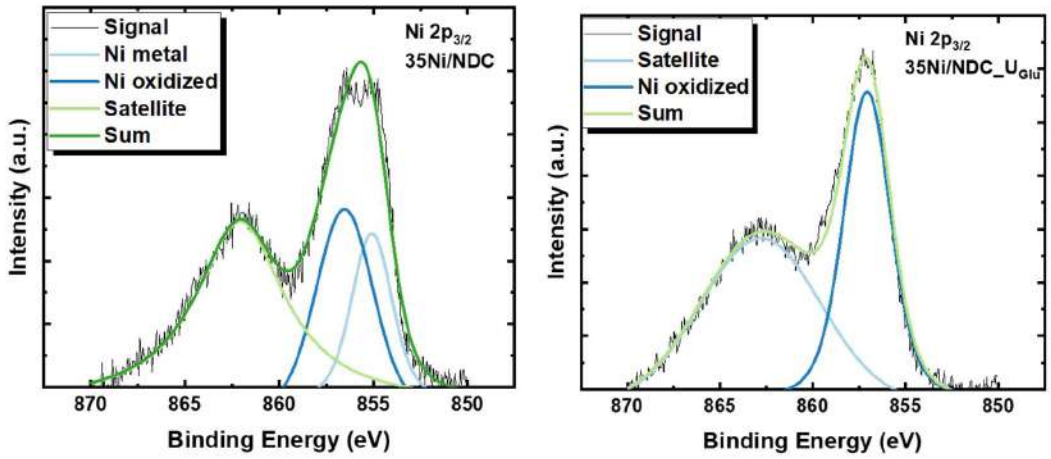

Figure C13. XPS spectra for the fresh 35Ni/NDC and spent catalyst in glucose hydrogenation (35NI/NDC_U_{Glu}).

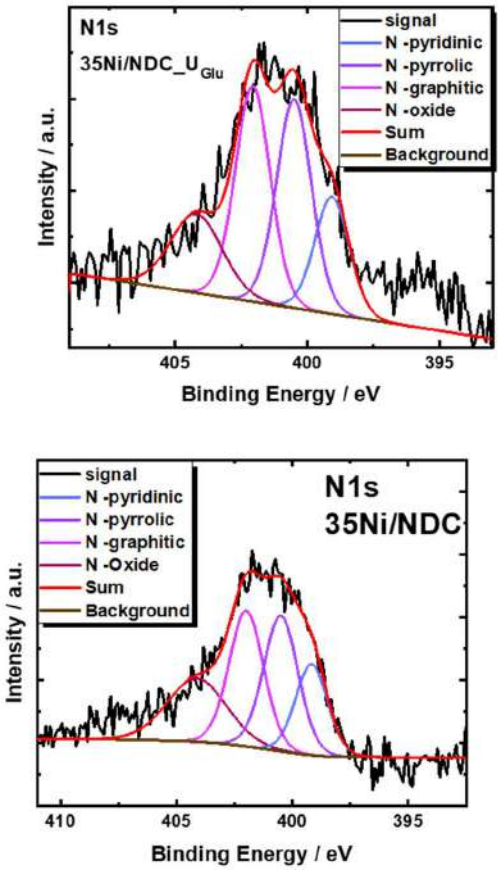

Figure C14. N1s XPS profile of the fresh 35Ni/NDC and the used 35Ni/NDC_U_{Glu} catalyst.

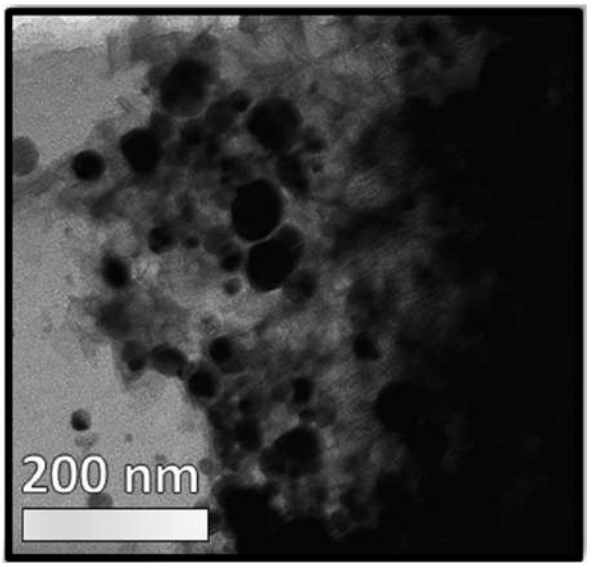

Figure C15. TEM image of spent catalyst (35Ni/NDC_U_{Glu}).

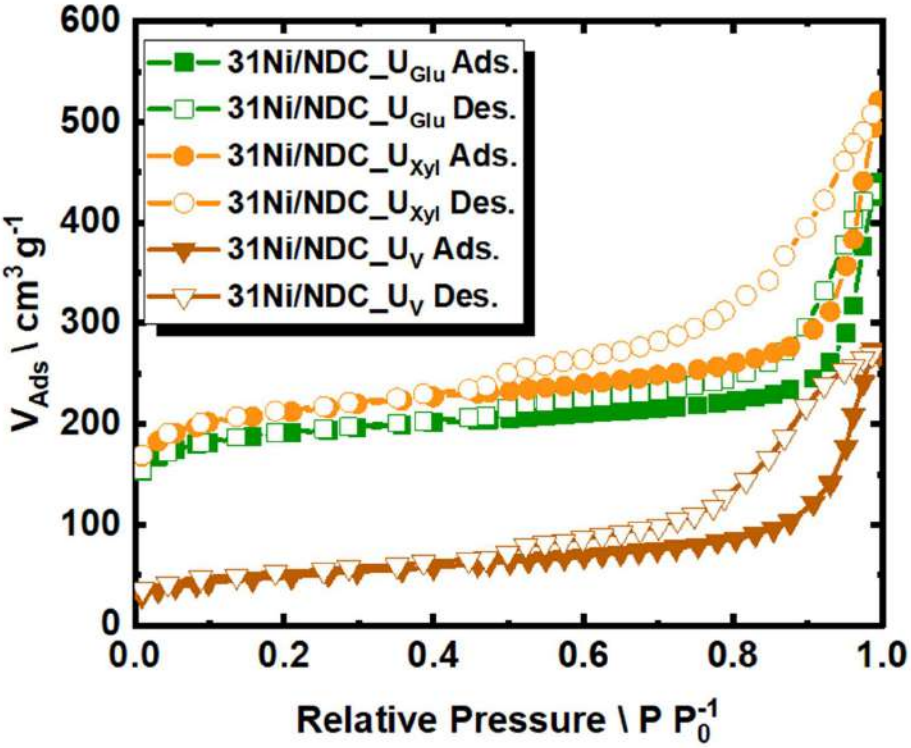

Figure C16. N_2 sorption isotherms of the spent catalysts measured at 77 K.

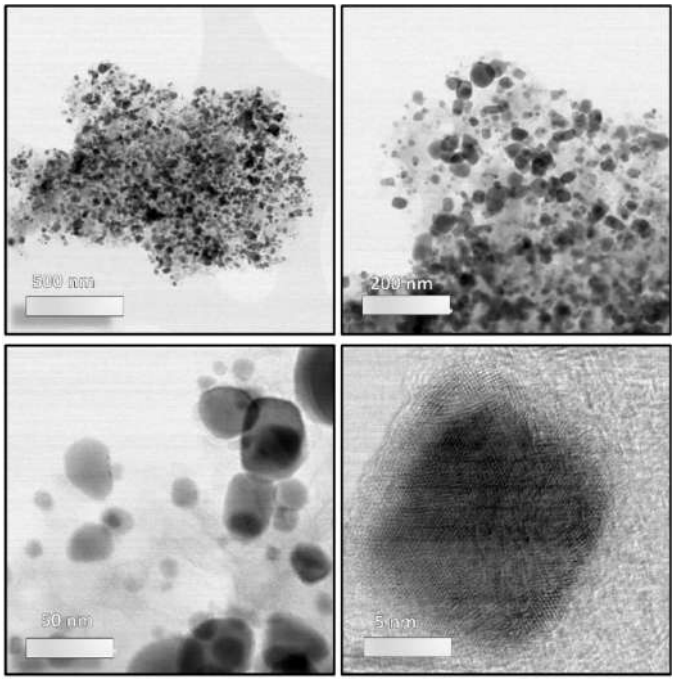

Figure C17. HR-STEM images of the regenerated 35Ni/NDC_$R_{Glu.}$

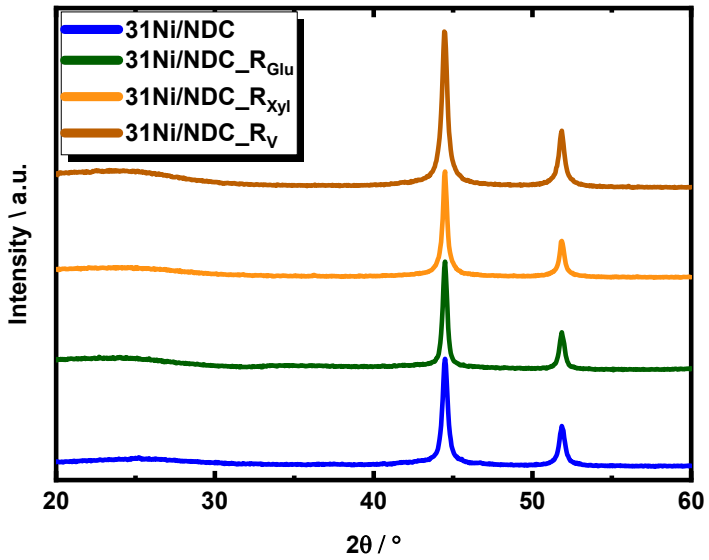

Figure C18. XRD diffraction patterns of regenerated catalysts 35Ni/NDC_R_{Glu}, 35NI/NDC_R_{Xyl} and 35NI/NDC_$R_{V,}$ compared to the fresh one 35Ni/NDC.

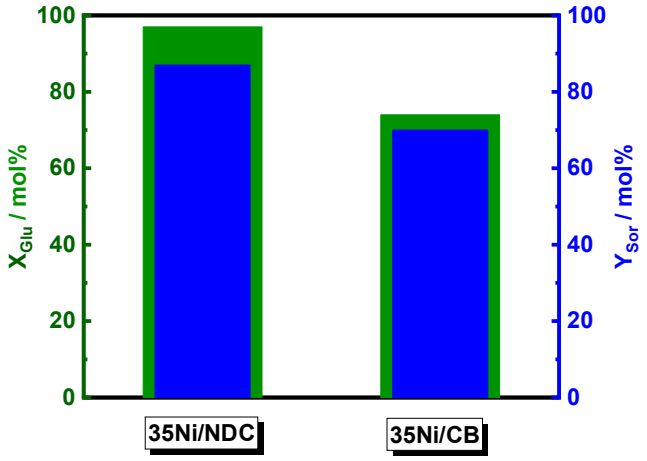

Figure C19. The conversion of glucose (X_{Glu}) and the yield of sorbitol (Y_{sor}) over 35Ni/NDC and 35Ni/CB in the aqueous-phase hydrogenation of Glu to Sor; reaction conditions: c_{Glu} = 56 mM (1.0 wt.-%), T = 423 K, $m_{catalyst}$ = 1.0 g, Q_{educt} = 0.3 mL min^{-1} (τ= 4.2 h mol_{Ni} mol_{Glu}^{-1}), Q_{H_2} = 15 mL min^{-1}, p = 2.5 MPa.

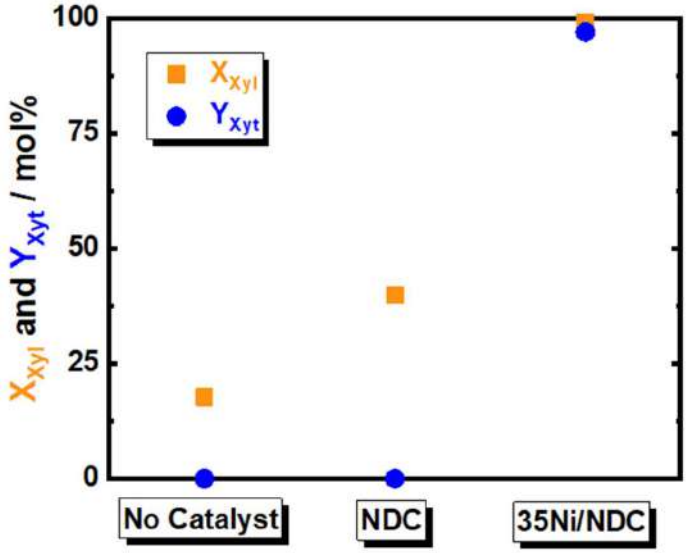

Figure C20. The conversion of Xyl (X_{Xyl}) and the yield of Xyt (Y_{Xyt}) in the absence of catalyst, in the presence of NDC and using 35Ni/NDC in the aqueous-phase hydrogenation of Xyl to Xyt; reaction conditions: c_{Xyl} = 68 mM (1.0 wt.-%), T = 423 K, Q_{educt} = 0.3 mL min^{-1} (τ= 3.6 h mol_{Ni} mol_{Xyl}^{-1}), $m_{catalyst}$= 1.0 g, Q_{H_2} = 15 mL min^{-1}, p = 2.5 MPa.

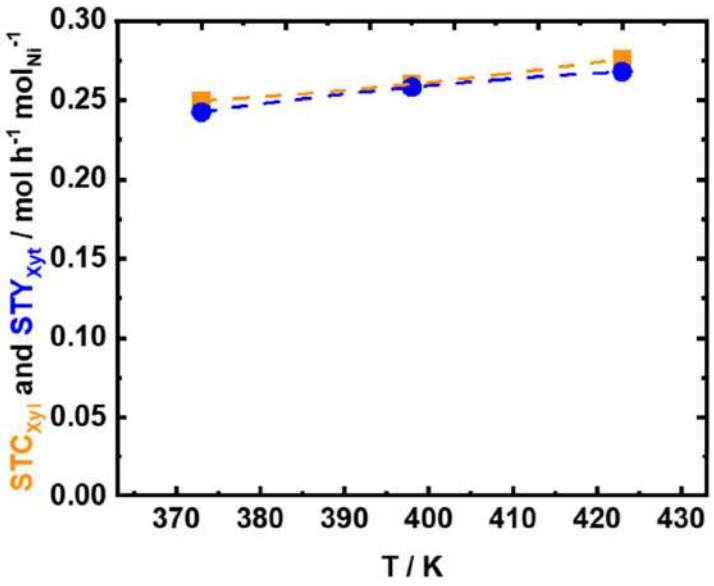

Figure C21. The space time conversion of Xyl (STC_{Xyl}) and space time yield of Xyt (STY_{Xyt}) as a function of temperature "T" using 35Ni/NDC in the aqueous-phase hydrogenation of Xyl to Xyt; reaction conditions: c_{Xyl} = 68 mM (1.0 wt.-%), T = 373 K, 398 K and 423 K, Q_{educt} = 0.3 mL min^{-1} (τ= 3.6 h mol$_{Ni}$ mol$_{Xyl}^{-1}$), Q_{H_2} = 15 mL min^{-1}, p = 2.5 MPa.

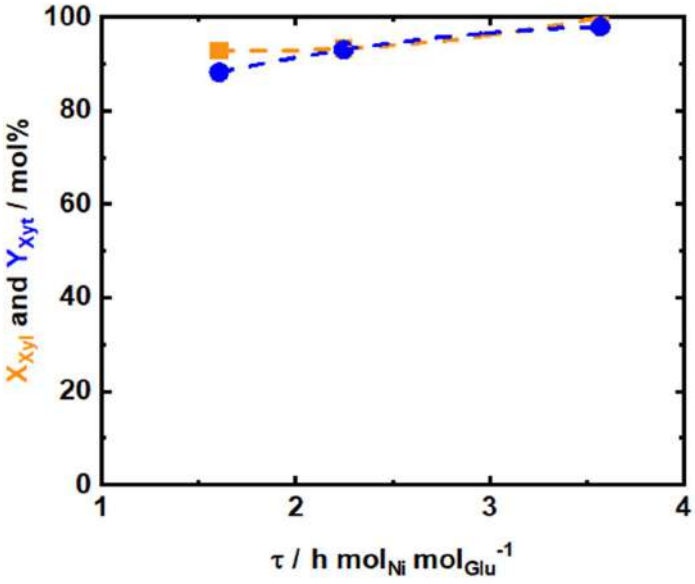

Figure C22. The space time conversion of Xyl (STC_{Xyl}) and space time yield of Xyt (STY_{Xyt}) as a function of the space time "τ" using 35Ni/NDC in the aqueous-phase hydrogenation of Xyl to Xyt; reaction conditions: c_{Xyl} = 68 mM (1.0 wt.-%), T = 423 K, Q_{educt} = 0.3, 0.5 and 0.7 mL min^{-1} (τ= 3.6, 2.2 and 1.6 h mol$_{Ni}$ mol$_{Xyl}^{-1}$), Q_{H_2} = 15 mL min^{-1}, p = 2.5 MPa.

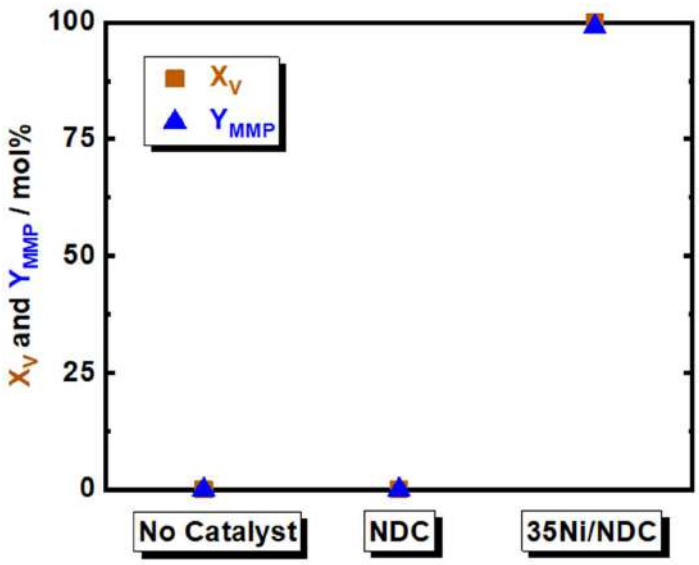

Figure C23. The conversion of V (X_V) and yield of MMP (Y_{MMP}) in the absence of catalyst, in the presence of NDC and using 35Ni/NDC in the aqueous-phase hydrogenation of V to MMP; reaction conditions: c_V = 71 mM (1.0 wt.-%), T = 423 K, $m_{catalyst}$ = 1.0 g, Q_{educt} = 0.5 mL min^{-1} (τ = 3.4, h mol_{Ni} mol_V^{-1}), Q_{H_2} = 15 mL min^{-1}, p = 2.5 MPa.

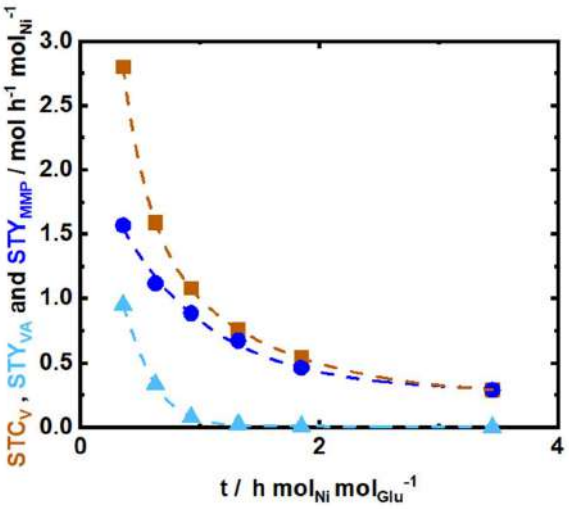

Figure C24. The space time conversion of V (STC_V), the space time yield of VA (STY_{VA}) and space time yield of MMP (STY_{MMP}) as a function of space time "τ" using 35Ni/NDC in the aqueous-phase hydrogenation of V to MMP; reaction conditions: c_V = 72 mM, T = 423 K, Q_{educt} = 0.3, 0.5, 0.7, 1.0, 1.5 and 3.0 mL min^{-1} (0.35, 0.63, 0.92, 1.3, 1.8, 3.5 h mol_{Ni} mol_V^{-1}) , Q_{H_2} = 15 mL min^{-1} and p = 2.5 MPa.

Supporting information Chapter 4.4.2

Table C2. Textural properties deduced from N_2-sorption, for different Beta zeolites, NDC and 35Ni/NDC.

Catalyst	A_{BET} / m^2 g^{-1}	V_p / cm^3 g^{-1}	D_p / nm
Beta(12.5)	111	0.3	5.0
Beta(75)	520	0.3	5.7
Beta(150)	451	0.2	5.2
Beta(75)_ Spent	290	0.3	5.1
35Ni/NDC	700	0.4	4.0
35Ni/NDC_Spent	441	0.33	4.0

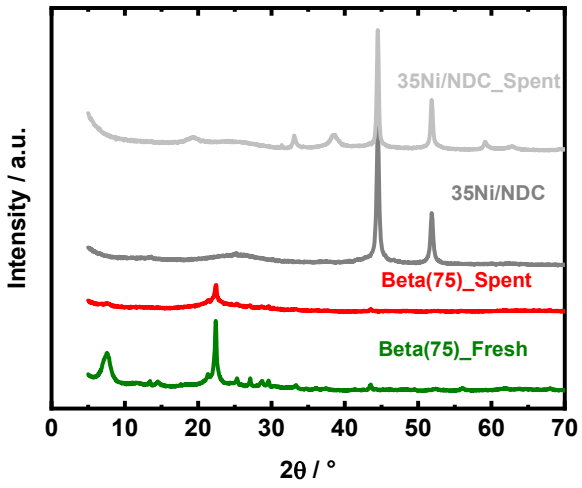

Figure C25. XRD patterns of the fresh and spent Beta (75) and the fresh and spent 35Ni/NDC.

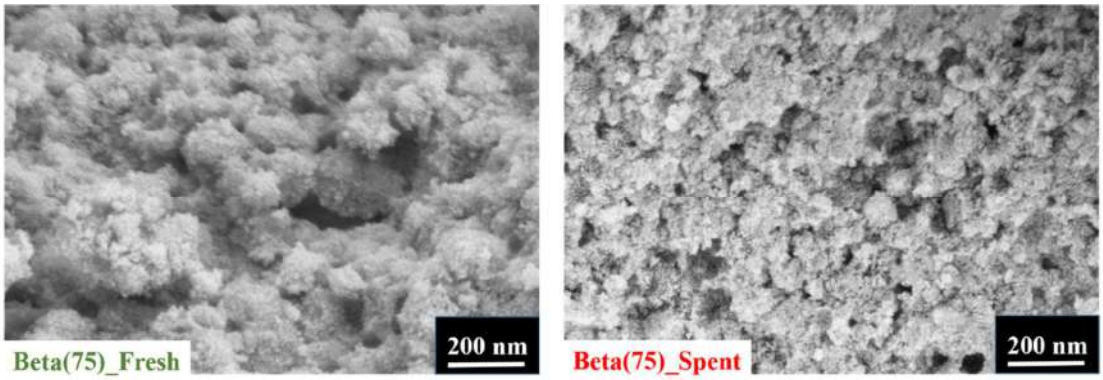

Figure C26. SEM images for the fresh and spent Beta(75).

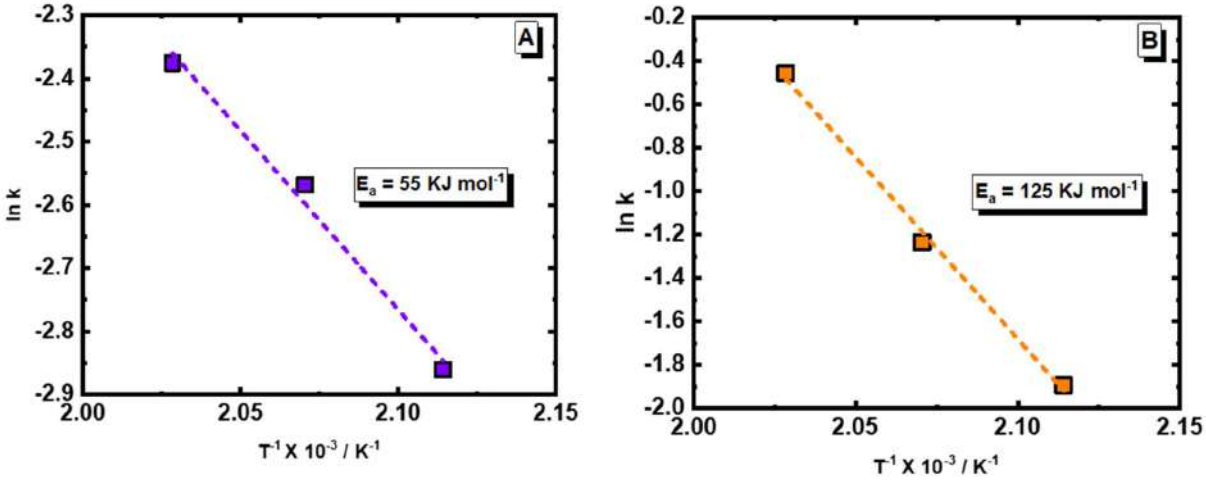

Figure C27. Arrhenius plot and activation energy (E_a) for the Sorbitol dehydration to 1,4-sorbitan (**A**) and further to isosorbide (**B**) at different reaction temperatures (483, 493and 503 K); reaction conditions: $c_{sorbitol}$ = 0.05 M, $Q_{solution}$ = 0.3 mL min^{-1}, $m_{catalyst}$ = 2.5 g, p_{system} = 4.0 MPa and space time = 3.0 h kg mol^{-1}.

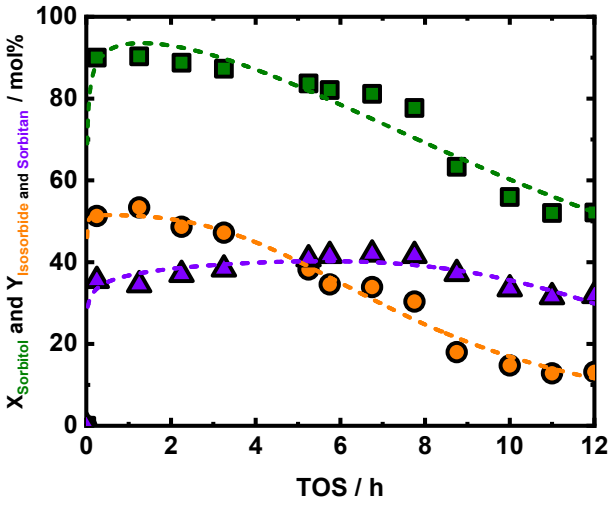

Figure C28. The conversion of sorbitol and the yield of isosorbide and 1,4-sorbitan as a function of space time; Reaction Conditions: $c_{sorbitol}$ = 0.05 M, $Q_{solution}$ = 1 mL min^{-1}, T = 503 K, $m_{catalyst}$ = 2.5 pressure = 4.0 MPa g and space time = 0.8 h kg mol^{-1}.

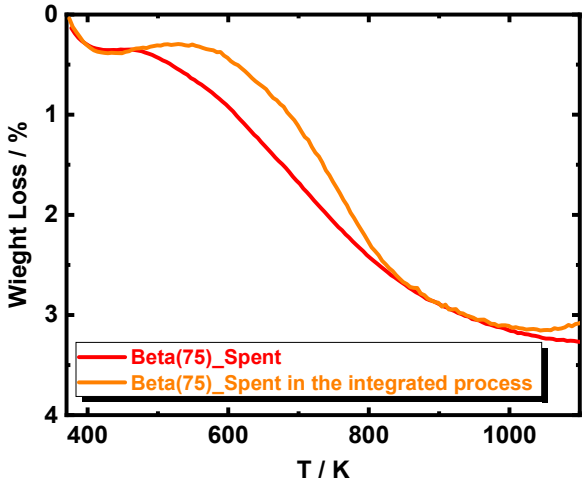

Figure C29. TGA in synthetic air of the spent Beta(75) in sorbitol to isosorbide, as well as in glucose to isosorbide.

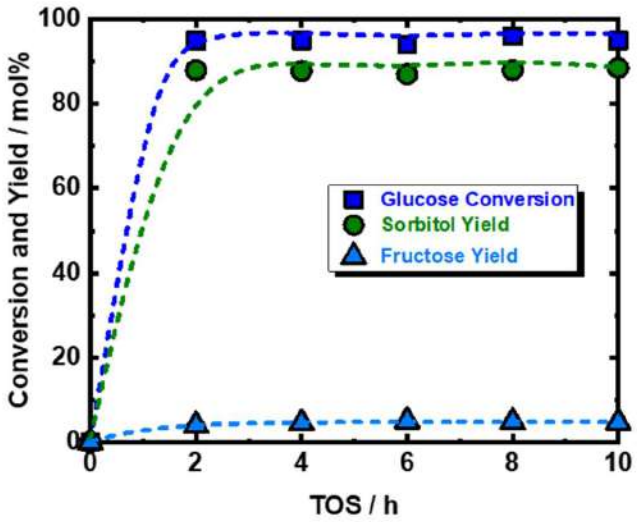

Figure C30. The conversion of glucose and the yield of sorbitol and fructose as a function of time on stream (TOS) using 35Ni/NDC; Reaction conditions: $c_{glucose}$ = 0.05 M, $Q_{solution}$ = 0.7 mL min^{-1}, T = 423 K p_{H_2} = 4.0 MPa, $m_{catalyst}$ = 10 g and space time = 4.9 h kg mol^{-1}.

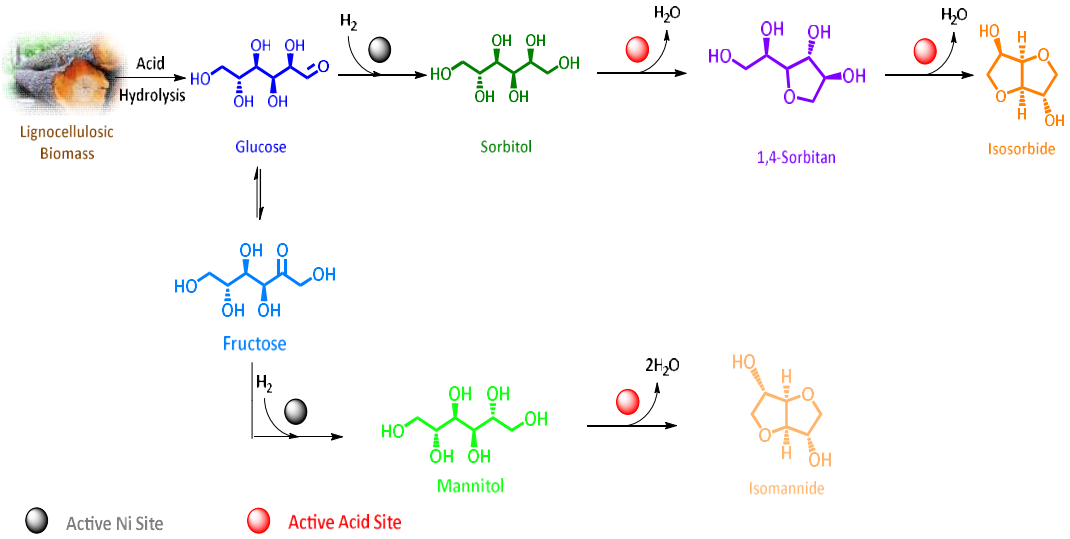

Scheme C1. Proposed synthesis of isosorbide by hydrogenation of glucose to sorbitol over 35Ni/NDC, followed by sorbitol dehydration to 1,4-sorbitan and finally to isosorbide over Beta(75).

Beta zeolite acid sites discussion

The textural properties of all the used Beta zeolites, i.e., Beta(12.5), Beta(75) and Beta(150), were characterized via N_2-sorption, XRD, SEM and Pyr-IR. The detailed description of the used methods is reported in **Section B2** of **Appendix.** The specific surface area (A_{BET}), the pore volume (V_p) and the average pore-diameter (D_p) were deduced from N_2-sorption, (**Table C2**) Beta(75) and Beta(150) exhibited higher specific surface area of 520 m^2 g^{-1} and 451 m^2 g^{-1} with respect to Beta(12.5*), i.e.,* 111 m^2 g^{-1}. Similar trend was found for specific pore volume, whereas average pore diameter (D_p) was in the mesopore range (D_p ~ 5 nm) for all used Beta zeolites, (**Table C2**).

Table C3. Brønsted acid sites (BAS), Lewis acid sites densities (LAS) measured at 423 K, 523 K and 623 K and silanol groups densities deduced from Pyr-IR for Beta(12.5), Beta(75) and Beta(150).

Catalyst	BAS / µmol g^{-1}			LAS / µmol g^{-1}			Silanols / µmol g^{-1}
	423 K	523 K	623 K	423 K	523 K	623 K	
Beta(12.5)	227	203	137	222	190	137	591
Beta(75)	73	69	64	20	14	10	1289
Beta(150)	52	50	43	5	4	3	2542

The Brønsted (BAS) and Lewis (LAS) acid site densities of the fresh Beta zeolites has been quantified using Pyr-IR at different temperatures, i.e., 423 K, 523 K and 623 K, (**Table C3)**. At all measured temperatures, the amount of total acid sites decreases with the increase of the Si/Al molar ratio of the zeolites. At the temperature of 523 K (the closest to the reaction temperature), the total acid site densities (BAS and LAS) were 393 µmol g^{-1}, 83 µmol g^{-1} and 54 µmol g^{-1} for Beta(12.5), Beta (75) and Beta(150), respectively. As expected, increasing the Si/Al molar ratio, i.e., Beta(12,5), Beta(75) and Beta(150), the BAS has been found to be decreased in all utilized Beta zeolite at 523 K. Beta(75) showed a BAS of 69

μmol g^{-1} and LAS of 14 μmol g^{-1} at 523 K, while Beta(150) possesses lower BAS of 50 μmol g^{-1} and LAS of 4 μmol g^{-1} at 523K, with respect to Beta(12.5) and Beta(150). To investigate the strength of these acidic sites, pyr-IR measurements was performed at 423K, 523 K and 623 K. In all cases, increasing the measurement temperatures is combined with drop in BAS or LAS acid site density (**Table C3**). Noteworthy to be mentioned that LAS significantly dropped at Beta(75) and Beta(150) by increasing the temperature of pyr-IR measurements to 10 μmol g^{-1} and 3 μmol g^{-1}, respectively. This indicated that BAS was found to be the strong and stable acid sites in these Beta zeolites at elevated measurement temperatures, which show that BAS are the responsible sites of the activity of Beta zeolites in the dehydration of sorbitol to isosorbide at 503 K. In addition, the silanols group amount in all three Beta zeolites has been deducted from the FT-IR measurements. It has been found that silanol groups are directly dependent on the Si/Al molar ratio, and amounted 591 μmol g^{-1}, 1289 μmol g^{-1} and 2542 μmol g^{-1} for Beta(12.5), Beta(75) and Beta(150), respectively.

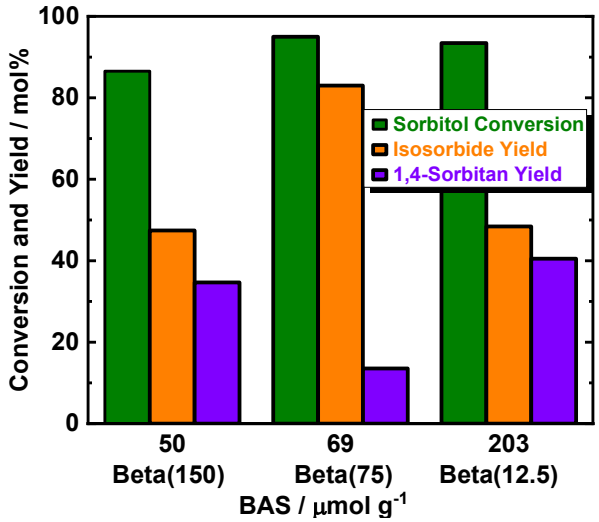

Figure C31. The conversion of sorbitol and the yield of 1,4-sorbitan and isosorbide as a function of Brønsted acid sites at three different Beta zeolites, i.e., Beta(12.5), Beta(75) and Beta(150); Reaction conditions: $c_{sorbitol}$ = 0.05 M, $Q_{solution}$ = 0.3 mL min^{-1}, T = 503 K, p_{system} = 4.0 MPa, $m_{catalyst}$ = 2.5 g and space time = 3.0 h kg mol^{-1}.

Aiming to fully understand the role of the acid sites for isosorbide production from sorbitol, we investigated Beta zeolites with different Si/Al molar ratios (12.5, 75 and 150) under the optimum reaction conditions (**Figure C31**). The density and the nature of the active acid sites over the different zeolites were determined by pyridine adsorption and desorption at 523 K, followed by infrared spectroscopy (IR). The high wavenumber zone of the spectra of the different zeolites after activation (prior to pyridine adsorption) show a different distribution of the superficial sites (**Figure C32**). Regardless the difference in the distribution of the superficial sites, all Beta zeolites showed a sorbitol conversion between 90-95 mol%, however, a difference in the isosorbide yields was observed (**Figure C31**). Beta(75) with 69 μmol g^{-1} Brønsted acid sites (BAS) showed the maximal isosorbide yield (83 mol%), while Beta(12.5) with 203 μmol g^{-1} BAS, and Beta(150) with 50 μmol g^{-1} BAS only gave isosorbide yields of ~ 50 mol% (**Figure C31** and **C33**). Correspondingly, 1,4-sorbitan yield was minimized (12 mol%) using Beta(75). A low Si/Al molar ratio, Beta(12.5), led to a fast dehydration of sorbitol to 1,4-sorbitan (41 mol%), but a slow follow up reaction to isosorbide, leading to the formation of undesired mono dehydration product (1,4-sorbitan) with yields of 49 mol%. This observation could be explained by the fact that removal of water molecules in dehydration reactions in aqueous media is thermodynamically favored by using a catalyst with enhanced hydrophobicity, i.e., high Si/Al ratio.[177, 323, 324]

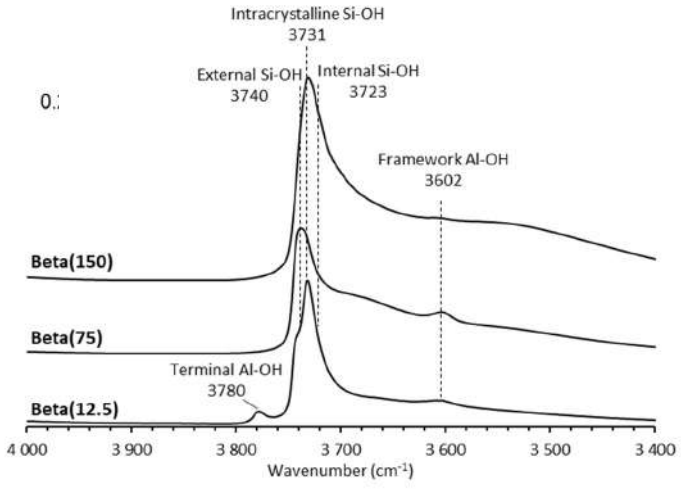

Figure C32. Infrared spectra of the different Beta zeolites in the region of v(OH) stretching bands (3400-4000 cm^{-1}) after activation at 673 K under secondary vacuum.

Next to the amount of acid sites, the nature of the superficial sites offering the acidity to the material plays an important role in driving the selectivity of the reaction.[319] Indeed, the presence of terminal Al-OH (3780 cm^{-1}) in significant proportions over Beta(12.5) may explain the poor selectivity of this latter, as they were seen to have a certain affinity to pyridine molecules (**Figure C32**).[325, 326] Over Beta(75), Al-OH species are mainly present in the structure in the form of framework Al-OH (3602 cm^{-1}), which lead us to believe in their role in the selective production of isosorbide. We should note that an excess in the framework Al-OH amount may enhance the hydrophilic nature of the material and thus leads to the formation of undesired mono dehydration product (1,4-sorbitan).[327] A further increase in Si/Al molar ratio from 75 to 150 is coupled with a reduction of the amount of BAS together with an increase in the amount of silanol Si-OH species. As a result, the use of Beta(150) lowers the isosorbide yield from 83 to 52 mol%. These results are in a strong agreement with the finding of Kobayashi *et al*. [177] for the melt phase synthesis in batch system at 400 K. However, the sorbitol conversion, and isosorbide and 1,4-sorbitan yields were found higher over the whole range of Si/Al ratio, which we attribute to the higher temperature, *i.e.* 503 K, as well as the absence of diffusion limitation due to the continuous flow system usage.

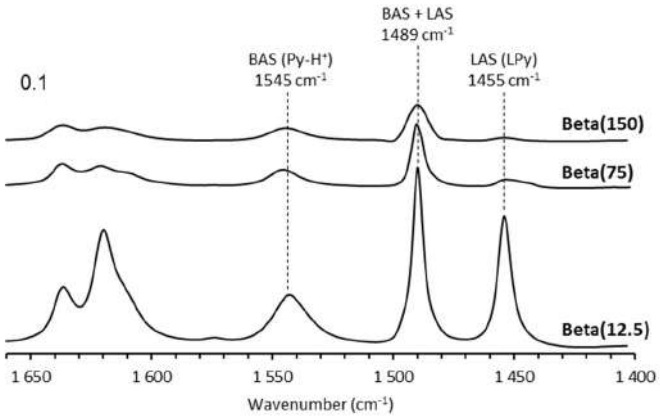

Figure C33. Infrared spectra of the residual pyridine species over the different Beta zeolites after adsorption and desorption at 523 K under secondary vacuum.

C.3 Supporting information chapter 5

Supporting information chapter 5.2

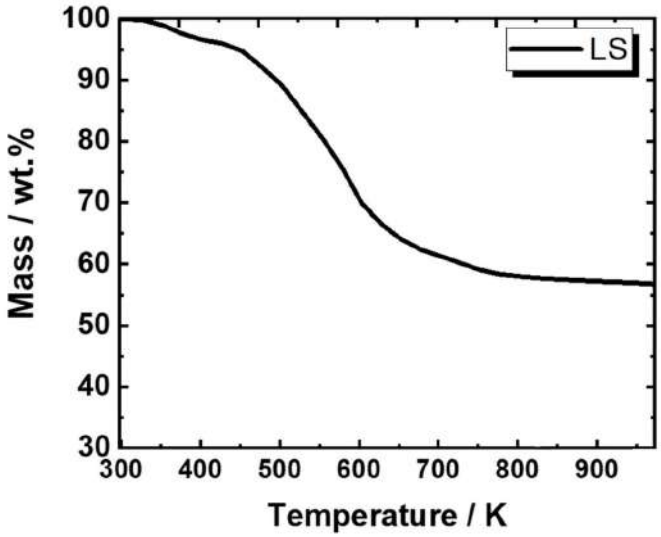

Figure C34. TGA of sodium lignosulfonate (LS) in synthetic air.

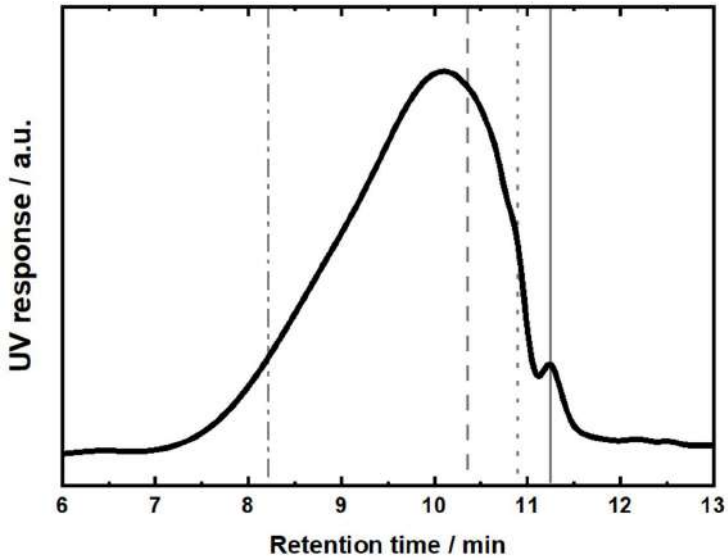

Figure C35. SEC chromatograms of LS. The straight line indicates the eluents buffer reference peak ($NaHPO_3$), dotted and dashed lines show the analytical standard peaks (sodium poly-(styrene sulfonate)) with Mw of 246 g mol^{-1} (RT = 10.9 min) and with M_w of 891 g mol^{-1} (RT= 10.4 min), respectively.

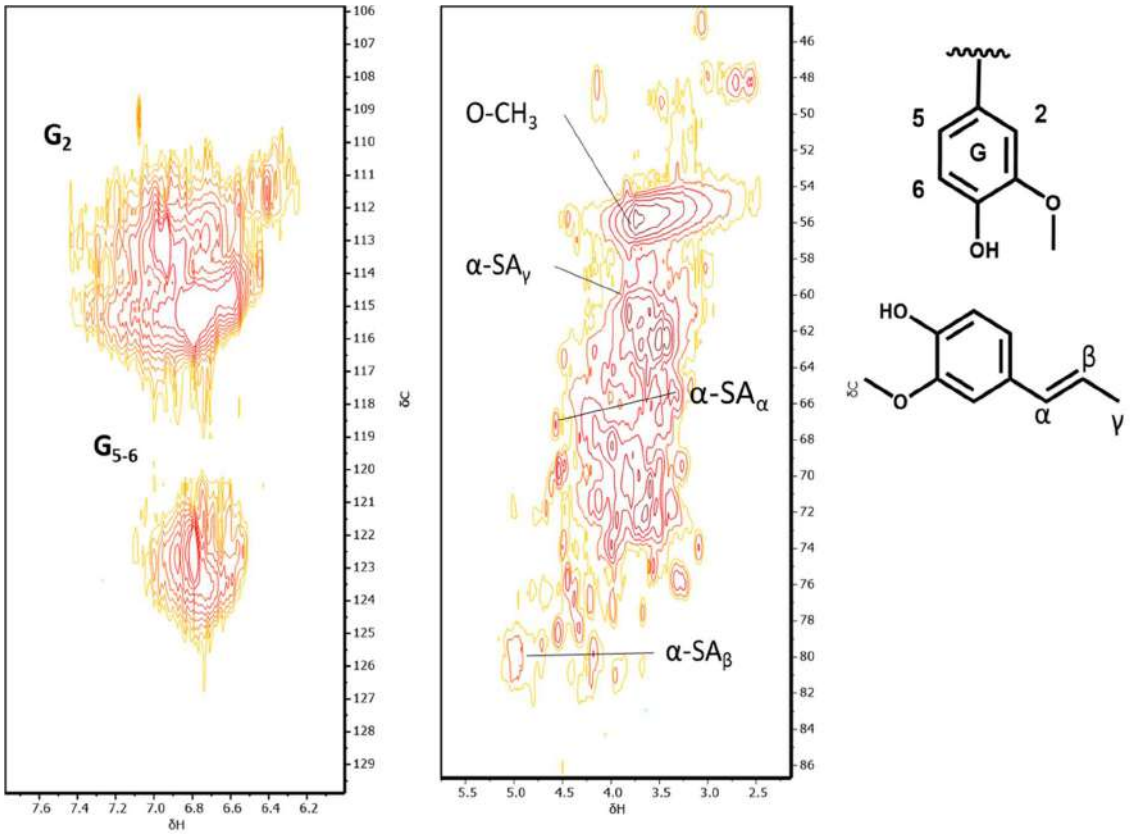

Figure C36. 2DHSQC NMR spectra of LS. Selected structural motif are highlighted: Guaiacyl units ($G_{2,5,6}$) and sulfo-groups (α-$S_{\beta\gamma}$).

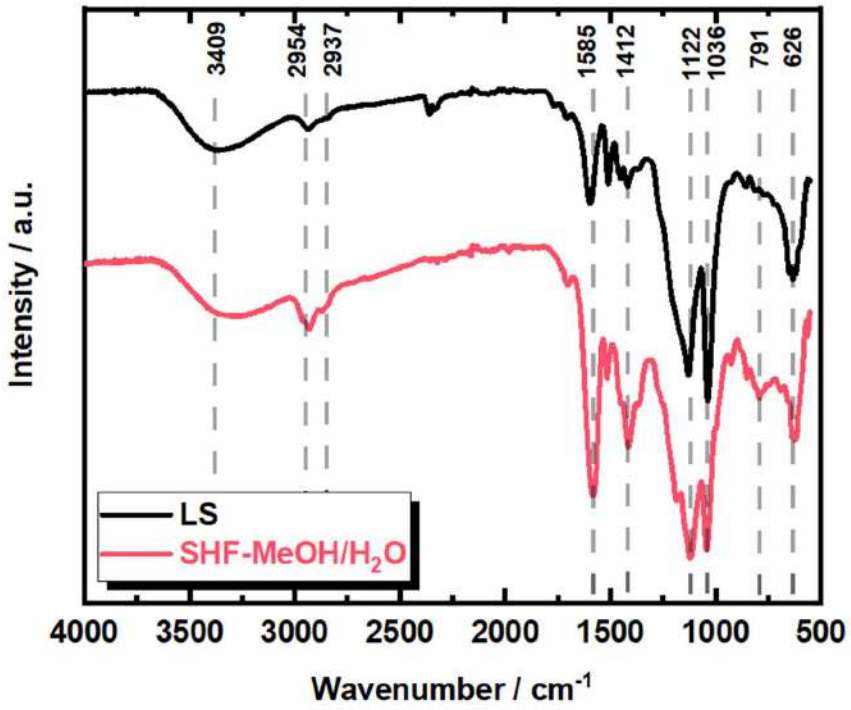

Figure C37. FTIR of sodium lignosulfonate (LS) and of the residual LS after **SHF-MeOH/H_2O** treatment. The highlighted peaks e assigned in **Table C4**.

Table C4 Main FTIR peak assignment from **Figure C37,** according to literature.

Wave number / cm^{-1}	functional group	reference
3450-3300	O-H stretching vibration	[328] [329] [330]
2934	C-H stretching CH_3 (and O-CH_3)	[328] [329]
2854	C-H stretching CH_2	[328] [329]
2359	CO_2 noise	n.a.
1713	C=O stretching vibration	[328]
1585	C=C stretching (aromatic) and C=O stretching	[329]
1390-1487	Aromatic ring breathing	[328] [329]
1150-1200	O=S=O symmetric stretching	[329] [330] [290]
1122	C-O alkoxy group vibration	[288]
1036	S=O stretching	[330] [288]
791	Aromatic C-H out of plane	[328] [329]
626	C=O ketone vibration breathing	[328]

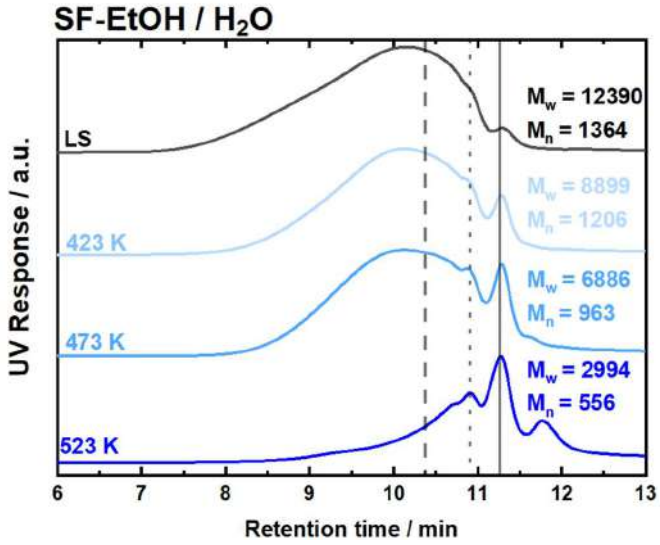

Figure C38. GPC chromatograms of the thermal fractionation (SF) of LS in EtOH/H_2O (1:1 wt.-% Ratio). Reaction conditions: c_{LS} = 1.0 wt.-%, T = 423 K, 473 K and 523 K, p = 7.0 MPa, Q_{educt} = 1.0 mL min^{-1},Q_{H_2} = 20 mL $min^{-1}$and $t_{residence}$ = 50 min. The straight line indicates the eluents buffer reference peak ($NaHPO_3$), dotted and dashed lines show the analytical standard peaks (sodium poly-(styrene sulfonate)) with Mw of 246 g mol^{-1} (RT = 10.9 min) and with M_w of 891 g mol^{-1} (RT= 10.4 min), respectively.

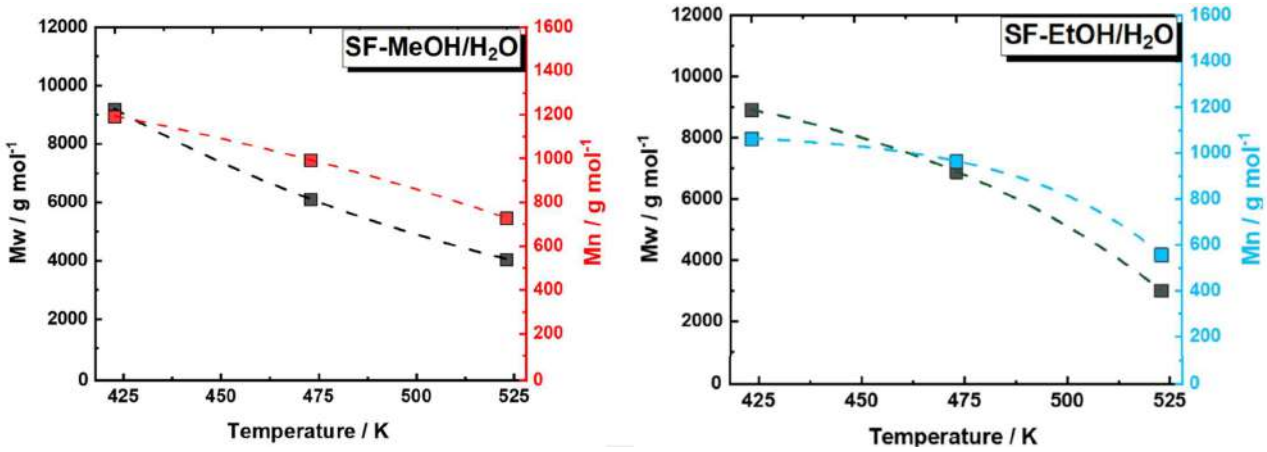

Figure C39. Mass-average (M_w) and number-average (M_n) molar mass for LS thermal fractionation (SF) with MeOH/H_2O (up) and EtOH/H_2O (down) as a function of reaction temperature. Reaction conditions: c_{LS} = 1.0 wt.-%, T = 423 K, 473 K and 523 K, p = 7.0 MPa, Q_{educt} = 1.0 mL min^{-1},Q_{H_2} = 20 mL min^{-1} and $t_{residence}$ = 50 min. The straight line indicates the eluents buffer reference peak ($NaHPO_3$), dotted and dashed lines show the analytical standard peak (sodium poly-(styrene sulfonate)) with Mw of 246 g mol^{-1} (RT = 10.9 min) and with M_w of 891 g mol^{-1} (RT= 10.4 min), respectively.

Table C5. Weight- (M_w) and number- (M_n) averaged molecular weight distribution and dispertity (Đ) values calculated from SEC in function of different solvents in SF and SHF experiments.

Sample	LS	SF-MeOH/H_2O			SF-EtOH/H_2O			SHF-MeOH/H_2O			SHF-EtOH/H_2O		
T / K	n.a.	423	473	523	423	473	523	423	473	523	423	473	523
M_w / g mol^{-1}	12390	9132	6093	3856	8899	6886	2994	10104	3106	433	8457	1556	502
M_n / g mol^{-1}	1364	1192	991	586	1206	963	556	993	589	360	968	583	485
Đ	9.1	7.7	6.1	6.5	7.4	7.1	5.3	10	5.3	1.2	8.7	2.7	1.1

n.a.: not applicable

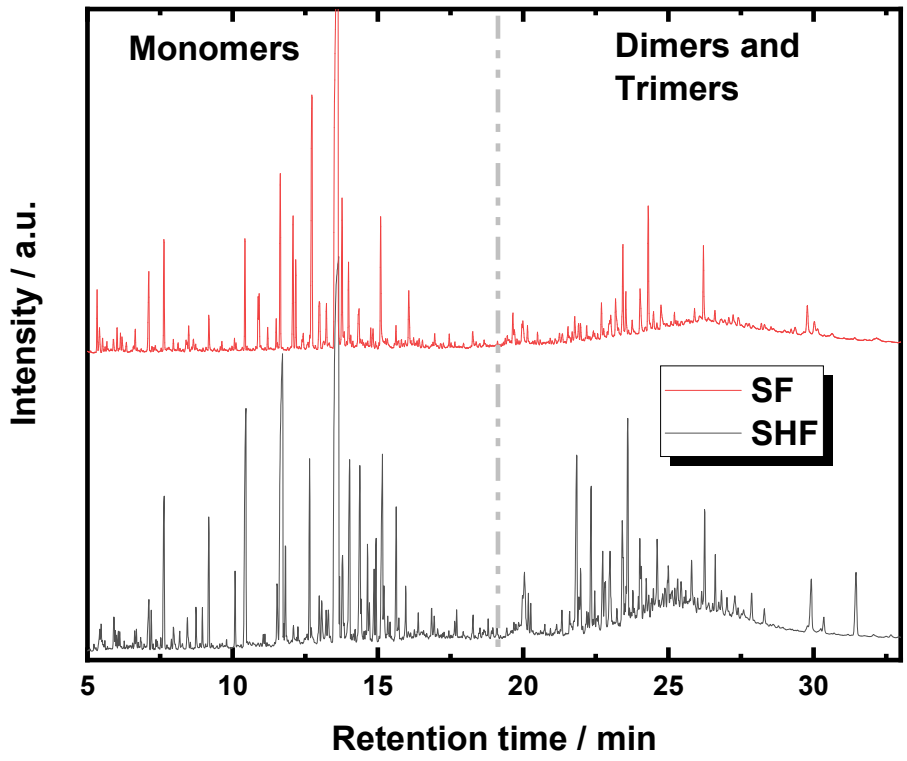

Figure C40. Chromatograms of solvothermal frgamentation (SF) of LS and solvothermal combined with catalytic hydrogenolyisi/hydrogenation (SHF) with MeOH/H_2O solvent mixture.Reaction conditions: c_{LS} = 1.0 wt.-%, T = 423 K, 473 K and 523 K, p = 7.0 MPa, Q_{educt} = 1.0 mL min^{-1},Q_{H_2} = 20 mL min^{-1}and $t_{residence}$ = 50 min. solvent system: MeOH/H_2O and EtOH/H_2O with weight ratio (1:1).m_{cat} = 10.0 g.

Table C6. identified compounds from GC-MS of the solvothermal fragmentation (SF) experiment with MeOH/H_2O.

RT / Min	Name	Structure
7.563	Guaiacol	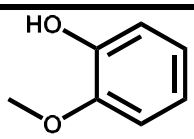
10.061	4-propylphenol	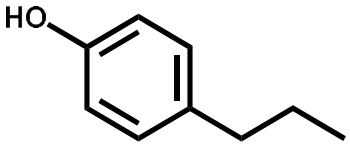
10.423	4-Ethyl guaiacol	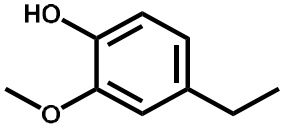
10.911	Ethanone,1-(2-hydroxy-5-ethylphenyl)-	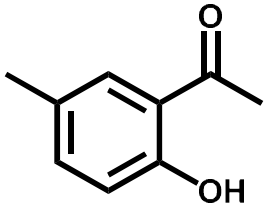
11.542	*p*-Cymene-2,5-diol	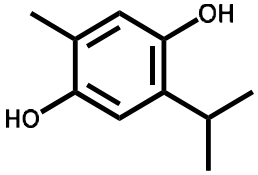
11.637	Phenol, 2-methoxy-4-propyl	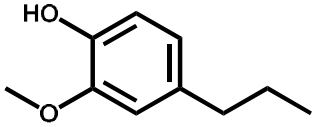
12.079	Vanillin	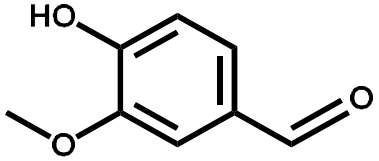
12.171	Isoeugenol	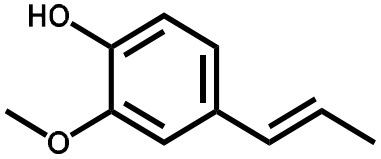
12.730	Eugenol	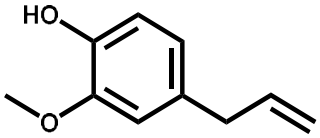
13.226	*t*-butylhydroquinone	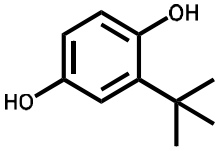

13.645	BHT – (MeTHF stabilizer)	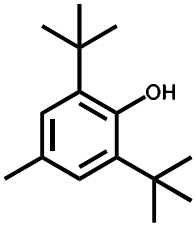
13.765	Homovanillyl alcohol	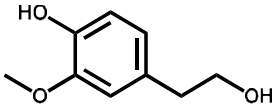
13.988	Benzene, 4 butyl-1,2-dimethoxy	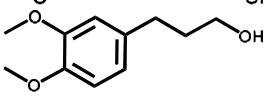
14.753	Butanone,4-(4-hydroxy-3-methoxyphenyl)-	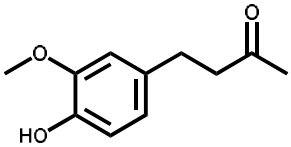
15.093	Di-hydroconyferyl alcohol	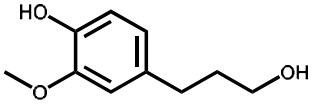
16.061	Benzeneacetic acid, 3,4 dimethoxy	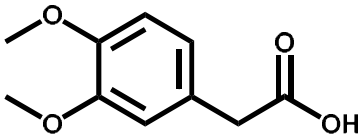

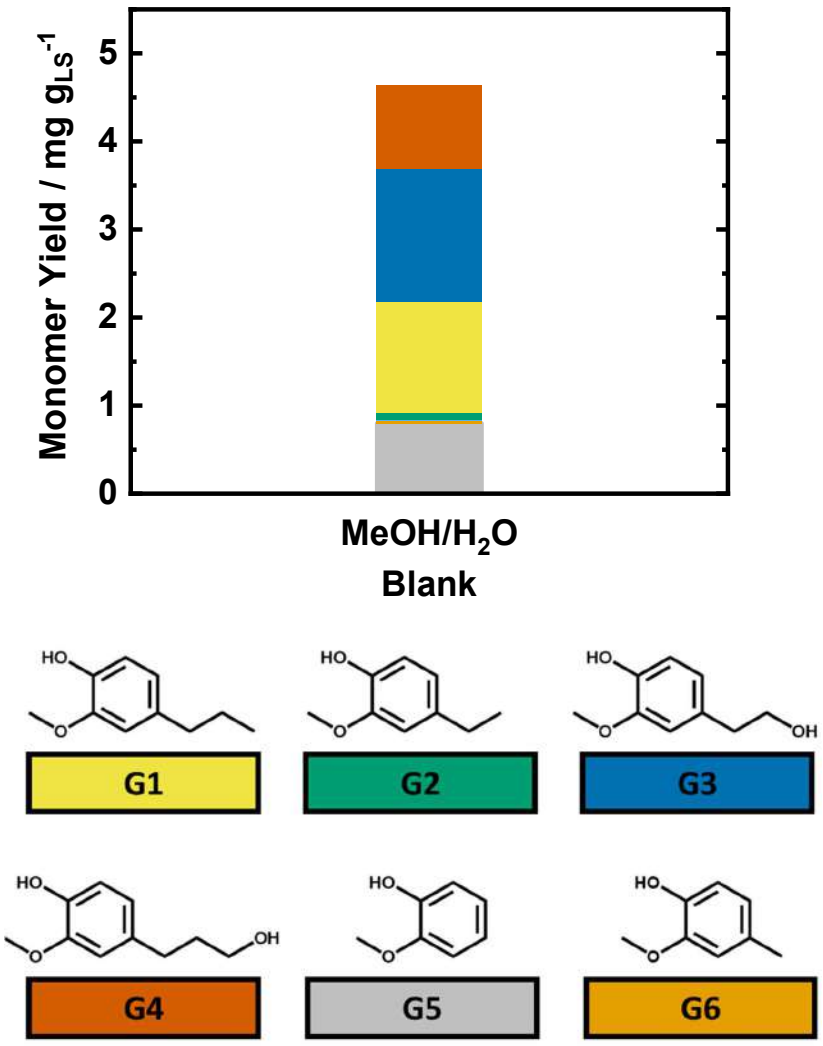

Figure C41. Monomer yield for the MeOH/H2O solvothermal fragmentation (SF) – (**up**) and identified monomers structure (**down**) Reaction conditions: c_{LS} = 1.0 wt.-%, T = 523 K, p = 7.0 MPa, Q_{educt} = 1.0 mL min^{-1},Q_{H_2} = 20 mL $min^{-1}$and $t_{residence}$ = 50 min. solvent system: MeOH/H_2O with weight ratio (1:1).m_{cat} = 10.0 g.

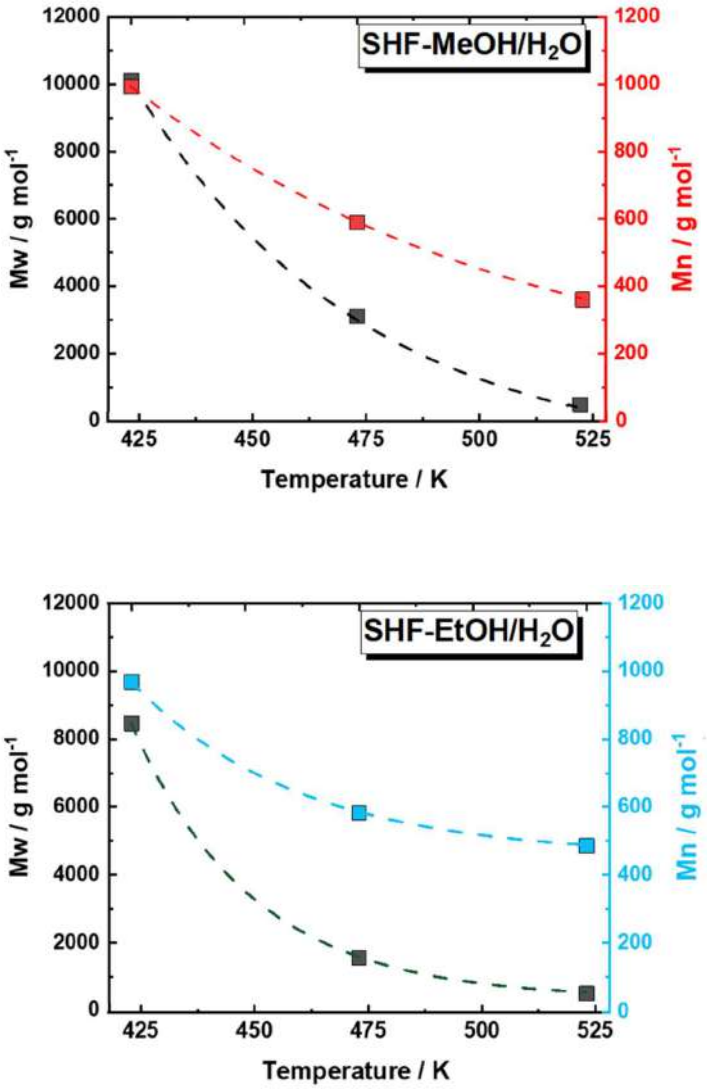

Figure C42. Mass-average (M_w) and number-average (M_n) molar mass fot SHF-MeOH (**up**) and SHF-EtOH/H_2O (**down**) as a function of reaction temperature. **Reaction conditions**: T = 423 K, 473 K, and 523 K, P = 7.0 MPa, Q_{educt} = 1.0 mL min^{-1},Q_{H2} = 20 mL min^{-1}, $t_{residence}$ = 50 min, m_{cat} = 10 g.

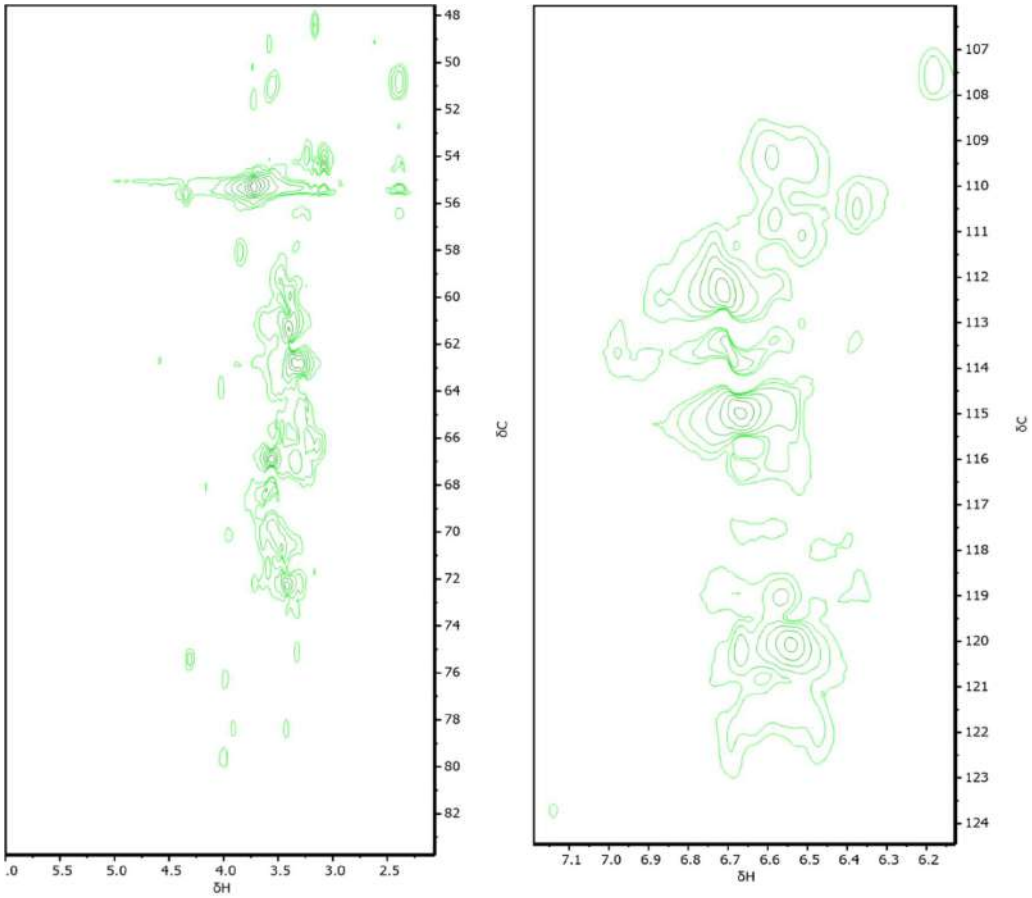

Figure C43. 2DHSQC NMR spectra of SHF-MeOH/H_2O. **Reaction conditions**: c_{LS} = 1.0 wt.-%, T = 523 K, p = 7.0 MPa, Q_{educt} = 1.0 mL min^{-1},Q_{H_2} = 20 mL $min^{-1}$and $t_{residence}$ = 50 min. solvent system: MeOH/H_2O and EtOH/H_2O with weight ratio (1:1).m_{cat} = 10.0 g.

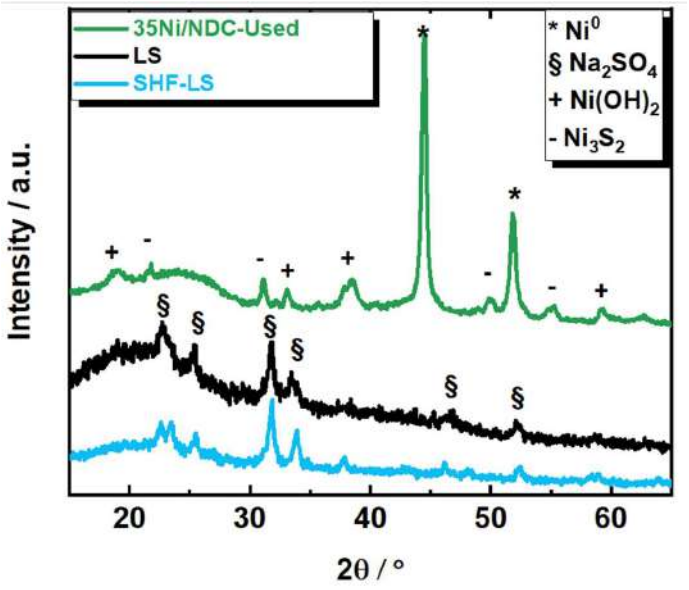

Figure C44. Mass-average (M_w) and number-average (M_n) molar mass fot SHF-MeOH/H_2O as a function of reaction temperature. Reaction conditions: T = 523 K, P = 7.0 MPa, Q_{educt} = 1.0 mL min^{-1},Q_{H2} = 20 mL min^{-1}, $t_{residence}$ = 50 min, m_{cat} = 10 g.

Table C7. Identified compounds from GC-MS of SHF experiment with MeOH/H_2O.

RT / Min	Name	Structure
7.563	Guaiacol	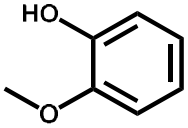
8.742	Phenol 2-ethyl	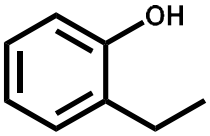
8.961	Ethyl *p*-hydroxybenzoate	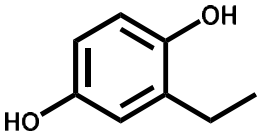
9.180	Creosol	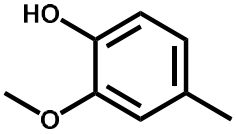
10.061	4-Propylphenol	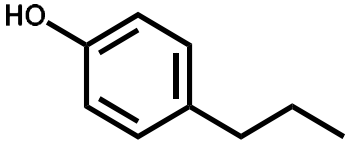
10.423	4-Ethyl guaiacol	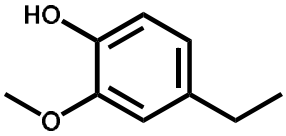
11.542	p-Cymene-2,5-diol	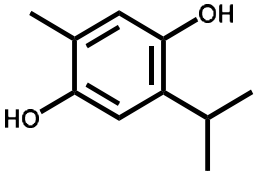
11.726	Propyl Guaiacol	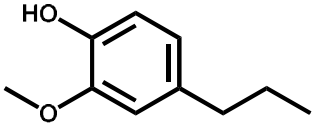
12.079	Vanillin	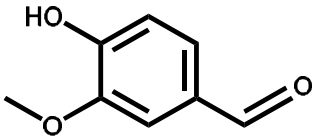
12.171	Isoeugenol	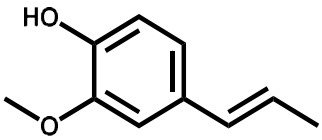
12.730	Eugenol	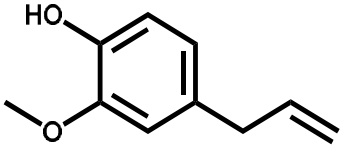

13.306	t-Butylhydroquinone	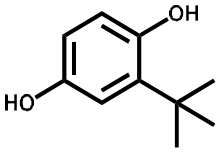
13.645	BHT – MeTHF stabilizer	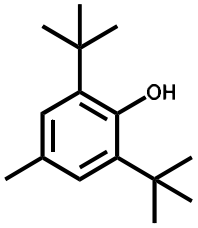
13.765	Homovanillyl alcohol	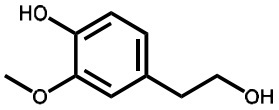
13.988	Benzene, 4 butyl-1,2-dimethoxy	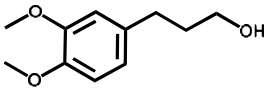
14.389	3,4-Dimethoxyphenyl alcohol	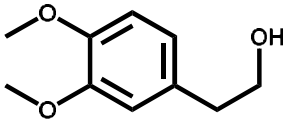
14.753	Butanone,4-(4-hydroxy-3-ethoxyphenyl)-	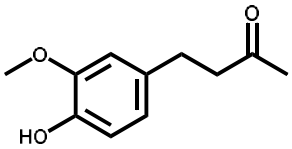
15.093	Dihydroconyferyl alcohol	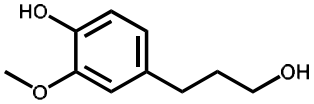
16.061	Benzeneacetic acid, 3,4 dimethoxy	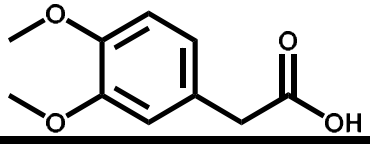

Table C8. Quantified compound, via GC-FID of the SHF- LS fragmentation experiments.

GC-MS RT/ Min	GC-FID RT/ Min	structure	Name	abbreviation
11.653	17.70	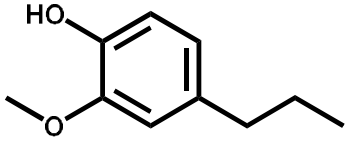	Propyl guaiacol	**G1**
10.428	13.548	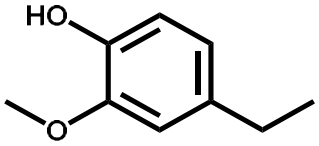	Ethyl guaiacol	**G2**
13.735	16.802	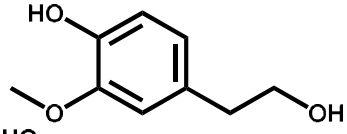	Homovanillic alcohol	**G3**
15.098	18.137	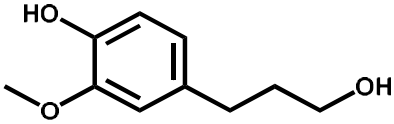	Dihydroconiferyl alcohol	**G4**
7.632	10.810	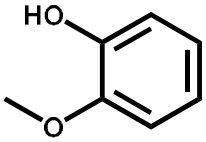	Guaiacol	**G5**
9.158	12.330	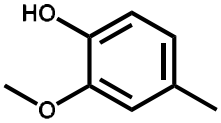	Creosol	**G6**
10.058	13.134	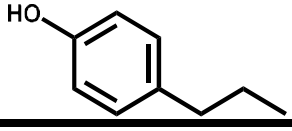	4- Propyl phenol	**H1**

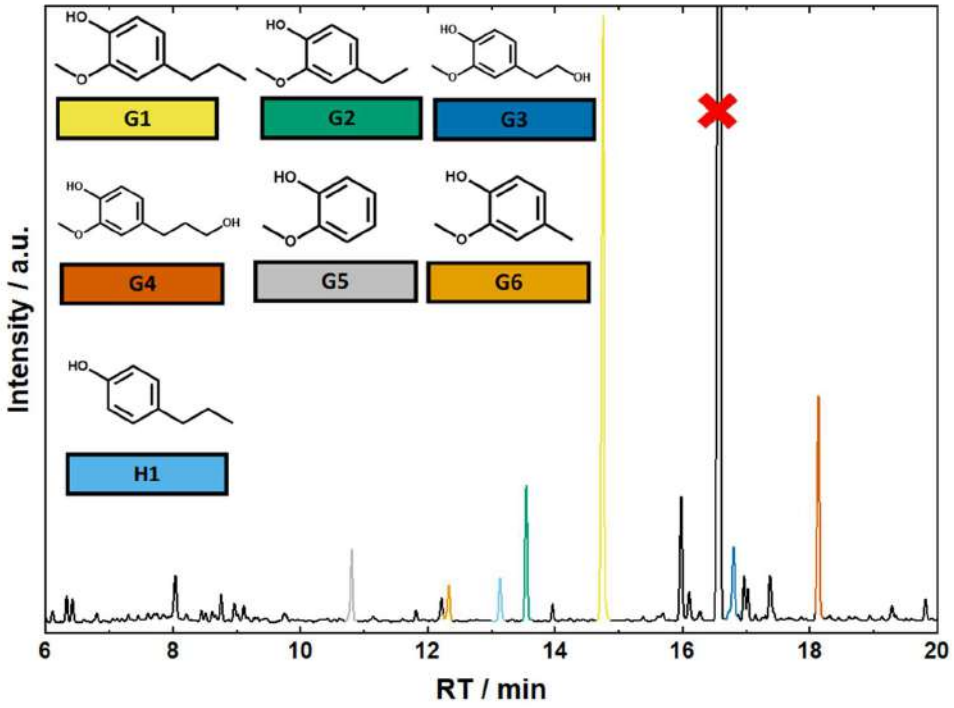

Figure C45. GC-FID Chromatogram of the MeTHF fraction extracted from the SHF of LS using MeOH/H_2O solvent mixture at 523 K. The red cross of the peak at 16.8 corresponds to the BHT stabilizer of MeTHF. Reaction conditions: c_{LS} = 1.0 wt.-%, T = 523 K, p = 7.0 MPa, Q_{educt} = 1.0 mL min^{-1},Q_{H_2} = 20 mL $min^{-1}$and $t_{residence}$ = 50 min. solvent system: MeOH/H_2O with weight ratio (1:1).m_{cat} = 10.0 g.

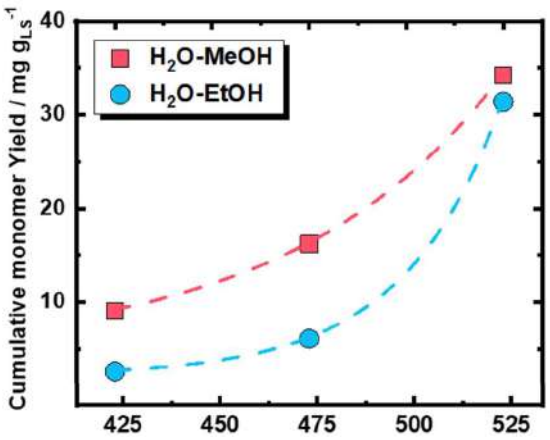

Figure C46. Cumulative monomer yield for the SHF-MeOH/H_2O and SHF-EtOH/H_2O as function of temperature Reaction conditions: c_{LS} = 1.0 wt.-%, T = 423 K, 473 K and 523 K , p = 7.0 MPa, Q_{educt} = 1.0 mL min^{-1},Q_{H_2} = 20 mL $min^{-1}$and $t_{residence}$ = 50 min. solvent system: MeOH/H_2O and EtOH/H_2O with weight ratio (1:1).m_{cat} = 10.0 g.

Table C9. Weight- (M_w) and number- (M_n) averaged molecular weight distribution and dispesity (Đ) values calculated from SEC. The reaction conditions are reported in **Figure 5.6** of **Chapter 5**

Sample	LS	SHF-MeOH/H_2O	Flow 2.5 wt.-%	Two Reactors	Batch 3h	Batch 1h
M_w / g mol^{-1}	12390	433	430	393	684	491
M_n / g mol^{-1}	1364	360	391	337	6942	1615
Đ	9.1	1.2	1.1	1.1	10	3.3

Supporting information Chapter 5.3

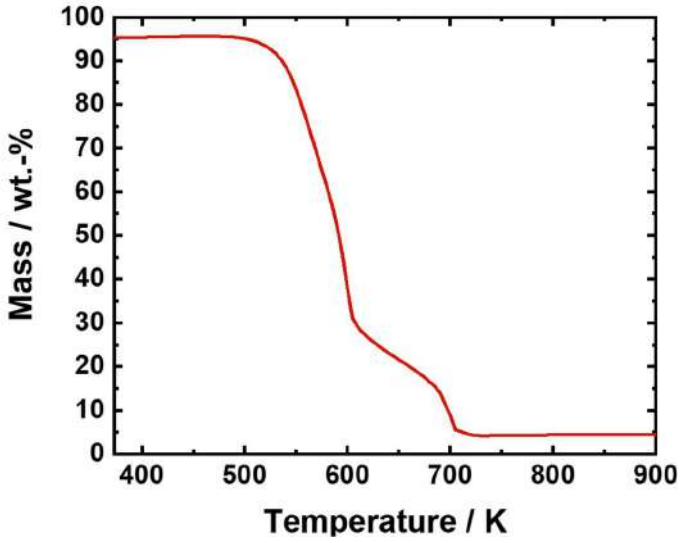

Figure C47. TGA in synthetic air of BWS.

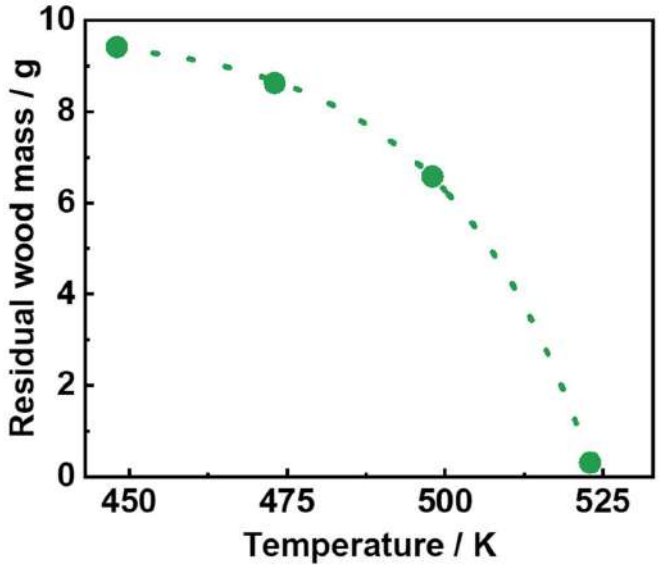

Figure C48. Residual BWS mass as function of temperature in SF process using MeTHF as solvent. . **Reaction conditions**: $M_{35Ni/NDC}$ = 10 g, m_{BWS} = 10 g, $T_{extraction}$= 448, 473 K, 498 K, 523 K, p= 7.0 MPa, Q_{educt} = 1.0 mL min^{-1}, $t_{residence}$ = 50 min.

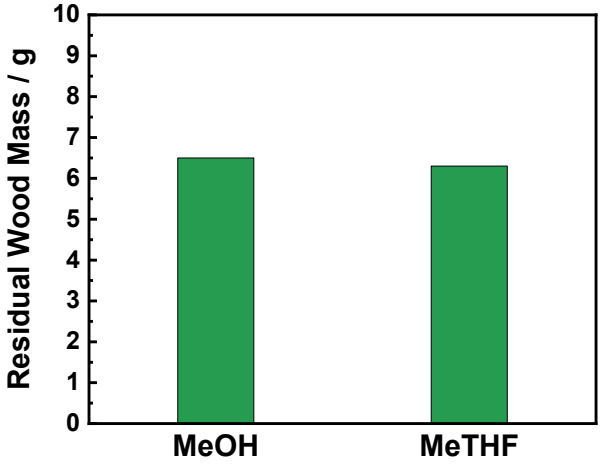

Figure C49. Residual Wood Mass after SF experiment MeOH and MeTHF as solvents; **Reaction conditions**: m_{BWS} = 10 g, $T_{extraction}$= 498 K, p= 7.0 MPa, Q_{educt} = 1.0 mL min^{-1}, $t_{residence}$ = 50 min.

Table C10: Mass- (M_w) and number-(M_n) molecular weight distribution, and the dispersity (Đ) calculated from SEC

	Mw/ g mol^{-1}	M_n/ g mol^{-1}	Đ
MeTHF	1160	896	1.3
MeOH	1239	903	1.3

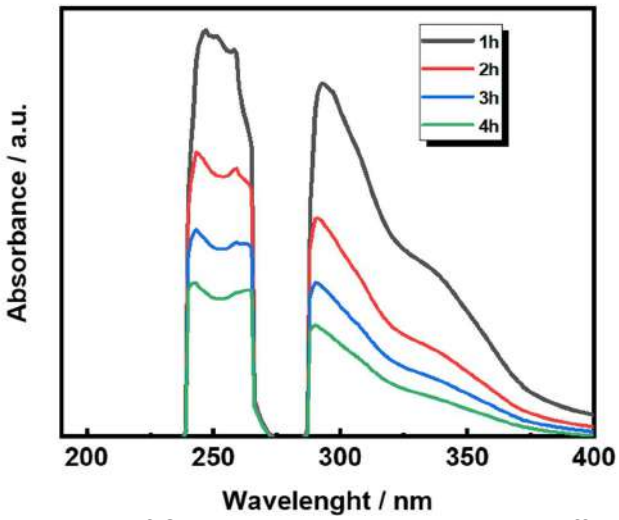

Figure C50. UV-Vis spectra of SF using MeTHF as solvent at different times. **Reaction conditions**: m_{BWS} = 10 g, $T_{extraction}$= 498 K, p= 7.0 MPa, Q_{educt} = 1.0 mL min^{-1}, $t_{residence}$= 50 min. **Caution:** Due to the presence of BHT (UV inhibitor), which strongly adsorb UV in the MeTHF in both the reference cell and in the measuring cell, the absorbance presented negative peaks at 280 nm and 220 nm.

Table C11: Retention time and structure of the quantified compound with GC-FID

RT –GC FID / Min	Name	Structure	Symbol
10.6	Guaiacol	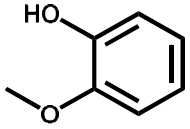	**G5**
12.1	Creosol	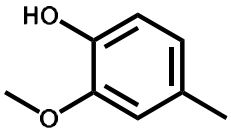	**G6**
13.4	4-Ethyl guaicaol	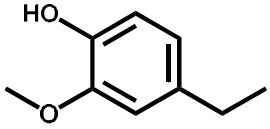	**G2**
14.5	4-propyl guaiacol	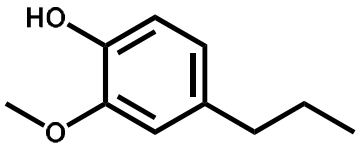	**G1**
16.6	Homovanyllic alcohol	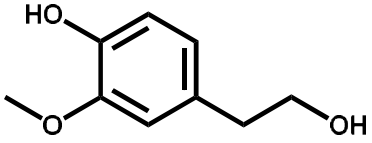	**G3**
18.0	Dihydro-coniferyl alcohl	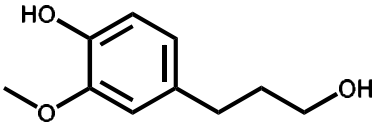	**G4**
15.6	Isoeugenol	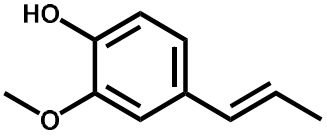	**G7**
14.4	Syringol	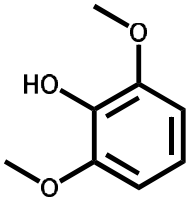	**S1**
15.5	4-Methyl syringol	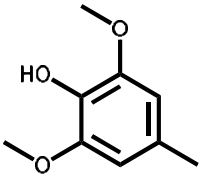	**S2**

16.5	4-Ethyl syringol	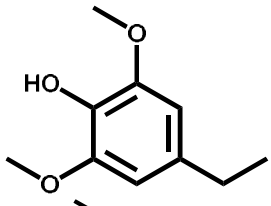	**S3**
17.5	4-Propyl syringol	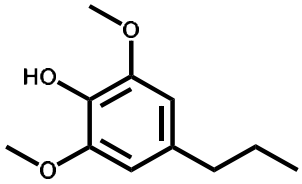	**S4**
19.4	Syringyl ethyl alcohol	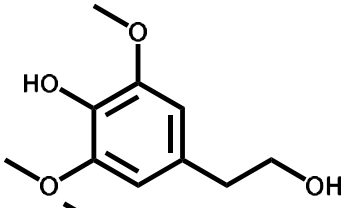	**S5**
20.5	Dihydro sinapyl alcohl	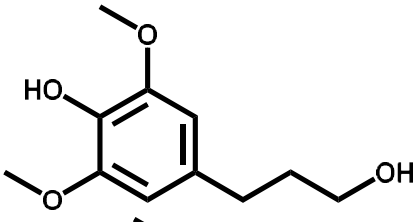	**S6**
18.3	Allyl syringol	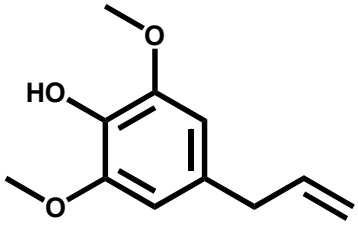	**S7**
18.5	Isoallyl syringol	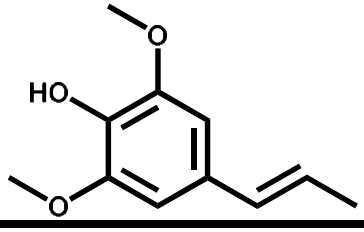	**S8**

Table C12. Monomer yield of the identified compounds using MeTHF as solvent at different time on stream (TOS) and of the total after 10 h. **Reaction conditions:** $m_{35Ni/NDC}$ = 10 g, m_{BWS} = 10 g, $T_{extraction}$= 498 K $T_{reduction}$ = 498 K, p= 7.0 MPa, Q_{educt} = 1.0 mL min^{-1}, Q_{H2} = 48 mL min^{-1}, $t_{residence1}$= $t_{residence2}$ = 50 min, TOS= 10 h.

S8/ mg g $_{KL}^{-1}$	S7/ mg g $_{KL}^{-1}$	S6/ mg g $_{KL}^{-1}$	S5/ mg g $_{KL}^{-1}$	S4/ mg g $_{KL}^{-1}$	S3/ mg g $_{KL}^{-1}$	S2/ mg g $_{KL}^{-1}$	S1/ mg g $_{KL}^{-1}$	G7/ mg g $_{KL}^{-1}$	G4/ mg g $_{KL}^{-1}$	G3/ mg g $_{KL}^{-1}$	G1/ mg g $_{KL}^{-1}$	G2/ mg g $_{KL}^{-1}$	G6/ mg g $_{KL}^{-1}$	G5/ mg g $_{KL}^{-1}$	**MeTHF TOS/ h**
0.16	0.20	0.95	/	5.12	0.81	0.20	0.21	0.12	0.30	0.05	2.28	0.04	0.45	0.18	**1**
0.13	0.18	1.02	/	4.47	0.85	0.18	0.22	0.11	0.35	0.02	1.31	0.02	0.43	0.07	**2**
/	0.16	0.91	/	3.02	0.77	0.13	0.22	0.10	0.22	0.10	0.72	0.07	0.39	0.06	**3**
/	0.15	0.59	/	1.94	0.66	0.09	0.21	/	0.17	/	0.47	/	0.37	0.05	**4**
/	0.14	0.29	/	0.87	0.46	0.05	0.18	/	0.14	/	0.13	/	0.37	/	**8**
/	0.14	0.27	/	0.80	0.47	0.06	0.19	/	0.13	/	0.28	/	0.37	/	**10**
1.50	2.62	12.3	0.26	32.7	12.7	2.52	3.47	1.58	3.92	0.19	15.6	1.82	6.23	0.94	**total**

Table C13. Monomer yield of the identified compounds using MeOH as solvent at different time on stream (TOS) and of the total after 10 h. Reaction conditions: $m_{35Ni/NDC}$ = 10 g, m_{BWS} = 10 g, $T_{extraction}$= 498 K $T_{reduction}$ = 498 K, p= 7.0 MPa, Q_{educt} = 1.0 mL min^{-1}, Q_{H2} = 48 mL min^{-1}, $t_{residence1}$= $t_{residence2}$ = 50 min, TOS= 10 h.

S8/ mg g $_{KL}^{-1}$	S7/ mg g $_{KL}^{-1}$	S6/ mg g $_{KL}^{-1}$	S5/ mg g $_{KL}^{-1}$	S4/ mg g $_{KL}^{-1}$	S3/ mg g $_{KL}^{-1}$	S2/ mg g $_{KL}^{-1}$	S1/ mg g $_{KL}^{-1}$	G7/ mg g $_{KL}^{-1}$	G4/ mg g $_{KL}^{-1}$	G3/ mg g $_{KL}^{-1}$	G1/ mg g $_{KL}^{-1}$	G2/ mg g $_{KL}^{-1}$	G6/ mg g $_{KL}^{-1}$	G5/ mg g $_{KL}^{-1}$	**MeOH TOS/ h**
0.18	0.32	1.86	0.028	12.2	0.84	0.44	0.34	0.11	0.64	0.013	4.12	0.22	0.60	0.19	**1**
/	0.29	1.80	0.014	7.30	0.79	0.30	0.39	0.09	0.49	/	2.07	0.13	0.51	0.19	**2**
/	0.21	1.34	/	3.16	0.53	0.15	0.27	0.10	0.33	/	0.88	0.02	0.44	0.13	**3**
/	0.17	0.85	/	1.80	0.42	0.10	0.23	0.10	0.24	/	0.55	/	0.41	0.09	**4**
/	0.15	0.53	/	1.14	0.34	0.07	0.21	0.10	0.19	/	0.42	/	0.42	0.07	**8**
/	0.14	0.38	/	0.64	0.31	0.05	0.19	0.10	0.16	/	0.32	/	0.39	0.06	**10**
1.71	3.55	22.0	0.63	91.2	10.1	4.00	4.55	1.67	6.23	0.05	29.7	2.37	5.99	2.18	**total**

Table C14. Monomer yield of the identified compounds using MeOH as solvent at different time on stream (TOS) and of the total after 10 h. **Reaction conditions:** $m_{35Ni/NDC}$ = 10 g, m_{BWS} = 10 g, $T_{extraction}$= 508 K $T_{reduction}$ = 498 K, p= 7.0 MPa, Q_{educt} = 1.0 mL min^{-1}, Q_{H2} = 48 mL min^{-1}, $t_{residence1}$= $t_{residence2}$ = 50 min, TOS= 10 h.

S8/ mg g $_{KL}^{-1}$	S7/ mg g $_{KL}^{-1}$	S6/ mg g $_{KL}^{-1}$	S5/ mg g $_{KL}^{-1}$	S4/ mg g $_{KL}^{-1}$	S3/ mg g $_{KL}^{-1}$	S2/ mg g $_{KL}^{-1}$	S1/ mg g $_{KL}^{-1}$	G7/ mg g $_{KL}^{-1}$	G4/ mg g $_{KL}^{-1}$	G3/ mg g $_{KL}^{-1}$	G1/ mg g $_{KL}^{-1}$	G2/ mg g $_{KL}^{-1}$	G6/ mg g $_{KL}^{-1}$	G5/ mg g $_{KL}^{-1}$	**MeOH TOS/ h**
0.34	0.29	5.31	0.04	18.5	1.22	0.49	0.52	0.13	1.59	0.01	4.70	0.27	0.48	0.21	**1**
0.15	0.30	3.37	0.04	9.40	1.23	0.39	0.58	0.10	0.81	/	2.32	0.27	0.58	0.12	**2**
0.14	0.23	2.18	0.03	4.25	0.76	0.22	0.45	/	0.48	/	1.01	0.09	0.51	0.09	**3**
0.13	0.18	1.13	0.02	2.38	0.57	0.14	0.31	/	0.31	/	0.64	/	0.50	0.07	**4**
/	0.15	0.50	0.01	1.23	0.42	0.09	0.25	/	0.19	/	0.39	/	0.43	/	**8**
/	0.14	0.34	/	0.72	0.32	0.055	0.21	/	0.15	/	0.26	/	0.40	/	**10**
2.87	1.82	23.5	1.13	81.4	9.95	3.66	4.45	0.64	7.45	0.07	26.3	2.78	3.20	1.00	**total**

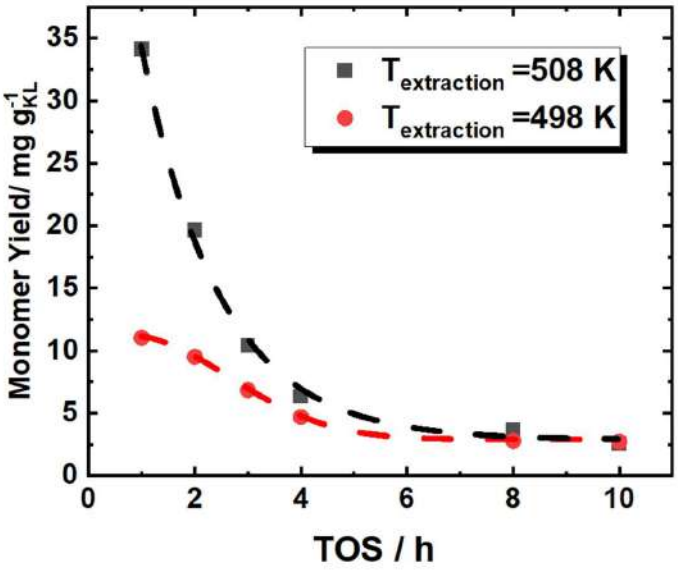

Figure C51. Cumulative monomer yield as a funtion of time on stream at different T of extraction using MeOH as solvent. **Reaction conditions**: $m_{35Ni/NDC}$ = 10 g, m_{BWS} = 10 g, $T_{extraction}$= 498 K and 508 K $T_{reduction}$ = 498 K, p= 7.0 MPa, Q_{educt} = 1.0 mL min^{-1}, Q_{H2} = 48 mL min^{-1}, $t_{residence1}$= $t_{residence2}$ = 50 min.

List of publications

Publications

- **F. Brandi**, M. Bäumel, V. Molinari, I. Shekova, I. Lauermann, T. Heil, M. Antonietti, M. Al-Naji, Nickel on nitrogen-doped carbon pellets for continuous-flow hydrogenation of biomass-derived compounds in water, *Green Chem*. **2020**, 22,9, 2755-2766
- J.A. Mendoza Mesa, **F. Brandi**, I. Shekova, M. Antonietti, M. Al-Naji p-Xylene from 2,5-dimethylfuran and acrylic acid using zeolite in continuous flow system, *Green Chem*. **2020**.
- **F. Brandi**, M. Bäumel, I. Shekova, V. Molinari, M. Al-Naji, 5-Hydroxymethylfurfural Hydrodeoxygenation to 2,5-Dimethylfuran in Continuous-Flow System over Ni on Nitrogen-Doped Carbon, *Sustain. Chem.*, **2020**, 1,2, 106-115
- **F. Brandi**, I. Khalil, M. Antonietti, M. Al-Naji, Continuous-Flow Production of Isosorbide from Aqueous-Cellulosic Derivable Feed over Sustainable Heterogeneous Catalysts, *Acs Sustain. Chem. Eng.*, **2021**, 9,2,927-935.
- **F. Brandi**, M. Antonietti, M. Al-Naji, Mechanistic insights to control sodium lignosulfonate depolymerization in continuous flow reactor: from solvothermal fragmentation to catalytic hydrogenolysis/hydrogenation and monomer protection, *Submitted*.
- C.A. Smith, **F.Brandi,** M. Al-Naji, R. Gutterman, Resin-supported iridium complex for low-temperature vanillin hydrogenation using formic acid in water, RCS Adv., *Just accepted.*

Conference Presentations

- **F. Brandi**, M. Bäumel, V. Molinari, I. Shekova, M. Antonietti, M. Al-Naji, Synthesis of an Innovative Ni Catalyst Supported on Higly Porous Carbon for the Continuous Flow5-Hydroxymethylfurfural conversion Toward 2,5-Dimethylfuran. Poster presentation delivered at the 2019 International Symposium of Green Chemistry, La Rochelle, France, April 2019.

References

[1] H.J. Schellnhuber, S. Rahmstorf, R. Winkelmann, Why the right climate target was agreed in Paris, *Nat Clim Change*. **2016**, 6,7, 649.

[2] J.M. Tour, C. Kittrell, V.L. Colvin, Green carbon as a bridge to renewable energy, *Nat. Mater.*, **2010**, 9,11, 871-874.

[3] S. Pacala, R. Socolow, Stabilization wedges: solving the climate problem for the next 50 years with current technologies, *Science*. **2004**, 305,5686, 968-972.

[4] D.M. Alonso, J.Q. Bond, J.A. Dumesic, Catalytic conversion of biomass to biofuels, *Green Chem.*, **2010**, 12,9, 1493-1513.

[5] P.T. Anastas, J.C. Warner, Green Chemistry: Theory and Practice, Oxford University Press, New York, **1998**. pag. 30. .

[6] F. Gomollon-Bel, Ten Chemical Innovations That Will Change Our World IUPAC identifies emerging technologies in Chemistry with potential to make our planet more sustainable, *Chem. Int.*, **2019**, 41,12-17.

[7] A.J. Ragauskas, C.K. Williams, B.H. Davison, G. Britovsek, J. Cairney, C.A. Eckert, W.J.J. Friedrick, J.P. Hallet, D.J. Leak, C.L. Liotta, J.R. Mielenz, R. Murphy, R. Templer, T.J. Tschaplinski, The path froward for biofuels and biomaterials, *Science*. **2006**, 311,7.

[8] F.H. Isikgor, C.R. Becer, Lignocellulosic biomass: a sustainable platform for the production of bio-based chemicals and polymers, *Polym. Chem.*, **2015**, 6,25, 4497-4559.

[9] A. Corma, S. Iborra, A. Velty, Chemical routes for the transformation of biomass into chemicals, *Chem. Rev.*, **2007**, 107,6, 2411-2502.

[10] F. Yang, M. Antonietti, Artificial Humic Acids: Sustainable Materials against Climate Change, *Adv. Sci.* . **2020**, 7,5, 1902992.

[11] L. Qin, W.C. Li, J.Q. Zhu, B.Z. Li, Y.J. Yuan, Hydrolysis of Lignocellulosic Biomass to Sugars, in: Z. Fang, R.L.J. Smith, X. Qi (Eds.) Production of Platform Chemicals from Suistainable Resources, Springer Nature, Singapore, **2017**.

[12] G.W. Huber, S. Iborra, A. Corma, Synthesis of Transportation Fuels from Biomass: Chemistry, Catalysts, and Engineering, *Chem. Rev.*, **2006**, 106,9, 4044-4098.

[13] J.S. Luterbacher, D.M. Alonso, J.A. Dumesic, Targeted chemical upgrading of lignocellulosic biomass to platform molecules, *Green Chem.*, **2014**, 16,12, 4816-4838.

[14] D. Esposito, M. Antonietti, Redefining biorefinery: the search for unconventional building blocks for materials, *Chem. Soc. Rev.*, **2015**, 44,16, 5821-5835.

[15] R. Rinaldi, F. Schüth, Design of solid catalysts for the conversion of biomass, *Energy Environ. Sci.*, **2009**, 2,6.

[16] S. Van den Bosch, S.F. Koelewijn, T. Renders, G. Van den Bossche, T. Vangeel, W. Schutyser, B. Sels, Catalytic Strategies Towards Lignin-Derived Chemicals, in: L. Serrano, R. Luque, B. Sels (Eds.) Lignin Chemistry, Springer Nature Switzerland, Cham, **2020**, pp. 129-168.
[17] J.L. Wertz, M. Deleu, S. Coppee, A. Richel, Hemicellulose and Lignin in Biorefineries, CRC Press Taylor & Francis Group LLC, New York, **2018,** Chapter 1: Introduction. pag. 1-20.
[18] D. Klemm, B. Heublein, H.P. Fink, A. Bohn, Cellulose: fascinating biopolymer and sustainable raw material, *Angew. Chem. Int. Ed.* **2005**, 44,22, 3358-3393.
[19] L. Taiz, E. Zeiger, I.M. Moller, A. Murphy, Plant Physiology and Development 6th Edition, Oxford University Press Inc., United States (US), **2018**. pag.
[20] Z. Sun, B. Fridrich, A. de Santi, S. Elangovan, K. Barta, Bright Side of Lignin Depolymerization: Toward New Platform Chemicals, *Chem. Rev.*. **2018**, 118,2, 614-678.
[21] S. Van den Bosch, S.F. Koelewijn, T. Renders, G. Van den Bossche, T. Vangeel, W. Schutyser, B.F. Sels, Catalytic Strategies Towards Lignin-Derived Chemicals, Topics Curr Chem **2018**.
[22] J. Zakzeski, P.C. Bruijnincx, A.L. Jongerius, B.M. Weckhuysen, The Catalytic Valorization of Lignin for the Production of Renewable Chemicals, *Chem. Rev.*, **2010**, 110,6, 3552-3599.
[23] R. Rinaldi, R. Jastrzebski, M.T. Clough, J. Ralph, M. Kennema, P.C.A. Bruijnincx, B.M. Weckhuysen, Paving the Way for Lignin Valorisation: Recent Advances in Bioengineering, Biorefining and Catalysis, *Angew. Chem. Int. Ed.*, **2016**, 55,29, 8164-8215.
[24] G. Brunow, K. Lundquist, Functional Groups and Bonding Patterns in Lignin (Includinc the Lignin-Carbohydrates Complexes), Lignin and Lignans: Advances in Chemistry, CRC Press, Taylor & Francis Group **2010**, pp. 267-299.
[25] S. Constant, H.L.J. Wienk, A.E. Frissen, P.d. Peinder, R. Boelens, D.S. van Es, R.J.H. Grisel, B.M. Weckhuysen, W.J.J. Huijgen, R.J.A. Gosselink, P.C.A. Bruijnincx, New insights into the structure and composition of technical lignins: a comparative characterisation study, *Green Chem.*, **2016**, 18,9, 2651-2665.
[26] M. Graglia, N. Kanna, D. Esposito, Lignin Refinery: Towards the Preparation of Renewable Aromatic Building Blocks, *ChemBioEng Rev.*, **2015**, 2,6, 377-392.
[27] K.E. Achyuthan, A.M. Achyuthan, P.D. Adams, S.M. Dirk, J.C. Harper, B.A. Simmons, A.K. Singh, Supramolecular self-assembled chaos: polyphenolic lignin's barrier to cost-effective lignocellulosic biofuels, *Molecules*. **2010**, 15,12, 8641-8688.
[28] W. Schutyser, T. Renders, S. Van den Bosch, S.F. Koelewijn, G.T. Beckham, B.F. Sels, Chemicals from lignin: an interplay of lignocellulose fractionation, depolymerisation, and upgrading, *Chem. Soc. Rev.*, **2018**, 47,3, 852-908.
[29] C. Li, X. Zhao, A. Wang, G.W. Huber, T. Zhang, Catalytic Transformation of Lignin for the Production of Chemicals and Fuels, *Chem Rev*. **2015**, 115,21, 11559-11624.

[30] C. Xu, R.A. Arancon, J. Labidi, R. Luque, Lignin depolymerisation strategies: towards valuable chemicals and fuels, *Chem. Soc. Rev.*, **2014**, 43,22, 7485-7500.
[31] B. Kamm, P.R. Gruber, M. Kamm, Biorefineries-Industrial Processes and Products, Ullmann's Encyclopedia of Industrial Chemistry, Wiley - VCH Verlag GmbH & Co KGaA, Weinheim, **2016**.
[32] J. Sadhukhan, K.S. Ng, E.H. Martinez, Biorefineries and Chemical Processes, John Wiley & Sons, Ltd **2014**. pag. 1-39.
[33] M. Dusselier, M. Mascal, B. Sels, Top Chemical Opportunities from Carbohydrate Biomass: A Chemist's View of the Biorefinery in: K.M. Nicholas (Ed.) Selective Catalysis for Renewable Feedstocks and Chemicals, Springer International Publishing **2014**, pp. 85-125.
[34] F. Cherubini, The biorefinery concept: Using biomass instead of oil for producing energy and chemicals, *Energy Convers. Manag*. **2010**, 51,7, 1412-1421.
[35] S.K. Maity, Opportunities, recent trends and challenges of integrated biorefinery: Part I, *Renew. Sustain. Energy Rev*. **2015**, 43,1427-1445.
[36] R.A. Sheldon, Metrics of Green Chemistry and Sustainability: Past, Present, and Future, *ACS Sustain. Chem. Eng.*, **2017**, 6,1, 32-48.
[37] R.A. Sheldon, Green chemistry and resource efficiency: towards a green economy, *Green Chem*. **2016**, 18,11, 3180-3183.
[38] R.A. Sheldon, Biocatalysis and biomass conversion: enabling a circular economy, *Philos. Trans. A Math. Phys. Eng. Sci.*, **2020**, 378,2176, 20190274.
[39] J.H. Clark, T.J. Farmer, L. Herrero-Davila, J. Sherwood, Circular economy design considerations for research and process development in the chemical sciences, *Green Chem*. **2016**, 18,14, 3914-3934.
[40] R.A. Sheldon, Green solvents for sustainable organic synthesis: state of the art, *Green Chem*. **2005**, 7,5.
[41] P.G. Jessop, Searching for green solvents, *Green Chem.*, **2011**, 13,6.
[42] P. Anastas, N. Eghbali, Green chemistry: principles and practice, *Chem. Soc. Rev.*, **2010**, 39,1, 301-312.
[43] A.-G.C. Institute Green Chemistry Pocket Guide, https://www.acs.org/content/acs/en/greenchemistry/principles/12-principles-of-green-chemistry.html, accessed on 1 February 2021.
[44] J.C. Serrano-Ruiz, R. Luque, A. Sepúlveda-Escribano, Transformations of biomass-derived platform molecules: from high added-value chemicals to fuels via aqueous-phase processing, *Chem. Soc. Rev.*, **2011**, 40,11, 5266-5281.
[45] V.B. Agbor, N. Cicek, R. Sparling, A. Berlin, D.B. Levin, Biomass pretreatment: fundamentals toward application, *Biotechnol. Adv.*, **2011**, 29,6, 675-685.
[46] C.H. Zhou, X. Xia, C.X. Lin, D.S. Tong, J. Beltramini, Catalytic conversion of lignocellulosic biomass to fine chemicals and fuels, *Chem. Soc. Rev.*, **2011**, 40,11, 5588-5617.
[47] N. Mosier, C. Wyman, B. Dale, R. Elander, Y.Y. Lee, M. Holtzapple, M. Ladisch, Features of promising technologies for pretreatment of lignocellulosic biomass, *Bioresour. Technol.*, **2005**, 96,6, 673-686.

[48] H.J. Huang, S. Ramaswamy, Overview of Biomass Conversion Processes and Separation and Purification Technologiesw in Biorefineries, in: S. Ramaswamy, H.J. Huang, B.V. Ramaro (Eds.) Separation and Purification in Biorefineries, John Wiley & Sons, Ltd, Chichester, United Kingdom, **2013**, pp. 3-37.
[49] J. Castilla-Archilla, V. O'Flaherty, L.N.L. Piert, Biorefineries: Industrial Innovation and Tendencies, in: J.R. Bastidas-Oyanedel, J.E. Schmidts (Eds.) Biorefinery, Integrated Sustainable Processes for Biomass Conversion to Biomaterials, Biofuels, and Fertilizers, Springer Nature Switzerland AG, Cham, Switzerland, **2019**, pp. 3-37.
[50] R. Hackl, S. Harvey,Opportunities for Process Integrated Biorefinery Concepts in the Chemical Cluster in Stenungsund, Division of Heat and Power Technology of the, Department of Energy and Environment at Chalmers University of Technology, **2010**,
[51] K.S. Denny, K.S. Ng, T.L. Rex, Integrated Biorefineries, Encyclopedia of Sustainable Technology, Elsevier **2017**, pp. 299-314.
[52] M.T. Ashraf, A.E. Torres, J.E. Schmidt, G. Stephanopoulos, Analysis and Optimization of Mulit-actor Biorefineries, in: J.R. Bastidas-Oyanedel, J.E. Schmidt (Eds.) Biorefrinery, Integrated Sustainable Processes for Biomass Conversion to Biomaterials, Biofuels, and Fertilizers, Springer Nature Switzerland Chem, Switzerland, **2019**, pp. 49-75.
[53] T. Schröder, L.-P. Lauven, J. Geldermann, Improving biorefinery planning: Integration of spatial data using exact optimization nested in an evolutionary strategy, *Eur J Oper Res*. **2018**, 264,3, 1005-1019.
[54] S.S. Hassan, G.A. Williams, A.K. Jaiswal, Moving towards the second generation of lignocellulosic biorefineries in the EU: Drivers, challenges, and opportunities, *Renew. Sustain. Energy Rev*. **2019**, 101,590-599.
[55] B. Kamm, M. Kamm, Principles of biorefineries, *Appl Microbiol Biotechnol*. **2004**, 64,2, 137-145.
[56] L.R. Lynd, J.H. Cushman, R.J. Nichols, C. Wyman, Fuel Ethanol from Cellulosic Biomass, *Science*. **1991**, 251,4999, 1318-1323.
[57] R.A. Sheldon, Green and sustainable manufacture of chemicals from biomass: state of the art, *Green Chem*. **2014**, 16,3, 950-963.

[58] A. Retno Ardiyanti, R.H. Van Der Bosch, W. Yin, H.J. Heeres, Catalytic Hydrotreatment of Fast Pyrolysis Oils Using Supported Metal catalysts, in: R. Rinaldi (Ed.) Catalytic Hydrogenation for Biomass Valorization, RCS Energy and Environment Series No. 13 **2015**, pp. 151-173.
[59] J.C. Serrano-Ruiz, J.A. Dumesic, Catalytic Production of Liquid Hydrocarbon Transportation Fuels, Catalysis for Alternative Energy Generation **2012**, pp. 29-56.
[60] M. Puig-Arnavat, T. Pape Thomsen, G. Ravenni, L. Rongaard Clausen, Z. Sarossy, J. Ahrenfeldt, Pyrolysis and Gasification of Lignocellulosic Biomass, in: J.R. Bastidas-Oyanedel, J.E. Schmidt (Eds.) Biorefineriy, Integrated Sustainable

Processes for Biomass Conversion to Biomaterials, Biofuels, and Fertilizers, Springer Nature Switzerland, Chem, Switzerland, **2019**, pp. 79-111.
[61] X.L. Tong, Y. Ma, Y.D. Li, Biomass into chemicals: Conversion of sugars to furan derivatives by catalytic processes, *Appl Catal a-Gen*. **2010**, 385,1-2, 1-13.
[62] M. Besson, P. Gallezot, C. Pinel, Conversion of biomass into chemicals over metal catalysts, *Chem. Rev.*, **2014**, 114,3, 1827-1870.
[63] M.J. Climent, A. Corma, S. Iborra, Conversion of biomass platform molecules into fuel additives and liquid hydrocarbon fuels, *Green Chem.*, **2014**, 16,2, 516-547.
[64] J.J. Bozell, G.R. Petersen, Technology development for the production of biobased products from biorefinery carbohydrates-the US Department of Energy's "Top 10" revisited, *Green Chem.*, **2010**, 12,4, 539-554.
[65] T. Werpy, G. Petersen, Top Value Added Chemicals From Biomass,U.S. Department of Energy, http://www.osti.gov/bridge, accessed on 23 January 2021.
[66] Avantium Company Avantium YXY technology, https://www.avantium.com/technologies/yxy/, accessed on 04 Marrch 2021.
[67] BASF News Release: Succinity produces first commercial quantities of biobased succinic acid, https://www.basf.com/fi/en/media/news-releases/2014/03/p-14-0303-ci.html, accessed on 04 March 2021.
[68] GF-biochemicals Atlas technology for levulinic acid, http://www.gfbiochemicals.com/company/, accessed on 04 March 2021.
[69] R. Davis, N.J. Grundl, L. Tao, M.J. Biddy, E.C. Tan, G.T. Beckham, D. Humbird, Process design and economics for the conversion of lignocellulosic biomass to hydrocarbon fuels and coproducts: 2018 Biochemical design case update; Biochemical deconstruction and conversion of biomass to fuels and products via integrated biorefinery pathways, Report NREL/TP-5100-71949, National Renewable Energy Lab. (NREL), Golden, CO, USA, https://www.nrel.gov/docs/fy19osti/71949.pdf., accessed on 1 February 2020.
[70] M. Al-Naji, H. Schlaad, M. Antonietti, New (and Old) Monomers from Biorefineries to Make Polymer Chemistry More Sustainable, *Macromol. Rapid Commun.*, **2020**, e2000485.
[71] M.M. Abu-Omar, K. Barta, G.T. Beckham, J. Luterbacher, J. Ralph, R. Rinaldi, Y. Roman-Leshkov, J. Samec, B. Sels, F. Wang, Guidelines for performing lignin-first biorefining, *Energ. Environ. Sci.*, **2020**.
[72] P. Gallezot, Conversion of biomass to selected chemical products, *Chem. Soc. Rev.*, **2012**, 41,4, 1538-1558.
[73] Z. Sun, B. Fridrich, A. de Santi, S. Elangovan, K. Barta, Bright Side of Lignin Depolymerization: Toward New Platform Chemicals, *Chem. Rev.*, **2018**, 118,2, 614-678.
[74] Statista.com Production of Paper and Cardboard in Selected Countries, https://www.statista.com/statistics/270314/production-of-paper-and-cardboard-in-selected-countries/, accessed on 31 january 2021.

[75] J. Martin, M. Haggith Enviromental Paper Network: The State of Global Paper Industry, www.environmentalpaper.org, accessed on 27 January 2021.
[76] I.F. Demuner, J.L. Colodette, A.J. Demuner, C.M. Jardim, Biorefinery Review: Wide-Reaching Products Through Kraft Lignin, *Bioresour Technol*. 14,3, 7543-7581.
[77] J. Ruwoldt, A Critical Review of the Physicochemical Properties of Lignosulfonates: Chemical Structure and Behavior in Aqueous Solution, at Surfaces and Interfaces, *Surfaces*. **2020**, 3,4, 622-648.
[78] Y. Liao, S.-F. Koelewijn, G. Van den Bossche, J. Van Aelst, S. Van den Bosch, T. Renders, K. Navare, T. Nicolaï, K. Van Aelst, M. Maesen, B. Sels, A sustainable wood biorefinery for low–carbon footprint chemicals production, *Science*. **2020**, 367,6484, 1385-1390.
[79] Y. Li, L. Shuai, H. Kim, A.H. Motagamwala, J.K. Mobley, F. Yue, Y. Tobimatsu, D. Havkin-Frenkel, F. Chen, R.A. Dixon, J.S. Luterbacher, J.A. Dumesic, J. Ralph, An "ideal lignin" facilitates full biomass utilization, *Sci. Adv.*, **2018**, 4,9, 1-10.
[80] T. Renders, G. Van den Bossche, T. Vangeel, K. Van Aelst, B. Sels, Reductive catalytic fractionation: state of the art of the lignin-first biorefinery, *Curr Opin Biotechnol*. **2019**, 56,193-201.
[81] E. Cooreman, T. Vangeel, K. Van Aelst, J. Van Aelst, J. Lauwaert, J.W. Thybaut, S. Van den Bosch, B.F. Sels, Perspective on Overcoming Scale-Up Hurdles for the Reductive Catalytic Fractionation of Lignocellulose Biomass, *Ind Eng Chem Res*. **2020**, 59,39, 17035-17045.
[82] P.C.A. Bruijnincx, R. Rinaldi, B.M. Weckhuysen, Unlocking the potential of a sleeping giant: lignins as sustainable raw materials for renewable fuels, chemicals and materials, *Green Chem.*, **2015**, 17,11, 4860-4861.
[83] X. Jiang, C.A. de Assis, M. Kollman, R. Sun, H. Jameel, H.-m. Chang, R. Gonzalez, Lignin Fractionation from Laboratory to Commercialization: Chemistry, Scalability and Techno-economic Analysis, *Green Chem.*, **2020**.
[84] Borregaard press release: The flavour that carries - vanillin for 50 years, https://www.borregaard.com/News/The-flavor-that-carries-Vanillin-for-50-years, accessed on 03 February 2021.
[85] Y.M. Questell-Santiago, M.V. Galkin, K. Barta, J.S. Luterbacher, Stabilization strategies in biomass depolymerization using chemical functionalization, *Nat. Rev. Chem.*, **2020**, 4,6, 311-330.
[86] E. Paone, T. Tabanelli, F. Mauriello, The rise of lignin biorefinery, *Curr. Opin. Green Sustain. Chem*. **2020**, 24,1-6.
[87] T. Vangeel, W. Schutyser, T. Renders, B.F. Sels, Perspective on Lignin Oxidation: Advances, Challenges, and Future Directions, *Topics Curr Chem*. **2018**, 376,4.
[88] R. Gerardy, D.P. Debecker, J. Estager, P. Luis, J.M. Monbaliu, Continuous Flow Upgrading of Selected C2-C6 Platform Chemicals Derived from Biomass, *Chem. Rev.*, **2020**, 120, 15,15, 7219-7347.
[89] S.G. Newman, K.F. Jensen, The role of flow in green chemistry and engineering, *Green Chem.*, **2013**, 15,6.

[90] M. Baumann, T.S. Moody, M. Smyth, S. Wharry, A Perspective on Continuous Flow Chemistry in the Pharmaceutical Industry, *Org. Process Res. Dev.*, **2020**, 24,10, 1802-1813.
[91] R. Ciriminna, M. Pagliaro, R. Luque, Heterogeneous Catalysis under flow for the 21st century fine chemical industry, *Green Energy Environ.*, **2020**.
[92] R. Gérardy, N. Emmanuel, T. Toupy, V.-E. Kassin, N.N. Tshibalonza, M. Schmitz, J.-C.M. Monbaliu, Continuous Flow Organic Chemistry: Successes and Pitfalls at the Interface with Current Societal Challenges, *Eur J Org Chem*. **2018**, 2018,20-21, 2301-2351.
[93] R. Gérardy, R. Morodo, J. Estager, P. Luis, D.P. Debecker, J.-C.M. Monbaliu, Sustaining the Transition from a Petrobased to a Biobased Chemical Industry with Flow Chemistry, *Topics Curr Chem*. **2018**, 377,1, 1.
[94] P. Anastas, J.B. Zimmerman, Through the 12 Principles of Green Engineering, *Environ. Sco. Teechnol.*, **2003**, 37,5, 94A-101A.
[95] D. Dallinger, C.O. Kappe, Why flow means green – Evaluating the merits of continuous processing in the context of sustainability, *Curr. Opin. Green Sustain. Chem.*, **2017**, 7,6-12.
[96] J.C. McWilliams, A.D. Allian, S.M. Opalka, S.A. May, M. Journet, T.M. Braden, The Evolving State of Continuous Processing in Pharmaceutical API Manufacturing: A Survey of Pharmaceutical Companies and Contract Manufacturing Organizations, *Org. Process Res. Dev.*, **2018**, 22,9, 1143-1166.
[97] C. Moreno-Marrodan, F. Liguori, P. Barbaro, Continuous-flow processes for the catalytic partial hydrogenation reaction of alkynes, *Beilstein J Org Chem*. **2017**, 13,734-754.
[98] M.B. Plutschack, B. Pieber, K. Gilmore, P.H. Seeberger, The Hitchhiker's Guide to Flow Chemistry parallel, *Chem Rev*. **2017**, 117,18, 11796-11893.
[99] L. Vaccaro, D. Lanari, A. Marrocchi, G. Strappaveccia, Flow approaches towards sustainability, *Green Chem.*, **2014**, 16,8, 3680-3704.
[100] J.C. Serrano-Ruiz, R. Luque, J.M. Campelo, A.A. Romero, Continuous-Flow Processes in Heterogeneously Catalyzed Transformations of Biomass Derivatives into Fuels and Chemicals, *Challenges*. **2012**, 3,2, 114-132.
[101] D. Reay, C. Ramshaw, A. Harvey, Process Intensification – An Overview, Process Intensification, Engineering for Efficiency, Sustainability and Flexibility Second Edition, Elsevier Ltd **2013**, pp. 27-55.
[102] M. Movsisyan, E.I. Delbeke, J.K. Berton, C. Battilocchio, S.V. Ley, C.V. Stevens, Taming hazardous chemistry by continuous flow technology, *Chem. Soc. Rev*. **2016**, 45,18, 4892-4928.
[103] J.C. Serrano-Ruiz, R. Luque, A. Sepulveda-Escribano, Transformations of biomass-derived platform molecules: from high added-value chemicals to fuels via aqueous-phase processing, *Chem. Soc. Rev.*, **2011**, 40,11, 5266-5281.
[104] G. Van der Vorst, W. Aelterman, B. De Witte, B. Heirman, H. Van Langenhove, J. Dewulf, Reduced resource consumption through three generations of Galantamine·HBr synthesis, *Green Chem.*, **2013**, 15,3.

[105] M. Colella, C. Carlucci, R. Luisi, Supported Catalysts for Continuous Flow Synthesis, in: T. Noel, R. Luque (Eds.) Accounts on Sustainable Flow Chemistry, Springer Nature Switzerland AG Gewerbestrasse 11, 6330 Cham, Switzerland, **2020**, pp. 28-65.
[106] C. Wiles, P. Watts, Continuous flow reactors: a perspective, *Green Chem.*, **2012**, 14,1, 38-54.
[107] B. Gutmann, C.O. Kappe, Forbidden chemistries — paths to a sustainable future engaging continuous processing, *J. Flow Chem.*, **2017**, 7,3–4, 65-71.
[108] A.D. McNaught A. Wilkinson "Catalyst" in I.U.PAC. Compendium of Chemical Terminology, 2nd ed. (the "Gold Book") , Oxford (1997). ,Blackwell Scientific Publications, https://doi.org/10.1351/goldbook., accessed on 5 February 2021.
[109] J.A. Dumesic, G.W. Huber, M. Boudart, Principles of Heterogeneous Catalysis, in: G. Ertl, H. Knözinger, F. Schüth, J. Weitkamp (Eds.) Handbook of Heterogeneous Catalysis Wiley-VCH Verlag GmbH& Co KGaA, Weinheim, Germany, **2008**, pp. 1-16.
[110] H. Knözinger, K. Kochlöfl, T. Turek, Heterogeneous Catalysis and Solid Catalysts, Ullmann's Encyclopedia of Industrial Chemistry, Wiley-VCH Verlag GmbH & Co. KGaA,, Weinheim, **2009**, pp. 1-62.
[111] D.W. Krevelen, J. Schuyer, Coal science: aspects of coal constitution, Elsevier publishing company, Amsterdam, **1957**. pag.
[112] Y. Román-Leshkov, C.J. Barrett, Z.Y. Liu, J.A. Dumesic, Production of dimethylfuran for liquid fuels from biomass-derived carbohydrates, *Nature*. **2007**, 447,7147, 982-985.
[113] T. Ennaert, W. Schutyser, J. Dijkmans, M. Dusselier, B.F. Sels, Conversion of Biomass to Chemicals: The Catalytic Role of Zeolites, in: B.F. Sels, L.M. Kustov (Eds.) Zeoilite and Zeoilte-like Materials, Elsevier, 2016,
[114] L.T. Mika, E. Csefalvay, A. Nemeth, Catalytic Conversion of Carbohydrates to Initial Platform Chemicals: Chemistry and Sustainability, *Chem. Rev.*, **2018**, 118,2, 505-613.
[115] Y. Jing, Y. Guo, Q. Xia, X. Liu, Y. Wang, Catalytic Production of Value-Added Chemicals and Liquid Fuels from Lignocellulosic Biomass, *Chem*. **2019**, 5,10, 2520-2546.
[116] H. Kobayashi, H. Ohta, A. Fukuoka, Noble-Metal Catalysts for Conversion of Lignocellulose under Hydrogen Pressure, in: R. Rinaldi (Ed.) Catalytic Hydrogenation for Biomass Valorization, RCS Energy and Environment Series No. 13 **2015**, pp. 52-71.
[117] K.I. Galkin, V.P. Ananikov, When Will 5-Hydroxymethylfurfural, the "Sleeping Giant" of Sustainable Chemistry, Awaken?, *Chemsuschem*. **2019**, 12,13, 2976-2982.
[118] R.J. van Putten, J.C. van der Waal, E. de Jong, C.B. Rasrendra, H.J. Heeres, J.G. de Vries, Hydroxymethylfurfural, a versatile platform chemical made from renewable resources, *Chem Rev*. **2013**, 113,3, 1499-1597.

[119] D. Zhang, M.-J. Dumont, Advances in polymer precursors and bio-based polymers synthesized from 5-hydroxymethylfurfural, *J. Polym. Sci. A Polym. Chem.*, **2017**, 55,9, 1478-1492.
[120] Y.T. Cheng, Z. Wang, C.J. Gilbert, W. Fan, G.W. Huber, Production of p-xylene from biomass by catalytic fast pyrolysis using ZSM-5 catalysts with reduced pore openings, *Angew. Chem. Int. Ed.*, **2012**, 51,44, 11097-11100.
[121] M. Braun, M. Antonietti, A continuous flow process for the production of 2, 5-dimethylfuran from fructose using (non-noble metal based) heterogeneous catalysis, *Green Chem.*, **2017**, 19,16, 3813-3819.
[122] S. Chen, R. Wojcieszak, F. Dumeignil, E. Marceau, S. Royer, How Catalysts and Experimental Conditions Determine the Selective Hydroconversion of Furfural and 5-Hydroxymethylfurfural, *Chem Rev*. **2018**, 118,22, 11023-11117.
[123] I.F. Teixeira, B.T. Lo, P. Kostetskyy, M. Stamatakis, L. Ye, C.C. Tang, G. Mpourmpakis, S.C. Tsang, From Biomass-Derived Furans to Aromatics with Ethanol over Zeolite, *Angew. Chem. Int. Ed.*, **2016**, 55,42, 13061-13066.
[124] L. Ni, J. Xin, H. Dong, X. Lu, X. Liu, S. Zhang, A Simple and Mild Approach for the Synthesis of p-Xylene from Bio-Based 2,5-Dimethyfuran by Using Metal Triflates, *Chemsuschem*. **2017**, 10,11, 2394-2401.
[125] J. Luo, L. Arroyo-Ramírez, J. Wei, H. Yun, C.B. Murray, R.J. Gorte, Comparison of HMF hydrodeoxygenation over different metal catalysts in a continuous flow reactor, *Appl. Catal. A-Gen.* of 2,5-dimethylfuran from 5-hydroxymethylfurfural over carbon supported Ni–Co bimetallic catalyst, *Journal of Energy Chemistry*. **2016**, 25,6, 1015-1020.
[127] W. Han, M. Tang, J. Li, X. Li, J. Wang, L. Zhou, Y. Yang, Y. Wang, H. Ge, Selective hydrogenolysis of 5-hydroxymethylfurfural to 2, 5-dimethylfuran catalyzed by ordered mesoporous alumina supported nickel-molybdenum sulfide catalysts, *Appl. Catal. B-Environ*. **2020**, 268,118748.
[128] R. Goyal, B. Sarkar, A. Bag, N. Siddiqui, D. Dumbre, N. Lucas, S.K. Bhargava, A. Bordoloi, Studies of synergy between metal–support interfaces and selective hydrogenation of HMF to DMF in water, *J Catal*. **2016**, 340,248-260.
[129] M. Al-Naji, J. Van Aelst, Y. Liao, M. d'Hullian, Z. Tian, C. Wang, R. Gläser, B.F. Sels, Pentanoic acid from γ-valerolactone and formic acid using bifunctional catalysis, *Green Chem.*, **2020**, 22,4, 1171-1181.
[130] G.C. Hayes, C.R. Becer, Levulinic acid: a sustainable platform chemical for novel polymer architectures, *Polym. Chem.*, **2020**, 11,25, 4068-4077.
[131] M. Al-Naji, A. Yepez, A.M. Balu, A.A. Romero, Z. Chen, N. Wilde, H. Li, K. Shih, R. Gläser, R. Luque, Insights into the selective hydrogenation of levulinic acid to γ-valerolactone using supported mono- and bimetallic catalysts, *J. Mol. Catal. A Chem.*, **2016**, 417,145-152.
[132] M. Al-Naji, M. Popova, Z. Chen, N. Wilde, R. Gläser, Aqueous-Phase Hydrogenation of Levulinic Acid Using Formic Acid as a Sustainable Reducing Agent Over Pt Catalysts Supported on Mesoporous Zirconia, *Acs Sustain. Chem. Eng.*, **2019**, 8,1, 393-402.

[133] H. Schiweck, A. Bär, R. Vogel, E. Schwarz, M. Kunz, C. Dusautois, A. Clement, C. Lefranc, B. Lüssem, M. Moser, Sugar alcohols, *Ullmann's encyclopedia of industrial chemistry*. **2000**.
[134] C. Marques, R. Tarek, M. Sara, S. Brar, Sorbitol production from biomass and its global market, Platform Chemical Biorefinery, Elsevier **2016**, pp. 217-227.
[135] M. Ahmed, B. Hameed, Hydrogenation of glucose and fructose into hexitols over heterogeneous catalysts: A review, *Journal of the Taiwan Institute of Chemical Engineers*. **2019**, 96,341-352.
[136] B. Garcia, J. Moreno, J. Iglesias, J.A. Melero, G. Morales, Transformation of Glucose into Sorbitol on Raney Nickel Catalysts in the Absence of Molecular Hydrogen: Sugar Disproportionation vs Catalytic Hydrogen Transfer, *Top Catal*. **2019**, 62,5-6, 570-578.
[137] B. Kusserow, S. Schimpf, P. Claus, Hydrogenation of glucose to sorbitol over nickel and ruthenium catalysts, *Adv. Synth. Catal.*, **2003**, 345,1-2, 289-299.
[138] E. Crezee, B.W. Hoffer, R.J. Berger, M. Makkee, F. Kapteijn, J.A. Moulijn, Three-phase hydrogenation of D-glucose over a carbon supported ruthenium catalyst—mass transfer and kinetics, *Appl. Catal. A-Gen.* **2003**, 251,1, 1-17.
[139] J. Pan, J. Li, C. Wang, Z. Yang, Multi-wall carbon nanotubes supported ruthenium for glucose hydrogenation to sorbitol, *Reaction Kinetics and Catalysis Letters*. **2007**, 90,2, 233-242.
[140] D.K. Mishra, A.A. Dabbawala, J.J. Park, S.H. Jhung, J.-S. Hwang, Selective hydrogenation of d-glucose to d-sorbitol over HY zeolite supported ruthenium nanoparticles catalysts, *Catal Today*. **2014**, 232,99-107.
[141] A. Romero, E. Alonso, Á. Sastre, A. Nieto-Márquez, Conversion of biomass into sorbitol: Cellulose hydrolysis on MCM-48 and d-Glucose hydrogenation on Ru/MCM-48, *Microporous and Mesoporous Materials*. **2016**, 224,1-8.
[142] P.A. Lazaridis, S. Karakoulia, A. Delimitis, S.M. Coman, V.I. Parvulescu, K.S. Triantafyllidis, D-Glucose hydrogenation/hydrogenolysis reactions on noble metal (Ru, Pt)/activated carbon supported catalysts, *Catal Today*. **2015**, 257,281-290.
[143] R.M. Ravenelle, J.R. Copeland, A.H. Van Pelt, J.C. Crittenden, C. Sievers, Stability of Pt/γ-Al 2 O 3 catalysts in model biomass solutions, *Top Catal*. **2012**, 55,3-4, 162-174.
[144] D. Messou, L. Vivier, C. Canaff, C. Especel, Biofuel Synthesis from Sorbitol by Aqueous Phase Hydrodeoxygenation over Bifunctional Catalysts: In-depth Study of the Ru–Pt/SiO2–Al2O3 Catalytic System, *Catalysts*. **2019**, 9,2, 146.
[145] X. Zhang, L.J. Durndell, M.A. Isaacs, C.M. Parlett, A.F. Lee, K. Wilson, Platinum-catalyzed aqueous-phase hydrogenation of d-glucose to d-sorbitol, *Acs Catal*. **2016**, 6,11, 7409-7417.
[146] L. Silvester, F. Ramos, J. Thuriot-Roukos, S. Heyte, M. Araque, S. Paul, R. Wojcieszak, Fully integrated high-throughput methodology for the study of Ni-and Cu-supported catalysts for glucose hydrogenation, *Catal Today*. **2019**.
[147] F. Delbecq, M.R. Khodadadi, D. Rodriguez Padron, R. Varma, C. Len, Isosorbide: Recent advances in catalytic production, *Molecular Catalysis*. **2020**, 482.

[148] Y.-R. Du, B.-H. Xu, J.-S. Pan, Y.-W. Wu, X.-M. Peng, Y.-F. Wang, S.-J. Zhang, Confinement of Brønsted acidic ionic liquids into covalent organic frameworks as a catalyst for dehydrative formation of isosorbide from sorbitol, *Green Chemistry*. **2019**, 21,17, 4792-4799.
[149] M. Yabushita, Acid-Catalyzed Dehydration of Sorbitol to 1,4-Sorbitan, A Study on Catalytic Conversion of Non-Food Biomass into Chemicals **2016**, pp. 127-140.
[150] J.R. Ochoa-Gómez, T. Roncal, Production of sorbitol from Biomass, Production of Platform Chemicals from Sustainable Resources, Springer **2017**, pp. 265-309.
[151] C. Dussenne, T. Delaunay, V. Wiatz, H. Wyart, I. Suisse, M. Sauthier, Synthesis of isosorbide: an overview of challenging reactions, *Green Chem.*, **2017**, 19,22, 5332-5344.
[152] M. Rose, R. Palkovits, Isosorbide as a renewable platform chemical for versatile applications—quo vadis?, *Chemsuschem*. **2012**, 5,1, 167-176.
[153] P. Barbaro, F. Liguori, C. Moreno-Marrodan, Selective direct conversion of C 5 and C 6 sugars to high added-value chemicals by a bifunctional, single catalytic body, *Green Chem.*, **2016**, 18,10, 2935-2940.
[154] P. Barbaro, F. Liguori, C. Moreno-Marrodan, Selective direct conversion of C5 and C6 sugars to high added-value chemicals by a bifunctional, single catalytic body, *Green Chemistry*. **2016**, 18,10, 2935-2940.
[155] Polysorb registered product from Roquette, 2019, https://www.roquette.com/industries/selected-products/industry-performance-materials-isosorbide, accessed on 03 March 2021.
[156] Mitshubishi Chemical Corporation. News Release: A first in Europe: Mitshubishi Chemical′s DURABIO Bio-based Engineering Plastic Adopted for Outer Mask for Speedometer-Tachometer Combo of Renault' s New Clio, **2016**, https://www.mchemical.co.jp/en/news/kagaku/pdf/00437/00499.pdf , accessed on 03 March 2021.
[157] Teijin Company. News Release: Teijin Develops Formable Gasoline-Resistant Bioplastic Film for Vehicle Door Handles Integrated with Smart-Entry Systems, 2018, https://www.teijin.com/products/resin/planext/pdf/planext_related_01.pdf, accessed on 03 March 2021.
[158] J.N. Cohn, G. Johnson, S. Ziesche, F. Cobb, G. Francis, F. Tristani, R. Smith, W.B. Dunkman, H. Loeb, M. Wong, A comparison of enalapril with hydralazine–isosorbide dinitrate in the treatment of chronic congestive heart failure, *N. Engl. J. Med.*, **1991**, 325,5, 303-310.
[159] NIH, LiverTox: clinical and research information on drug-induced liver injury, *Nih. gov https://livertox. nih. gov*. **2017**.
[160] F.W. Lichtenthaler, Carbohydrates: Occurrence, Structures and Chemistry, Ullmann's Encyclopedia of Industrial Chemistry **2010**.
[161] P. Kamm, B. Kamm, Biorefineries–Industrial Processes and Products, *Ullmans Encyclopedia of Industrial Chemistry*. **2015**.

[162] H. Schiweck, R. Vogel, E. Schwartz, M. Kunz, C. Dusautois, A. Clement, C. Lefranc, B. Lussem, M. Moser, S. Peters, Sugar Alcohols, *Ullman's Encyclopedia of Industrial Chemistry*. **2012**.
[163] I. Ahmed, N.A. Khan, D.K. Mishra, J.S. Lee, J.-S. Hwang, S.H. Jhung, Liquid-phase dehydration of sorbitol to isosorbide using sulfated titania as a solid acid catalyst, *Chemical Engineering Science*. **2013**, 93,91-95.
[164] J. Zou, D. Cao, W. Tao, S. Zhang, L. Cui, F. Zeng, W. Cai, Sorbitol dehydration into isosorbide over a cellulose-derived solid acid catalyst, *RSC Advances*. **2016**, 6,55, 49528-49536.
[165] D. Cao, B. Yu, S. Zhang, L. Cui, J. Zhang, W. Cai, Isosorbide production from sorbitol over porous zirconium phosphate catalyst, *Appl. Catal. A-Gen*. **2016**, 528,59-66.
[166] A. Cubo, J. Iglesias, G. Morales, J.A. Melero, J. Moreno, R. Sánchez-Vázquez, Dehydration of sorbitol to isosorbide in melted phase with propyl-sulfonic functionalized SBA-15: Influence of catalyst hydrophobization, *Appl. Catal. A-Gen*. **2017**, 531,151-160.
[167] M.J. Ginés-Molina, R. Moreno-Tost, J. Santamaría-González, P. Maireles-Torres, Dehydration of sorbitol to isosorbide over sulfonic acid resins under solvent-free conditions, *Appl. Catal. A-Gen,* **2017**, 537,66-73.
[168] S. Jeong, K.-J. Jeon, Y.-K. Park, B.-J. Kim, K.-H. Chung, S.-C. Jung, Catalytic Properties of Microporous Zeolite Catalysts in Synthesis of Isosorbide from Sorbitol by Dehydration, *Catalysts*. **2020**, 10,2.
[169] M.R. Kamaruzaman, X.X. Jiang, X.D. Hu, S.Y. Chin, High yield of isosorbide production from sorbitol dehydration catalysed by Amberlyst 36 under mild condition, *Chemical Engineering Journal*. **2020**, 388.
[170] J. Li, A. Spina, J.A. Moulijn, M. Makkee, Sorbitol dehydration into isosorbide in a molten salt hydrate medium, *Catalysis Science & Technology*. **2013**, 3,6.
[171] I. Polaert, M.C. Felix, M. Fornasero, S. Marcotte, J.-C. Buvat, L. Estel, A greener process for isosorbide production: Kinetic study of the catalytic dehydration of pure sorbitol under microwave, *Chemical Engineering Journal*. **2013**, 222,228-239.
[172] P. Sun, D.H. Yu, Y. Hu, Z.C. Tang, J.J. Xia, H. Li, H. Huang, H3PW12O40/SiO2 for sorbitol dehydration to isosorbide: High efficient and reusable solid acid catalyst, *Korean J. Chem. Eng.*, **2010**, 28,1, 99-105.
[173] D. Yuan, L. Li, F. Li, Y. Wang, F. Wang, N. Zhao, F. Xiao, Solvent-Free Production of Isosorbide from Sorbitol Catalyzed by a Polymeric Solid Acid, *ChemSusChem*. **2019**, 12,22, 4986-4995.
[174] X. Zhang, A.I.M. Rabee, M. Isaacs, A.F. Lee, K. Wilson, Sulfated Zirconia Catalysts for D-Sorbitol Cascade Cyclodehydration to Isosorbide: Impact of Zirconia Phase, *ACS Sustainable Chemistry & Engineering*. **2018**, 6,11, 14704-14712.
[175] Y. Zhang, T. Chen, G. Zhang, G. Wang, H. Zhang, Efficient production of isosorbide from sorbitol dehydration over mesoporous carbon-based acid catalyst, *Appl. Catal. A-Gen*. **2019**, 575,38-47.

[176] A.A. Dabbawala, D.K. Mishra, G.W. Huber, J.-S. Hwang, Role of acid sites and selectivity correlation in solvent free liquid phase dehydration of sorbitol to isosorbide, *Appl. Catal. A-Gen*. **2015**, 492,252-261.
[177] H. Kobayashi, H. Yokoyama, B. Feng, A. Fukuoka, Dehydration of sorbitol to isosorbide over H-beta zeolites with high Si/Al ratios, *Green Chem.*, **2015**, 17,5, 2732-2735.
[178] R. Otomo, T. Yokoi, T. Tatsumi, Synthesis of isosorbide from sorbitol in water over high-silica aluminosilicate zeolites, *Appl. Catal. A-Gen.,* **2015**, 505,28-35.
[179] A. Yamaguchi, N. Hiyoshi, O. Sato, M. Shirai, Sorbitol dehydration in high temperature liquid water, *Green Chemistry*. **2011**, 13,4.
[180] M. Gu, D. Yu, H. Zhang, P. Sun, H. Huang, Metal (IV) Phosphates as Solid Catalysts for Selective Dehydration of Sorbitol to Isosorbide, *Catalysis Letters*. **2009**, 133,1-2, 214-220.
[181] J. Xia, D. Yu, Y. Hu, B. Zou, P. Sun, H. Li, H. Huang, Sulfated copper oxide: An efficient catalyst for dehydration of sorbitol to isosorbide, *Catal Commun*. **2011**, 12,6, 544-547.
[182] X. Zhang, D. Yu, J. Zhao, W. Zhang, Y. Dong, H. Huang, The effect of P/Ta ratio on sorbitol dehydration over modified tantalum oxide by phosphoric acid, *Catal Commun*. **2014**, 43,29-33.
[183] Y. Luo, Z. Li, X. Li, X. Liu, J. Fan, J.H. Clark, C. Hu, The production of furfural directly from hemicellulose in lignocellulosic biomass: A review, *Catal Today*. **2019**, 319,14-24.
[184] J.B. Binder, J.J. Blank, A.V. Cefali, R.T. Raines, Synthesis of furfural from xylose and xylan, *Chemsuschem*. **2010**, 3,11, 1268-1272.
[185] R. Xing, W. Qi, G.W. Huber, Production of furfural and carboxylic acids from waste aqueous hemicellulose solutions from the pulp and paper and cellulosic ethanol industries, *Energy Environ. Sci.*, **2011**, 4,6.
[186] R. Weingarten, G.A. Tompsett, W.C. Conner, G.W. Huber, Design of solid acid catalysts for aqueous-phase dehydration of carbohydrates: The role of Lewis and Brønsted acid sites, *J. Catal.*, **2011**, 279,1, 174-182.
[187] R.K. Mishra, V.B. Kumar, A. Victor, I.N. Pulidindi, A. Gedanken, Selective production of furfural from the dehydration of xylose using Zn doped CuO catalyst, *Ultrason Sonochem*. **2019**, 56,55-62.
[188] M. Yadav, D.K. Mishra, J.S. Hwang, Catalytic hydrogenation of xylose to xylitol using ruthenium catalyst on NiO modified TiO2 support, *Appl Catal a-Gen*. **2012**, 425,110-116.
[189] J.P. Mikkola, H. Vainio, T. Salmi, R. Sjoholm, T. Ollonqvist, J. Vayrynen, Deactivation kinetics of Mo-supported Raney Ni catalyst in the hydrogenation of xylose to xylitol, *Appl. Catal. A Gen.*, **2000**, 196,1, 143-155.
[190] J.C. Lee, Y. Xu, G.W. Huber, High-throughput screening of monometallic catalysts for aqueous-phase hydrogenation of biomass-derived oxygenates, *Appl Catal B-Environ*. **2013**, 140,98-107.

[191] D.K. Mishra, A.A. Dabbawala, J.S. Hwang, Ruthenium nanoparticles supported on zeolite Y as an efficient catalyst for selective hydrogenation of xylose to xylitol, *J Mol Catal a-Chem*. **2013**, 376,63-70.
[192] H.M. Baudel, C.A.M. de Abreu, C.Z. Zaror, Technical Note - Xylitol production via catalytic hydrogenation of sugarcane bagasse dissolving pulp liquid effluents over Ru/C catalyst, *J. Chem. Technol. Biotechnol.*, **2005**, 80,2, 230-233.
[193] C. Hernandez-Mejia, E.S. Gnanakumar, A. Olivos-Suarez, J. Gascon, H.F. Greer, W.Z. Zhou, G. Rothenberg, N.R. Shiju, Ru/TiO2-catalysed hydrogenation of xylose: the role of the crystal structure of the support, *Catal Sci Technol*. **2016**, 6,2, 577-582.
[194] A.B. Bindwal, P.D. Vaidya, Reaction Kinetics of Vanillin Hydrogenation in Aqueous Solutions Using a Ru/C Catalyst, *Energ Fuel*. **2014**, 28,5, 3357-3362.
[195] I.K. Ilic, K. Leus, J. Schmidt, J. Hwang, M. Maranska, S. Eigler, C. Liedel, Polymerization in Carbone: A Novel Method for the Synthesis of More Sustainable Electrodes and Their Application as Cathodes for Lithium–Organic Energy Storage Materials Based On Vanillin, *Acs Sustain. Chem. Eng.*, **2020**, 8,8, 3055-3064.
[196] M. Fache, E. Darroman, V. Besse, R. Auvergne, S. Caillol, B. Boutevin, Vanillin, a promising biobased building-block for monomer synthesis, *Green Chem.*, **2014**, 16,4, 1987-1998.
[197] F. Liguori, C. Moreno-Marrodan, P. Barbaro, Biomass-derived chemical substitutes for bisphenol A: recent advancements in catalytic synthesis, *Chem. Soc. Rev.*, **2020**, 49,17, 6329-6363.
[198] H.A. Meylemans, T.J. Groshens, B.G. Harvey, Synthesis of renewable bisphenols from creosol, *Chemsuschem*. **2012**, 5,1, 206-210.
[199] F.M. Zhang, S. Zheng, Q. Xiao, Y.J. Zhong, W.D. Zhu, A. Lin, M.S. El-Shall, Synergetic catalysis of palladium nanoparticles encaged within amine-functionalized UiO-66 in the hydrodeoxygenation of vanillin in water, *Green Chem.*, **2016**, 18,9, 2900-2908.
[200] J.L. Santos, M. Alda-Onggar, V. Fedorov, M. Peurla, K. Eranen, P. Maki-Arvela, M.A. Centeno, D.Y. Murzin, Hydrodeoxygenation of vanillin over carbon supported metal catalysts, *Appl Catal a-Gen*. **2018**, 561,137-149.
[201] S.C. Shit, R. Singuru, S. Pollastri, B. Joseph, B.S. Rao, N. Lingaiah, J. Mondal, Cu-Pd bimetallic nanoalloy anchored on a N-rich porous organic polymer for high-performance hydrodeoxygenation of biomass-derived vanillin, *Catal Sci Technol*. **2018**, 8,8, 2195-2210.
[202] R.F. Nie, H.H. Yang, H.F. Zhang, X.L. Yu, X.H. Lu, D. Zhou, Q.H. Xia, Mild-temperature hydrodeoxygenation of vanillin over porous nitrogen-doped carbon black supported nickel nanoparticles, *Green Chem.*, **2017**, 19,13, 3126-3134.
[203] R.Y. Fan, C. Chen, M.M. Han, W.B. Gong, H.M. Zhang, Y.X. Zhang, H.J. Zhao, G.Z. Wang, Highly Dispersed Copper Nanoparticles Supported on Activated Carbon as an Efficient Catalyst for Selective Reduction of Vanillin, *Small*. **2018**, 14,36.

[204] C.M. Bernt, G. Bottari, J.A. Barrett, S.L. Scott, K. Barta, P.C. Ford, Mapping reactivities of aromatic models with a lignin disassembly catalyst. Steps toward controlling product selectivity, *Catal Sci Technol*. **2016**, 6,9, 2984-2994.
[205] Z. Sun, J. Cheng, D. Wang, T.Q. Yuan, G. Song, K. Barta, Downstream Processing Strategies for Lignin-First Biorefinery, *Chemsuschem*. **2020**.
[206] J. Behaghel de Bueren, F. Héroguel, C. Wegmann, G.R. Dick, R. Buser, J.S. Luterbacher, Aldehyde-Assisted Fractionation Enhances Lignin Valorization in Endocarp Waste Biomass, *Acs Sustain. Chem. Eng.*, **2020**, 8,45, 16737-16745.
[207] T. Renders, S. Van den Bosch, S.F. Koelewijn, W. Schutyser, B.F. Sels, Lignin-first biomass fractionation: the advent of active stabilisation strategies, *Energ Environ Sci*. **2017**, 10,7, 1551-1557.
[208] S. Van den Bosch, W. Schutyser, R. Vanholme, T. Driessen, S.F. Koelewijn, T. Renders, B. De Meester, W.J.J. Huijgen, W. Dehaen, C.M. Courtin, B. Lagrain, W. Boerjan, B.F. Sels, Reductive lignocellulose fractionation into soluble lignin-derived phenolic monomers and dimers and processable carbohydrate pulps, *Energ Environ Sci*. **2015**, 8,6, 1748-1763.
[209] T. Renders, S. Van den Bosch, T. Vangeel, T. Ennaert, S.-F. Koelewijn, G. Van den Bossche, C.M. Courtin, W. Schutyser, B.F. Sels, Synergetic Effects of Alcohol/Water Mixing on the Catalytic Reductive Fractionation of Poplar Wood, *Acs Sustain. Chem. Eng.*, **2016**, 4,12, 6894-6904.
[210] T. Renders, E. Cooreman, S. Van den Bosch, W. Schutyser, S.F. Koelewijn, T. Vangeel, A. Deneyer, G. Van den Bossche, C.M. Courtin, B.F. Sels, Catalytic lignocellulose biorefining in n-butanol/water: a one-pot approach toward phenolics, polyols, and cellulose, *Green Chem.*, **2018**, 20,20, 4607-4619.
[211] K. Van Aelst, E. Van Sinay, T. Vangeel, E. Cooreman, G. Van den Bossche, T. Renders, J. Van Aelst, S. Van den Bosch, B.F. Sels, Reductive catalytic fractionation of pine wood: elucidating and quantifying the molecular structures in the lignin oil, *Chem. Sci.*, **2020**.
[212] M.L. Stone, E.M. Anderson, K.M. Meek, M. Reed, R. Katahira, F. Chen, R.A. Dixon, G.T. Beckham, Y. Román-Leshkov, Reductive Catalytic Fractionation of C-Lignin, *Acs Sustain. Chem. Eng.*, **2018**, 6,9, 11211-11218.
[213] P.Y. Dapsens, C. Mondelli, J. Pérez-Ramírez, Biobased Chemicals from Conception toward Industrial Reality: Lessons Learned and To Be Learned, *Acs Catal*. **2012**, 2,7, 1487-1499.
[214] P. Lanzafame, S. Perathoner, G. Centi, S. Gross, E.J.M. Hensen, Grand challenges for catalysis in the Science and Technology Roadmap on Catalysis for Europe: moving ahead for a sustainable future, *Catal. Sci. Technol.*, **2017**, 7,22, 5182-5194.
[215] S. Mitchell, N.L. Michels, J. Perez-Ramirez, From powder to technical body: the undervalued science of catalyst scale up, *Chem. Soc. Rev.*, **2013**, 42,14, 6094-6112.
[216] G.T. Whiting, S.-H. Chung, D. Stosic, A.D. Chowdhury, L.I. van der Wal, D. Fu, J. Zecevic, A. Travert, K. Houben, M. Baldus, B.M. Weckhuysen, Multiscale

Mechanistic Insights of Shaped Catalyst Body Formulations and Their Impact on Catalytic Properties, *Acs Catal*. **2019**, 9,6, 4792-4803.
[217] J. Hagen, Industrial Catalysis: A Practical Approach, WILEY-VCH Verlag GmbH & Co, KGaA, Weinheim, **2006**. pag. 223-260.
[218] L. Lakiss, J.-P. Gilson, V. Valtchev, S. Mintova, A. Vicente, A. Vimont, R. Bedard, S. Abdo, J. Bricker, Zeolites in a good shape: Catalyst forming by extrusion modifies their performances, *Microporous Mesoporous Mater.*, **2020**, 299,110114.
[219] C. Mondelli, G. Gozaydin, N. Yan, J. Perez-Ramirez, Biomass valorisation over metal-based solid catalysts from nanoparticles to single atoms, *Chem. Soc. Rev.*, **2020**, 49,12, 3764-3782.
[220] D. Astruc, Introduction: Nanoparticles in Catalysis, *Chem. Rev*. **2020**, 120,2, 461-463.
[221] I. Sádaba, M.L. Granados, A. Riisager, E. Taarning, Deactivation of solid catalysts in liquid media: the case of leaching of active sites in biomass conversion reactions, *Green Chem.*, **2015**, 17,8, 4133-4145.
[222] T. Van Haasterecht, C. Ludding, K. De Jong, J. Bitter, Toward stable nickel catalysts for aqueous phase reforming of biomass-derived feedstock under reducing and alkaline conditions, *J Catal*. **2014**, 319,27-35.
[223] U.K. Singh, S.W. Krska, Y. Sun, Deactivation of heterogeneous hydrogenation catalysts by alcoholic solvents, *Org Process Res Dev*. **2006**, 10,6, 1153-1156.
[224] R.M. Ravenelle, F. Schüβler, A. D'Amico, N. Danilina, J.A. Van Bokhoven, J.A. Lercher, C.W. Jones, C. Sievers, Stability of zeolites in hot liquid water, *J. Phys.Chem. C*. **2010**, 114,46, 19582-19595.
[225] H.N. Pham, A.E. Anderson, R.L. Johnson, K. Schmidt-Rohr, A.K. Datye, Improved hydrothermal stability of mesoporous oxides for reactions in the aqueous phase, *Angew. Chem. Int. Ed.*. **2012**, 51,52, 13163-13167.
[226] R.M. Ravenelle, J.R. Copeland, W.-G. Kim, J.C. Crittenden, C. Sievers, Structural changes of γ-Al2O3-supported catalysts in hot liquid water, *Acs Catal*. **2011**, 1,5, 552-561.
[227] A.H. Van Pelt, O.A. Simakova, S.M. Schimming, J.L. Ewbank, G.S. Foo, E.A. Pidko, E.J. Hensen, C. Sievers, Stability of functionalized activated carbon in hot liquid water, *Carbon*. **2014**, 77,143-154.
[228] M.M. Titirici, R.J. White, N. Brun, V.L. Budarin, D.S. Su, F. del Monte, J.H. Clark, M.J. MacLachlan, Sustainable carbon materials, *Chem. Soc. Rev.*, **2015**, 44,1, 250-290.
[229] T.W. van Deelen, C. Hernández Mejía, K.P. de Jong, Control of metal-support interactions in heterogeneous catalysts to enhance activity and selectivity, *Nat. Catal.*, **2019**, 2,11, 955-970.
[230] S.J. Tauster, Strong metal-support interactions, *Acc. Chem. Res.*, **1987**, 20,11, 389-394.
[231] M. Antonietti, N. Lopez-Salas, A. Primo, Adjusting the Structure and Electronic Properties of Carbons for Metal-Free Carbocatalysis of Organic Transformations, *Adv. Mater.*, **2019**, 31,13.

[232] M. Antonietti, M. Oschatz, The Concept of “Noble, Heteroatom-Doped Carbons,” Their Directed Synthesis by Electronic Band Control of Carbonization, and Applications in Catalysis and Energy Materials, *Adv. Mater.*, **2018**, 30,21, 1706836.
[233] Z.B. Zhuang, S.A. Giles, J. Zheng, G.R. Jenness, S. Caratzoulas, D.G. Vlachos, Y.S. Yan, Nickel supported on nitrogen-doped carbon nanotubes as hydrogen oxidation reaction catalyst in alkaline electrolyte, *Nat. Comm.*, **2016**, 7.
[234] Z.H. Xue, J.T. Han, W.J. Feng, Q.Y. Yu, X.H. Li, M. Antonietti, J.S. Chen, Tuning the Adsorption Energy of Methanol Molecules Along Ni-N-Doped Carbon Phase Boundaries by the Mott-Schottky Effect for Gas-Phase Methanol Dehydrogenation, *Angew. Chem. Int. Ed.* . **2018**, 57,10, 2697-2701.
[235] S. Büchele, Z. Chen, S. Mitchell, R. Hauert, F. Krumeich, J. Pérez-Ramírez, Tailoring Nitrogen-Doped Carbons as Hosts for Single-Atom Catalysts, *Chemcatchem*. **2019**, 11,12, 2812-2820.
[236] L. He, F. Weniger, H. Neumann, M. Beller, Synthesis, Characterization, and Application of Metal Nanoparticles Supported on Nitrogen-Doped Carbon: Catalysis beyond Electrochemistry, *Angew. Chem. Int. Ed.*, **2016**, 55,41, 12582-12594.
[237] X.H. Li, M. Antonietti, Metal nanoparticles at mesoporous N-doped carbons and carbon nitrides: functional Mott-Schottky heterojunctions for catalysis, *Chem. Soc. Rev.*, **2013**, 42,16, 6593-6604.
[238] H. Wang, Y. Shao, S. Mei, Y. Lu, M. Zhang, J.K. Sun, K. Matyjaszewski, M. Antonietti, J. Yuan, Polymer-Derived Heteroatom-Doped Porous Carbon Materials, *Chem. Rev.*, **2020**, 120,17, 9363-9419.
[239] S.K. Kaiser, Z. Chen, D. Faust Akl, S. Mitchell, J. Perez-Ramirez, Single-Atom Catalysts across the Periodic Table, *Chem. Rev.*, **2020**, 120,21, 11703-11809.
[240] S. Lama, M. Antonietti, Efficiency of Ni-nanoparticles deposited on a hierarchically porous carbon doped with nitrogen for kraft lignin hydrogenolysis in flow and batch systems, *Abstr Pap Am Chem S*. **2017**, 253.
[241] H. Su, K.X. Zhang, B. Zhang, H.H. Wang, Q.Y. Yu, X.H. Li, M. Antonietti, J.S. Chen, Activating Cobalt Nanoparticles via the Mott-Schottky Effect in Nitrogen-Rich Carbon Shells for Base-Free Aerobic Oxidation of Alcohols to Esters, *J. Am. Chem. Soc.*, **2017**, 139,2, 811-818.
[242] Z.H. Xue, J.T. Han, W.J. Feng, Q.Y. Yu, X.H. Li, M. Antonietti, J.S. Chen, Tuning the Adsorption Energy of Methanol Molecules Along Ni-N-Doped Carbon Phase Boundaries by the Mott-Schottky Effect for Gas-Phase Methanol Dehydrogenation, *Angew. Chem. Int. Ed.*, **2018**, 57,10, 2697-2701.
[243] V.G. Ramu, A. Bordoloi, T.C. Nagaiah, W. Schuhmann, M. Muhler, C. Cabrele, Copper nanoparticles stabilized on nitrogen-doped carbon nanotubes as efficient and recyclable catalysts for alkyne/aldehyde/cyclic amine A3-type coupling reactions, *App. Catal. A Gen.*, **2012**, 431-432,88-94.

[244] A.D. Roberts, X. Li, H. Zhang, Porous carbon spheres and monoliths: morphology control, pore size tuning and their applications as Li-ion battery anode materials, *Chem. Soc. Rev.*, **2014**, 43,13, 4341-4356.
[245] X.Y. Yang, L.H. Chen, Y. Li, J.C. Rooke, C. Sanchez, B.L. Su, Hierarchically porous materials: synthesis strategies and structure design, *Chem. Soc. Rev.*, **2017**, 46,2, 481-558.
[246] T.P. Fellinger, A. Thomas, J. Yuan, M. Antonietti, 25th anniversary article: "Cooking carbon with salt": carbon materials and carbonaceous frameworks from ionic liquids and poly(ionic liquid)s, *Adv. Mater.*, **2013**, 25,41, 5838-5854.
[247] N. Fechler, T.P. Fellinger, M. Antonietti, "Salt templating": a simple and sustainable pathway toward highly porous functional carbons from ionic liquids, *Adv. Mater.*, **2013**, 25,1, 75-79.
[248] R. Hirschler, Whiteness, yellowness, and browning in food colorimetry, *Color in Food: Technological and Psychophysical Aspects. Editorial JL Caivano & Buera MP EE. UU*. **2012**, 93-104.
[249] FAO - Food and Agricolture Organization of the United Nations,The state of Food Agricolture 2019. Moving forward on food loss and waste reduction, **2019**,
[250] G. Chen, Y. Li, Aggregation behavior of semolina gluten during dough production and fresh pasta cooking upon kansui treatment, *Food Chem.*, **2019**, 278,579-586.
[251] J. Buchert, D. Ercili Cura, H. Ma, C. Gasparetti, E. Monogioudi, G. Faccio, M. Mattinen, H. Boer, R. Partanen, E. Selinheimo, R. Lantto, K. Kruus, Crosslinking food proteins for improved functionality, *Annu. Rev. Food. Sci .Technol.*, **2010**, 1,113-138.
[252] H.M.C. Azeredo, K.W. Waldron, Crosslinking in polysaccharide and protein films and coatings for food contact – A review, *Trends Food Sci. Technol.*, **2016**, 52,109-122.
[253] R. Rothe, M. Antonietti, N. Fechler, The bakery of high-end sorption carbons: sugar-urea doughs as processable precursors for functional carbons, *J Mater Chem A*. **2017**, 5,31, 16352-16358.
[254] R. Yan, K. Leus, J.P. Hofmann, M. Antonietti, M. Oschatz, Porous nitrogen-doped carbon/carbon nanocomposite electrodes enable sodium ion capacitors with high capacity and rate capability, *Nano Energy*. **2019**, 104240.
[255] P. Strubel, S. Thieme, T. Biemelt, A. Helmer, M. Oschatz, J. Bruckner, H. Althues, S. Kaskel, ZnO Hard Templating for Synthesis of Hierarchical Porous Carbons with Tailored Porosity and High Performance in Lithium-Sulfur Battery, *Adv. Funct. Mater.*, **2015**, 25,2, 287-297.
[256] S.M.G. Lama, J. Pampel, T.P. Fellinger, V.P. Beskoski, L. Slavkovic-Beskoski, M. Antonietti, V. Molinari, Efficiency of Ni Nanoparticles Supported on Hierarchical Porous Nitrogen-Doped Carbon for Hydrogenolysis of Kraft Lignin in Flow and Batch Systems, *Acs Sustain. Chem. Eng*. **2017**, 5,3, 2415-2420.
[257] Z.H. Xue, J.T. Han, W.J. Feng, Q.Y. Yu, X.H. Li, M. Antonietti, J.S. Chen, Tuning the Adsorption Energy of Methanol Molecules Along Ni-N-Doped Carbon

Phase Boundaries by the Mott–Schottky Effect for Gas-Phase Methanol Dehydrogenation, *Angew. Chem. Int. Ed.*, **2018**, 57,10, 2697-2701.
[258] C.M. Mani, M. Braun, V. Molinari, M. Antonietti, N. Fechler, A High-Throughput Composite Catalyst based on Nickel Carbon Cubes for the Hydrogenation of 5-Hydroxymethylfurfural to 2,5-Dimethylfuran, *Chemcatchem*. **2017**, 9,17, 3388-3394.
[259] K.P. Gierszal, M. Jaroniec, T.W. Kim, J. Kim, R. Ryoo, High temperature treatment of ordered mesoporous carbons prepared by using various carbon precursors and ordered mesoporous silica templates, *New J. Chem.*, **2008**, 32,6, 981-993.
[260] M. Bäumel, Upgrading of Lignocellulosic Biomass Derived Carbohydrates to Vallue-added Chemicals via Heterogeneously Catalyzed Flow Processes, *Technische Universität Berlin*. **2019**, Diplom-Chemieingenieur.
[261] S.K.R. Patil, J. Heltzel, C.R.F. Lund, Comparison of Structural Features of Humins Formed Catalytically from Glucose, Fructose, and 5-Hydroxymethylfurfuraldehyde, *Energ Fuel*. **2012**, 26,8, 5281-5293.
[262] N. Shi, Q.Y. Liu, R.M. Ju, X. He, Y.L. Zhang, S.Y. Tang, L.L. Ma, Condensation of alpha-Carbonyl Aldehydes Leads to the Formation of Solid Humins during the Hydrothermal Degradation of Carbohydrates, *Acs Omega*. **2019**, 4,4, 7330-7343.
[263] D.S. Hall, D.J. Lockwood, C. Bock, B.R. MacDougall, Nickel hydroxides and related materials: a review of their structures, synthesis and properties, *Proceedings of the Royal Society A: Mathematical, Physical and Engineering Sciences*. **2015**, 471,2174, 20140792.
[264] M.M. Li, J. Deng, Y.K. Lan, Y. Wang, Efficient Catalytic Hydrodeoxygenation of Aromatic Carbonyls over a Nitrogen-Doped Hierarchical Porous Carbon Supported Nickel Catalyst, *Chemistryselect*. **2017**, 2,27, 8486-8492.
[265] J. Xi, Y. Zhang, D. Ding, Q. Xia, J. Wang, X. Liu, G. Lu, Y. Wang, Catalytic production of isosorbide from cellulose over mesoporous niobium phosphate-based heterogeneous catalysts via a sequential process, *Appl. Catal. A-Gen.* **2014**, 469,108-115.
[266] J.U. Oltmanns, S. Palkovits, R. Palkovits, Kinetic investigation of sorbitol and xylitol dehydration catalyzed by silicotungstic acid in water, *Appl. Catal. A-Gen.*. **2013**, 456,168-173.
[267] M. Al-Naji, J. Van Aelst, Y. Liao, M. d'Hullian, Z. Tian, C. Wang, R. Gläser, B.F. Sels, Pentanoic acid from γ-valerolactone and formic acid using bifunctional catalysis, *Green Chem*. **2020**, 22,4, 1171-1181.
[268] L. Zhang, K. Chen, B. Chen, J.L. White, D.E. Resasco, Factors that Determine Zeolite Stability in Hot Liquid Water, *J Am Chem Soc*. **2015**, 137,36, 11810-11819.
[269] B. Op de Beeck, J. Geboers, S. Van de Vyver, J. Van Lishout, J. Snelders, W.J. Huijgen, C.M. Courtin, P.A. Jacobs, B.F. Sels, Conversion of (ligno)cellulose

feeds to isosorbide with heteropoly acids and Ru on carbon, *ChemSusChem*. **2013**, 6,1, 199-208.
[270] T. Aro, P. Fatehi, Production and application of lignosulfonates and sulfonated lignin, *Chemsuschem*. **2017**, 10,9, 1861-1877.
[271] Z. Strassberger, S. Tanase, G. Rothenberg, The pros and cons of lignin valorisation in an integrated biorefinery, *RSC Adv.*, **2014**, 4,48, 25310-25318.
[272] S. Laurichesse, L. Avérous, Chemical modification of lignins: Towards biobased polymers, *Prog. Polym. Sci.*, **2014**, 39,7, 1266-1290.
[273] P. Fatehi, Y. Ni, Integrated Forest Biorefinery − Sulfite Process Pedram in: B. Zhu (Ed.) Sustainable Production of Fuels, Chemicals, and Fibers from Forest Biomass, ACS Symposium Series; American Chemical Society: , Washington, DC, **2011**.
[274] J.E. Holladay, J.F. White, J.J. Bozell, D. Johnson Top value-added chemicals from biomass-Volume II—Results of screening for potential candidates from biorefinery lignin, Pacific Northwest National Lab.(PNNL), Richland, WA (United States), **2007**,
[275] M.Y.A. Mollah, W. Yu, R. Schennach, D.L. Cocke, A Fourier transform infrared spectroscopic investigation of the early hydration of Portland cement and the influence of sodium lignosulfonate, *Cemen. Concr. Research*. **2000**, 30, 267-273.
[276] L. Hu, Y. Zhou, M. Zhang, R. Liu, Characterization and properties of a lignosulfonate-based phenolic foam, *Bioresources*. **2012**, 7,1, 554-564.
[277] Borregaard Potential applications for different lignin sources based on experience from Borregaard,https://www.google.com/url?sa=t&rct=j&q=&esrc=s&source=web&cd=&ved=2ahUKEwit0eSf7KruAhURahQKHRtFCFoQFjAAegQIBxAC&url=http%3A%2F%2Fwww.lth.se%2Ffileadmin%2Fenergiportalen%2FEnergy_Portal%2FFiles%2FPres_Rodsrud.pdf&usg=AOvVaw2jH3uyvQBINJ-PiQySZp9l, accessed on 27 January 2021.
[278] Y. Qin, D. Yang, X. Qiu, Hydroxypropyl Sulfonated Lignin as Dye Dispersant: Effect of Average Molecular Weight, *Acs Sustain. Chem. Eng.*, **2015**, 3,12, 3239-3244.
[279] S. Gao, Z. Cheng, X. Zhou, Y. Liu, R. Chen, J. Wang, C. Wang, F. Chu, F. Xu, D. Zhang, Unexpected role of amphiphilic lignosulfonate to improve the storage stability of urea formaldehyde resin and its application as adhesives, *Int. J. Biol. Macromol*. **2020**, 161,755-762.
[280] B.V.K.J. Schmidt, V. Molinari, D. Esposito, K. Tauer, M. Antonietti, Lignin-based polymeric surfactants for emulsion polymerization, *Polymer*. **2017**, 112,418-426.
[281] C. Che, M. Vagin, U. Ail, V. Gueskine, J. Phopase, R. Brooke, R. Gabrielsson, M.P. Jonsson, W.C. Mak, M. Berggren, X. Crispin, Twinning Lignosulfonate with a Conducting Polymer via Counter-Ion Exchange for Large-Scale Electrical Storage, *Adv. Sustain. Syst.*, **2019**, 3,9.

[282] R. Guterman, V. Molinari, E. Josef, Ionic Liquid Lignosulfonate: Dispersant and Binder for Preparation of Biocomposite Materials, *Angew. Chem. Int. Ed.*, **2019**, 58,37, 13044-13050.
[283] X. Zhang, A.L. Licon, T.I. Harris, P.F. Oliveira, B.J. McFarland, B.E. Taurone, B.J. Walsh, B.E. Bell, C.T. Walker, R.V. Lewis, J.A. Jones, Silkworms with Spider Silklike Fibers Using Synthetic Silkworm Chow Containing Calcium Lignosulfonate, Carbon Nanotubes, and Graphene, *ACS Omega*. **2019**, 4,3, 4832-4838.
[284] J. Pang, W. Zhang, H. Zhang, J. Zhang, H. Zhang, G. Cao, M. Han, Y. Yang, Sustainable nitrogen-containing hierarchical porous carbon spheres derived from sodium lignosulfonate for high-performance supercapacitors, *Carbon*. **2018**, 132,280-293.
[285] V. Molinari, M. Antonietti, Lignin-based composite materials and methods for its preparation, (European patent office Patent No EP 3 266 810 A1), 2018,
[286] H. Sadeghifar, A. Ragauskas, Perspective on Technical Lignin Fractionation, *Acs Sustain. Chem. Eng.*, **2020**, 8,22, 8086-8101.
[287] J. Horáček, J.-P. Mikkola, A. Samikannu, G. Šťávová, W. Larsson, L. Hora, D. Kubička, Studies on Sodium Lignosulfonate Depolymerization Over Al2O3 Supported Catalysts Loaded with Metals and Metal Oxides in a Continuous Flow Reactor, *Top Catal*. **2013**, 56,9-10, 794-799.
[288] R. Shu, Y. Xu, L. Ma, Q. Zhang, T. Wang, P. Chen, Q. Wu, Hydrogenolysis process for lignosulfonate depolymerization using synergistic catalysts of noble metal and metal chloride, *RSC Adv.*, **2016**, 6,91, 88788-88796.
[289] Q. Song, F. Wang, J. Xu, Hydrogenolysis of lignosulfonate into phenols over heterogeneous nickel catalysts, *Chem. Commun.*, **2012**, 48,56, 7019-7021.
[290] P. Cui, H.-X. Fang, C. Qian, M.-H. Cheng, Detection and Identification of Lignosulfonate Depolymerization Products Using UPLC-QTOF-MS and a Self-Built Database, *Chromatographia*. **2019**, 83,1, 87-93.
[291] M. Fache, B. Boutevin, S. Caillol, Vanillin Production from Lignin and Its Use as a Renewable Chemical, *Acs Sustain. Chem. Eng.*, **2015**, 4,1, 35-46.
[292] S.G. Parto, J.M. Christensen, L.S. Pedersen, A.B. Hansen, F. Tjosås, C. Spiga, C.D. Damsgaard, D.B. Larsen, J.Ø. Duus, A.D. Jensen, Liquefaction of Lignosulfonate in Supercritical Ethanol Using Alumina-Supported NiMo Catalyst, *Energ Fuel*. **2019**, 33,2, 1196-1209.
[293] S. Ghafarnejad Parto, J. Munkholt Christensen, L. Saaby Pedersen, F. Tjosås, A. Degn Jensen, Solvothermal Conversion of Lignosulfonate Assisted by Ni Catalyst: Investigation of the Role of Ethanol and Ethylene Glycol as Solvents, *Catalysts*. **2018**, 8,11.
[294] O. Musl, I. Sulaeva, M. Bacher, A.K. Mahler, T. Rosenau, A. Potthast, Hydrophobic Interaction Chromatography in 2 D Liquid Chromatography Characterization of Lignosulfonates, *Chemsuschem*. **2020**.
[295] B.F. Lutnaes, B.O. Myrvold, R.A. Lauten, M.M. Endeshaw, 1H and 13C NMR data of benzylsulfonic acids-model compounds for lignosulfonate, *Magn Reson Chem*. **2008**, 46,3, 299-305.

[296] M. Alonso, M. Oliet, F. Rodriguez, G. Astarloa, J. Echeverría, Use of a methylolated softwood ammonium lignosulfonate as partial substitute of phenol in resol resins manufacture, *J. App. Polym. Sci.*, **2004**, 94,2, 643-650.
[297] K. Fukuhara, K. Nakajima, M. Kitano, S. Hayashi, M. Hara, Synthesis and acid catalysis of zeolite-templated microporous carbons with SO3H groups, *Phys Chem Chem Phys*. **2013**, 15,23, 9343-9350.
[298] E.M. Anderson, M.L. Stone, R. Katahira, M. Reed, G.T. Beckham, Y. Román-Leshkov, Flowthrough Reductive Catalytic Fractionation of Biomass, *Joule*. **2017**, 1,3, 613-622.
[299] W. Schutyser, S. Van den Bosch, T. Renders, T. De Boe, S.F. Koelewijn, A. Dewaele, T. Ennaert, O. Verkinderen, B. Goderis, C.M. Courtin, B.F. Sels, Influence of bio-based solvents on the catalytic reductive fractionation of birch wood, *Green Chem.*, **2015**, 17,11, 5035-5045.
[300] B.D. Mar, H.W. Qi, F. Liu, H.J. Kulik, Ab Initio Screening Approach for the Discovery of Lignin Polymer Breaking Pathways, *J. Phys. Chem. A*. **2015**, 119,24, 6551-6562.
[301] J.H. Li, C.F. Lin, W. Qin, X.B. Xiao, L. Wei, Synergetic Effect of Mercury Adsorption on the Catalytic Decomposition of CO over Perfect and Reduced Fe2O3[001] Surface, *Acta Phys-Chim Sin*. **2016**, 32,11, 2717-2723.
[302] S.M.G. Lama, J. Pampel, T.-P. Fellinger, V.P. Beškoski, L. Slavković-Beškoski, M. Antonietti, V. Molinari, Efficiency of Ni Nanoparticles Supported on Hierarchical Porous Nitrogen-Doped Carbon for Hydrogenolysis of Kraft Lignin in Flow and Batch Systems, *Acs Sustain Chem Eng*. **2017**, 5,3, 2415-2420.
[303] N.M. Clauser, S. Gutiérrez, M.C. Area, F.E. Felissia, M.E. Vallejos, Techno-economic assessment of carboxylic acids, furfural, and pellet production in a pine sawdust biorefinery, *Biofuels, Bioprod. Bioref*. **2018**, 12,6, 997-1012.
[304] A. Kożuch, J. Banaś, The Dynamics of Beech Roundwood Prices in Selected Central European Markets, *Forests*. **2020**, 11,9.
[305] J.M. Harkin Uses for Sawdust, Shavings, and Waste Chips, U.S. Departement of Agricolture - Forest Service - Forest Products Laboratory, **1969**,
[306] R. Rinaldi, A Tandem for Lignin-First Biorefinery, *Joule*. **2017**, 1,3, 427-428.
[307] E.M. Anderson, M.L. Stone, M.J. Hülsey, G.T. Beckham, Y. Román-Leshkov, Kinetic Studies of Lignin Solvolysis and Reduction by Reductive Catalytic Fractionation Decoupled in Flow-Through Reactors, *Acs Sustain. Chem. Eng.*, **2018**, 6,6, 7951-7959.
[308] W. Lan, Y.P. Du, S. Sun, J. Behaghel de Bueren, F. Héroguel, J.S. Luterbacher, Continuous hydrogenolysis of acetal-stabilized lignin in flow, *Green Chem*. **2021**, 23,1, 320-327.
[309] J. Gong, J. Li, J. Xu, Z. Xiang, L. Mo, Research on cellulose nanocrystals produced from cellulose sources with various polymorphs, *RSC Advances*. **2017**, 7,53, 33486-33493.
[310] S. Yasuda, K. Fukushima, A. Kakehi, Formation and CHemical Structure of Acid-soluble Lignin I : Sulfuric Acid Treatment ans Acid-soluble Lignin Content of Hardwood, *J Wood Sci.*, **2001**, 47,69-72.

[311] I. Kumaniaev, E. Subbotina, J. Sävmarker, M. Larhed, M.V. Galkin, J.S.M. Samec, Lignin depolymerization to monophenolic compounds in a flow-through system, *Green Chem*. **2017**, 19,24, 5767-5771.
[312] R. El Hage, N. Brosse, L. Chrusciel, C. Sanchez, P. Sannigrahi, A. Ragauskas, Characterization of milled wood lignin and ethanol organosolv lignin from miscanthus, *Polymer Degradation and Stability*. **2009**, 94,10, 1632-1638.
[313] A.M.L. Seca, J.A.S. Cavaleiro, F.M.J. Domingues, A.J.D. Silvestre, D. Evtuguin, C. Pascoal Neto, Structural Characterization of the Lignin from the Nodes and Internodes of Arundo donax Reed, *J. Agric. Food Chem*. **2000**, 48,3, 817-824.
[314] T. Kishimoto, W. Chiba, K. Saito, K. Fukushima, Y. Uraki, M. Ubukata, Influence of syringyl to guaiacyl ratio on the structure of natural and synthetic lignins, *J Agric. Food. Chem*. **2010**, 58,2, 895-901.
[315] Y. Gu, F. Jerome, Bio-based solvents: an emerging generation of fluids for the design of eco-efficient processes in catalysis and organic chemistry, *Chem. Soc. Rev.*, **2013**, 42,24, 9550-9570.
[316] I. Lauermann, A. Steigert, CISSY: A station for preparation and surface/interface analysis of thin film materials and devices, *Journal of large-scale research facilities JLSRF*. **2016**, 2,67.
[317] I. Khalil, H. Jabraoui, G. Maurin, S. Lebègue, M. Badawi, K. Thomas, F. Maugé, Selective Capture of Phenol from Biofuel Using Protonated Faujasite Zeolites with Different Si/Al Ratios, *The Journal of Physical Chemistry C*. **2018**, 122,46, 26419-26429.
[318] C. Emeis, Determination of integrated molar extinction coefficients for infrared absorption bands of pyridine adsorbed on solid acid catalysts, *J. Catal.*, **1993**, 141,2, 347-354.
[319] I. Khalil, K. Thomas, H. Jabraoui, P. Bazin, F. Maugé, Selective elimination of phenol from hydrocarbons by zeolites and silica-based adsorbents—Impact of the textural and acidic properties, *Journal of hazardous materials*. **2020**, 384,121397.
[320] J.P. Gallas, J.M. Goupil, A. Vimont, J.C. Lavalley, B. Gil, J.P. Gilson, O. Miserque, Quantification of water and silanol species on various silicas by coupling IR spectroscopy and in-situ thermogravimetry, *Langmuir*. **2009**, 25,10, 5825-5834.
[321] J. Nakano, G. Meshitsuka, The Detection of Lignin, in: S.Y. Lin, C.W. Dence (Eds.) Methods in Lignin chemistry, Springer-Verlag, Berlin-Heidelberg, **1992**, pp. 23-61.
[322] P. Hergrtsberg, V. Molinari, *Max Planck Research Magazine*. **2019**, 1-2019,1. 2019, 66.
[323] N.H. S. NAMBA, T. YASHIMA, Catalytic application for hydrophopic properties of high silica zeolite *J. Catal.*, **1981**, 72, 16-20.
[324] J. Zhang, L. Wang, F. Liu, X. Meng, J. Mao, F.-S. Xiao, Enhanced catalytic performance in dehydration of sorbitol to isosorbide over a superhydrophobic mesoporous acid catalyst, *Catal Today*. **2015**, 242,249-254.

[325] I. Khalil, C.M. Celis-Cornejo, K. Thomas, P. Bazin, A. Travert, D.J. Pérez-Martínez, V.G. Baldovino-Medrano, J.F. Paul, F. Maugé, In Situ IR-ATR Study of the Interaction of Nitrogen Heteroaromatic Compounds with HY Zeolites: Experimental and Theoretical Approaches, *Chemcatchem*. **2019**, 12,4, 1095-1108.
[326] A. Palcic, V.V. Ordomsky, Z. Qin, V. Georgieva, V. Valtchev, Tuning Zeolite Properties for a Highly Efficient Synthesis of Propylene from Methanol, *Chemistry*. **2018**, 24,50, 13136-13149.
[327] H. Jabraoui, I. Khalil, S. Lebègue, M. Badawi, Ab initio screening of cation-exchanged zeolites for biofuel purification, *Molecular Systems Design & Engineering*. **2019**, 4,4, 882-892.
[328] C. Mei, C. Hu, Q. Hu, C. Sun, L. Li, X. Liang, Y. Dong, X. Gu, Effective Depolymerization of Sodium Lignosulfonate over SO42−/TiO2 Catalyst, *Catalysts*. **2020**, 10,9.
[329] V. Hemmilä, R. Hosseinpourpia, S. Adamopoulos, A. Eceiza, Characterization of Wood-based Industrial Biorefinery Lignosulfonates and Supercritical Water Hydrolysis Lignin, *Waste and Biomass Valorization*. **2019**, 11,11, 5835-5845.
[330] W. Chen, X.-w. Peng, L.-x. Zhong, Y. Li, R.-c. Sun, Lignosulfonic Acid: A Renewable and Effective Biomass-Based Catalyst for Multicomponent Reactions, *Acs Sustain. Chem. Eng.*, **2015**, 3,7, 1366-1373.

[331] L.A. Colon, L.J. Baird, Modern Practice of Gas Chromatography, R. Grob, L. Barry, Eds, John Wiley & Sons, Inc, 2004 pag 275-337

Declaration

Die vorliegende Dissertation entstand in dem Zeitraum zwischen Januar 2019 und März 2021 am Max-Planck-Institut für Kolloid- und Grenzflächenforschung unter Betreuung von Prof. Dr. Dr. h.c. Markus Antonietti.

Hiermit erkläre ich, dass die vorliegende Arbeit selbstständig angefertigt wurde und keine anderen als die angegebenen Hilfsmittel und Quelle verwendet wurden.

Die Arbeit wurde bisher weder im Inland noch im Ausland in gleicher oder ähnlicher Form einer anderen Prüfungsbehörde vorgelegt. Es habe bisher keine früheren erfolglosen Promotionsverfahren stattgefunden.

The present work was carried during the period between January 2019 and March 2021 at the Max Planck Institute of Colloids and Interfaces under the supervision of Prof. Dr. Dr. h.c. Markus Antonietti.

I declare that I have written this work on my own and used no other than the named aids and references. This thesis was not submitted to another examination board in this or other countries. There were no unsuccessful examination processes.

Francesco Brandi

POTSDAM, den 28.03.2021